

Copyright  
by  
Arjang Gandomkar  
2018

**The Dissertation Committee for Arjang Gandomkar Certifies that this is the approved version of the following dissertation:**

**THERMOPOROELASTIC WELLBORE STABILITY MODEL WITH  
LOCAL THERMAL NON-EQUILIBRIUM**

**Committee:**

---

Kenneth E. Gray, Supervisor

---

Hugh Daigle

---

John Jones

---

Jon Olson

---

Harry Millwater

---

Arturo Montoya

**THERMOPOROELASTIC WELLBORE STABILITY MODEL WITH  
LOCAL THERMAL NON-EQUILIBRIUM**

**by**

**Arjang Gandomkar**

**Dissertation**

Presented to the Faculty of the Graduate School of  
The University of Texas at Austin  
in Partial Fulfillment  
of the Requirements  
for the Degree of

**Doctor of Philosophy**

**The University of Texas at Austin**

**December 2018**

*Dedicated to my family  
for their endless love, encouragement, and support*

## **Acknowledgements**

I would like to express my sincerest gratitude to my supervisor, Dr. Kenneth E. Gray for giving me the opportunity to conduct research in the Wider Windows research program. I appreciated his effort, support, and invaluable guidance throughout my research. His profound and vast knowledge has taught me a lot of priceless lessons.

I acknowledge my colleagues and friends in our research group and Petroleum and Geosystems Engineering department, Yongcun Feng, Chiranth Hegde, Chao Gao, Xiaorong Li, Cesar Soares, Azor Nwachukwu, Chris Griffith, Peidong Zhao, Mayowa Oyedere, Hamza Jaffal, Ali Abouei, Alireza Sanaei, and many other friends who are not mentioned for all their technical discussions and moral support. I would not have enjoyed such a memorable and productive time without them at school.

I would like to thank my dissertation committee members Dr. Harry Millwater, Dr. Jon Olson, Dr. Arturo Montoya, Dr. Hugh Daigle, and Mr. John Jones for their helpful suggestions and support.

I acknowledge the staff of PGE department at The University of Texas at Austin: Frankie Hart, Amy Stewart, Mary Pettengil, Jessica Yeager, Glen Baum, Dr. Ewegeny Podnos, John Cassibry, and Dr. Kamy Sephernoori for their technical and administrative support.

The research presented in this dissertation is under the Wider Windows Industrial Affiliate Program at the University of Texas at Austin. The program is sponsored by BHP Billiton, British Petroleum, Chevron, ConocoPhillips, Halliburton, Marathon, National Oilwell Varco, Occidental Oil and Gas, and Shell. I am grateful for the sponsors' financial support. The findings, conclusions, and recommendations expressed herein are those of the

author and do not necessarily reflect the views of the sponsors.

Finally, I express my sincere appreciation to my beloved family for their endless love and their incredible support through my entire life.

# **THERMOPOROELASTIC WELLBORE STABILITY MODEL WITH LOCAL THERMAL NON-EQUILIBRIUM**

Arjang Gandomkar, Ph.D.

The University of Texas at Austin, 2018

Supervisor: Kenneth E. Gray

Wellbore stability is a key challenge for the exploration and production industry since it adds a great deal of additional cost. Traditional wellbore stability models such as elastic and poroelastic models are not sufficient in modeling the stability and produce erroneous results since they consider an isothermal condition. The industry also overlooks the potential impact of thermal effects on wellbore stability and utilizes a trivial approach in modeling the thermal stresses.

During the drilling phase, the drilling fluid temperature is different from the formation temperature due to geothermal gradient and circulation of the mud inside the wellbore. Therefore, the assumption of an isothermal condition will not predict the correct wellbore stability condition, especially for high pressure and high temperature wells.

The knowledge of in-situ stresses, breakout, and breakdown is vital to oil and gas industry, affecting wellbore stability, well location, production rate, completion and casing designs. Determination of breakout pressure helps avoid wellbore enlargement and shear failure, while, breakdown pressure aids in knowledge of the formation fracture gradient and the limits for the drilling mud weight window. Estimations of breakout and breakdown gradients can substantially be affected by the induced thermal stresses that occur during the drilling phase of a wellbore.

The fully coupled thermoporoelastic model developed in this dissertation reveals the importance of induced thermal stress in stress resolution and wellbore stability evaluation. It produces reasonable results compared to uncoupled models and models with isothermal assumption.

Most existing thermoporoelastic models utilize the assumption of local thermal equilibrium. The local thermal equilibrium assumption ignores additional pore and thermal stresses in the porous medium caused by temperature variations of the fluid and solid phases. This dissertation investigates the effect of thermal stresses on stress resolution around a wellbore and wellbore stability in a fully coupled condition with consideration of local thermal non-equilibrium heat transfer. The model is applicable for any wellbore trajectories in low and high permeable formations with consideration of conductive and convective heat transfers.



## Table of Contents

List of Tables .....	xii
List of Figures .....	xiii
Nomenclature .....	xix
<b>CHAPTER 1: INTRODUCTION.....</b>	<b>1</b>
1.1 Motivation and objectives.....	1
1.2 Dissertation outline .....	4
<b>CHAPTER 2: WELLBORE STABILITY.....</b>	<b>6</b>
2.1 Wellbore stability issues .....	6
2.2 Factors influencing wellbore stability.....	11
2.2.1 Uncontrollable.....	11
2.2.2 Controllable.....	11
2.3 Existing wellbore stability models.....	12
2.4 Thermoporoelastic model .....	17
<b>CHAPTER 3: INDUCED THERMAL STRESSES EFFECT ON BREAKDOWN AND BREAKOUT</b> <b>.....</b>	<b>25</b>
3.1 Wellbore stability: breakout and breakdown .....	26
3.2 Breakout and breakdown models.....	27
3.3 Results.....	34
3.4 Conclusions.....	42
<b>CHAPTER 4: THERMOPOROELASTIC MODEL BACKGROUND .....</b>	<b>44</b>
4.1 Mathematical preliminaries .....	44
4.1.1 Indicial notation .....	44
4.1.2 Calculus of tensors.....	45
4.1.3 Stress and strain analyses.....	45
4.1.3.1 Analysis of stress .....	45
4.1.3.2 Analysis of strain .....	51
4.2 Thermoporoelastic formulation .....	54

4.3 Material properties dependency on temperature and pore pressure.....	61
4.3.1 Thermal conductivity .....	62
4.3.2 Thermal expansion coefficient.....	66
4.3.3 Fluid thermal expansion.....	67
4.3.4 Porosity .....	67
4.3.5 Tensile strength.....	68
4.3.6 Elastic parameters .....	69
4.4 Local heat exchange theory .....	71
<b>CHAPTER 5: THERMOPOROELASTIC MODELS.....</b>	<b>75</b>
5.1 Introduction.....	75
5.2 Irrotational displacement .....	75
5.2.1 Displacement decoupling from temperature and pore pressure fields .....	75
5.3 Simplified cases .....	77
5.3.1 Case 1: analytical solution for low permeability formation.....	77
5.3.1.1 Solutions for modes 1 through 3 .....	80
5.3.2 Case 2: numerical solution for high permeable formation.....	82
5.3.2.1 Stress solution .....	84
5.3.3 Remarks .....	86
5.4 Failure criteria.....	86
5.4.1 Mohr-Coulomb .....	86
5.4.2 Modified Lade.....	88
5.4.3 Failure criteria comparisons.....	88
<b>CHAPTER 6: THERMOPOROELASTIC SOLUTIONS .....</b>	<b>94</b>
6.1 Induced thermal stresses .....	94
6.2 Case 1: analytical solution for low permeability formation.....	96
6.3 Case 2: numerical solution for high permeable formation.....	104
6.4 Conclusions.....	116
<b>CHAPTER 7: LOCAL THERMAL NON-EQUILIBRIUM.....</b>	<b>120</b>
7.1 Introduction to local thermal non-equilibrium.....	120

7.2	Conductive heat transfer .....	121
7.2.1	LTNE conductive model.....	122
7.2.2	Results for conductive case.....	125
7.3	Conductive and convective heat transfers.....	131
7.3.1	LTNE conductive and convective model.....	132
7.3.2	Results for conductive and convective heat transfers .....	132
7.3.3	Finite element modeling .....	141
7.4	Thermoporoelectricity under ltne .....	143
7.4.1	Case 1: analytical solution for low permeability formation.....	143
7.4.2	Case 2: numerical solution for high permeable formation.....	149
7.4.3	Remarks on numerical solution approach.....	155
7.5	Conclusions.....	158
<b>CHAPTER 8: CONCLUSIONS AND RECOMMENDATIONS .....</b>		<b>160</b>
8.1	Conclusions.....	160
8.2	Recommendations.....	161
<b>APPENDIX.....</b>		<b>164</b>
<b>REFERENCES.....</b>		<b>166</b>

## List of Tables

Table 2. 1: Lost circulation guidelines [46] .....	20
Table 2. 2: Wellbore strengthening (WBS) methods with field applications [47]	20
Table 2. 3: Shear and tensile failure types around a borehole with geometry and orientation [48].....	21
Table 2. 4: Homogenous parameters used in ABAQUS isotropic and anisotropic study .....	24
Table 3. 1: Parameters data for the effect rock properties on thermal stress .....	43
Table 3. 2: Data for breakout and breakdown models .....	43
Table 4. 1: Parameters for LTE validation.....	74
Table 6. 1: Parameters for case 1-low permeability formation with conductive heat transfer domination .....	118
Table 6. 2: Parameters for case 1-high permeability formation with convective heat transfer domination .....	119
Table 7. 1: Properties for the LTNE model .....	159

## List of Figures

Figure 1.1: High pressure high temperature drilling activities around the globe [4]1

Figure 2. 1: Schematic mud weight window .....6

Figure 2. 2: Extreme case of Gumbo shale instability- flow to the surface due to incompatible mud type with the formation [49] .....8

Figure 2. 3: (a) Caving cuttings-sign of wellbore instability vs. (b) normal cuttings observed on shale shaker [50].....9

Figure 2. 4: Image log of a wellbore with breakouts (dark area) on the wellbore wall due to excessive formation stress [51] .....9

Figure 2. 5: Image log showing typical drilling-induced tensile wall fractures in a vertical borehole and inclined tensile fractures in a deviated borehole [52].....10

Figure 2. 6: Values of Young’s modulus at 50% peak strength exhibiting a nonlinear trend with confining pressure [20] .....13

Figure 2. 7: Distribution of tangential stresses around a wellbore based on linear and non-linear dependency of Young’s Modulus.  $r_w$  is the wellbore radius .....14

Figure 2. 8: Isotropic vs. Anisotropic fracture propagation in ABAQUS finite element analysis. Different fracture paths are observed.....16

Figure 2. 9: Coupling mechanisms for a thermoporoelastic system (modified after, Li [2]).....18

Figure 3. 1: Coordinate reference for the breakout and breakdown models. Maximum horizontal stress acts in the x-axis direction, Minimum horizontal stress in y-direction, and vertical load in the z-axis direction .....28

Figure 3. 2: Top view of wellbore breakout angle or failure arc. $\omega$ is the failure angle .....	29
Figure 3. 3: Thermal expansion coefficient effect on tangential thermal stress at various temperature changes.....	35
Figure 3. 4: Young's modulus vs. tangential thermal stress at different temperature changes.....	36
Figure 3. 5: Poisson's ratio vs. tangential thermal stress at various temperature changes.....	36
Figure 3. 6: Normalized breakout pressure predictions by various models.....	38
Figure 3. 7: Error analysis of all models compared against the thermoporoelastic model.....	39
Figure 3. 8: Breakout (shear failure) arc/angle prediction along Min. horizontal stress for different models.....	39
Figure 3. 9: Normalized breakdown pressure predictions by various models.....	40
Figure 3. 10: Error analysis for breakdown pressure versus the thermoporoelastic model.....	41
Figure 3. 11: Breakdown (tensile failure) arc/angle along Max. horizontal stress for the developed models.....	41
Figure 4. 1: Arbitrary body occupying some volume $V$ in space .....	46
Figure 4. 2: Arbitrary body with arbitrary force acting on the surface.....	47
Figure 4. 3: Parallelepiped with arbitrary tractions and stress components .....	47
Figure 4. 4: Tetrahedron under arbitrary tractions and body force.....	48
Figure 4. 5: Arbitrary body under traction and body force.....	49
Figure 4. 6: An object under arbitrary Lagrangian and Eulerian deformations.....	51
Figure 4. 7: Displacements of arbitrary points in space.....	52

Figure 4. 8: Stress effect on thermal conductivity. Conductivity of a rock will increase with increasing stress. However, the increase in thermal conductivity with stress is generally small [41].....	62
Figure 4. 9: Temperature effect on thermal conductivity at 5 MPa. (a) dense limestone, marble, and dolostone, in directions parallel and perpendicular to bedding, with decimal solidity in parentheses (b) Temperature effect on thermal conductivity at 5MPa of sandstones, quartzites, and shales, with quartz shown for comparison; decimal solidity in parentheses. [109] .....	65
Figure 4. 10: Temperature effect on linear thermal expansion coefficient [41] ....	66
Figure 4. 11: Tensile strength vs. temperature [76] .....	69
Figure 4. 12: Biot’s coefficient as a function of effective pressure at two different temperatures [102] .....	70
Figure 4. 13: Skempton’s coefficient as a function of effective pressure [102] ....	71
Figure 4. 14: Temperature profile for porous media. (a) LTE temperature profile prediction (b) LTNE temperature profile.....	72
Figure 4. 15: Temperature profile for different phases under LTNE condition ....	73
Figure 5. 1: Schematic wellbore subjected to non-hydrostatic stress field, wellbore pressure and temperature .....	79
Figure 5. 2: Permeability effect on thermal and hydraulic diffusivities .....	82
Figure 5. 3: Stress transformation around a borehole [112] .....	85
Figure 5. 4: Schematic Mohr-Coulomb diagram with friction angle and initial cohesion .....	87
Figure 5. 5: Mohr-Coulomb criteria plot with effective stresses [13] .....	89
Figure 5. 6: Drucker-Prager criteria plot with effective stresses [13].....	89

Figure 5. 7: Modified Lade criteria plot with effective stresses [13].....	90
Figure 5. 8: Mogi-Coulomb criteria plot with effective stresses [13].....	90
Figure 5. 9: 3D Hoek-Brown criteria plot with effective stresses [13].....	91
Figure 5. 10: Minimum overbalance pressure in Dunham dolomite based on different rock criteria [13] .....	92
Figure 6. 1: Leak-off pressure tests at various bottom-hole temperatures [125] ...	95
Figure 6. 2: Effective tangential stress along radial distance for various periods - low permeability formation with conductive heat transfer domination. Blue dashed line is the thermoporoelastic model developed in this dissertation, and green curve is for the analytical solution developed by Wang and Papamichos. The analytical solution in transformed from the Laplace domain into time domain using Stehfest method .....	101
Figure 6. 3: Effective radial stress along radial distance (a) 1 min, (b) 10 min, and (c) 20 min - low permeability formation with conductive heat transfer domination .....	104
Figure 6. 4: Effective hoop stress without thermal stress (isothermal condition) - high permeability formation with convective heat transfer domination .	107
Figure 6. 5: Tensile failure for case 2, without thermal stress. Blue color represents no failure .....	108
Figure 6. 6: Shear failure based on Mohr-Coulomb criteria for case 2 at 10 min. Red area represents the failure region .....	109
Figure 6. 7: Compressive (shear) failure based on modified Lade criteria for case 2 at 10 min .....	110
Figure 6. 8: Effective hoop stress including thermally induced stress - high permeability formation with convective heat transfer domination .	111



Figure 6. 9: Tensile failure prediction for high permeability formation with convective heat transfer domination (case 2) at 10 min .....	112
Figure 6. 10: Compressive (shear) failure based on Mohr-Coulomb for case 2, thermally induced stress at 10 min.....	113
Figure 6. 11: Compressive (shear) failure based on modified Lade for case 2, thermally induced stress, at 10 min.....	114
Figure 6. 12: Shear and tensile failures evolution - at different times. (a) 10 sec, (b) 300 sec, and (c) 600 sec .....	116
Figure 7. 1: A borehole in an infinite rock formation subjected to a constant temperature at the borehole.....	123
Figure 7. 2: Normalized temperature profiles along radial distance for pure conductive heat transfer at short periods (a) $\tau = 0.01$ and (b) $\tau = 0.1$ .....	127
Figure 7. 3: Normalized temperature profiles along radial distance for conductive heat transfer for moderate times (a) $\tau = 0.5$ and (b) $\tau = 1.0$ .....	129
Figure 7. 4: Normalized temperature profiles along radial distance for conductive heat transfer for longer periods (a) $\tau = 1.5$ and (b) $\tau = 2.0$ .....	131
Figure 7. 5: Comparison among normalized temperature profiles produced by the exact and numerical models along radial distance for $\tau = 0.01$ .....	133
Figure 7. 6: Normalized temperature profiles with LTNE effects along radial distance for conductive and convective heat transfers at $\tau = 0.01$ .....	136
Figure 7. 7: Normalized temperature profiles with LTNE effects under conductive and convective heat transfers for $\tau = 0.05$ .....	137
Figure 7. 8: Normalized temperature profiles with LTNE effects along radial distance for $\tau = 0.1$ - conductive and convective heat transfers.....	138

Figure 7. 9: Fluid velocity effect on porous media temperature along radial distance for $\tau = 0.04$ under conductive and convective heat transfers .....	139
Figure 7. 10: Normalized temperature profiles along radial distance with conductive and convective heat transfers for $\tau = 0.04$ , $\kappa=50$ mD, and $\mu=1$ cp with various heat transfer coefficients at (a) 50 W/m <sup>2</sup> /K, (b) 500 W/m <sup>2</sup> /K, and (c) 800 W/m <sup>2</sup> /K .....	141
Figure 7. 11: LTNE conductive model verses COMSOL finite element model in (a) schematic diagram of COMSOL model (b) results produced by the models .....	143
Figure 7. 12: Effective tangential stress along radial distance produced by different stress models under pure conductive heat transfer for (a) 1 min, (b) 10 min, and (c) 20 min. Red solid line: poroelastic model, blue dashed line: thermoporoelastic model, and black dotted line: thermoporoelastic model under LTNE condition .....	146
Figure 7. 13: Effective radial stress along radial distance under pure conductive heat transfer (a) 1 min, (b) 10 min, and (c) 20 min .....	149
Figure 7. 14: Effective tangential stress along radial distance under both conductive and convective heat transfer mechanisms (a) 1 min, (b) 10 min, and (c) 20 min .....	152
Figure 7. 15: Effective radial stress along radial distance under both conductive and convective heat transfer mechanisms (a) 1 min, (b) 10 min, and (c) 20 min .....	155
Figure 7.16: Effect of grid sizes on simulation results and convergence. (a) large grid sizes (b) small grid size.....	157
Figure 7.17: Grid size effect on norm and simulation stability .....	158

## Nomenclature

$a$ & $r_w$ :	wellbore radius
$f$ :	fluid phase
$m$ :	rock matrix
$r$ :	radial, radial distance
$s$ :	solid phase e.g. rock matrix
$T$ :	temperature
$\sigma_z$ :	effective vertical stress
$\sigma_t$ :	effective tangential stress
$\sigma_r$ :	effective radial stress
TS :	tensile strength
$S_{hmax}$ & $S_H$ :	maximum horizontal stress
$S_{hmin}$ & $S_h$ :	minimum horizontal stress
$S_{r,m}$ :	total mechanical radial stress
$S_{\theta,m}$ :	total mechanical tangential stress
$P_w$ :	wellbore pressure
$P$ :	pore pressure
$\theta$ :	angle around the wellbore
$\theta_i$ :	temperature change of "i" phase
$\sigma_{r,m}$ :	effective mechanical radial stress
$\sigma_{\theta,m}$ :	effective mechanical tangential stress
$\sigma_{\theta,p}$ :	change in hoop stress due to the pore pressure change
$\sigma_{r,T}$ :	radial stress due to the temperature change
$\sigma_{\theta,T}$ :	tangential stresses due to the temperature change
$\alpha_T$ :	thermal expansion coefficient
$\alpha^{T,p}$ :	volumetric thermal expansion of pore space
$\alpha$ & $\alpha_b$ :	Biot's coefficient
B :	Skempton's coefficient

$\nu$ :	Poisson's ratio
$\nu^u$ :	undrained Poisson's ratio
$E$ :	Young's modulus
$G$ :	shear modulus
$K$ :	bulk modulus
$P_{bd}$ :	breakdown pressure
$S_o$ :	rock cohesion
UCS :	unconfined cohesive strength
$\beta$ :	friction angle
$\mu$ :	friction coefficient
$\eta$ :	internal friction of a rock
$\omega$ :	breakout failure arc angle
$\gamma$ :	breakdown arc angle
$\epsilon_{ijk}$ :	Levi-Civita symbol
$\sigma_{ij}$ :	stress matrix/components
$\epsilon_{ij}$ :	strain components
$S_{kl}$ :	total stress component
$\kappa$ :	permeability
$\phi$ :	porosity
$\rho$ :	density
$c$ & $C$ :	specific heat capacity
$c_f$ :	fluid diffusivity coefficient
$c_T$ :	thermal diffusivity coefficient
$k$ :	thermal conductivity
$h$ :	heat transfer coefficient
$v$ :	fluid velocity
$K_0$ :	modified Bessel function of zeroth order
$K_1$ :	modified Bessel function of first order
$K_2$ :	modified Bessel function of second order
$T_{BHT}$ :	wellbore bottom hole temperature

# CHAPTER 1: INTRODUCTION

## 1.1 MOTIVATION AND OBJECTIVES

The demand for oil and gas throughout the world is driving the exploration and production industry to look for new frontiers and resources. Over 50% of the proven oil and gas reserves in the US lie below 14,000 ft subsea according to the US Minerals Management Services. High pressure and high temperature (HPHT) wells are associated with these deep-water explorations. HPHT drilling has been ramped up in recent years around the globe as shown in Figure 1.1. Drilling into these deep-water fields has become possible with the advancement in drilling technology and tools. However, reaching to these reservoirs imposes their own challenges. One of the key challenges to manage in development of these fields is the wellbore stability. Traditional wellbore stability models such as poroelastic models with isothermal assumption are not sufficient in modeling the stability and produce erroneous results.

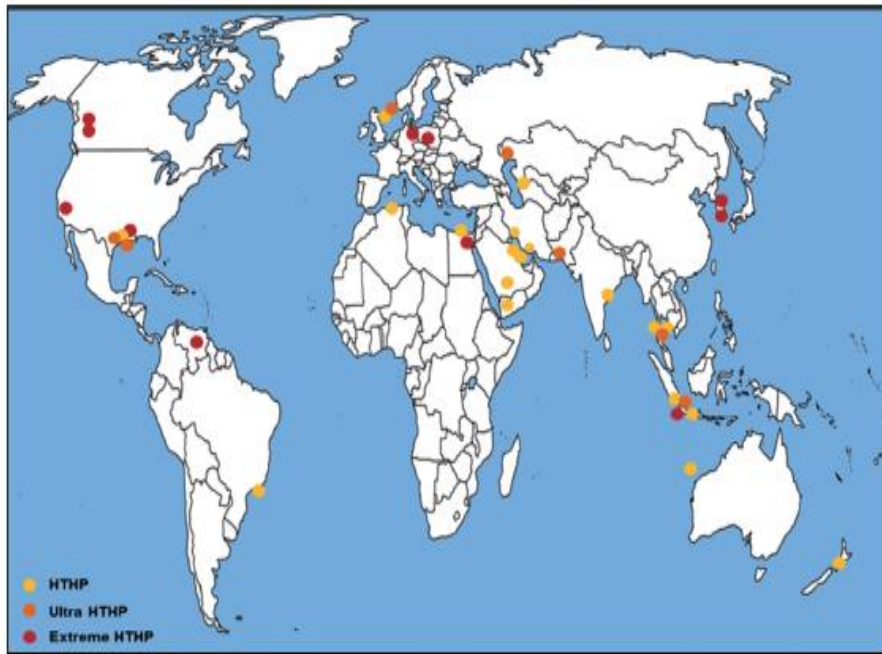


Figure 1.1: High pressure high temperature drilling activities around the globe [4]

During the drilling phase, the drilling fluid temperature is different from the formation temperature. Usually, the drilling fluid is cooler than the formation that is being drilled due to geothermal gradient. As borehole deepens, the same section will be heated up by the drilling fluid that is heated up farther downhole. This temperature change will substantially change the stress and pore pressure near the wellbore. Therefore, the assumption of isothermal condition will not predict the correct wellbore stability condition, especially for high temperature wells.

Wellbore stability is always a challenging subject to oil and gas industry. Wellbore stability issues add great deal of additional costs to the oil and gas industry. In fact, drilling instability has cost the industry over \$6B in 2005 [1]. Wellbore instability can happen anytime during lifetime of a wellbore. In general, wellbore stability is associated with the stresses around the wellbore. If the stresses are not compatible with the local stresses and strength of the formation, a wellbore instability will occur. The costs highly depend on types of environment and formations. For instance, weak, friable, plastic formations, or tectonically active areas where formations are highly stressed and discontinuous are prone to wellbore instabilities [2]. High pressure and high temperature formations can also impose wellbore instability due to their narrow mud weight window. The knowledge of in-situ stresses, breakout, and breakdown is vital to oil and gas industry, affecting wellbore stability, well location and design, and production rate. Determination of breakout pressure helps avoid wellbore enlargement and shear failure, while, breakdown pressure aids in knowledge of the formation fracture gradient and the limit for the drilling mud weight. Estimations of breakout and breakdown can substantially be affected by the induced thermal stresses.

When a wellbore is drilled, the rock is replaced by a drilling fluid that has a different temperature gradient compared to that rock. Therefore, an induced thermal stress zone

occurs around the wellbore. Stresses in poroelastic media are defined not only by in-situ stresses and pore pressure, but also depends on thermal stresses. Any change in pore pressure will redefine the stress resolution in the media. In turn, it could lead into deformation of the media. This effect is stimulated with thermal loadings, either expansion or contraction. It is important to realize that a small change in temperature change can lead into a large pore pressure change due to small thermal expansion coefficient of the media. In fact, a temperature-pressure ratio of 1, meaning a 1°C change induces a 1 MPa pore pressure change, has been measured in the field [3].

The industry has accepted that drilling is a non-isothermal process, however, it overlooks the potential impact of thermal effects on wellbore stability. Although, there are several reports and papers emphasizing thermal effect for time-delayed borehole failures. The industry utilizes a trivial approach in modeling thermal stress that is not coupled. For instance, thermal expansion and mechanical properties of formation, and temperature changes are only considered in induced thermal stress estimations, and ignoring the coupling among mechanical, thermal, and hydraulic stresses.

The fully coupled thermoporoelastic model developed in this dissertation reveals the importance of thermal stresses in wellbore stability evaluation. It produces more significant results compared to uncoupled models and models with isothermal assumption. Most of the existing thermoporoelastic models utilize the assumption of local thermal equilibrium. In classical thermodynamics in porous media such as rock formations, a single temperature is defined for the medium regardless of phases presented in the medium. This is due to the assumption that the fluid temperature and solid temperature reach a local temperature equilibrium instantly, also known as local thermal equilibrium (LTE) theory. LTE ignores additional pore and thermal stresses in the porous medium caused by temperature variations of the fluid and solid phases. Therefore, a more realistic approach

is necessary to model both temperatures separately, known as local thermal non-equilibrium (LTNE). The thermoporoelastic model in this dissertation uses LTNE and quantifies the impact of this approach.

This dissertation investigates the effect of thermal stresses on wellbore stability in a fully coupled condition. The model is applicable for any orientation and azimuth of wellbore in shale or sandstone formations.

## **1.2 DISSERTATION OUTLINE**

Chapter 1 is an overview of the research motivations and objectives. It briefly explains the importance of thermal stresses in wellbore stability modeling and evaluation.

Chapter 2 is a review of wellbore stability, including the type of wellbore failure with the root causes and remedies. This chapter explains different types of shear and tensile failures. An overview of most commonly referred wellbore stability models is included in this chapter. Also, it touches on material nonlinearity and anisotropy effects briefly.

Chapter 3 emphasizes on impact of thermal stresses in prediction of breakdown and breakout during drilling a borehole. The effect of rock elastic moduli on induced thermal stresses is investigated. The effect of stress anisotropy between far field in-situ stresses on shear and tensile failures are also studied.

Chapter 4 explains the required knowledge of several areas of applied mathematics for the theories of elasticity, stress, and heat transfer. A set of necessary governing equations in formulating thermoporoelastic model is provided. Step by step analysis in deriving the thermoporoelastic model is discussed. The material dependency of rock parameters on temperature and pressure are investigated. This chapter also briefly invokes the assumption of LTE and measures the impact of it.



Chapter 5 covers a series of analytical and numerical solutions for the thermoporoelastic model with assumption of irrotational displacement for any wellbore orientations. All the required equations for stress resolutions are stated in this chapter. A comparison among different failure criteria is conducted and impact of each failure criterion on wellbore stability is quantified.

Chapter 6 describes the results produced by the thermoporoelastic model using appropriate data. The developed thermoporoelastic model in this dissertation is compared against another thermoporoelastic model for its accuracy and predictions. Two scenarios are modeled, one in a shale formation and the other one in a sandstone formation.

Chapter 7 formulates the effect of LTNE on the thermoporoelastic model. LTE and LTNE effects for fully saturated porous media (rock formation) are considered in this chapter. Using LTNE, transient temperature profiles for solid (rock matrix) and fluid phases are defined. Using the weighted average method, a temperature for the porous medium is established. LTNE effects are examined on the developed thermoporoelastic model for a borehole in an infinite rock medium undergoing convective and conductive heat transfers.

Chapter 8 gives a summary of the research conducted in this dissertation. Recommendations are made for future development based on the current model.

## CHAPTER 2: WELLBORE STABILITY

### 2.1 WELLBORE STABILITY ISSUES

Wellbore stability issues, also known as instability, add great deal of additional costs to the oil and gas industry. Drilling instability has cost the industry billions of dollars [1]. The costs highly depend on types of environment and formations. For instance, weak, friable, plastic formations, or tectonically active areas where formations are highly stressed and discontinuous are prone to wellbore instability [2]. High pressure and high temperature, HPHT, formations can also impose wellbore instability due to their narrow mud weight windows. Mud weight window is a range of equivalent density or pressure gradient. As long as the drilling activity is within this range, drilling problems and wellbore instability may be avoided as shown in Figure 2.1.

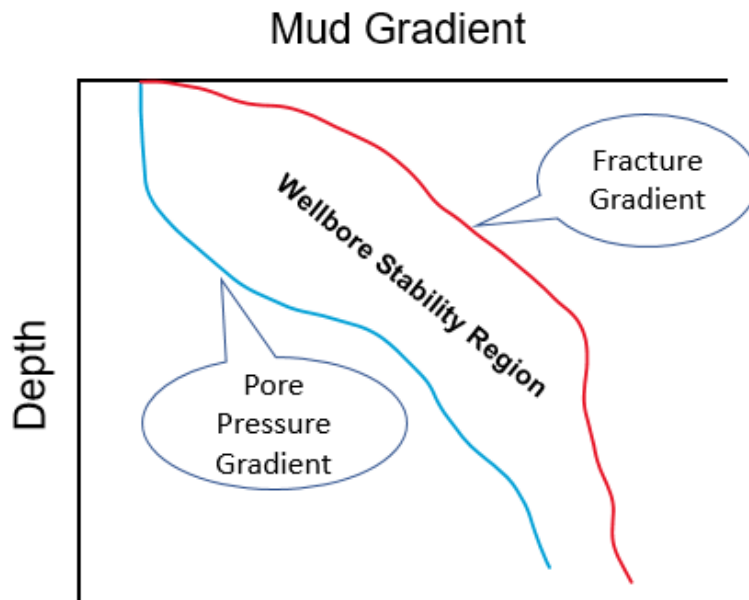


Figure 2. 1: Schematic mud weight window

Wellbore instability is not exclusive to the drilling phase, but also, plays an infamous role in completion and production phases. In fact, it can happen anytime during lifetime of a well. In general, wellbore stability is associated with the stresses around the wellbore. If

the stresses are not compatible with the local stresses and strength of the formation, a wellbore failure and instability occur. Wellbore stresses are formed in a combination of mechanical, thermal, hydraulic (pore pressure), and chemical stresses.

The wellbore instability can be classified into these categories:

1. Wellbore collapse: wellbore wall caves into the wellbore because of ductile compressive shear failure. In this instance, the local stresses near the wellbore are higher than the wellbore pressure. Failure of this type is prone in weak and friable formations such as salt dome or shale formations. The chances of this kind of failure will increase by heating up the near wellbore region. This may occur if the circulating fluid temperature inside the wellbore is hotter than the formation temperature. Differential sticking and casing collapse are severe results of this instability.
2. Chemical related stability (shale formations): wellbore instabilities are often experienced while drilling through shale formations. The instabilities usually occur due to reactions between water sensitive shale formation and the drilling fluid. Low permeability and free charged ions in shale make these problems very complex. There is a class of shale that is permeable known as Gumbo shale. The water flux and ions exchange are much larger in this type of medium, therefore, the failure is very different. In fact, Gumbo shale swells and softens during failure, sometimes flowing to the surface as shown in Figure 2.2. Instabilities in shale formations can be mitigated by controlling drilling fluid type, chemistry, and temperature.



Figure 2. 2: Extreme case of Gumbo shale instability- flow to the surface due to incompatible mud type with the formation [49]

3. Wellbore enlargement (breakout): very similar to wellbore collapse with a difference of brittle compressive shear failure, as shown in an image log in Figure 2.3. Only some parts of the wellbore wall cave in, known as washout. In this type of failure, blocky cavings (‘rubbles’) will be seen on shale shaker, shown in Figure 2.4. Bad cement job and poor hole cleaning are the results of this type of failure. One remedy for this issue is to raise the mud weight.

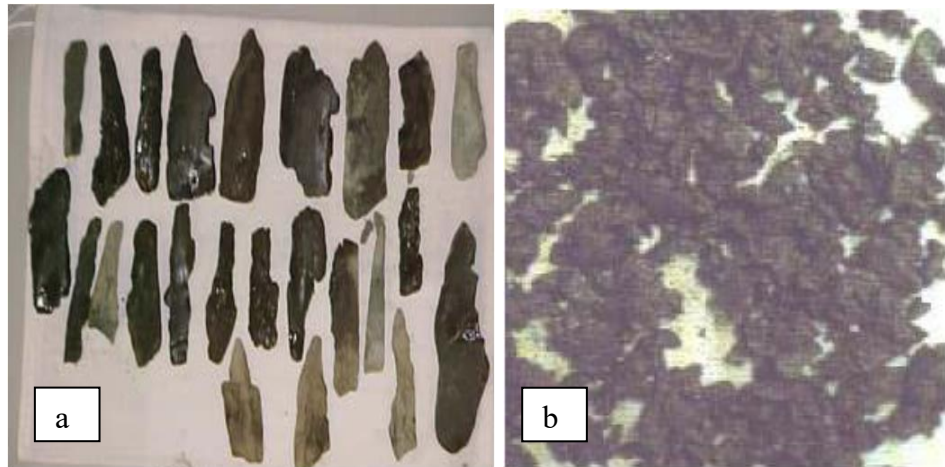


Figure 2. 3: (a) Caving cuttings-sign of wellbore instability vs. (b) normal cuttings observed on shale shaker [50]

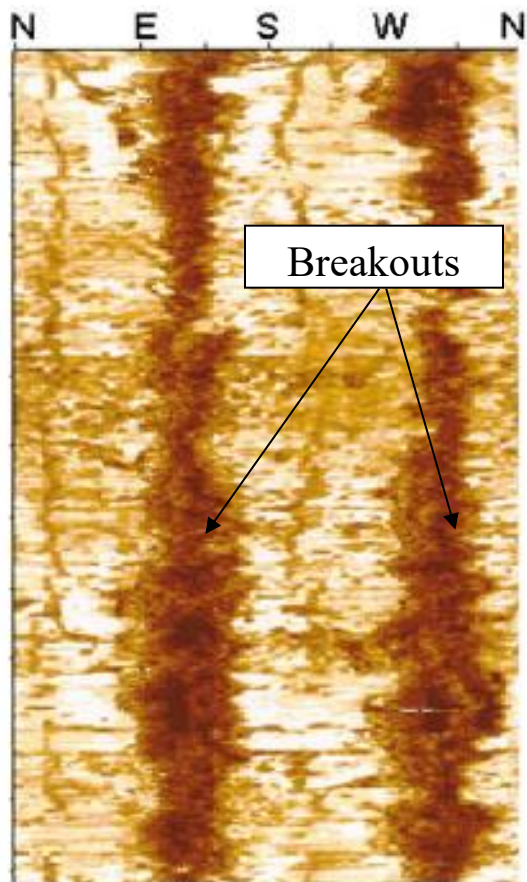


Figure 2. 4: Image log of a wellbore with breakouts (dark area) on the wellbore wall due to excessive formation stress [51]

4. Wellbore fracturing (breakdown): unintended fractures will form near the wellbore when the wellbore stress is higher than the tensile strength of the formation. Figure 2.5 shows image logs recorded in vertical and horizontal wellbores experiencing breakdown. In this type of failure, drilling mud is lost into the formation, leading to higher non-productive time (NPT). If this failure is not treated properly it may lead into a severe problem known as blowout, jeopardizing the whole drilling project. Wellbore fracturing can be avoided with a good knowledge of formation anisotropy and wellbore inclination. When wellbore temperature is cooler than the formation temperature, a cooling zone occurs, increasing the chance of wellbore fracturing failure. Lowering the mud weight and applying wellbore strengthening techniques (WBS), adding lost circulation material (LCM), are the solutions for this problem. Table 2.1 and 2.2 list different lost circulation scenarios and methods for the WBS.

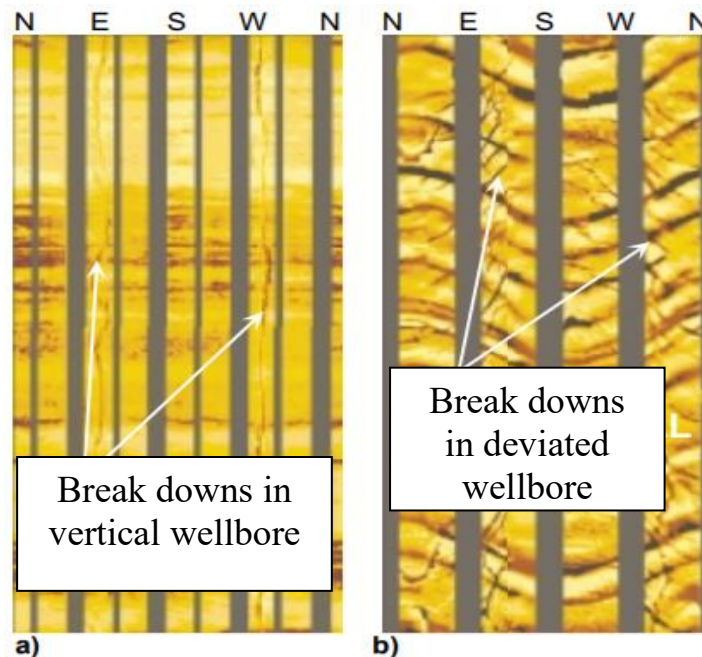


Figure 2. 5: Image log showing typical drilling-induced tensile wall fractures in a vertical borehole and inclined tensile fractures in a deviated borehole [52]

5. Sanding: when drawdown or production rate is high from weak or loose formations, a large amount of particle, sands, can be produced into the surface or cause blocking of the pores near the wellbore. Sanding problems limit production and damage the downhole and surface equipment. Remedies are to lower the production rate and install sand screens.

Table 2.3 categorizes and summarizes the different types of shear and tensile failures around a borehole.

## **2.2 FACTORS INFLUENCING WELLBORE STABILITY**

Wellbore stability factors can be divided into two groups, uncontrollable and controllable.

### **2.2.1 Uncontrollable**

In-situ stresses or geological stresses, formation pore pressure, formation temperature, rock properties are all uncontrollable factors that influence the mud weight window and wellbore stability. Accurately predicting each of these factors is an important task to successfully strike a balance between uncontrollable and controllable factors in the design of mud weight window.

### **2.2.2 Controllable**

Mud properties, circulation rate, wellbore orientation, mud temperature and chemical compositions, and additives are important controllable factors. However, not much attention has been given to the effect of mud temperature, even though, there are several models that describe this phenomenon. Less attention to the temperature effect is due to the traditional thought that it is not a significant issue as well as time consuming process in formulizing solution for its effect.

### 2.3 EXISTING WELLBORE STABILITY MODELS

Hubbert and Willis [5] are the pioneers in formulating stability model in the 50's. They applied Kirsch's solution [6] to predict wellbore instability for a vertical wellbore subjected to non-hydrostatic in-situ stresses with constant pore pressure. Considerable efforts and progress have been made in modeling wellbore instability ever since. Now models such as elastic/plastic, poroelastic, thermoporoelastic, and discontinuous mechanics are available.

Elastic model, first developed by Hubbert and Willis, does not consider the effect of pore pressure change. In fact, the pore pressure is constant, and the effective stress is unchanged. Fairhurst [7] modified Hubbert and Willis solution to an inclined wellbore by adding induced anti-plane shear. Bradley [8] took Fairhurst model and analyzed the effect of in-situ stresses and inclination on wellbore stability. Hubbert and Willis, Fairhurst, and Bradley works provided most significant insights into effect of in-situ stresses and wellbore inclination on wellbore stability. Their works are the most referred in the wellbore stability studies.

Poroelastic wellbore stability model was first developed by Haimson and Fairhurst [9], based on Biot's [10] work. Detournay and Cheng derived the fully-coupled poroelastic semi-analytical model for a vertical wellbore subjected to non-hydrostatic in-situ stress field [11]. Their work was extended to inclined wellbore by Cui et al. [12]. There are different models accounting for poroplastic wellbore stability with steady state or transient pore pressure [13] [14]. However, they are not fully-coupled and they are limited to hydrostatic stress field and one-dimension conditions. The major setbacks are the mathematical difficulties in solving these problems analytically and understanding of fully coupled poroplastic constitutive behavior. Finite element modeling has shed some hope in dealing with these difficulties in recent years.



Discontinuous mechanics introduced by Goodman joint element [15], Goodman and Shi key block theory [16], and Cundall distinct elements [17] in the late 70's. A popular approach for rock engineering problems such as tunneling and mining. With aid of finite element modeling and powerful computers, this type of modeling is becoming more popular specially in fracture network modeling or well logging technologies. It is very important to model the discontinuity for wellbore stability model when deformations of discontinuity dominate the rock response.

All rock formations show some level of nonlinearity and anisotropy [18]. While the assumption of linear elasticity is commonly used to simplify analyses, non-linear behavior has been used by Morita and Gray [19] to illustrate more complex rock behavior. As show in Figure 2.6, a formation Young's modulus exhibits a nonlinear trend with varying confining pressure. Therefore, it can change the stress resolution predicted by the classical models assuming linearly elastic media, e.g. Kirsch's solution. The nonlinearly elastic model accounts for nonlinearity by allowing pressure dependency of elastic moduli such as Young's modulus.

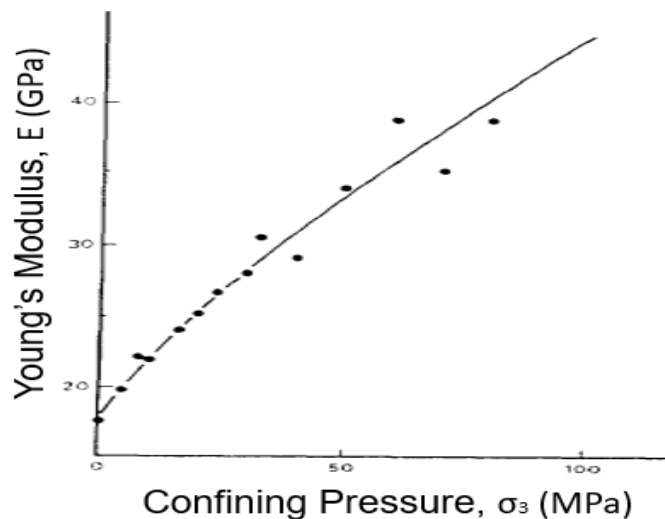


Figure 2. 6: Values of Young's modulus at 50% peak strength exhibiting a nonlinear trend with confining pressure [20]

The stresses at the wellbore wall either at shear or tensile failure cannot be measured directly in wellbore stability studies [20]. Two techniques have been developed: 1. comparing the stresses at the wellbore wall calculated using linearly elastic theory with peak strengths of the rock measured in compression test (e.g. triaxial test) [21], and 2. using elastic-plastic analyses to predict fracture propagation [22]. However, neither of the techniques can predict the extent of the fracture or excavation around the wellbore reliably [23].

Stress vs. strain graphs of rock samples often show nonlinear trends amplifying the nonlinear behavior of the rocks. The Young's modulus of a rock often depends on the confining pressure and will have different values at different confining pressures. Based on these observations, it is concluded that rocks behave nonlinearly. Therefore, Santerelli et al. revisited linearly elastic stress and strain equations to develop a series of equations to account for nonlinearities based on the pressure dependency of Young's modulus [20]. The result of the nonlinearly elastic model is shown in Figure 2.7.

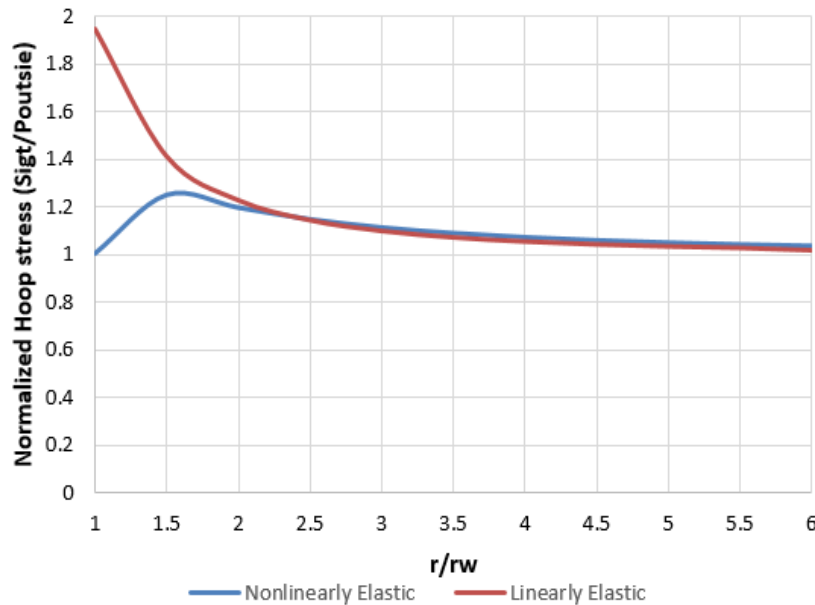


Figure 2. 7: Distribution of tangential stresses around a wellbore based on linear and non-linear dependency of Young's Modulus.  $r_w$  is the wellbore radius

It is important to note that the maximum tangential stress may not occur at the wellbore wall. This is in contradiction with linearly elastic theory stating that the maximum tangential stress is always at the wellbore wall. Also, the tangential stress is much lower near the wellbore compared with the linearly elastic model. Field and lab observations suggest that linear-elastic models give a higher stress concentration around a wellbore, therefore, requiring a higher mud weight to prevent shear failure [24] [25]. Linear models do not account for the large deformations before failure, which releases a certain amount of energy or stress.

If the elastic response of a material depends on the material's orientation for a given stress configuration, the material is said to be anisotropic [18]. Therefore, elastic moduli are different in each direction of the material. Anisotropy can be classified into two groups: 1. intrinsic, and 2. induced. Intrinsic anisotropy is formed during the deposition of the rock sample, so it depends on lithology of the rock. Induced is due to deviatoric stress that causes microcracks. Anisotropy and heterogeneity in rock samples can introduce difficulty in hydraulic fracturing design since fracture initiation and propagation is highly affected [26]. This complexity will ultimately alter the production rate. Heterogeneity can improve the total surface area and production rate; on the other hand, it can arrest the fracture propagation [27]. Stiffness of a formation defines the effect of anisotropy and heterogeneity. If the fracture faces a soft zone, the fracture will propagate comfortably. However, in hard formations, the fracture cannot propagate, and it will be arrested. Young's modulus of the material highly influences the stiffness of a formation.

The effect of anisotropy on hydraulic fracturing is investigated using ABAQUS. Due to symmetry, half of a 2D plain strain block was used. The half circular concentric opening represents the wellbore as shown in Figure 2.8. Parameters used for the study are listed in Table 2.4. Only Young's modulus is changed since it plays a major role in

hydraulic fracturing compared to Poisson's ratio. In the anisotropic case, the Young's moduli are  $3 \times 10^6$  and  $2.5 \times 10^6$  psi in the x- and y- directions, respectively. In fact, this model is an orthotropic model since Young's modulus is depended directionally, meaning Young's modulus magnitude is constant in each plane (x- and y- directions).

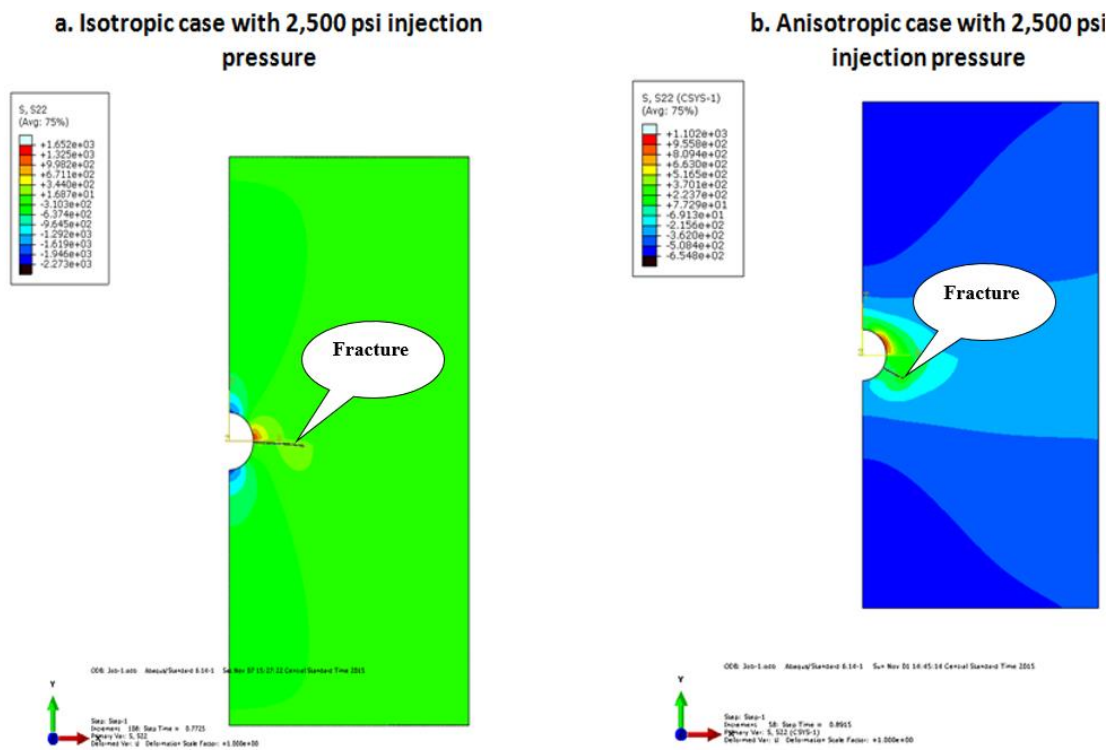


Figure 2. 8: Isotropic vs. Anisotropic fracture propagation in ABAQUS finite element analysis. Different fracture paths are observed

The model was used in two different cases. The first case was conducted using a homogenous media. It was assumed that Young's modulus is constant and independent of direction and location. The second case was done for the orthotropic case. In Figure 2.8 (a), the fracture propagates in the direction of maximum horizontal stress and opens against the minimum horizontal stress as expected since fracture takes the path of least resistance. This result also follows the linear elastic fracture mechanics theory prediction, stating that a fracture extends in the direction of the maximum compressive stress. However, Figure

2.4 (b) displays a different trend. The fracture is not opening in the direction of the maximum stress. It opened and propagated in some other direction, not following the elastic theory's prediction. It can be concluded that the propagation path depends on the local material stiffness more than stress anisotropy. Also, the homogenous case required a higher injection pressure compared to orthotropic case. This was also observed by Yang et al. in their work [28]. It can also be seen in Figure 2.8 (b), that the stress distribution around the wellbore as well as throughout the block is very different compared to the homogenous case. The fracture initiation and propagation have been estimated using ABAQUS XFEM module.

#### **2.4 THERMOPOROELASTIC MODEL**

The wellbore temperature is different from that of the rock formation due to geothermal gradient. Any changes in pore pressure will redefine the stress resolution in the media. In turn, this can lead to deformation of the media. This effect is stimulated with thermal loadings, either expansion or contraction. It is important to realize that a small change in temperature change can result in a large pore pressure change due to the small thermal expansion coefficient of the rock. This temperature difference (thermal stress) in any type of formation such as sandstone or shale may induce fluid flow and changes in pore pressure. Since temperature and pore pressure are coupled together, the fully coupled equation must be developed.

Schiffman [29] introduced the first thermoporoelastic model by extending the Biot's theory to non-isothermal systems. Substantial modeling and progress have been done after him in modeling fully coupled thermoporoelastic model. The need for a fully coupled thermoporoelastic model can be seen in different engineering applications such as nuclear waste disposal [30] [31] [32], geothermal energy production [33], water flooding,

thermal enhance oil recovery [34], gas well with high rate production, hydraulic fracturing [35], and wellbore stability during drilling phase [36]. Various techniques in solving thermoporoelastic model have been offered due to diverse forms of governing equations and boundary and initial conditions [37] [38]. A few have attempted to present a solution in two- or three-dimensional geometry [39]. In fact, most solutions are provided in one-dimension geometry because of axisymmetric boundary condition assumption. The complexity increases with the level of coupling. Coupling is the effect of thermal stress on mechanical and pore pressure (hydraulic) stresses or vice versa, as shown in Figure 2.9. In the early development of thermoporoelastic model, researchers chose the coupling of induced thermal stress on mechanical stress and ignored mechanical effect on thermal stress based on the observation that the temperature variation caused by mechanical deformations is very small [40]. In field of rock mechanics, a few studies have considered the effect of mechanical stress on thermal stress [41]. They suggest that mechanical stress may change the thermal properties, therefore, a non-linear thermal behavior can be expected.

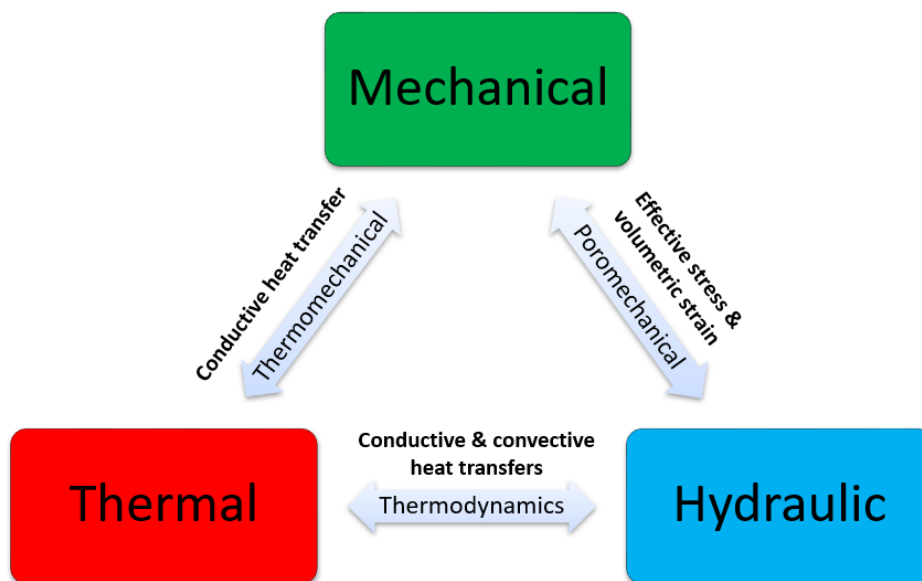


Figure 2. 9: Coupling mechanisms for a thermoporoelastic system (modified after, Li [2])

Fully coupled fluid flow and heat transfer models were developed in the 70's in conjunction with geothermal energy research. Various models such as distributed parameters, one or two-way coupling mechanism, and multiphase were developed. Their solutions relied on numerical procedures such as finite difference or finite element. Some of the models are non-linear due to convective heat transfer or non-linear thermodynamics parameters. Implicit and Newton-Raphson methods were used in dealing with nonlinear problems [42].

Pore pressure-mechanical coupling mechanism is important in studies of subsidence and consolidation. Most of the developed linear and non-linear poroelastic/plastic models assume one-way coupling, which is the effect of pore pressure on mechanical stress [43] [44]. Although, several studies have taken two-way coupling and investigate the effect of mechanical stress on pore pressure [45].

Table 2. 1: Lost circulation guidelines [46]

Classification	Typical Loss Rate	Typical Formation Characteristics	Preventative Solutions	Mitigation Solutions
Seepage	<10 bbl/hr	<ul style="list-style-type: none"> <li>Sands</li> <li>Sandstones</li> <li>Silt</li> </ul>	<ul style="list-style-type: none"> <li>Particulate LCM</li> <li>Managed Pressure Drilling</li> <li>Drilling with Casing</li> </ul>	<ul style="list-style-type: none"> <li>Particulate LCM</li> </ul>
Partial	10-50 bbl/hr	<ul style="list-style-type: none"> <li>Unconsolidated sand or gravel</li> <li>Small natural fractures</li> <li>Small induced fractures</li> </ul>	<ul style="list-style-type: none"> <li>Particulate LCM</li> <li>Managed Pressure Drilling</li> <li>Drilling with Casing</li> <li>Solid Expandable Systems</li> </ul>	<ul style="list-style-type: none"> <li>Particulate/Fiber LCM</li> <li>Cross-linkable LCM</li> </ul>
Severe	>50 bbl/hr	<ul style="list-style-type: none"> <li>Unconsolidated sand or gravel</li> <li>Large natural fractures</li> <li>Large induced fractures</li> </ul>	<ul style="list-style-type: none"> <li>Managed Pressure Drilling</li> <li>Drilling with Casing</li> <li>Solid Expandable Systems</li> </ul>	<ul style="list-style-type: none"> <li>Particulate/Fiber LCM</li> <li>Cross-linkable LCM</li> </ul>
Total	No returns	<ul style="list-style-type: none"> <li>Cavernous formations</li> <li>Large, and/or numerous natural and/or induced fractures</li> </ul>	<ul style="list-style-type: none"> <li>Managed Pressure Drilling</li> <li>Drilling with Casing</li> <li>Solid Expandable Systems</li> </ul>	<ul style="list-style-type: none"> <li>Particulate/Fiber LCM</li> <li>Cross-linkable LCM</li> </ul>

Table 2. 2: Wellbore strengthening (WBS) methods with field applications [47]

Author	Materials	Material Size	Material Strength	Tip Isolation	Rock Stress	Method	Field Applications
Fuh et al., 1992	LPM	Important	Selected Strength	Required	Not Changing	Fracture Pressure Inhibitor	California (Ventura)/ Oklahoma (Newkirk)
Alberty and McLean, 2004	Calcium Carbonate	Important	Important	Not Required	Changing	Stress Cage (SC)	Gulf of Mexico
Dupriest, 2008	DSF	Unimportant	Unimportant	Required	Changing	Fracture Closure Stress(FCS)	Malaysia (Jerneh field)/ East Texas (Trawick field)
Wang et al., 2007a, 2007b	DVCS	Important	Important		Changing	Stress Cage (SC)	Gulf of Mexico/ South Texas
Van Oort et al., 2009		Important	Unimportant	Required	Not Changing	Fracture Propagation Resistance (FPR)	Gulf of Mexico
Aadnoy and Belayneh, 2008	High Strength Materials	Important	Very Important		Not Changing	Fracture Healing	North Sea



Table 2. 3: Shear and tensile failure types around a borehole with geometry and orientation [48]

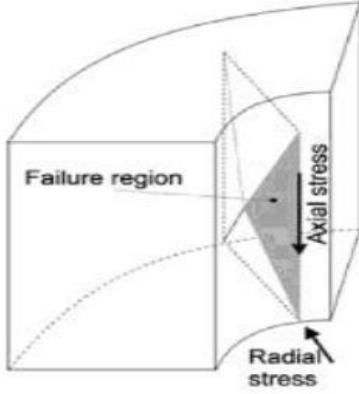
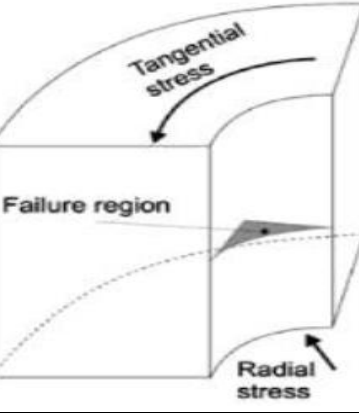
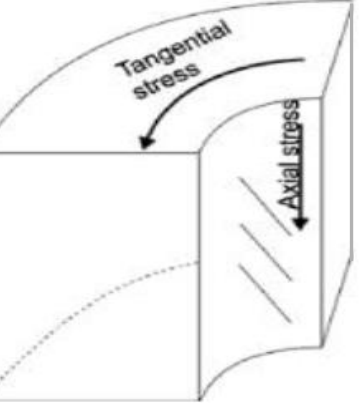
Failure Type	Geometry and Orientation	Figure
<p>Shear Failure, shallow knockout</p> $\sigma_z > \sigma_t > \sigma_r$	<p>Failure is in radial/axial plane because the max (<math>\sigma_z</math>) and min (<math>\sigma_r</math>) stresses are oriented in this plane (a vertical plane)</p>	
<p>Shear Failure, wide breakout</p> $\sigma_t > \sigma_z > \sigma_r$	<p>Failure is in radial/tangential plane because the max (<math>\sigma_t</math>) and min (<math>\sigma_r</math>) stresses are oriented in this plane (a horizontal plane)</p>	
<p>Shear Failure, wide breakout</p> $\sigma_z > \sigma_r > \sigma_t$	<p>Failure is in axial/tangential plane because the max (<math>\sigma_z</math>) and min (<math>\sigma_t</math>) stresses are oriented in this arc (the borehole arc)</p>	

Table 2. 3, cont.

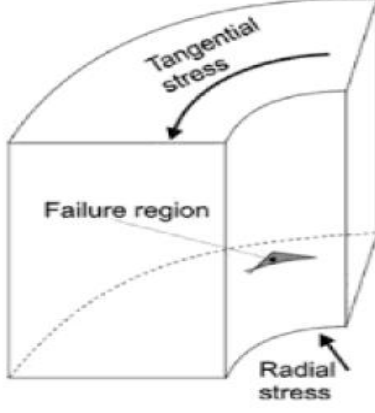
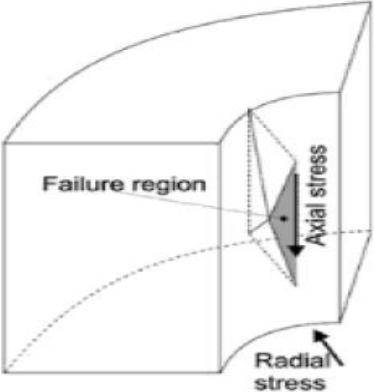
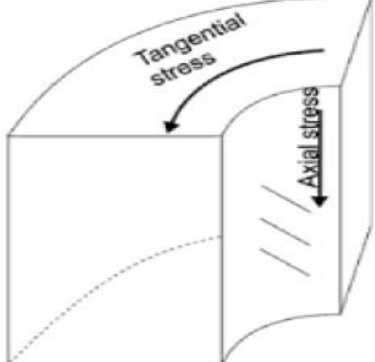
Failure Type	Geometry and Orientation	Figure
<p>Shear Failure, narrow breakout  <math>\sigma_r &gt; \sigma_z &gt; \sigma_t</math></p>	<p>Failure is in radial/tangential plane because the max (<math>\sigma_r</math>) and min (<math>\sigma_t</math>) stresses are oriented in this plane (the horizontal plane)</p>	
<p>Shear Failure, deep knockout  <math>\sigma_r &gt; \sigma_t &gt; \sigma_z</math></p>	<p>Failure is in radial/axial plane because the max (<math>\sigma_r</math>) and min (<math>\sigma_z</math>) stresses are oriented in this plane (the vertical plane)</p>	
<p>Shear Failure, low angle echelon  <math>\sigma_t &gt; \sigma_r &gt; \sigma_z</math></p>	<p>Failure is in tangential/axial plane because the max (<math>\sigma_t</math>) and min (<math>\sigma_z</math>) stresses are oriented in this arc (the borehole arc)</p>	

Table 2. 3, cont.

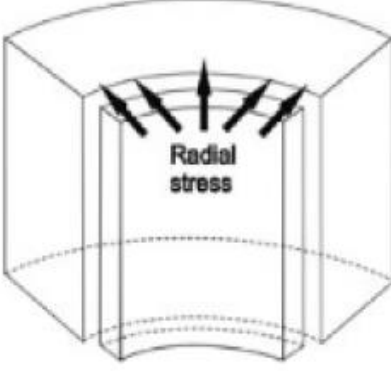
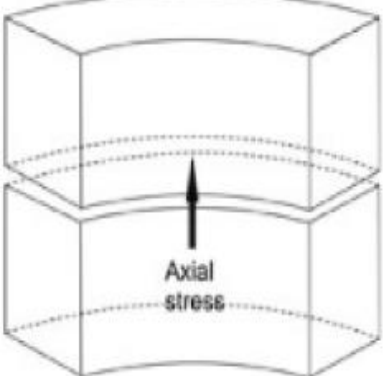
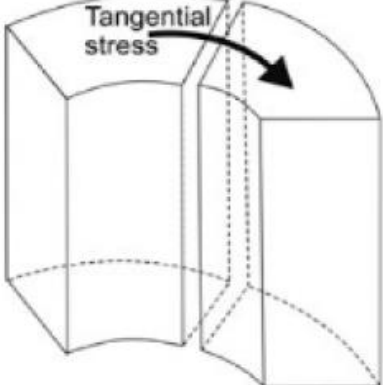
Failure Type	Geometry and Orientation	Figure
<p>Tensile Failure cylindrical  <math>\sigma_r \leq -TS</math></p>	<p>This failure is concentric with the borehole. A low mud weight creates the failure since magnitude of <math>\sigma_r</math> is lower than tensile strength of the rock</p>	
<p>Tensile Failure horizontal  <math>\sigma_z \leq -TS</math></p>	<p>This failure creates horizontal fractures since <math>\sigma_z</math> is the lowest stress</p>	
<p>Tensile Failure vertical  <math>\sigma_t \leq -TS</math></p>	<p>This failure creates vertical fractures parallel with the maximum horizontal in-situ stress direction since <math>\sigma_t</math> must overcome the smallest formation tensile strength</p>	

Table 2. 4: Homogenous parameters used in ABAQUS isotropic and anisotropic study

Young's modulus	3,000,000	psi
Poisson's ratio	0.3	
$S_{Hmax}$	1,500	psi
$S_{Hmin}$	1,200	psi
Pore pressure	800	psi
Well radius	3	in
Length and width block	30	in

### **CHAPTER 3: INDUCED THERMAL STRESSES EFFECT ON BREAKDOWN AND BREAKOUT**

The knowledge of in-situ stresses, breakout, and breakdown is vital to oil and gas industry, affecting wellbore stability, well location and design, and production rate. Determination of breakout pressure helps avoid wellbore enlargement and shear failure, while, breakdown pressure aids in knowledge of the formation fracture gradient and the limit for the drilling mud weight. The purpose of this section is to formulate a theoretical/indirect method to predict breakout and breakdown pressures and their failure sizes on the wellbore wall. Stresses in porous media are defined not only by mechanical stresses such as in-situ stresses, but also depends on pore pressure and thermal stresses. The wellbore temperature is different from that of the rock formation due to geothermal gradient and circulation of mud inside the wellbore. This temperature differential causes induced thermal stresses that substantially changes the stress resolution around the wellbore.

Most stress resolution models include the effect of pore pressure, known as poroelasticity, defined by Biot [10]. However, the effect of induced thermal stresses is often ignored. The pore and temperature differentials always affect borehole stability by altering the stress concentration near the wellbore through induced poroelastic and thermoelastic stresses. This chapter modifies Kirsch's solution to include the induced thermal stresses using the Detournay and Cheng method [11]. The comparisons among elastic, poroelastic and thermoporoelastic models are investigated. Models ignoring thermal stresses predict unreliable breakdown pressures and higher mud weights to overcome shear failure. A parametric analysis was done to explore the effect of rock parameters on the induced thermal stresses. Formations with large Young's modulus will exhibit large induced thermal stresses. Failure size/arc around a wellbore is also computed

for shear and tensile failures along the principal in-situ stresses, minimum and maximum horizontal stresses. Stress anisotropy is also studied in this chapter. Higher stress anisotropy between geological stresses increases the chance of shear and tensile failures.

### **3.1 WELLBORE STABILITY: BREAKOUT AND BREAKDOWN**

Wellbore stability is always a challenging subject to drilling engineers. Establishing a systematic knowledge in breakout and breakdown gradients is an important task in wellbore stability and design, in-situ stress estimation and direction. Breakout is often identified directly from caliper, image, and petrophysical logs [53]. When pressure in a wellbore is lower than the effective stress of a formation, shear failure (breakout) will occur. This leads into many problems such as borehole enlargement, poor borehole cleaning, stuck pipe, and poor cement job. On the other hand, when the pressure is higher than the rock strength, tensile failure (breakdown) occurs. This scenario is the basis for lost circulation. Lost circulation is considered the biggest problem in the drilling industry, significantly increasing the non-productive time and costing the industry nearly a billion dollars each year [54] [55] [56]. Estimation of breakdown pressure is important in leak-off test, fracture gradient, casing design, and hydraulic fracturing [57]. Most drilling stability models incorporate mechanical and poroelastic effects, while ignoring the effect of temperature. Temperature change around the wellbore changes the stresses and creates thermally induced breakout and breakdown [58]. The main purpose of this chapter is to establish analytical solutions in prediction of wellbore breakout and breakdown pressures and their failure magnitudes for hard (consolidated) formations. The magnitude is the affected arc/location around the wellbore as shown in Figure 3.2. Soft and unconsolidated/shallow formations require an elasto-plastic model which is beyond the scope of this dissertation [59] [60].

When a wellbore is drilled, the rock is replaced by a drilling mud that has a different temperature gradient compared to that rock. This difference creates an induced thermal stress near the wellbore. The stresses around the wellbore can be described by a linearly elastic, homogenous, and isotropic model known as Kirsch's solution. However, nonlinearity has been described fully by Morita and Gray to illustrate more complex rock behavior [19]. Changes in pore pressure and temperature alter the stress resolution which modifies breakout and breakdown predictions compared to a purely elastic model. The purpose of this chapter is to illustrate the effect of pore pressure and temperature changes in the stress resolution model, breakout, and breakdown. First, Detournay and Cheng method was followed to add the induced stresses caused by pore pressure and temperature changes around a wellbore to Kirsch's solution [11]. Second, necessary equations for breakdown and breakout pressures and their sizes have been derived. Third, a parametric study on the rock properties that influence the induced thermal stress was provided. Finally, the comparison and error analyses have been done for elastic, poroelastic, thermoelastic, and thermoporoelastic models. This chapter shows how important it is to include induced thermal stresses in stress estimation around a wellbore since other models ignoring this effect produce unreliable results.

### **3.2 BREAKOUT AND BREAKDOWN MODELS**

The assumptions in all the models are:

- Linearly elastic, isotropic, and homogenous media
- Rock properties do not vary with temperature or pressure
- Maximum horizontal stress is along x-axis and minimum horizontal is along y-axis as shown in Figure 3.1
- Tensile failure happens at  $0^\circ$  and shear failure happens at  $90^\circ$

- Intact, vertical, and perfect circular wellbore
- Wellbore pressure is greater than the pore pressure

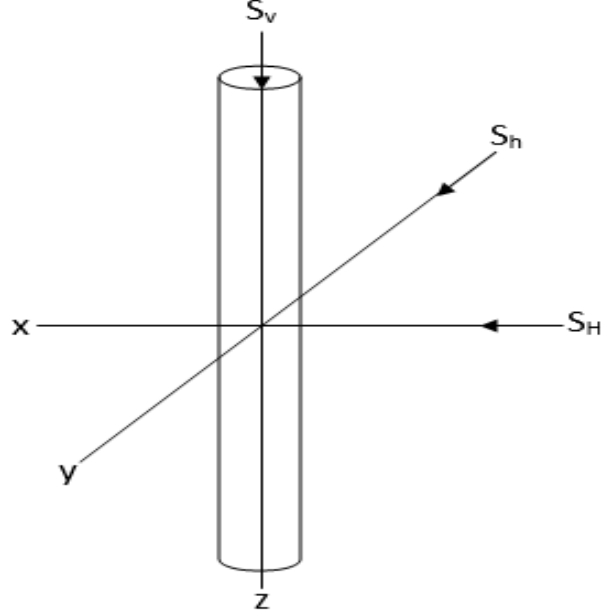


Figure 3. 1: Coordinate reference for the breakout and breakdown models. Maximum horizontal stress acts in the x-axis direction, Minimum horizontal stress in y-direction, and vertical load in the z-axis direction

Following Detournay and Cheng [11], stresses can be solved by dividing the load into three loading modes, and superimposing the results from the three loading modes onto the virgin formation condition. The first mode is due to the in-situ stresses, mechanical stresses. Zoback presents the total radial and tangential stresses for a wellbore based on Kirsch's solution with modification to include shear stress as [61]:

$$S_{r,m} = \frac{1}{2}(S_H + S_h)\left(1 - \frac{a^2}{r^2}\right) + \frac{1}{2}(S_H - S_h)\left(1 + 3\frac{a^4}{r^4} - 4\frac{a^2}{r^2}\right)\cos(2\theta) + \tau\left(1 + 3\frac{a^4}{r^4} - 4\frac{a^2}{r^2}\right)\sin(2\theta) + \frac{a^2}{r^2}(P_w) \quad (3.1)$$

$$S_{\theta,m} = \frac{1}{2}(S_H + S_h)\left(1 + \frac{a^2}{r^2}\right) - \frac{1}{2}(S_H - S_h)\left(1 + 3\frac{a^4}{r^4}\right)\cos(2\theta) + \tau\left(1 + 3\frac{a^4}{r^4}\right)\sin(2\theta) - \frac{a^2}{r^2}(P_w) \quad (3.2)$$



where  $S_H$  and  $S_h$  are the total maximum horizontal in-situ stresses.  $\tau$  is the shear stress.  $S_{r,m}$  and  $S_{\theta,m}$  are the total radial and tangential (hoop) stresses based on mechanical stresses respectively.  $\theta$  is the wellbore angle measured around the wellbore wall from the x-axis (maximum horizontal stress) as shown in Figure 3.2.  $a$  is the wellbore radius and  $r$  is the distance away from the wellbore wall into the formation.  $P_w$  is the wellbore pressure.

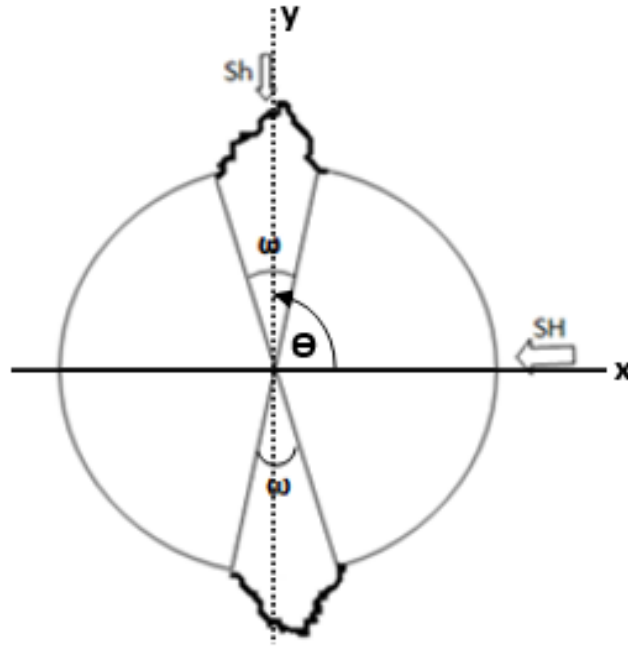


Figure 3. 2: Top view of wellbore breakout angle or failure arc.  $\omega$  is the failure angle

Equations (3.1) and (3.2) only consider the mechanical stresses, not pore pressure nor thermal effects. For a vertical wellbore, when geological stresses align with principal axes, the stress resolution on the wellbore wall in terms of effective stress is reduced to:

$$\sigma_{r,m} + P = P_w \quad (3.3)$$

$$\sigma_{\theta,m} + P = (S_H + S_h) - 2(S_H - S_h) \cos(2\theta) - P_w \quad (3.4)$$

where  $\sigma_{r,m}$  and  $\sigma_{\theta,m}$  are the effective radial and tangential (hoop) stresses respectively.  $P$  is the pore pressure. The stresses shown here are analyzed on the wellbore wall since, in this chapter, it is assumed that the onset of the failure and highest stress concentration are

located there [9] [61] [62].

If the maximum horizontal stress is in direction of x-axis, tangential stress is minimum, for instance, at  $\theta = 0^\circ$ , and fractures are assumed to initiate at these points. Therefore, hoop (tangential) stress at these points becomes:

$$\sigma_{\theta,m} = 3S_h - S_H - P_w - P \quad (3.5)$$

In equation (3.5), the effect of poroelasticity, mode 2, defined by Biot, must be added to account for pore pressure changes. It is defined as:

$$\sigma_{\theta,p} = \frac{\alpha_b(1-2\nu)}{1-\nu}(P_w - P) \quad (3.6)$$

where  $\alpha_b$  is the Biot's coefficient of the rock.  $\sigma_{\theta,p}$  is the change in hoop stress due to the pore pressure change. Another important component missing in the equations is the induced thermal stresses, mode 3.

The wellbore temperature is different from that of the rock formation due to geothermal gradient and circulation of mud inside the wellbore. This temperature difference in any type of formation such as sandstone or shale may induce fluid flow and change in pore pressure. The Nowacki analytical solution, derived based on fundamental principles of thermodynamics, may be used to capture induced radial and tangential thermal stresses [63]. The solution is applicable to heat transfer by conduction in an infinite hollow cylinder with constant wellbore temperature.

$$\sigma_{\theta,T} = \frac{E\alpha_T}{(1-\nu)} \left[ \left( \frac{1}{r^2} \int_{r_w}^r T(r,t)rdr \right) - T(r,t) \right] \quad (3.7)$$

$$\sigma_{r,T} = \frac{E\alpha_T}{(1-\nu)} \frac{1}{r^2} \int_{r_w}^r T(r,t)rdr \quad (3.8)$$

where  $\sigma_{r,T}$  and  $\sigma_{\theta,T}$  are the radial and tangential stresses due to the temperature change and function of radial distance and time.  $\alpha_T$  is the linear thermal expansion coefficient,  $\nu$  is the

Poisson's ratio, and E is the Young's modulus of the rock.  $r_w$  is the wellbore radius. The solution only accounts for thermal conduction and not convection. It is important to couple thermal stress and pore pressure with time through the diffusivity equation for model improvement [2] [64] [65], and this is done in the following chapter.

Stephens and Voight [62] have presented solutions to equations (3.7) and (3.8) using Ritchie and Sakakura [66] series expansion method as follow:

$$\sigma_{\theta,T} = \frac{E\alpha_T\Delta T}{(1-\nu)} \left[ \left( \frac{a}{2r} - \frac{1}{2} - \ln\left(\frac{r}{a}\right) \right) I_0^{-1} - \left( \frac{1}{2} + \frac{a}{2r} \right) \right] \quad (3.9)$$

$$\sigma_{r,T} = \frac{E\alpha_T\Delta T}{(1-\nu)} \left[ \left( -\frac{a}{2r} + \frac{1}{2} - \ln\left(\frac{r}{a}\right) \right) I_0^{-1} - \left( \frac{1}{2} - \frac{a}{2r} \right) \right] \quad (3.10)$$

The solutions are valid for times of approximately one day. It may seem that these equations cannot be applied in drilling operations since the minimum required time is large. However, the equations can still be used since the investigation is focused on the wellbore wall since equations (3.9) and (3.10) are reduced to:

$$\sigma_{\theta,T} = \frac{E\alpha_T\Delta T}{(1-\nu)} \quad (3.11)$$

$$\sigma_{r,T} = 0 \quad (3.12)$$

$I_0^{-1}$  is an integral function that can be approximated by series function. The solutions are tabulated in papers of Ritchie and Sakakura and Jaeger [67].

The general tangential stress solution including thermal and pore stresses now can be obtained by superposing modes 1 through 3, equations (3.5), (3.6), and (3.11). Due to seepage of mud into the permeable formation, the initial pore pressure is replaced by wellbore pressure ( $P_w$ ) in equation (3.4) on the wellbore wall. Therefore, the final equation is:

$$\sigma_{\theta} = \sigma_{\theta,m} + \sigma_{\theta,p} + \sigma_{\theta,T} \quad (3.13)$$

$$\sigma_{\theta} + P_w = 3S_h - S_H - P_w + \left( \frac{\alpha_b(1-2\nu)}{1-\nu} \right) (P_w - P) + \frac{E\alpha_T\Delta T}{(1-\nu)} \quad (3.14)$$

After combining the similar terms, (3.14) is rewritten as:

$$\sigma_{\theta} = 3S_h - S_H + \frac{E\alpha_T\Delta T}{(1-\nu)} - \left( \frac{\alpha_b(1-2\nu)}{1-\nu} \right) P - \left( 2 - \frac{\alpha_b(1-2\nu)}{1-\nu} \right) P_w \quad (3.15)$$

When the hoop stress is equal or greater than the tensile strength of the rock, a fracture occurs. Therefore, the maximum wellbore pressure (breakdown pressure) can be defined as:

$$P_w = P_{bd} = \frac{3S_h - S_H + \frac{E\alpha_T\Delta T}{(1-\nu)} - \left( \frac{\alpha_b(1-2\nu)}{1-\nu} \right) P + TS}{\left( 2 - \frac{\alpha_b(1-2\nu)}{1-\nu} \right)} \quad (3.16)$$

where  $P_{bd}$  is the breakdown pressure and TS is the tensile strength of the rock. In case of an impermeable formation, (3.16) is reduced to:

$$P_{bd} = 3S_h - S_H - P + \frac{E\alpha_T\Delta T}{(1-\nu)} + TS \quad (3.17)$$

Schmitt and Zoback demonstrated experimentally that the poroelastic stress is negligible for low permeability formations under rapid loading conditions [68]. Therefore, equations (3.1) and (3.2) may be applicable for formations such as shale. However, temperature effect was not included in their study. Temperature change induces the pore pressure away from the wellbore wall, therefore, the poroelastic stress becomes important in the wellbore stability [69] [70] [71]. However, this is not within the scope of this chapter since the analysis is focused on the wellbore wall. In the following chapters, the coupling between the modes and stress profiles beyond the wellbore wall are investigated. Shear failure or breakout pressures can also be analyzed using Mohr-Coulomb as follows on the wellbore wall:

$$\sigma_{\theta} = n\sigma_r + \text{UCS} \quad (3.18)$$

It is assumed that the hoop stress is the biggest stress compared to other stresses acting on the wellbore wall ( $\sigma_{\theta} > \sigma_z > \sigma_r$ ). If the maximum horizontal stress is in direction of the x-axis, compressive stress is maximum, for instance, at  $\theta = 90^\circ$  or  $270^\circ$ , and shear failure (breakout) is assumed to initiate at these locations. Therefore, by substituting equations (3.3) and (3.16) into (3.18), the final equation is:

$$P_w = P_{bo} = \frac{3S_H - S_h + \left( n - \frac{\alpha_b(1-2\nu)}{1-\nu} \right) P + \frac{E\alpha_T\Delta T}{(1-\nu)} - \text{UCS}}{\left( n + 2 - \frac{\alpha_b(1-2\nu)}{1-\nu} \right)} \quad (3.19)$$

for permeable formations, and:

$$P_{bo} = \frac{3S_H - S_h + (n-1)P + \frac{E\alpha_T\Delta T}{(1-\nu)} - \text{UCS}}{(n+1)} \quad (3.20)$$

for impermeable formations.

$$\text{UCS} = \frac{2S_o}{(\sqrt{1+\mu^2} - \mu)^2} \quad (3.21)$$

$$\mu = \tan \beta \quad (3.22)$$

$$n = \left( \sqrt{1+\mu^2} + \mu \right)^2 \quad (3.23)$$

where  $S_o$ , UCS,  $\beta$ , and  $\mu$  are the cohesion, unconfined cohesive strength, friction angle, and friction coefficient of the rock respectively. Note that Mohr-Coulomb tends to over-estimate the failure envelope by ignoring the intermediate stress [72].

The failure arc shows the size of the damaged zone/arc around the wellbore wall. For instance, Figure 3.2 shows the breakout failure angle/arc, measured from the center of the wellbore. It is assumed that the breakout failure arc is axisymmetric along the maximum principal stress ( $S_H$ ), while breakdown failure arc is axisymmetric along the minimum principal stress ( $S_h$ ). The breakout angle can be used in estimation of in-situ stresses

magnitudes and their directions [73] [74]. The breakout failure arc angle ( $\omega$ ) can be analyzed as follow:

$$\omega = \pi - \arccos \left( \frac{S_h + S_H + \left( n - \frac{\alpha_b(1-2\nu)}{1-\nu} \right) P - \left( n + 2 - \frac{\alpha_b(1-2\nu)}{1-\nu} \right) P_w + \frac{E\alpha_T\Delta T}{(1-\nu)} - UCS}{2(S_H - S_h)} \right) \quad (3.24)$$

for permeable formation, and

$$\omega = \pi - \arccos \left( \frac{S_h + S_H + (n-1)P - (n+1)P_w + \frac{E\alpha_T\Delta T}{(1-\nu)} - UCS}{2(S_H - S_h)} \right) \quad (3.25)$$

for impermeable formation.

The breakdown arc angle ( $\gamma$ ) can be analyzed in the same manner for breakdown (tensile failure):

$$\gamma = \pi - \arccos \left( \frac{S_h + S_H - \left( \frac{\alpha_b(1-2\nu)}{1-\nu} \right) P - \left( 2 - \frac{\alpha_b(1-2\nu)}{1-\nu} \right) P_w + \frac{E\alpha_T\Delta T}{(1-\nu)} + TS}{2(S_H - S_h)} \right) \quad (3.26)$$

for permeable formations, and

$$\gamma = \pi - \arccos \left( \frac{S_h + S_H - P - P_w + \frac{E\alpha_T\Delta T}{(1-\nu)} + TS}{2(S_H - S_h)} \right) \quad (3.27)$$

For impermeable formations.

### 3.3 RESULTS

An analysis was done for thermal tangential stress,  $\sigma_{\theta,T}$  to capture the effect of each parameter in equation (3.11). One parameter was changed while keeping the others

constant. Table 3.1 lists the data used in the parametric study. The data for variables in this study are within reasonable ranges suggested by Jackson School of Geology at University of Texas [142].

Figure 3.4 shows that Young's modulus has the most notable effect on the tangential stress. Thermal expansion has an insignificant effect on thermal hoop stress change, as shown in Figure 3.3. Poisson's ratio has a moderate effect on the thermal stress since most rocks have a Poisson's ratio value ranging between 0.2 to 0.3 [75], shown in Figure 3.5.

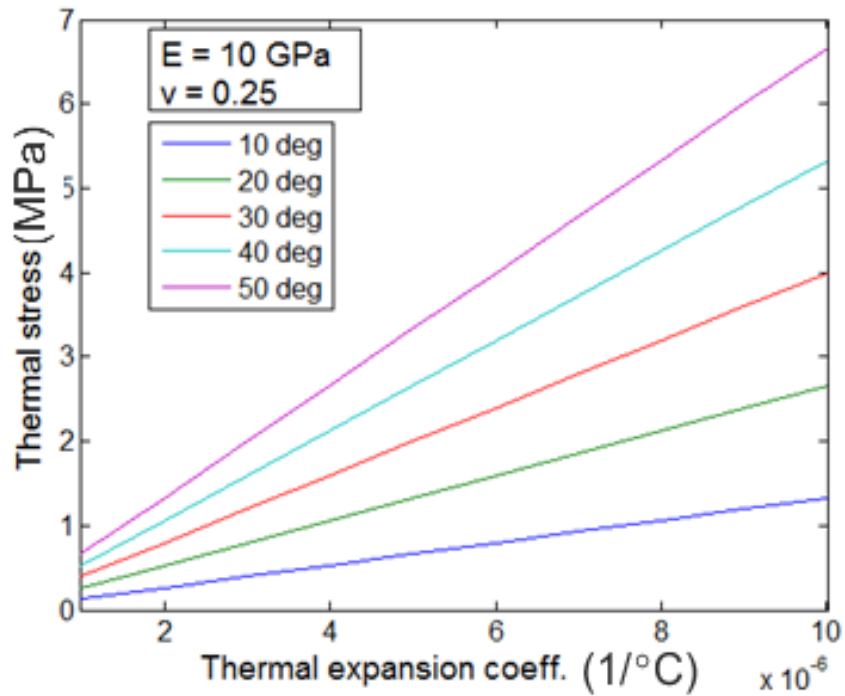


Figure 3. 3: Thermal expansion coefficient effect on tangential thermal stress at various temperature changes

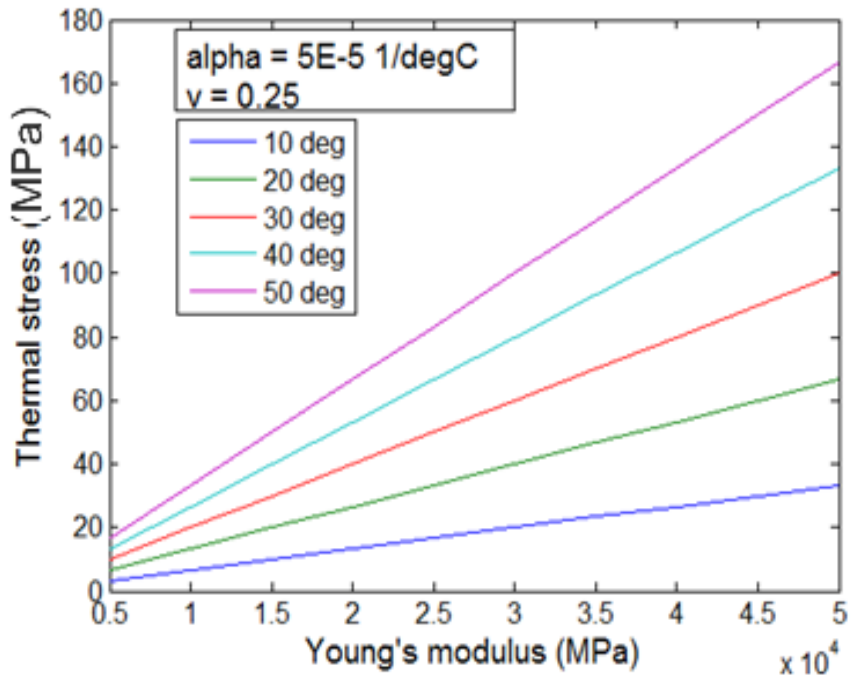


Figure 3. 4: Young's modulus vs. tangential thermal stress at different temperature changes

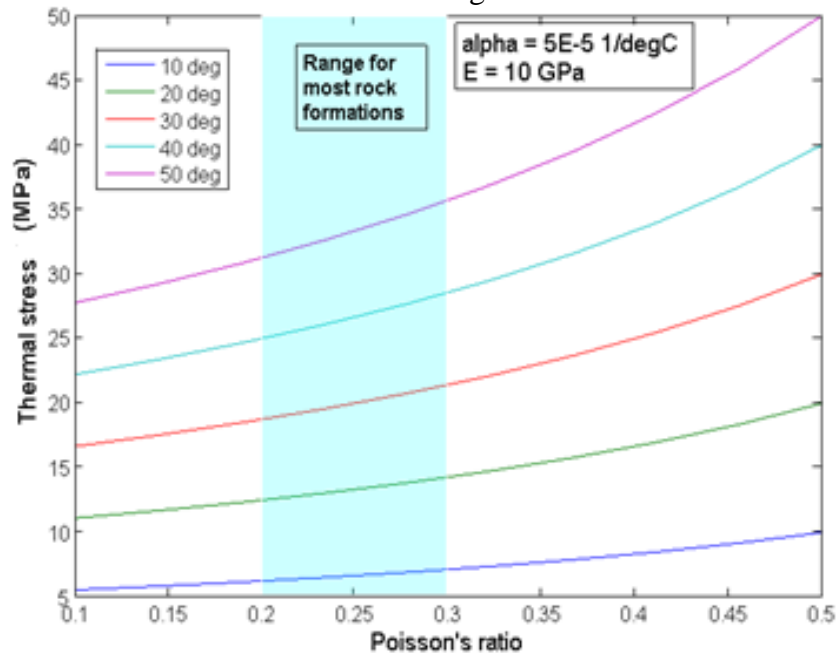


Figure 3. 5: Poisson's ratio vs. tangential thermal stress at various temperature changes



Next, the comparisons among different models, for instance, thermoporoelastic vs. poroelastic, using the breakdown and breakout equations are investigated. The data used in this study are shown in Table 3.2.

The minimum horizontal stress was kept constant while changing the maximum horizontal stress. Since the wellbore is assumed to be intact, meaning that there are no pre-existing fractures, the rock's actual tensile strength is not zero and should be considered. The tensile strength is assumed constant and independent of temperature variation. Vishal demonstrated that the tensile strength of rocks can depend on the temperature change [76]. The temperature change is a negative value because it is assumed that the mud temperature inside the wellbore is cooler than the formation temperature.

The breakout pressures were calculated using equations (3.19) and (3.20) for comparison study. The thermoelastic and elastic models may be suitable for very low permeable formations such as shale since there is no pore pressure change in these models [20]. When a wellbore is thermally cooled down, it will become more stable since the required breakout pressure is reduced.

The elastic, thermoelastic, poroelastic, and thermoporoelastic contributions are shown in Figure 3.6. The error, shown in equation (3.28), is defined based on the thermoporoelastic model since it is the base/true solution that includes all the components affecting stresses around a wellbore.

$$\text{Error} = \frac{\text{TPE} - X}{\text{TPE}} \times 100 \quad (3.28)$$

where TPE is the thermoporoelastic model results and X is the result from another model.

The error magnitude when thermal or pore stresses are ignored is shown in Figure 3.7. It can also be seen that the poroelastic and elastic models over-estimate breakout pressure, meaning it over-estimates required mud weight to overcome the shear failure.

Higher mud weight will increase the chance of formation breakdown (tensile failure) and lost circulation events. The thermoelastic model has a mixed trend. At low stress ratio, it tends to under-predict the breakdown pressure, while it over-predicts at higher stress ratio. Also, the poroelastic model decreases slightly as the stress ratio increases.

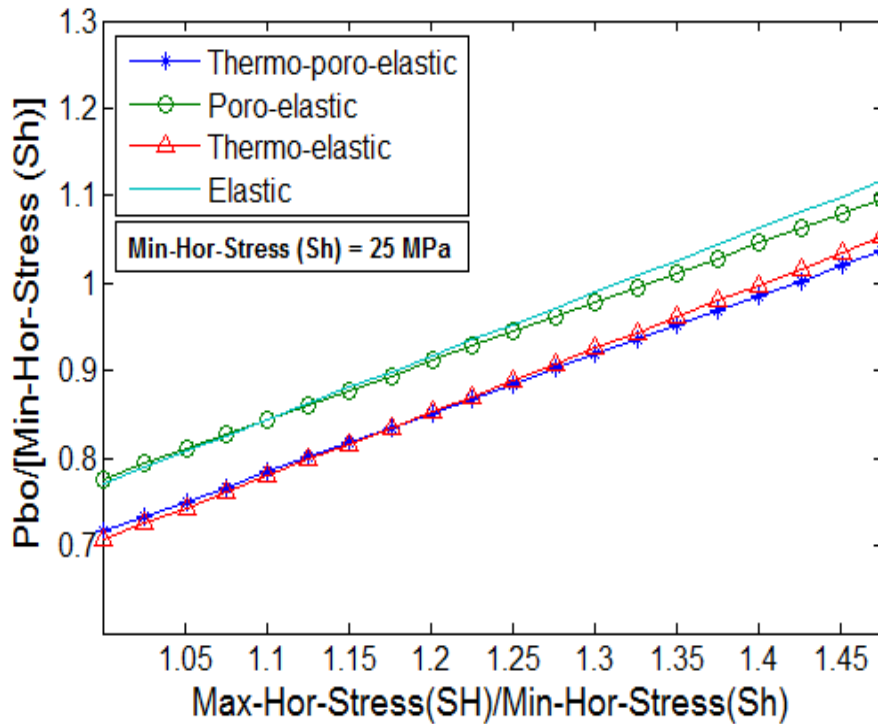


Figure 3. 6: Normalized breakout pressure predictions by various models

It can be concluded from Figure 3.6 that the induced pore pressure does not affect the breakout pressure as much as the induced thermal stress. The thermal stress substantially changes the stress and breakout pressure, when compared to elastic and poroelastic models.

Figure 3.8 shows the results for breakout failure angle/arc calculated using equations (3.24) and (3.25). the poroelastic and elastic models produce results substantially different than the models that include thermal stresses. The reason that the thermal models predict a lower failure arc or angle is because the cooler mud has reduced stresses around the wellbore, causing the wellbore to become more stable, resulting in less collapse (shear

failure). As the magnitude of maximum horizontal stress increases, the failure angle increases.

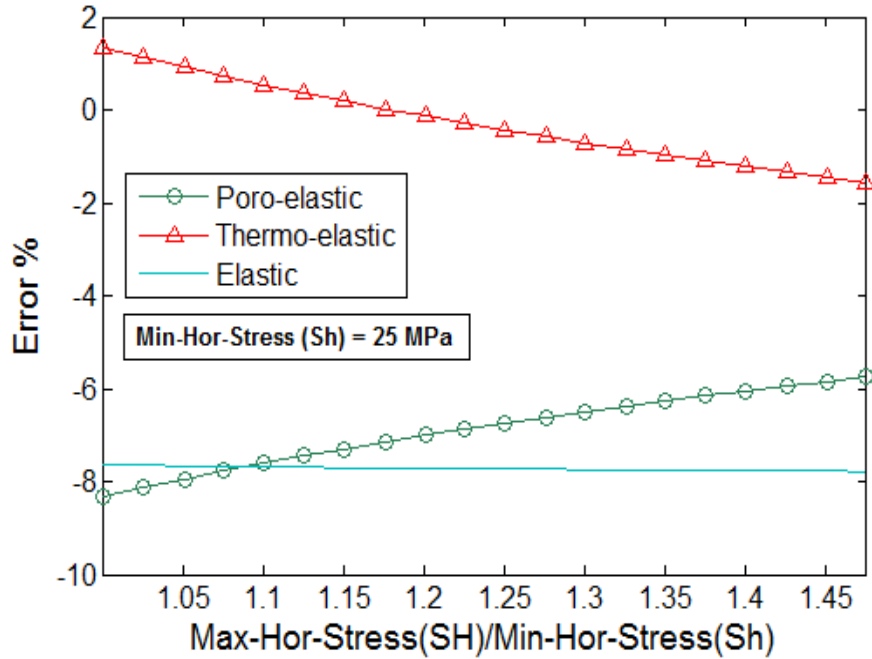


Figure 3. 7: Error analysis of all models compared against the thermoporoelectric model

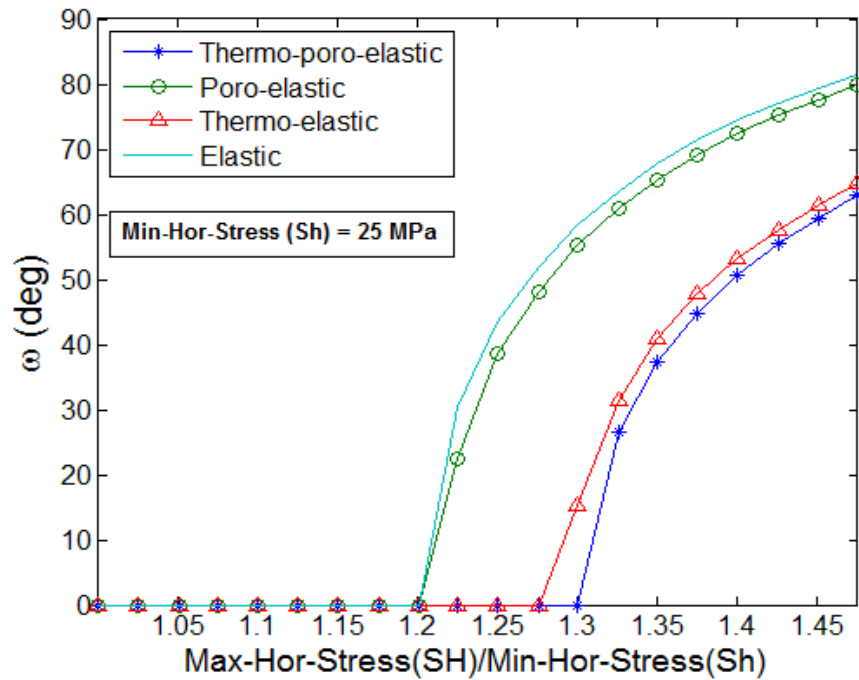


Figure 3. 8: Breakout (shear failure) arc/angle prediction along Min. horizontal stress for different models

Breakdown pressures calculated using equations (3.16) and (3.17) are shown in Figure 3.9. The results vary as the geological stresses values change. However, incorporating thermal stresses produces reasonable results since all models except thermoporoelastic model over-estimate the pressure required to breakdown the formation. As the formation is cooled down, its fracture gradient is reduced. Therefore, it is easier to break the formation down and cause fractures around the wellbore. This illustrates the importance of using the thermoporoelastic model for an accurate representation of stresses around a wellbore. Induced pore pressure also reduces the breakdown pressure. When mud penetrates into a formation, its local pore pressure elevates, therefore, the effective stresses around the wellbore decreases and the breakdown pressure will decrease too. This is consistent with Medlin and Masse [77], Yew and Weng [78], and Gao et al. [79] results showing a decrease in breakdown pressure with mud penetration.

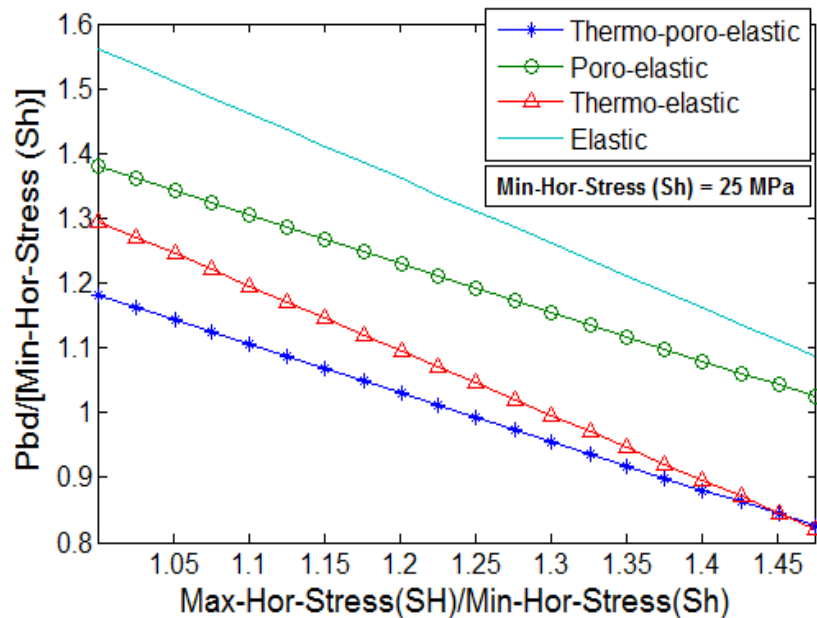


Figure 3. 9: Normalized breakdown pressure predictions by various models

Figure 3.10 shows the error in breakdown pressure predicted by all models compared to the thermoporoelastic model. Figure 3.11 shows the analyses for

breakdown arc/angle based on equations (3.26) and (3.27). All models predict no failure since the current mud pressure, i.e. 23 MPa, is less than the critical pressure predicted by all models in Figure 3.9.

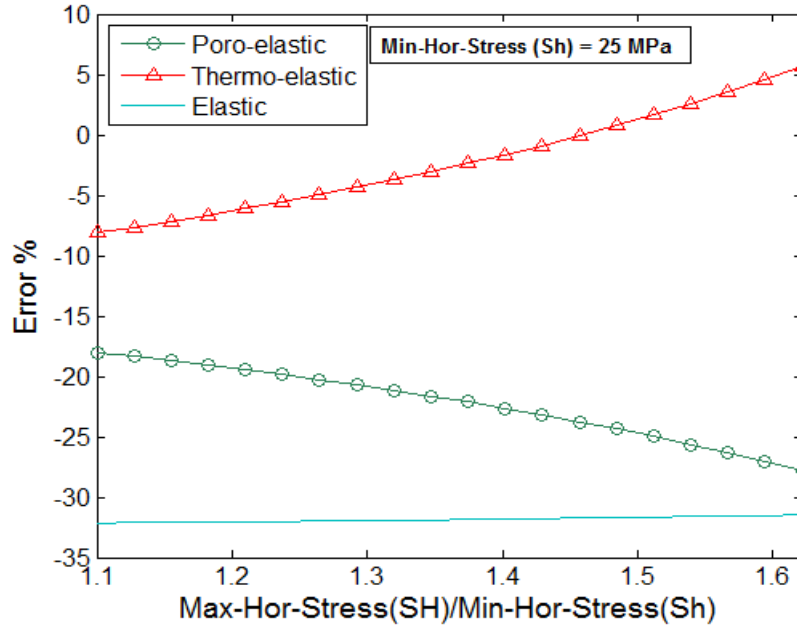


Figure 3. 10: Error analysis for breakdown pressure versus the thermoporoelastic model

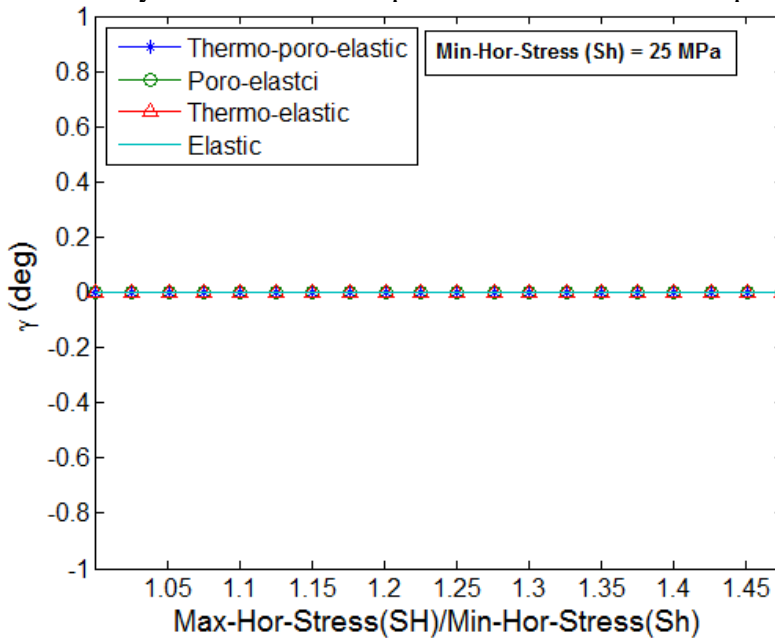


Figure 3. 11: Breakdown (tensile failure) arc/angle along Max. horizontal stress for the developed models

### 3.4 CONCLUSIONS

It can be concluded from the analyses that is crucial to include induced thermal stresses in calculation of stresses around the wellbore since models that do not include thermal stresses predict unreliable results. It may be safe to exclude pore pressure from stress estimation for formations with very low permeability values if the wellbore wall is the point of interest (failure initiates on the wellbore wall). Young's modulus has a substantial effect on the induced thermal stresses. Formations with large Young's modulus will exhibit large induced thermal stresses. High stress anisotropy between far field geological stresses, i.e.  $S_h$  and  $S_H$ , will increase the chance of shear and tensile failures. When a formation is cooled down, it will become more stable in shear failure region while the chance for breakdown (tensile failure) increases. When a formation is cooled down, its fracture gradient is reduced. Therefore, it is easier to break the formation down and cause fractures around the wellbore.

Table 3. 1: Parameters data for the effect rock properties on thermal stress

Parameters	Data	Unit
Temperature change ( $\Delta T$ )	10-50	$^{\circ}\text{C}$
Young's modulus (E)	$(0.5-5)\times 10^4$	MPa
Thermal expansion ( $\alpha_T$ )	$(1-10)\times 10^{-6}$	$1/^{\circ}\text{C}$
Poisson's ratio ( $\nu$ )	0.1-0.5	-

Table 3. 2: Data for breakout and breakdown models

Parameters	Data	Unit
Max-Hor-Stress ( $S_H$ )	25-40	MPa
Min-Hor-Stress ( $S_h$ )	25-37	MPa
Pore pressure (P)	21	MPa
Wellbore pressure ( $P_w$ )	23	MPa
Temperature change ( $\Delta T$ )	-25	$^{\circ}\text{C}$
Tensile strength (TS)	10	MPa
Biot's coefficient ( $\alpha_b$ )	1	-
Thermal expansion ( $\alpha_T$ )	2E-5	$1/^{\circ}\text{C}$
UCS	15	MPa
Friction angle ( $\beta$ )	30	deg
Young's modulus (E)	10,000	MPa
Poisson's ration ( $\nu$ )	0.25	-

## CHAPTER 4: THERMOPOROELASTIC MODEL BACKGROUND

### 4.1 MATHEMATICAL PRELIMINARIES

The theories of elasticity, stress, and heat transfer require knowledge of several areas of applied mathematics. They are formulated in terms of many different types of variables such as scalar, vector, and tensor fields, and this requires tensor notation along with tensor algebra and calculus.

#### 4.1.1 Indicical notation

Indicial notation is a shorthand scheme that a whole set of numbers is represented by a single symbol with subscripts [80]. For example,  $a_1, a_2, a_3$ , are denoted by the symbol  $a_i$ , where index (subscript)  $i$  will have the range 1, 2, 3. Similarly  $a_{ij}$  will have nine components, and can be written in a 3x3 matrix. The first index ( $i$ ) represents the rows, and second index ( $j$ ) indicates the columns of the matrix. If in a single term, the same index appears twice, summation over the index is implied, unless it is suspended by a “no-sum” phrase.

$$a_{ii} = a_{11} + a_{22} + a_{33} \quad (4.1)$$

$$a_{ii} \text{ (no - sum)} = [a_{11}, a_{22}, a_{33}] \quad (4.2)$$

Note that the same subscript cannot appear more than twice in the same term in an indicial equation, and free (unrepeated) indices in each term must agree. For instance, these are some non-sense cases of indicial notation use:

$$a_{ij} b_j = c_k \quad (4.3)$$

$$a_{ijj} b_j = d_i \quad (4.4)$$

The number of indices indicates the order of tensor. For example,  $a_i$  is a first-order tensor, also known as a vector, while,  $a_{ij}$  is a second-order tensor, and it is a matrix.



### 4.1.2 Calculus of tensors

Most variables in elasticity and heat transfer theories are field variables and, in some cases, temporal variables. Since these theories require differential and integral operations, it is necessary to understand the calculus in tensor fields [81] [82]. For partial differentiation, comma notation is used:

$$a_{,i} = \frac{\partial a}{\partial x_i} \quad (4.5)$$

$$a_{i,j} = \frac{\partial a_i}{\partial x_j} \quad (4.6)$$

$$a_{ij,k} = \frac{\partial a_{ij}}{\partial x_k} \quad (4.7)$$

$$a_{ij,kl} = \frac{\partial^2 a_{ij}}{\partial x_k \partial x_l} \quad (4.8)$$

$$a_{ij,kk} = \frac{\partial^2 a_{ij}}{\partial x_k^2} \quad (4.9)$$

Integration can be done in a similar manner with the use of integral operation:

$$\int_k a_{ijk\dots l,k} dk \quad (4.10)$$

### 4.1.3 Stress and strain analyses

This section will explore the basic formulations for stresses and strains in a body.

#### 4.1.3.1 Analysis of stress

Consider a body occupying some volume,  $V$  in space. Consider a volumetric element of that body,  $\Delta V$  as shown in Figure 4.1. Two types of forces act on the element:

- 1) Body forces: proportional to the mass contained in the element, e.g. gravity or centrifugal force
- 2) Surface forces: acting on the surface (area) of the element, e.g. hydrostatic pressure exerted by a fluid.

Let  $f$  represent a body force per unit volume, the resultant of the body force acting throughout  $V$  are  $R$ , and it is expressed as:

$$R_i = \int_V f_i dV \quad (4.11)$$

and resultant momentum due to the body force distribution is given by:

$$M_i = \int_V \epsilon_{ijk} x_j f_k dV \quad (4.12)$$

where  $\epsilon_{ijk}$  is the Levi-Civita symbol.

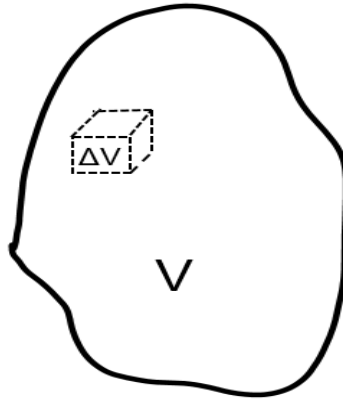


Figure 4. 1: Arbitrary body occupying some volume  $V$  in space

Consider an element  $\Delta A$  of the surface of the body contained in  $V$ . Let  $\mathbf{n}$  be the unit normal associated with  $\Delta A$ . Consider a resultant force  $\Delta \mathbf{F}$  acting on  $\Delta A$  shown in Figure 4.2.  $\Delta \mathbf{F}$  may not necessarily be parallel to  $\mathbf{n}$ . Traction vector is defined to represent the intensity of the resultant force  $\Delta \mathbf{F}$  on  $\Delta A$ . This becomes:

$$dF_i = T_i dA \implies F_i = \int_A T_i dA \quad (4.13)$$

Consider a rectangular parallelepiped referred to  $X_1$ ,  $X_2$ , and  $X_3$  is subjected to traction acting on each face, shown in Figure 4.3. Each traction can be represented by:

$$\mathbf{T}_i = \sigma_{ij} \mathbf{e}_j \quad (4.14)$$

$\sigma_{ij}$  is the stress components. First subscript,  $i$ , refers to the normal  $\mathbf{e}_i$  denoting the face on which the traction acts.  $j$ , refers to the direction  $\mathbf{e}_j$  in which the stress component acts.

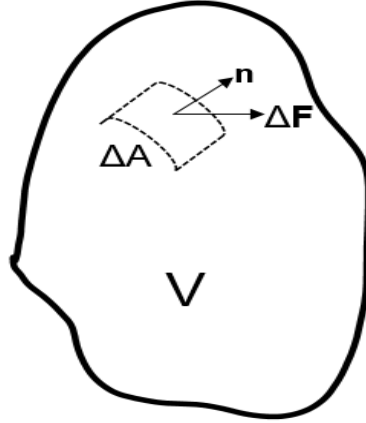


Figure 4. 2: Arbitrary body with arbitrary force acting on the surface

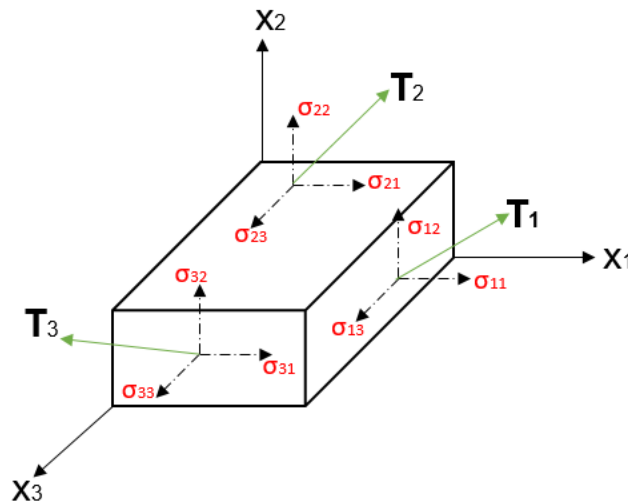


Figure 4. 3: Parallelepiped with arbitrary tractions and stress components

Now consider an arbitrary plane, shown in Figure 4.4, with normal  $\mathbf{n}$ , and define tractions in terms of stress components. The tractions acting on OBC, OCA, and OAB with  $dA_i$ . Let  $dA_n$  be the element of area ABC on which the traction acts, then:

$$\left. \begin{aligned} \text{OBC} &\implies dA_1 = dA_n \mathbf{n} \cdot \mathbf{e}_1 \\ \text{OCA} &\implies dA_2 = dA_n \mathbf{n} \cdot \mathbf{e}_2 \\ \text{OAB} &\implies dA_3 = dA_n \mathbf{n} \cdot \mathbf{e}_3 \end{aligned} \right\} \implies dA_i = dA_n \mathbf{n} \cdot \mathbf{e}_i = n_i dA_n \quad (4.15)$$

since  $\mathbf{n} \cdot \mathbf{e}_i = n_i = \cos(\mathbf{n}, \mathbf{e}_i)$ .

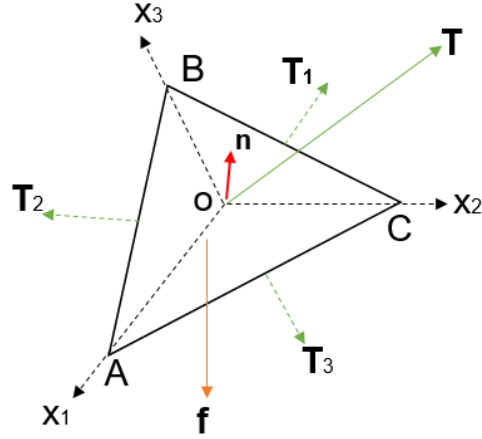


Figure 4. 4: Tetrahedron under arbitrary tractions and body force

The force equilibrium on the plane is:

$$\mathbf{T}dA_n = \mathbf{T}_1dA_1 + \mathbf{T}_2dA_2 + \mathbf{T}_3dA_3 - \mathbf{f}\left(\frac{1}{3}hdA_n\right) \quad (4.16)$$

where h is the altitude of the tetrahedron.

From equations (4.15) and (4.16), one obtains:

$$\mathbf{T}dA_n = \mathbf{T}_i dA_i - \mathbf{f}\left(\frac{1}{3}hdA_n\right) = \left(\mathbf{T}_i n_i - \mathbf{f} \frac{h}{3}\right) dA_n \quad (4.17)$$

Let

$$\mathbf{T}_n = \mathbf{T}_i \mathbf{e}_i \quad \text{and} \quad h = 0$$

From equation (4.14)

$$\mathbf{T}_i \mathbf{e}_i = \sigma_{ij} n_i \mathbf{e}_j = \sigma_{ji} n_j \mathbf{e}_i \implies \mathbf{T}_i = \sigma_{ji} n_j \quad (4.18)$$

but  $\mathbf{T}_i$  are traction components acting on any arbitrary plane, therefore, if  $\sigma_{ij}$  are known, the state of stress of a point is completely defined.

It is shown that  $\sigma_{ij}$  defines the stress state at a point. In general, it is expected that stress components to vary from point to point. Distribution of stress components are defined by equilibrium equations, derived from principle of linear and angular momentum.

Consider Figure 4.5, a body of volume  $V$  with surface area  $A$  subjected to a body force  $\mathbf{f}$  and surface traction  $\mathbf{T}$ , and density  $\rho$ .

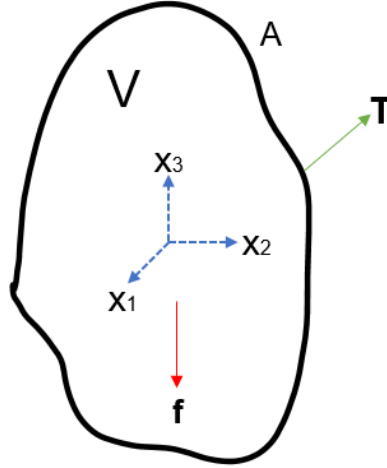


Figure 4. 5: Arbitrary body under traction and body force

The resultant of the body force and tractions is:

$$F_i = \int_V f_i dV + \int_A T_i dA_i \quad (4.19)$$

and linear momentum is:

$$L_i = \int_V \rho \ddot{u}_i dV \quad (4.20)$$

where  $\ddot{u}_i$  is the second derivative of velocity with respect to time. According to conservation of linear momentum  $F_i = L_i$

$$\int_V f_i dV + \int_A T_i dA_i = \int_V \rho \ddot{u}_i dV \quad (4.21)$$

and conservation angular momentum is

$$\int_V (\epsilon_{ijk} x_j f_k) dV + \int_A (\epsilon_{ijk} x_j T_k) dA_i = \int_V (\epsilon_{ijk} x_j \rho \ddot{u}_k) dV \quad (4.22)$$

For quasi-static problem, inertia terms are small, hence,  $\ddot{\mathbf{u}} = 0$ .

From equations (4.18) and (4.21), one gets:

$$\int_V \mathbf{f}_i dV + \int_A \sigma_{ji} n_j dA = 0 \quad (4.23)$$

and using equations (4.19) and (4.22) produce:

$$\int_V (\varepsilon_{ijk} x_j \mathbf{f}_k) dV + \int_A (\varepsilon_{ijk} x_j \sigma_{lk} n_l) dA = 0 \quad (4.24)$$

By applying the divergence theorem, equation (4.21) becomes:

$$\int_V (\mathbf{f}_i + \sigma_{ji,j} - \rho \ddot{\mathbf{u}}_i) dV = 0 \quad (4.25)$$

since  $dV$  is arbitrary, then:

$$\mathbf{f}_i + \sigma_{ji,j} - \rho \ddot{\mathbf{u}}_i = 0 \quad (4.26)$$

and for quasi-static problems:

$$\mathbf{f}_i + \sigma_{ji,j} = 0 \quad (4.27)$$

Equation (4.27) is the equilibrium equation.

Using angular momentum, it can be shown that stress components are symmetric as follow:

$$\int_V (\varepsilon_{ijk} x_j \mathbf{f}_k) dV + \int_A (\varepsilon_{ijk} x_j \mathbf{T}_k) dA = \int_V (\varepsilon_{ijk} x_j \rho \ddot{\mathbf{u}}_k) dV \quad (4.28)$$

applying the divergence theorem gives:

$$\int_V \left( \varepsilon_{ijk} x_j \mathbf{f}_k + (\varepsilon_{ijk} x_j \sigma_{lk})_{,j} - \varepsilon_{ijk} x_j \rho \ddot{\mathbf{u}}_k \right) dV = 0 \quad (4.29)$$

Expanding equation (4.29) and applying the equilibrium equation gives:

$$\int_V \varepsilon_{ijk} \sigma_{jk} dV = 0 \quad (4.30)$$

$dV$  is arbitrary, then:

$$\varepsilon_{ijk} \sigma_{jk} = 0 \quad (4.31)$$

If  $i$  and  $j$  varies from 1 to 3, then:

$$\left. \begin{array}{l} i=1 \quad \sigma_{23} - \sigma_{32} = 0 \\ i=2 \quad \sigma_{31} - \sigma_{13} = 0 \\ i=3 \quad \sigma_{12} - \sigma_{21} = 0 \end{array} \right\} \implies \sigma_{ij} = \sigma_{ji} \quad (4.32)$$

Therefore, stress components are symmetric. From equations (4.18) and (4.32)

$$\mathbf{T}_i = \sigma_{ji} \mathbf{n}_j = \sigma_{ij} \mathbf{n}_j \quad (4.33)$$

and equation (4.27) can be written as:

$$f_i + \sigma_{ij,j} = 0 \quad (4.34)$$

#### 4.1.3.2 Analysis of strain

Displacement of a body are made up of two parts:

- 1) Rigid body motion which is uniform throughout the body
- 2) Relative motions or distortion which translate into strain

Consider reference points P, P', Q, and Q' on the undeformed and deformed position of the body in Figure 4.6. P and Q and P' and Q' are separated by distances  $ds_0$  and  $ds$  respectively. There are two coordinates, Eulerian and Lagrangian, that overlying on each other, capital letter represents Eulerian coordinates.

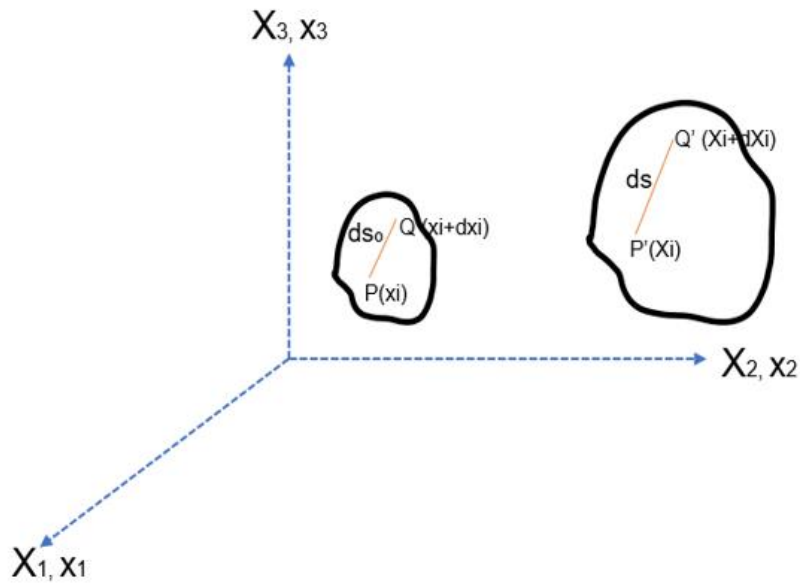


Figure 4. 6: An object under arbitrary Lagrangian and Eulerian deformations

$\mathbf{u}$  represents the displacement vector going from P to P' and  $\mathbf{u}+d\mathbf{u}$  represents Q to Q', shown in Figure 4.7.

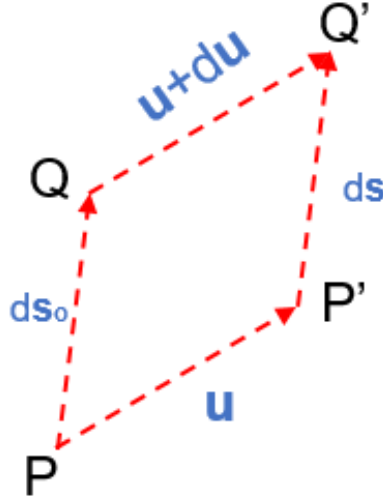


Figure 4. 7: Displacements of arbitrary points in space

Everything must be represented with respect to one coordinate system.

$$(ds_0)^2 = dx_1^2 + dx_2^2 + dx_3^2 = dx_i dx_i \quad (4.35)$$

$$(ds)^2 = dX_1^2 + dX_2^2 + dX_3^2 = dX_i dX_i \quad (4.36)$$

then,

$$d\mathbf{u} = ds - ds_0 \quad (4.37)$$

in component form:

$$(ds)^2 - (ds_0)^2 = dX_i dX_i - dx_i dx_i \quad (4.38)$$

Let consider Lagrangian coordinate first. The final coordinates  $X_i$  are considered to be the same function of  $x_i$ :

$$X_i = X_i(x_i) \quad (4.39)$$

and

$$dX_i = X_{i,j} dx_j \quad (4.40)$$

furthermore, the displacement  $\mathbf{u}$  is given by:

$$u_i = X_i - x_i \quad (4.41)$$



From equations (4.38), (4.39), and (4.40):

$$\begin{aligned}
(ds)^2 - (ds_o)^2 &= X_{i,j} dx_j X_{i,k} dx_k - dx_i dx_i \\
&\quad (X_{i,j} X_{i,k} - \delta_{ij} \delta_{ik}) dx_j dx_k \\
&\quad \left[ (x_i + u_i)_{,j} (x_i + u_i)_{,k} - \delta_{ik} \right] dx_j dx_k \\
&\quad \left[ (\delta_{ij} + u_{i,j}) (\delta_{ik} + u_{i,k}) \right] dx_j dx_k \\
&\quad \left[ u_{j,k} + u_{k,j} + u_{i,j} u_{j,k} \right] dx_j dx_k
\end{aligned} \tag{4.42}$$

rearranging indices gives:

$$(ds)^2 - (ds_o)^2 = (u_{i,j} + u_{j,i} + u_{k,i} u_{k,j}) dx_i dx_j \tag{4.43}$$

Let  $\varepsilon_{ij}^L$  be the components of the Lagrangian strain tensor (Green's strain tensor):

$$\varepsilon_{ij}^L = \frac{1}{2} (u_{i,j} + u_{j,i} + u_{k,i} u_{k,j}) \tag{4.44}$$

then:

$$(ds)^2 - (ds_o)^2 = 2\varepsilon_{ij}^L dx_i dx_j \tag{4.45}$$

Now consider referencing everything to the Xi coordinates, Eulerian description, then:

$$x_i = x_i(X_i) \tag{4.46}$$

and

$$dx_i = x_{i,j} dX_j \tag{4.47}$$

From equations (4.45), (4.46), and (4.47):

$$\begin{aligned}
(ds)^2 - (ds_o)^2 &= dX_i dX_i - x_{i,j} dX_j x_{i,k} dX_k \\
&\quad (\delta_{ij} \delta_{ik} - x_{i,j} x_{i,k}) dX_j dX_k \\
&\quad \left[ \delta_{ik} - (X_i - u_i)_{,j} (X_i - u_i)_{,k} \right] dX_j dX_k \\
&\quad \left[ u_{j,k} + u_{k,j} - u_{i,j} u_{j,k} \right] dX_j dX_k
\end{aligned} \tag{4.48}$$

rearranging indices gives:

$$(ds)^2 - (ds_o)^2 = (u_{i,j} + u_{j,i} - u_{k,i} u_{k,j}) dX_i dX_j \tag{4.49}$$

and introduce the Eulerian strain tensor (Almansi's strain tensor):

$$\varepsilon_{ij}^E = \frac{1}{2}(\mathbf{u}_{i,j} + \mathbf{u}_{j,i} - \mathbf{u}_{k,i}\mathbf{u}_{k,j}) \quad (4.50)$$

then:

$$(\mathbf{ds})^2 - (\mathbf{ds}_o)^2 = 2\varepsilon_{ij}^E dX_i dX_j \quad (4.51)$$

If the displacement gradients are small, for instance,  $\ll 1$ , then, the product terms in equation (4.50) can be neglected. Furthermore, the initial and final coordinate systems are the same, thus:

$$\frac{\partial()}{\partial x_i} = \frac{\partial()}{\partial X_i} \quad (4.52)$$

and

$$\varepsilon_{ij}^L = \varepsilon_{ij}^E = \varepsilon_{ij} = \frac{1}{2}(\mathbf{u}_{i,j} + \mathbf{u}_{j,i}) \quad (4.53)$$

Equation (4.53) represents the relationship between strains and displacements. With the conservation of angular momentum, linear momentum, and force equilibrium, it can be shown that the strain components are symmetric.

## 4.2 THERMOPOROELASTIC FORMULATION

The development of thermoporoelastic model is based on Biot's self-consistent theory for porous media saturated with fluid [10] [83] [84]. Infinitesimal strain theory has been used since the body geometry is assumed unchanged during the deformation process. Therefore, Eulerian strain tensor can be applicable, and Darcy's law can be defined in terms of absolute velocity. The assumption is valid as long as grain displacements do not exceed 5% of the thickness of the compacting unit [85]. It is assumed that the porous media are linearly elastic, isotropic, homogenous, and the saturating fluid is a single-phase liquid. Chemical, potential phase change, and creep effects are ignored. Inertia and body force have been ignored so that the deformations are quasi-static. Dufour and Soret effects are negligible and ignored. Finally, the displacements are assumed irrotational

It is assumed that the temperatures for both rock matrix and pore fluid are the same, which is based on local thermal equilibrium assumption. Local thermal equilibrium assumes that the heat exchange between the solid and pore fluid phases is rapid enough in comparison with global heat and fluid diffusion. Therefore, the solid and fluid will have the same temperature. Although this assumption has not been validated experimentally, **Section 4.4 and Chapter 7** will discuss about the theory's validity and updates the thermoporoelastic model with local thermal non-equilibrium assumption.

The governing equations can be defined in terms of field equations governing matrix deformation, fluid and heat flows in pore spaces and porous matrix. The field governing equations can be derived based on the constitutive relations, the conservation laws of mass, momentum, and energy for the porous material with fluid and heat diffusion. The derivations in this chapter closely follow the works of Li [2], Kurashige [64], Coussy [65], and Rice and Cleary [86].

By applying the thermodynamics principals for a fluid saturated thermoelastic porous media, [86] [87], constitutive equations are:

$$\varepsilon_{ij} = C_{ijkl} S_{kl} + B_{ij} p + \alpha_{ij}^T \Delta T \quad (4.54)$$

$$\Delta \phi = B_{kl} S_{kl} + D p + \alpha^{T,p} \Delta T \quad (4.55)$$

where  $\varepsilon_{ij}$ ,  $S_{kl}$ ,  $\Delta \phi$ ,  $p$ , and  $\Delta T$  are the average strain, total stress, change in porosity, pore pressure change, and temperature variation respectively.  $\alpha_{ij}^T$  and  $\alpha^{T,p}$  are the linear thermal expansion tensor and volumetric thermal expansion of pore space respectively.

The elastic moduli  $C_{ijkl}$ ,  $B_{ij}$ , and  $D$  for isotropic materials have the following form:

$$C_{ijkl} = \frac{1}{4G} (\delta_{ik} \delta_{jl} + \delta_{il} \delta_{kj} - \frac{2}{1+\nu} \delta_{ij} \delta_{kl}) \quad (4.56)$$

$$B_{ij} = \frac{3(\nu^u - \nu)}{2GB(1+\nu)(1+\nu^u)} \delta_{ij} \quad (4.57)$$

$$D = \frac{1}{B} \left( \frac{1}{K} - \frac{1}{K^s} \right) - \frac{\phi}{K^f} \quad (4.58)$$

where  $B$  is the Skempton's coefficient [88] and  $K$  is the bulk modulus:

$$B = \frac{3(v^u - v)}{\alpha(1-2v)(1+v^u)} \quad (4.59)$$

$$K = \frac{2G(1+v)}{3(1-2v)} \quad (4.60)$$

In the above equations,  $G$  is the shear modulus,  $v$  is the Poisson's ratio,  $v^u$  is the undrained Poisson's ratio,  $\phi$  is the porosity, and  $\alpha$  is the Biot's coefficient.  $K^s$  and  $K^f$  are the bulk moduli of solid and pore fluid. Implicit in Biot's theory is the assumption that no volume deformation is produced by a deviatoric stress. However, Skempton [88] allowed for the possibility that deviatoric stresses also induce pore pressure changes for undrained conditions. Linear thermal expansion can also be expressed in term of the porous matrix thermal expansion coefficient,  $\alpha^{T,m}$  :

$$\alpha_{ij}^T = \alpha^{T,m} \delta_{ij} \quad (4.61)$$

The elastic moduli  $B_{kl}$  is  $B_{ij}$ , while indices  $i$  and  $j$  have been changed to  $k$  and  $l$ .

Equation (4.54) can be expressed as follow:

$$\varepsilon_{ij} = \frac{1}{2G} \left( S_{ij} - \frac{v}{1+v} S_{kk} \delta_{ij} \right) + \frac{\alpha(1-2v)}{2G(1+v)} p \delta_{ij} + \frac{\alpha^{T,m}}{3} \Delta T \delta_{ij} \quad (4.62)$$

Or in terms of strain:

$$S_{ij} = 2G \left( \varepsilon_{ij} + \frac{v}{1-2v} \varepsilon_{kk} \delta_{ij} \right) - \alpha p \delta_{ij} - \frac{2G(1+v)}{3(1-2v)} \alpha^{T,m} \Delta T \delta_{ij} \quad (4.63)$$

$$S_{kk} = \frac{2G(1+v)}{1-2v} \varepsilon_{kk} - 3\alpha p - \frac{2G(1+v)}{(1-2v)} \alpha^{T,m} \Delta T \quad (4.64)$$

Fluid mass change per unit volume  $m$  can be expressed as:

$$\Delta m = \rho^f \Delta \phi + \Delta \rho^f \phi \quad (4.65)$$

Changes in fluid density is defined by changes in pore pressure and temperature as:

$$\Delta\rho^f = \frac{\Delta\rho^f}{\Delta p} \Delta p + \frac{\Delta\rho^f}{\Delta T} \Delta T \quad (4.66)$$

where  $\rho^f$  is the density of fluid. By definition:

$$\frac{\Delta\rho^f}{\Delta p} = \frac{\rho^f}{K^f}, \quad \frac{\Delta\rho^f}{\Delta T} = -\rho^f \alpha^{T,f} \quad (4.67)$$

$\alpha^{T,f}$  is the volumetric thermal expansion coefficient of the pore fluid. Equation (4.65)

becomes:

$$\Delta m = \rho^f (\Delta\phi + \frac{p}{K^f} \phi - \alpha^{T,f} \Delta T \phi) \quad (4.68)$$

By substituting equations (4.57) and (4.59) into (4.55), the following equation is:

$$\Delta\phi = \frac{3(v^u - v)}{2GB(1+v)(1+v^u)} S_{ij} \delta_{ij} + \frac{p}{B} \left( \frac{1}{K} - \frac{1}{K^s} \right) - \frac{\phi}{K^f} p + \alpha^{T,p} \Delta T \quad (4.69)$$

Using equations (4.68) and (4.69), the fluid mass change equations becomes:

$$\Delta m = \rho^f \left[ \frac{3(v^u - v)}{2GB(1+v)(1+v^u)} S_{ij} \delta_{ij} + \frac{p}{B} \left( \frac{1}{K} - \frac{1}{K^s} \right) + (\alpha^{T,p} - \alpha^{T,f}) \Delta T \right] \quad (4.70)$$

Or per unit reference volume:

$$\frac{\Delta m}{\rho^f} = \xi = \frac{3(v^u - v)}{2GB(1+v)(1+v^u)} S_{ij} \delta_{ij} + \frac{p}{B} \left( \frac{1}{K} - \frac{1}{K^s} \right) + (\alpha^{T,p} - \alpha^{T,f}) \Delta T \quad (4.71)$$

By applying the following relationship:

$$\frac{1}{B} \left( \frac{1}{K} - \frac{1}{K^s} \right) = \frac{9(v^u - v)}{2GB^2(1+v)(1+v^u)} \quad (4.72)$$

from equation (4.72), equation (4.71) becomes:

$$\xi = \frac{\alpha(1-2v)}{2G(1+v)} \left( S_{kk} + \frac{3p}{B} \right) + (\alpha^{T,p} - \alpha^{T,f}) \Delta T \quad (4.73)$$

Constitutive relations for the coupled mass and heat diffusion processes can be obtained by using positive entropy production assumption [64] [65]:

$$q_i = -\rho^f \kappa_{ij} p_{,j} + L_{ij} T_{,j} \quad (4.74)$$

$$h_i = -k_{ij}T_{,j} + L'_{ij}p_{,j} \quad (4.75)$$

where  $q$  and  $h$  are the fluid mass and heat flux respectively.  $\kappa$  is the permeability of the matrix and  $k$  is the thermal conductivity coefficient.  $L$  and  $L'$  are cross-effect coefficient.  $L$  represents the Soret's diffusion, while,  $L'$  is analogous to Dufour's effect. For isotropic material, permeability and thermal conductivity coefficient take single values, meaning they are constant and the same everywhere in the rock medium. Cross-effect terms are much smaller compared to the first terms in the equations (4.74) and (4.75), therefore, they can be ignored [2] [64]. They can be simplified further into:

$$q_i = -\rho^f \kappa p_{,i} \quad (4.76)$$

$$h_i = -kT_{,i} \quad (4.77)$$

The conservation laws are used for the further steps in deriving thermoporoelastic model. The first one is the equilibrium equation, derived in section 4.2. Using equation (4.34) without any body force, and replacing  $\sigma$  with  $S$ , one obtains:

$$S_{ij,j} = 0 \quad (4.78)$$

The second law is the local fluid mass conservation:

$$\frac{\partial m}{\partial t} + q_{j,j} = 0 \quad (4.79)$$

Substitution of (4.76) into (4.79), it becomes:

$$\frac{\partial m}{\partial t} - \rho^f \kappa p_{,ij} = 0 \quad (4.80)$$

or,

$$\frac{\partial \xi}{\partial t} - \kappa p_{,ij} = 0 \quad (4.81)$$

The third, and the final law is the conservation of energy. By ignoring the terms representing the interconvertibility of thermal and mechanical energy, the energy balance becomes:

$$\frac{\partial(\rho CT)}{\partial t} + h_{i,i} + (C^f T q_i)_{,i} = 0 \quad (4.82)$$

where  $\rho$  and  $C$  are the density and specific heat for the material, and  $C^f$  is the specific heat of pore fluid. The second term in equation (4.82) represents conductive heat transfer, while, convective heat transfer through pore fluid flow is captured in the third term.

Equation (4.82) is established based on the concept of effective heat transfer also known as local thermal equilibrium (LTE) theory. Based on this theory, a uniform temperature gradient is imposed in a fluid-saturated, homogenous porous medium. In other words, the mean temperature of the matrix solid and fluid phases for an elementary volume are equal. However, occurrence of a temperature difference between the solid and fluid phases are possible at high fluid velocity. Therefore, energy balance must distinguish the mean temperature between the matrix solid and the pore fluid. A separate energy balance equation is required for each phase, and the heat flux transferred from one phase to the other is expressed by the means of a heat transfer coefficient [87] [35]. This modeling becomes very complex since more parameters are involved. The complete derivation of local thermal non-equilibrium (LTNE) is discussed further in **Chapter 7**.

Strain equation for small (infinitesimal) deformations is given by equation (4.53):

$$\varepsilon_{ij} = \frac{1}{2}(u_{i,j} + u_{j,i}) \quad (4.83)$$

$$\varepsilon_{kk} = u_{k,k} \quad (4.84)$$

by substituting (4.83) and (4.84) into (4.63), one obtains the following modified Navier equation:

$$G u_{i,jj} + \frac{G}{1-2\nu} u_{j,ji} - \alpha p_{,i} - \frac{2G\alpha^{T,m}(1+\nu)}{3(1-2\nu)} T_{,i} = 0 \quad (4.85)$$

by differentiating equations (4.63) and (4.84) twice, it leads to:

$$S_{ii,jj} = 2G \frac{1+\nu}{1-2\nu} (\epsilon_{kk,jj} - \alpha^{T,m} T_{,jj}) - 3\alpha p_{,jj} = 0 \quad (4.86)$$

$$\epsilon_{kk,jj} = u_{i,ijj} \quad (4.87)$$

Differentiating (4.85) with respect to  $i$  and solving  $u_{i,ijj}$ , and substitute back into (4.87) then into (4.86), the following equation in terms of stress is obtained:

$$S_{ii,jj} + \frac{2\alpha(1-2\nu)}{1-\nu} p_{,jj} + \frac{4G(1+\nu)}{3(1-\nu)} \alpha^{T,m} T_{,jj} = 0 \quad (4.88)$$

differentiate (4.73) twice with respect to  $j$ , and substitute (4.88) into it, one obtains:

$$\xi_{,jj} = \frac{\alpha(1-2\nu)}{2G(1+\nu)} \left[ \left( \frac{3}{B} - \frac{2\alpha(1-2\nu)}{1-\nu} \right) p_{,jj} - \frac{4G(1+\nu)}{3(1-\nu)} \alpha^{T,m} T_{,jj} \right] + (\alpha^{T,p} - \alpha^{T,f} \phi) T_{,jj} \quad (4.89)$$

Solving  $p_{,jj}$  from (4.89) and substituting into (4.81), the fluid diffusivity equation is obtained:

$$\frac{\partial \xi}{\partial t} = c^f \left[ \xi_{,jj} + \left( \frac{2\alpha(1-2\nu)}{1-\nu} \frac{\alpha^{T,m}}{3} - (\alpha^{T,p} - \alpha^{T,f} \phi) \right) T_{,jj} \right] \quad (4.90)$$

where

$$c^f = \frac{2\kappa GB^2(1-\nu)(1+\nu^u)^2}{9(1-\nu^u)(\nu^u - \nu)} \quad (4.91)$$

is the fluid diffusivity coefficient. Differentiation of (4.71) with respect to  $t$ , and substituting into (4.81) and rearrange, the fluid diffusion equation can be expressed in terms of pore pressure:

$$\frac{\partial p}{\partial t} = \frac{2GB^2(1+\nu)(1+\nu^u)^2}{9(\nu^u - \nu)} \left[ \kappa p_{,jj} - (\alpha^{T,p} - \alpha^{T,f} \phi) \frac{\partial T}{\partial t} \right] - \frac{B}{3} \frac{\partial S_{kk}}{\partial t} \quad (4.92)$$

By applying relationship between  $S_{kk}$  and  $\epsilon_{kk}$ , equation (4.92) becomes:

$$\frac{\partial p}{\partial t} = M \left[ \kappa p_{,jj} - \alpha \frac{\partial \epsilon_{kk}}{\partial t} + (\alpha \alpha^{T,m} - \alpha^{T,p} + \alpha^{T,f} \phi) \frac{\partial T}{\partial t} \right] \quad (4.93)$$

where,



$$M = \frac{2G(v^u - v)}{\alpha^2(1 - 2v^u)(1 - 2v)} \quad (4.94)$$

is the Biot's modulus.

By substituting (4.76) and (4.72) into (4.82), one obtains:

$$\frac{\partial T}{\partial t} = c^T T_{,ii} + \frac{\kappa \rho^f C^f}{\rho C} (T p_{,i})_{,i} \quad (4.95)$$

where,

$$c^T = \frac{k}{\rho C} \quad (4.96)$$

is the thermal diffusivity coefficient for bulk material.

The equations derived for displacement, pore pressure, thermal field are completely coupled with each other. The coupling between pore pressure and thermal fields includes non-linearity. If  $S_{ij}$  replaces  $u_i$  and pore pressure,  $p$ , replaces  $\xi$ , the above field equations can be written as:

$$S_{ij,j} = 0 \quad (4.97)$$

$$\frac{dp}{dt} = M \left[ \kappa p_{,ij} - \alpha \frac{\partial \epsilon_{kk}}{\partial t} + (\alpha \alpha^{T,m} - \alpha^{T,p} + \alpha^{T,f} \phi) \frac{\partial T}{\partial t} \right] \quad (4.98)$$

$$\frac{dT}{dt} = c^T T_{,ii} + \frac{\kappa \rho^f C^f}{\rho C} (T p_{,i})_{,i} \quad (4.99)$$

Solving the three equations above simultaneously, one can define the displacement, pore pressure, and thermal fields for a fluid-saturated, isotropic, thermoporoelastic medium.

### 4.3 MATERIAL PROPERTIES DEPENDENCY ON TEMPERATURE AND PORE PRESSURE

Not only the parameters in the thermoporoelastic model are spatial and temporal dependent, but also, may vary with thermal and stress variations.

### 4.3.1 Thermal conductivity

Thermal conductivity of a porous media is inversely proportional to its pore spaces. The higher the pore space the lower the thermal conductivity will be since solid is a better conductor than fluid. In fact, conductivity of a rock will increase with increasing stress since the grains are compacted and more contacts between them are created (pore space is reduced). However, the increase in thermal conductivity with stress is generally small as shown in Figure 4.8.

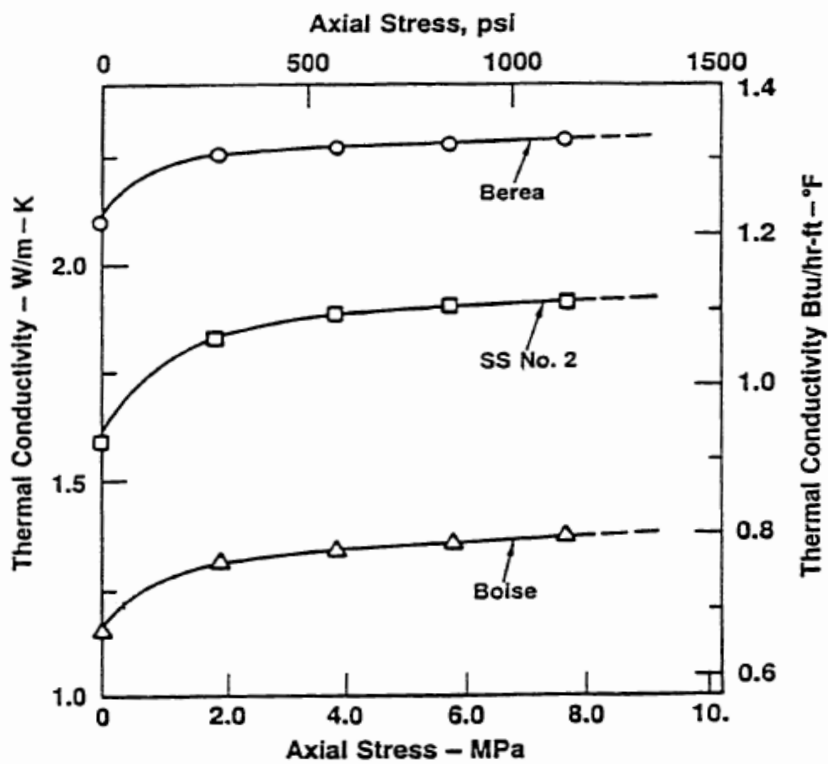


Figure 4. 8: Stress effect on thermal conductivity. Conductivity of a rock will increase with increasing stress. However, the increase in thermal conductivity with stress is generally small [41]

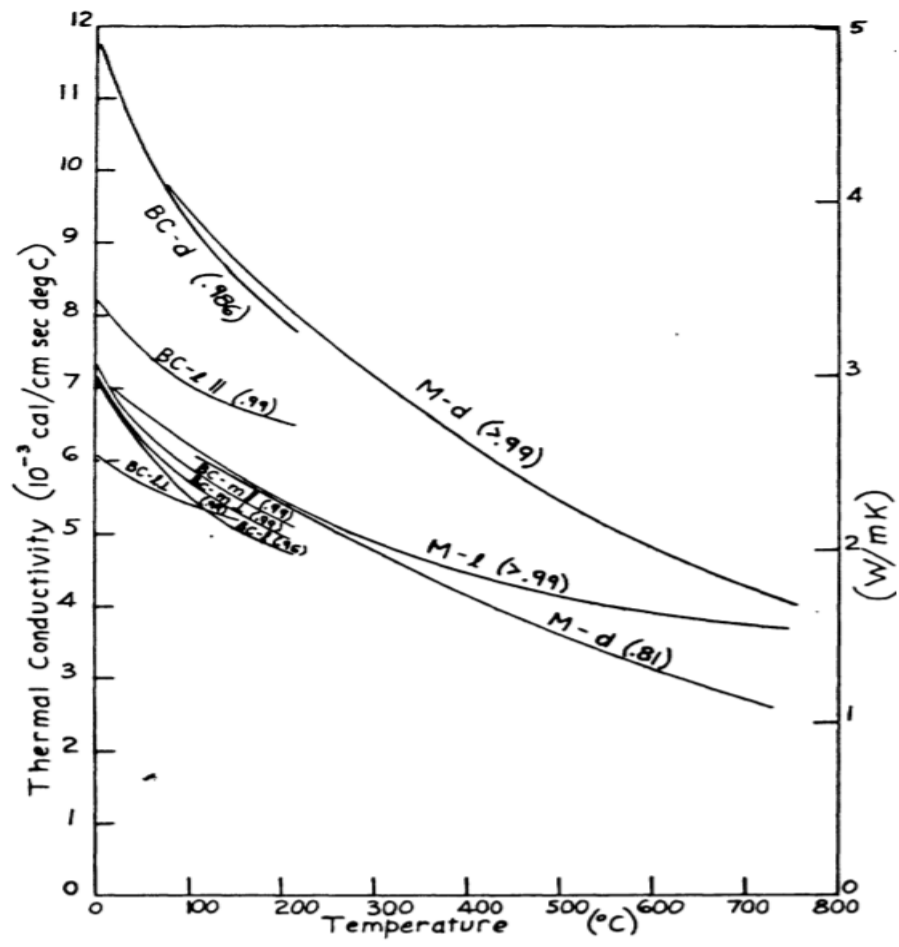
Edmondson [89] reported from 10-13% increase for about 7 MPa stress increase at low environmental stress level (6-25 MPa). Woodside and Messmer [90] reported a 12% increase per 7 MPa at low stress range (0-7 MPa), and 2.5% increase per 7 MPa at high

range stress (14-28MPa). Somerton [41] developed an empirical model for temperature dependent thermal conductivity of sandstone based on Tikhomirov's work [91]:

$$k^T = k^{T,20} - 10^{-3}(T - 293)(k^{T,20} - 1.38) \left[ k^{T,20} (1.8 \times 10^{-3} T)^{-0.25 k^{T,20}} + 1.28 \right] (k^{T,20})^{-0.64} \quad (4.100)$$

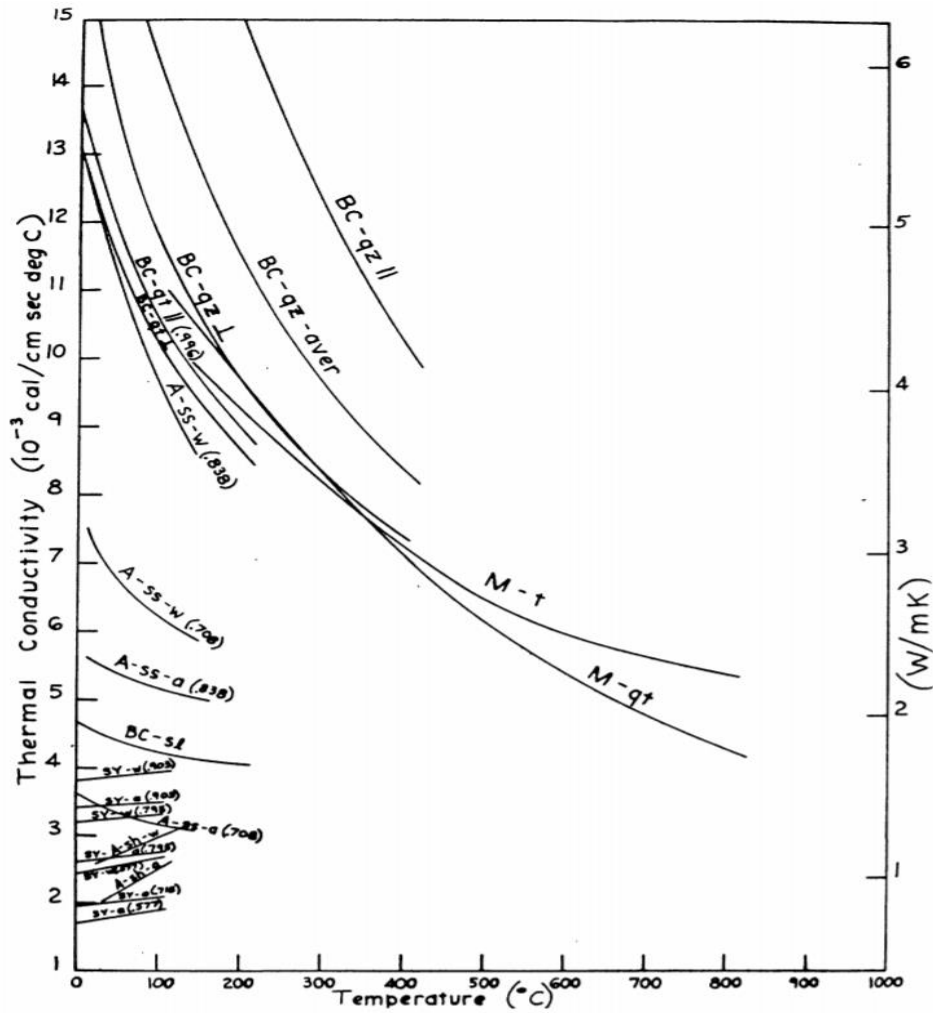
where  $k^{T,20}$  is the thermal conductivity at 20°C in W/m/K, T is in Kelvin. Tikhomirov and Somerton have shown moderate negative gradients of thermal conductivity for high conductivity rocks, but small positive gradients for low conductivity rocks.

Thermal conductivities of rocks usually decrease with increasing temperature. This can be observed at very high temperature as shown in Figure 4.9. However, in drilling conditions, the temperature changes are small, e.g., 20-60 degrees. This temperature change is not large enough to change thermal conductivity of the formation greatly.



(a)

Figure 4.9



(b)

Figure 4. 9: Temperature effect on thermal conductivity at 5 MPa. (a) dense limestone, marble, and dolostone, in directions parallel and perpendicular to bedding, with decimal solidity in parentheses (b) Temperature effect on thermal conductivity at 5MPa of sandstones, quartzites, and shales, with quartz shown for comparison; decimal solidity in parentheses. [109]

Abdulagatov et al. studied the effect of confining pressure and temperature on effective thermal conductivity (ETC) for several rock types [92]. They concluded that with increasing confining pressure, ETC will increase sharply from 0.1 MPa to 100 MPa. At higher pressure (>100 MPa) a weak linear relationship between ETC and confining pressure was observed. A decrease in ETC was observed with increasing temperature in

sedimentary rocks. The effect of temperature on ETC relies on the structure of the sample (crystalline vs. amorphous) as well as the conductivity of minerals associated with the sample [92].

### 4.3.2 Thermal expansion coefficient

Many papers have shown a nonlinear behavior of thermal expansion coefficient with temperature. However, below 400 °C, the trend can be treated as linear. Above the linear threshold, thermal expansion increases rapidly, and it stops at above a certain temperature (about 600 °C) as shown in Figure 4.10.

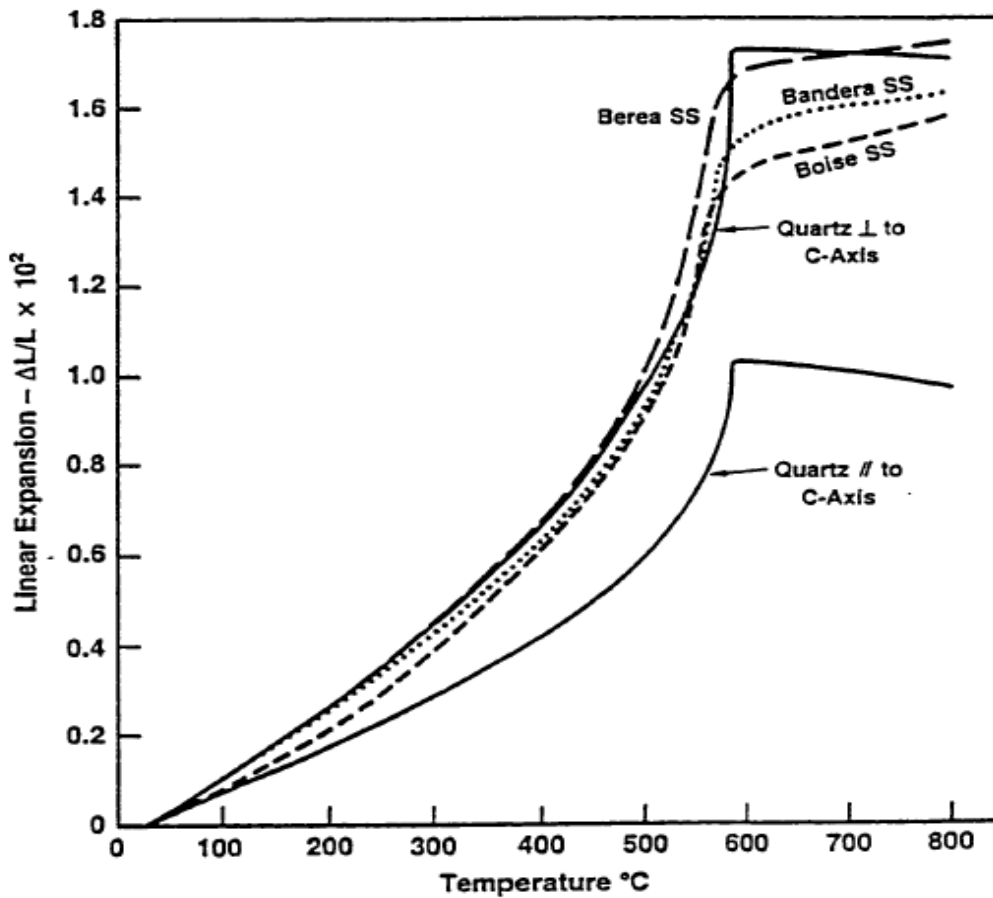


Figure 4. 10: Temperature effect on linear thermal expansion coefficient [41]

If the cooling causes permanent damage or plastic deformation, the thermal expansion will obey a different trend during the cooling phase, the thermal expansion experiences hysteresis. Thermal expansion also depends on stress. Sweet estimated 25% decrease in volumetric thermal expansion coefficient of low permeability sandstone when atmospheric pressure rose to 100 MPa [93]. Wong and Brace have shown the same magnitude of decrease under larger pressure variations, 100-500 MPa [94].

### 4.3.3 Fluid thermal expansion

Sorey suggested the following equation for temperature-dependent fluid thermal expansion coefficient [95]:

$$\alpha^{T,f} = \frac{\rho^{f,ref} - \rho^f}{p^{ref} (T - T^{ref})} \quad (4.101)$$

where superscript “ref” represents the reference state.

Perry’s [96] hand book can also be used to predict thermal expansion coefficient for liquids:

$$\alpha^{T,f} = \alpha T + \beta T^2 + \gamma T^3 \quad (4.102)$$

where  $\alpha$ ,  $\beta$ ,  $\gamma$  and are constants and vary for different materials. The temperature range for the above equation is 0-160 °C.

### 4.3.4 Porosity

Dependency of porosity on effective stress and pore pressure have been studied by numerous authors experimentally and theoretically. For instance, Geertsma [97] suggested:

$$\phi = \phi^n + \left( \frac{1}{K^s} - \frac{1 - \phi^n}{K} \right) (dp^c - dp) \quad (4.103)$$

where  $\phi^n$  and  $P^c$  are porosity at the previous loading stage and confining pressure respectively.  $K^s$  and  $K$  are solid grain and total bulk moduli respectively. Since

permeability is a function of porosity, it can be calculated using Carman-Kozeny's relation:

$$\kappa = \kappa^{\text{ref}} \left( \frac{\phi}{\phi^{\text{ref}}} \right)^3 \quad (4.104)$$

where  $\phi^{\text{ref}}$  and  $\kappa^{\text{ref}}$  are reference parameters of porosity and permeability.

Temperature dependency of porosity and permeability can be captured using [98], [98], [100]:

$$\phi = \phi^{\text{ref}} \exp \left[ \frac{3}{4G^s} (\sigma'^m - \sigma'^m) + (\alpha^{T,p} - \alpha^{T,m})(T - T^{\text{ref}}) \right] \quad (4.105)$$

$$\kappa = \kappa^{\text{ref}} \exp \left[ b \left( \frac{3}{4G^s} (\sigma'^m - \sigma'^m) + (\alpha^{T,p} - \alpha^{T,m})(T - T^{\text{ref}}) \right) \right] \quad (4.106)$$

where  $G^s$  and  $\sigma'^m$  are the shear modulus and stress of the rock matrix.  $\sigma'^{nm}$  is the stress acting on the non-matrix part.  $b$  is the power of porosity [101].

#### 4.3.5 Tensile strength

Rock formation tensile strength also is temperature dependent parameter. Experimental results have shown that the tensile strength of the rock increases gradually with temperature initially, but after a certain high temperature tends to decrease, as shown in Figure 4.11. The decrease is due to plastic deformation or permanent damage caused by molecular debonding [76].



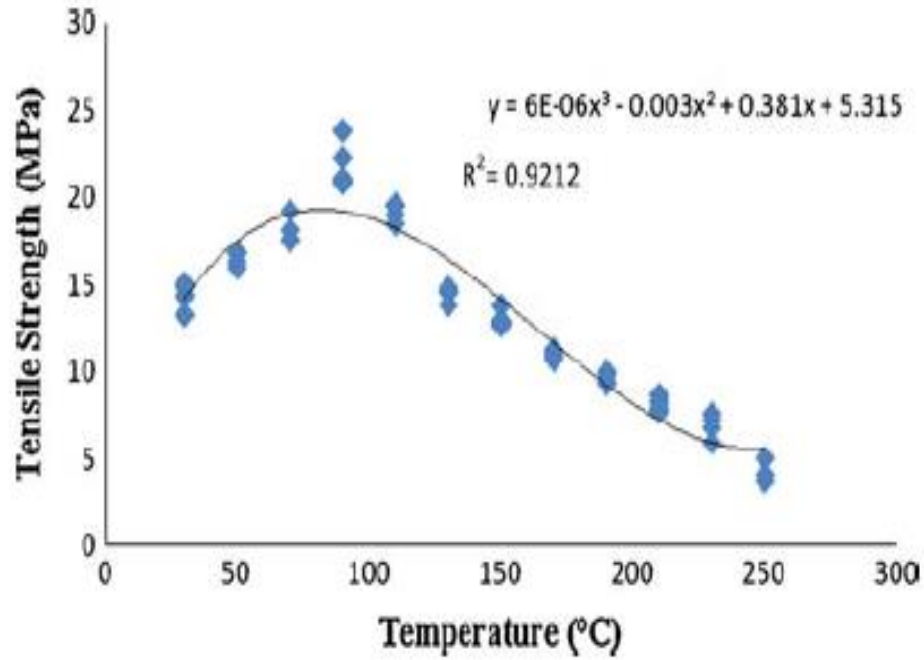


Figure 4. 11: Tensile strength vs. temperature [76]

#### 4.3.6 Elastic parameters

Elastic properties demonstrate non-linear trend with variations of pressure and temperature. the following equations have been suggested for them:

$$\frac{1}{K} = \frac{1}{K^s} \frac{1}{1 - \phi^n \exp(c)} (1 + a\phi^n \exp(c)) \quad (4.107)$$

$$G = G^s \left( 1 - \frac{15(1-\nu)}{7-5\nu} \phi^n \exp(c) \right) \quad (4.108)$$

$$\alpha = \frac{(1+a)\phi^n \exp(c)}{1 + a\phi^n \exp(c)} \quad (4.109)$$

$$B = \frac{1+a}{a + (1 - \phi^n \exp(c)) K^s / K^f + \phi^n \exp(c)} \quad (4.110)$$

where

$$a = \frac{1 + \nu}{2(1 - 2\nu)} \quad (4.111)$$

$$c = -\frac{3}{4G^s}(\sigma'^m - \sigma'^m) + (\alpha^{T,p} - \alpha^{T,m})(T - T^n) \quad (4.112)$$

Biot's coefficient and Skempton coefficients are two key parameters that will influence poroelastic coupling greatly. Hassanzadegan et al. have studied the effect of temperature and pressure on these coefficients [102]. They suggested that the temperature variation has a very little effect on Biot's and Skempton's coefficients, while pressure substantially influences the effects of the two coefficient and coupling of the poroelastic model as shown in Figures 4.12 and 4.13. The values of the parameters decreased with increasing effective pressure, indicating that the strength of poroelastic coupling decays as effective pressure increases. Experimental results have shown that mechanical properties such as grain bulk modulus  $K^s$ , can be taken as constant in the range of the stress change induced by drilling or production, even for hard rocks [103].

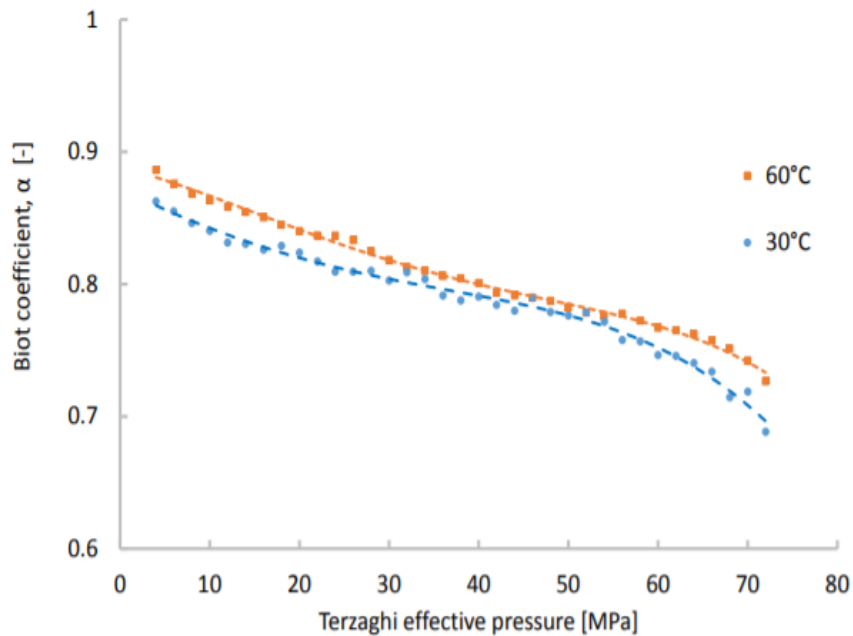


Figure 4. 12: Biot's coefficient as a function of effective pressure at two different temperatures [102]

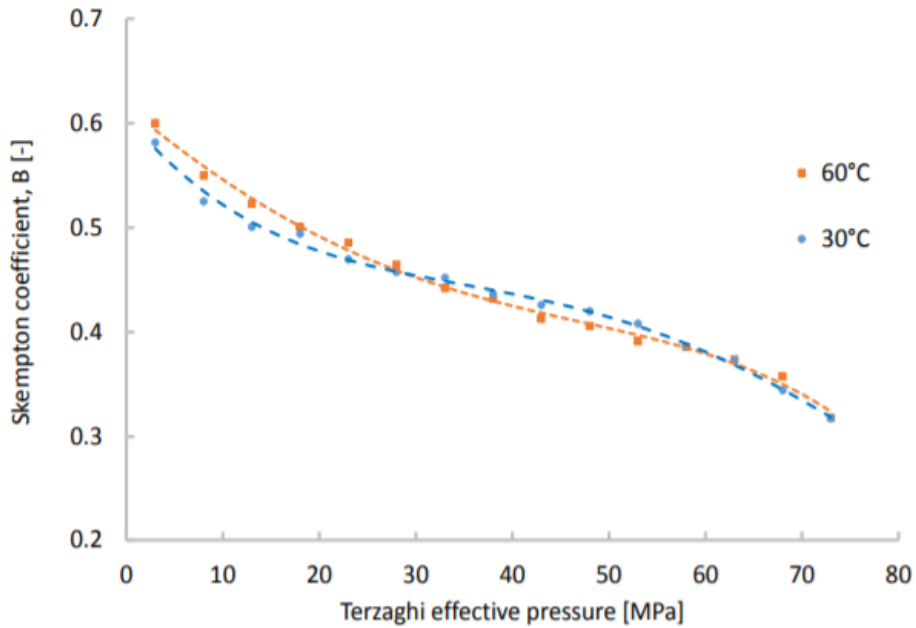


Figure 4. 13: Skempton's coefficient as a function of effective pressure [102]

#### 4.4 LOCAL HEAT EXCHANGE THEORY

Local heat exchange also known as instantaneous local thermal equilibrium (LTE) has always been employed for fluid flow and heat transfer inside the porous media for simplification. However, this theory has not been validated experimentally. LTE ignores additional pore and thermal stresses in the porous medium caused by temperature variations of the fluid and solid phases. Therefore, a more realistic approach is necessary to model both temperatures separately, known as local thermal non-equilibrium (LTNE). Lu and Xiang have done theoretical analyses on validity of the theory [104]. Based on their analyses, the discrepancies caused by using the LTE theory for heat exchange between rock matrix and fluid can be significant at locations close to the heat source and at early times of the process but reduce rather quickly to negligible levels as the distance to the heat source and the time increase. It is concluded that formations with fractures where flow

velocity is large, assumption of the LTE theory may produce erroneous results, whereas, in intact wellbore or low permeability formations the assumption may hold valid.

Combarinous and Bories [105], Vafai and Sozen [106], and Hojka et al. [35] analyses can be used to establish different temperature profile for rock matrix and the fluid where LTE theory is not applicable, as shown in Figure 4.14.

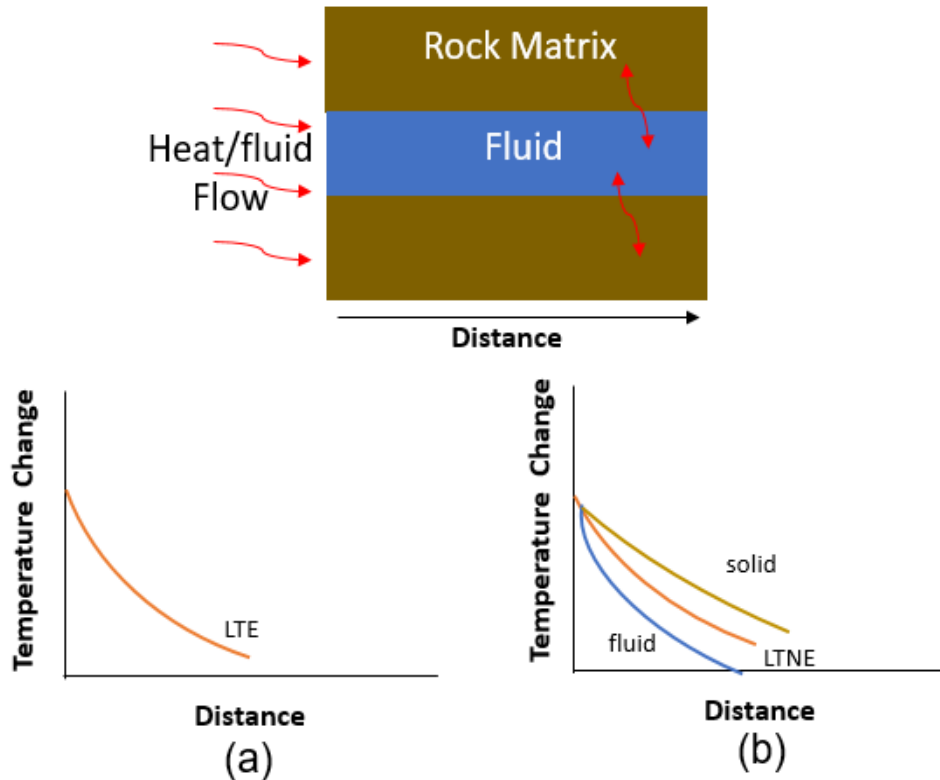


Figure 4. 14: Temperature profile for porous media. (a) LTE temperature profile prediction (b) LTNE temperature profile

Combarinous and Bories [105] and Nield and Bejan [107] formulated mathematical models by applying an energy balance approach on both the fluid phase and the solid phase:

$$\nabla \cdot (\phi k_f \nabla T_f) - \nabla \cdot [(\rho c)_f v T_f] = \frac{\partial}{\partial t} [\phi (\rho c)_f T_f] - h(T_s - T_f) \quad (4.115)$$

$$\nabla \cdot ((1 - \phi) k_s \nabla T_s) = \frac{\partial}{\partial t} [(1 - \phi) (\rho c)_s T_s] + h(T_s - T_f) \quad (4.116)$$

where,  $k_f$  and  $k_s$  are the thermal conductivity of fluid and rock matrix,  $v$  is the fluid velocity,  $h$  is the heat transfer coefficient,  $T_f$  and  $T_s$  are the fluid and solid temperatures.  $\rho$  is the density of the material and  $\phi$  is the porosity of the rock.

Hojka et al. presented an analytical solution for the effect of LTNE for a long period of time suitable for thermal oil recovery scenario [35]. However, our interest is short time which is suitable for drilling scenarios. Figure 4.15 shows the temperature profiles calculated using equations (4.115) and (4.116) using explicit finite difference method for solid matrix and fluid. The data for this analysis is shown in Table 1. The fluid temperature is ahead of the solid matrix invalidating LTE theory, claiming that the rock and fluid temperatures are instantaneously at equilibrium.

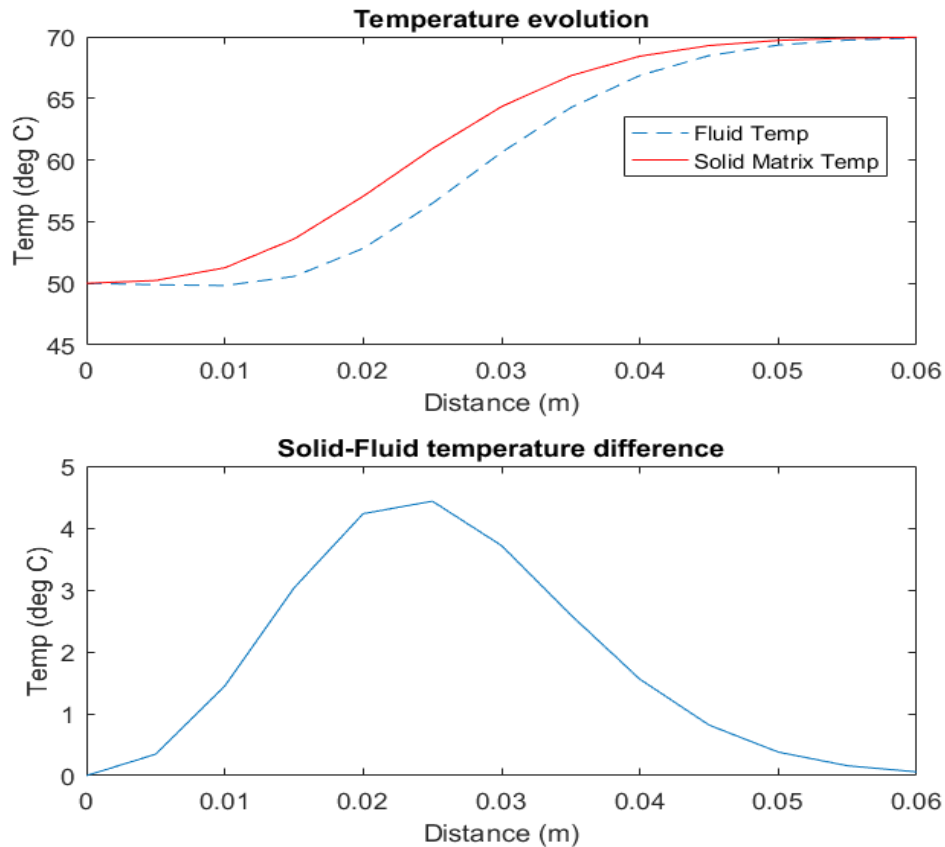


Figure 4. 15: Temperature profile for different phases under LTNE condition

According to Eckert, the heat transfer coefficient ( $h$ ) inversely proportional to the porous media grain size [108]. Therefore, the heat transfer coefficient is small for coarse size grain samples. Low heat transfer coefficient causes the temperature discrepancy to increase and invalidating the LTE theory.

**Chapter 7** will explore validity of LTE and effect of local thermal non-equilibrium in further details. The LTNE effects on temperature profile and the thermoporoelastic model will be provided through analyses. A series of analytical and numerical models are discussed in this chapter.

Table 4. 1: Parameters for LTE validation

<b>Parameter</b>	<b>value</b>
Initial temperature ( $^{\circ}\text{C}$ )	70
$\Delta T$ ( $^{\circ}\text{C}$ )	-20
Time (sec)	0.5
$h$ ( $\text{w}/\text{m}^2/\text{Kelvin}$ )	2000
Porosity	0.3
$v$ (m/s)	1.6
Well radius (m)	0.1
$r$ (m)	1
$(\rho c)_f$ ( $\text{J}/\text{m}^3/\text{Kelvin}$ )	4.19e6
$(\rho c)_s$ ( $\text{J}/\text{m}^3/\text{Kelvin}$ )	1.54e6
$k_s$ ( $\text{w}/\text{m}/\text{Kelvin}$ )	1.4
$k_f$ ( $\text{w}/\text{m}/\text{Kelvin}$ )	0.61

## CHAPTER 5: THERMOPOROELASTIC MODELS

### 5.1 INTRODUCTION

This section covers a series of analytical and numerical solutions for the thermoporoelastic model with assumption of irrotational displacement for any wellbore orientations. The borehole can be subjected to non-hydrostatic pressures.

### 5.2 IRROTATIONAL DISPLACEMENT

Irrotational displacement allows the decoupling of the displacement field from temperature and pore pressure fields. The irrotational displacement is allowed under the condition of axisymmetric loading. This decoupling simplifies the equations, therefore, finding the solutions becomes straightforward.

#### 5.2.1 Displacement decoupling from temperature and pore pressure fields

For the irrotational displacement field, the displacement can be expressed as a gradient of a scalar function  $\Psi$  [64], that is:

$$u_i = \Psi_{,i} \quad (5.1)$$

$$u_{i,i} = \Psi_{,ii} = \varepsilon_{ii} \quad (5.2)$$

Insert (5.2) into the Navier equation (4.85), one has:

$$G \Psi_{,ijj} + \frac{G}{1-2\nu} \Psi_{,ijj} - \alpha p_{,i} - \frac{2G\alpha^{T,m}(1+\nu)}{3(1-2\nu)} T_{,i} = 0 \quad (5.3)$$

Equation (5.3) can be rearranged to:

$$\Psi_{,ijj} \left( \frac{2G(1-\nu)}{1-2\nu} \right) = \alpha p_{,i} + \frac{2G\alpha^{T,m}(1+\nu)}{3(1-2\nu)} T_{,i} \quad (5.4)$$

Integrating equation (5.4) with respect to  $i$ , gives:

$$\Psi_{,jj} \left( \frac{2G(1-\nu)}{1-2\nu} \right) = \alpha p + \frac{2G\alpha^{T,m}(1+\nu)}{3(1-2\nu)} T + g(t) \quad (5.5)$$

Using (5.2), (5.5) becomes:

$$\varepsilon_{ij} \left( \frac{2G(1-\nu)}{1-2\nu} \right) = \alpha p + \frac{2G\alpha^{T,m}(1+\nu)}{3(1-2\nu)} T + g(t) \quad (5.6)$$

where  $g(t)$  is an arbitrary function of time. Substitute equation (5.6) into (4.64) and rearrange to obtain:

$$S_{kk} = -\frac{2(1-2\nu)}{1-\nu} \alpha p - \frac{4G(1+\nu)}{1-\nu} \alpha^{T,m} T + \frac{1+\nu}{1-\nu} g(t) \quad (5.7)$$

Pore pressure and temperature field equations can be formulated as follow:

Substituting (5.6) into (4.73) and rearranging:

$$\zeta_{,ij} = \frac{\alpha(1-2\nu)}{2G(1+\nu)} \left[ \frac{3}{B} - \frac{2\alpha(1-2\nu)}{1-\nu} \right] p_{,ij} - \left[ \frac{2\alpha(1-2\nu)}{3(1-\nu)} \alpha^{T,m} - (\alpha^{T,p} - \alpha^{T,f} \phi) \right] T_{,ij} + \frac{\alpha(1-2\nu)}{2G(1-\nu)} g(t) \quad (5.8)$$

Suspending indicial notation, and differentiation with respect to time while keeping coefficients constant, one has:

$$\frac{\partial}{\partial t} \zeta = \frac{\alpha(1-2\nu)}{2G(1+\nu)} \left[ \frac{3}{B} - \frac{2\alpha(1-2\nu)}{1-\nu} \right] \frac{\partial}{\partial t} p - \left[ \frac{2\alpha(1-2\nu)}{3(1-\nu)} \alpha^{T,m} - (\alpha^{T,p} - \alpha^{T,f} \phi) \right] \frac{\partial}{\partial t} T + \frac{\alpha(1-2\nu)}{2G(1-\nu)} \frac{\partial}{\partial t} g(t) \quad (5.9)$$

Substituting equation (5.9) into (4.81):

$$\frac{\alpha(1-2\nu)}{2G(1+\nu)} \left[ \frac{3}{B} - \frac{2\alpha(1-2\nu)}{1-\nu} \right] \frac{\partial}{\partial t} p = \kappa p_{,ij} + \left[ \frac{2\alpha(1-2\nu)}{3(1-\nu)} \alpha^{T,m} - (\alpha^{T,p} - \alpha^{T,f} \phi) \right] \frac{\partial}{\partial t} T - \frac{\alpha(1-2\nu)}{2G(1-\nu)} \frac{\partial}{\partial t} g(t) \quad (5.10)$$

Rearranging equation (5.10) gives:



$$\frac{\partial p}{\partial t} = c^f p_{,ij} + c^{T,p} \frac{\partial T}{\partial t} - c^g \frac{\partial g(t)}{\partial t} \quad (5.11)$$

where,

$$c^f = \frac{2\kappa GB^2(1+v^u)^2(1-v)}{9(v^u-v)(1-v^u)} \quad (5.12)$$

$$c^{T,p} = \frac{c^f}{\kappa} \left[ \frac{2\alpha(1-2\nu)}{3(1-\nu)} \alpha^{T,m} - (\alpha^{T,p} - \alpha^{T,f}\phi) \right] \quad (5.13)$$

$$c^g = \frac{B(1+v^u)}{3(1-v^u)} \quad (5.14)$$

For infinite or semi-infinite domains, the function  $g(t)$  approaches zero, since strains, pore pressure, and temperature fields are unchanged. Therefore, equation (5.11) reduced to:

$$\frac{\partial p}{\partial t} = c^f p_{,ij} + c^{T,p} \frac{\partial T}{\partial t} \quad (5.15)$$

It is obvious that the displacement field is decoupled from the pore pressure and the temperature fields. However, pore pressure and temperature fields are still coupled with each other temporally through convective heat transfer.

### 5.3 SIMPLIFIED CASES

Thermoporoelastic equations (4.99) and (5.15) are coupled with each other, with non-linearity in the temperature field, so they are very challenging to solve analytically. But in some specific cases, these equations can be decoupled and linearized. The simplification can be done by minimizing the effect of the coefficients in thermoporoelastic equations.

#### 5.3.1 Case 1: analytical solution for low permeability formation

Since the medium of interest is a low permeable formation, convective mechanism caused by fluid flow can be ignored. By ignoring the convective heat transfer in the thermal diffusivity equation (4.99), thermal diffusivity equation is decoupled, and pore pressure

diffusivity equation becomes linear. With this simplification, it can be concluded that the conductive heat transfer dominates the heat transfer mechanism inside the porous medium.

Therefore, the simplified equations will be:

$$\frac{\partial T}{\partial t} = c^T T_{,ii} \quad (5.16)$$

$$\frac{\partial p}{\partial t} = c^f p_{,ij} + c^{T,p} \frac{\partial T}{\partial t} \quad (5.17)$$

The analytical solution can easily be obtained under initial and boundary conditions. This case is suitable for low permeability formations such as shale where fluid flow is negligible.

Assuming the wellbore is aligned along one of the in-situ principal stress directions, the in-situ stresses are non-hydrostatic. The problem can be solved by dividing it into three loading modes using Detournay and Cheng technique [11]. The boundary conditions for the three loading modes are as follow:

Mode 1:

$$\sigma_r^{(1)} = H(t)(p_o - p_m) \quad (5.17)$$

$$\sigma_{r\theta}^{(1)} = 0 \quad (5.18)$$

$$p^{(1)} = 0 \quad (5.19)$$

$$T^{(1)} = 0 \quad (5.20)$$

Mode 2:

$$\sigma_r^{(2)} = 0 \quad (5.20)$$

$$\sigma_{r\theta}^{(2)} = 0 \quad (5.21)$$

$$p^{(2)} = H(t)(p_o - p_m) \quad (5.22)$$

$$T^{(2)} = H(t)(T_o - T_m) \quad (5.23)$$

Mode 3:

$$\sigma_r^{(3)} = -S_o H(t) \cos 2\theta \quad (5.24)$$

$$\sigma_{r\theta}^{(3)} = S_o H(t) \sin 2\theta \quad (5.25)$$

$$p^{(3)} = 0 \quad (5.26)$$

$$T^{(3)} = 0 \quad (5.27)$$

where are defined as:

$$p_o = \frac{S_x + S_y}{2} \quad (5.28)$$

$$S_o = \sqrt{\left(\frac{S_x - S_y}{2}\right)^2 - S_{xy}^2} \quad (5.29)$$

$$\theta = \frac{1}{2} \tan^{-1}\left(\frac{2S_{xy}}{S_x - S_y}\right) \quad (5.30)$$

as shown in Figure 5.1.  $p_m$  and  $T_m$  are the mud pressure and temperature during drilling.

$H(t)$  is the Heaviside unite step function.

$$H(t) = 0 \quad \text{for } t \leq 0 \quad (5.31)$$

$$H(t) = 1 \quad \text{for } t > 0 \quad (5.32)$$

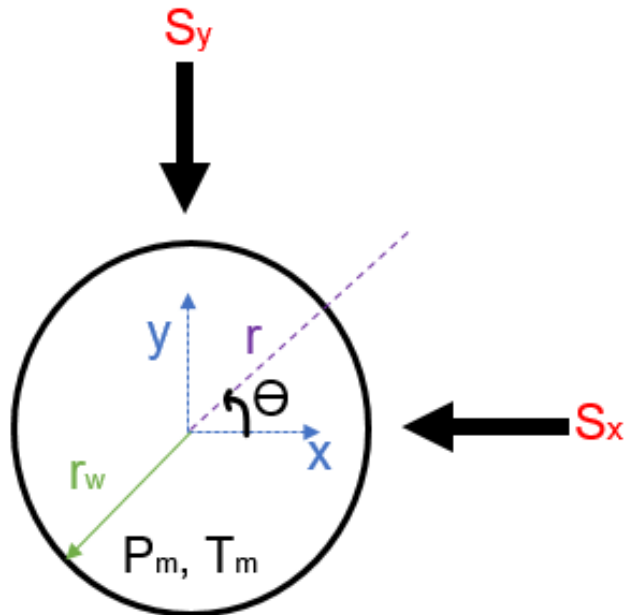


Figure 5. 1: Schematic wellbore subjected to non-hydrostatic stress field, wellbore pressure and temperature

### 5.3.1.1 Solutions for modes 1 through 3

Solutions for mode 1 and 3 can be found in Detournay and Cheng [11]. They are as follow:

Mode 1:

$$\sigma_{rr}^{(1)} = H(t)(p_o - p_m) \frac{r^2}{a^2} \quad (5.33)$$

$$\sigma_{\theta\theta}^{(1)} = -H(t)(p_o - p_m) \frac{r^2}{a^2} \quad (5.34)$$

Mode 3:

$$\frac{s\sigma_{rr}^{(3)}}{S_o \cos 2\theta} = \frac{B(1+v^u)}{3(1-v^u)} C_1 \left[ \frac{1}{\lambda r} K_1(\lambda r) + \frac{6}{(\lambda r)^2} K_2(\lambda r) \right] - \frac{C_2}{1-v^u} \frac{a^2}{r^2} - 3C_3 \frac{a^4}{r^4} \quad (5.35)$$

$$\frac{s\sigma_{\theta\theta}^{(3)}}{S_o \cos 2\theta} = \frac{B(1+v^u)}{3(1-v^u)} C_1 \left[ \frac{1}{\lambda r} K_1(\lambda r) + \left(1 + \frac{6}{(\lambda r)^2}\right) K_2(\lambda r) \right] + 3C_3 \frac{a^4}{r^4} \quad (5.36)$$

$$\frac{s\sigma_{r\theta}^{(3)}}{S_o \sin 2\theta} = \frac{2B(1+v^u)}{3(1-v^u)} C_1 \left[ \frac{1}{\lambda r} K_1(\lambda r) + \frac{3}{(\lambda r)^2} K_2(\lambda r) \right] - \frac{C_2}{2(1-v^u)} \frac{a^2}{r^2} - 3C_3 \frac{a^4}{r^4} \quad (5.37)$$

$$\frac{sp^{(3)}}{S_o \cos 2\theta} = \frac{B^2(1+v^u)^2(1-v)}{9(1-v^u)(v^u - v)} C_1 K_2(\lambda r) + \frac{B(1+v^u)}{3(1-v^u)} C_2 \frac{a^2}{r^2} \quad (5.38)$$

where,

$$C_1 = \frac{12\lambda a(1-v^u)(v^u - v)}{B(1+v^u)(D_2 - D_1)} \quad (5.39)$$

$$C_2 = \frac{4(1-v^u)D_2}{D_2 - D_1} \quad (5.40)$$

$$C_3 = \frac{\lambda a(D_2 + D_1) + 8(v^u - v) K_2(\lambda a)}{\lambda(D_2 - D_1)} \quad (5.41)$$

$$\lambda = \frac{s}{c^f} \quad (5.42)$$

$$D_1 = 2(v^u - v) K_1(\lambda a) \quad (5.43)$$

$$D_2 = \lambda a(1-v) K_2(\lambda a) \quad (5.44)$$

Carslaw and Jaeger techniques are used in finding solutions for mode 2 [110]. The

final solutions are:

$$s\sigma_{rr}^{(2)} = \frac{(1-2\nu)\alpha}{1-\nu} \left\{ \left[ (p_o - p_m) - \frac{c^{T,f}(T_o - T_m)}{1 - \frac{c^f}{c^T}} \right] \left[ \frac{K_1(\lambda r)}{r\lambda K_0(\lambda a)} - \frac{aK_1(\lambda a)}{r^2\lambda K_0(\lambda a)} \right] + \frac{c^{T,f}(T_o - T_m)}{1 - \frac{c^f}{c^T}} \left[ \frac{K_1(qr)}{rqK_0(qa)} - \frac{aK_1(qa)}{r^2qK_0(qa)} \right] \right\} + \frac{2G\alpha^{T,m}(1+\nu)}{3(1-\nu)} (T_o - T_m) \left[ \frac{K_1(qr)}{rqK_0(qa)} - \frac{aK_1(qa)}{r^2qK_0(qa)} \right] \quad (5.45)$$

$$s\sigma_{\theta\theta}^{(2)} = -\frac{(1-2\nu)\alpha}{1-\nu} \left\{ \left[ (p_o - p_m) - \frac{c^{T,f}(T_o - T_m)}{1 - \frac{c^f}{c^T}} \right] \left[ \frac{K_1(\lambda r)}{r\lambda K_0(\lambda a)} - \frac{aK_1(\lambda a)}{r^2\lambda K_0(\lambda a)} + \frac{K_0(\lambda r)}{K_0(\lambda a)} \right] + \frac{c^{T,f}(T_o - T_m)}{1 - \frac{c^f}{c^T}} \left[ \frac{K_1(qr)}{rqK_0(qa)} - \frac{aK_1(qa)}{r^2qK_0(qa)} + \frac{K_0(qr)}{K_0(qa)} \right] \right\} - \frac{2G\alpha^{T,m}(1+\nu)}{3(1-\nu)} (T_o - T_m) \left[ \frac{K_1(qr)}{rqK_0(qa)} - \frac{aK_1(qa)}{r^2qK_0(qa)} + \frac{K_0(qr)}{K_0(qa)} \right] \quad (5.46)$$

$K_0$ ,  $K_1$ , and  $K_2$  are the modified Bessel functions of zeroth, first, and second kinds.  $a$  is the wellbore radius. Solutions of modes 2 and 3 are in the Laplace domain, they can be converted into real domain using Stehfest algorithm method [111].

The final solution is the superposition of modes 1, 2, and 3 solutions:

$$\sigma_{rr} = -p_o + S_o \cos 2\theta + \sigma_{rr}^{(1)} + \sigma_{rr}^{(2)} + \sigma_{rr}^{(3)} \quad (5.47)$$

$$\sigma_{\theta\theta} = -p_o - S_o \cos 2\theta + \sigma_{\theta\theta}^{(1)} + \sigma_{\theta\theta}^{(2)} + \sigma_{\theta\theta}^{(3)} \quad (5.48)$$

$$\sigma_{zz} = \sigma_z + \nu(\sigma_{rr}^{(1)} + \sigma_{rr}^{(2)} + \sigma_{rr}^{(3)} + \sigma_{\theta\theta}^{(1)} + \sigma_{\theta\theta}^{(2)} + \sigma_{\theta\theta}^{(3)}) - \alpha(1-2\nu)(p^{(2)} + p^{(3)}) \quad (5.49)$$

$$\sigma_{r\theta} = -S_o \sin 2\theta + \sigma_{r\theta}^{(3)} \quad (5.50)$$

$$p = p_o + p^{(2)} + p^{(3)} \quad (5.51)$$

$$T = T_o + T^{(2)} \quad (5.52)$$

### 5.3.2 Case 2: numerical solution for high permeable formation

Opposite to case 1, if the fluid diffusion is much faster than the thermal diffusion, it can be assumed that the fluid diffusion becomes steady before the temperature begins to change. This case is suitable for high permeability formation such as sandstone or high-pressure injection. As permeability becomes larger, the effect of thermal diffusion becomes smaller, shown in Figure 5.2.

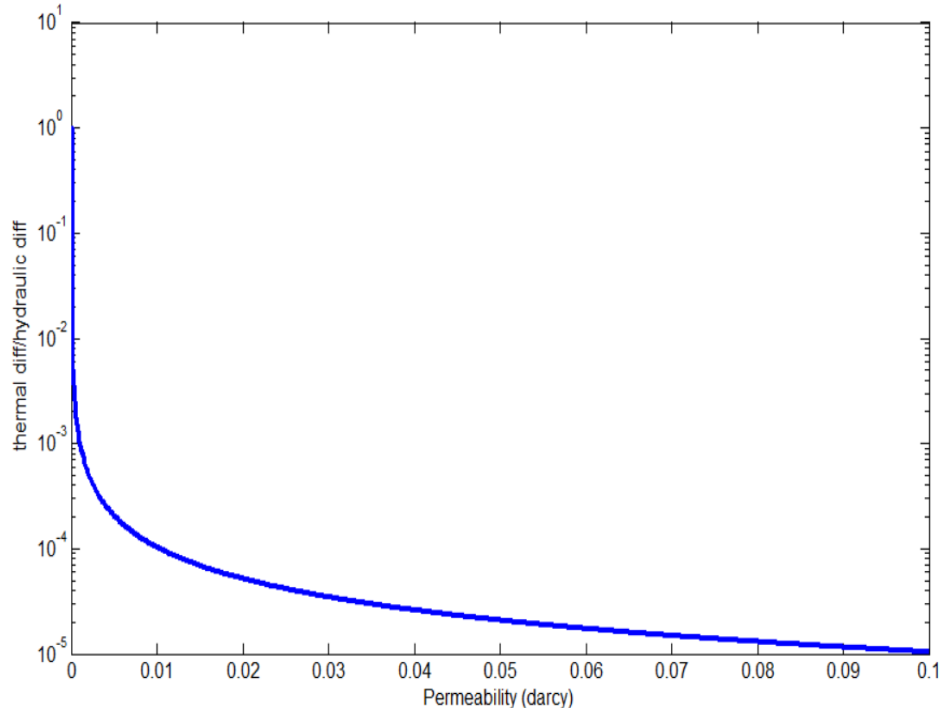


Figure 5. 2: Permeability effect on thermal and hydraulic diffusivities

Hojka et al. also concluded that heat transfer is dominated by hydraulic diffusion when permeability is above  $10^{-15} \text{ m}^2$  and is dominated by thermal diffusion when permeability is below  $10^{-18} \text{ m}^2$ . Both mechanisms, thermal and hydraulic diffusions, become important when permeability is between  $10^{-18}$  and  $10^{-15} \text{ m}^2$  [35].

The thermoporoelastic equations reduced to:

$$\frac{\partial T}{\partial t} = c^T T_{,ii} + \frac{\kappa \rho^f C^f}{\rho C} (T p_{,i})_{,i} \quad (5.53)$$

$$p_{,jj} = 0 \quad (5.54)$$

The non-linear PDE thermal diffusion equation can be solved numerically in equation (5.53). However,  $\frac{\partial P}{\partial r}$  is known from equation (5.54), therefore, it can be linearized and solved using implicit finite difference method as follow:

$$\begin{aligned} \frac{T_i^{n+1} + T_i^n}{\Delta t} = c^T & \left[ \frac{T_{i+1}^{n+1} + 2T_i^{n+1} - T_{i-1}^{n+1}}{\Delta r^2} + \frac{1}{r_w + i\Delta r} \frac{T_i^{n+1} - T_{i-1}^{n+1}}{\Delta r} \right] + \\ & + \frac{\kappa \rho^f C^f}{\rho C} \left[ \frac{T_i^{n+1} - T_{i-1}^{n+1}}{\Delta r} \frac{P_i^{n+1} - P_{i-1}^{n+1}}{\Delta r} + T_i^{n+1} \frac{P_{i+1}^{n+1} + 2P_i^{n+1} - P_{i-1}^{n+1}}{\Delta r^2} + \frac{1}{r_w + i\Delta r} \frac{P_i^{n+1} - P_{i-1}^{n+1}}{\Delta r} \right] \end{aligned} \quad (5.55)$$

with boundary conditions:

$$\begin{aligned} T(r_w, t) &= T_{BHT} \\ T(r_L, T) &= T_f \end{aligned} \quad (5.56)$$

and initial condition:

$$T(r, 0) = T_f \quad (5.57)$$

where  $T_{BHT}$  is the temperature of the wellbore and  $T_f$  is temperature of the formation.  $r_L$  is the distance away from the wellbore into the formation. Subscript “i” represents the radial location and its value depends on the discretization number (grid size). Before drilling the formation, the temperature of the formation is constant at  $T_f$  which satisfies the initial condition.

The solution to (5.54) is:

$$P(r) = C_1 + C_2 \ln(r) \quad (5.58)$$

where  $C_1$  and  $C_2$  can be solved with two boundary conditions. The pressure at the wellbore wall is equal to wellbore pressure ( $P_w$ ), and it is equal to the formation pore pressure at a distance away from the wellbore. These can be written as:

$$\begin{aligned} P(r_w) &= P_w \\ P(r_L) &= P \end{aligned} \quad (5.59)$$

where  $P$  is the pore pressure. After substituting (5.59) into (5.58) and discretizing the equation, it becomes:

$$P_i = \frac{P - P_w}{\text{Ln}(r_L / r_w)} \text{Ln}(r_w + i\Delta r) + P_w + \frac{P - P_w}{\text{Ln}(r_L / r_w)} \text{Ln}(r_w) \quad (5.60)$$

Equation (5.60) is updated into equation (5.55) at each time step to estimate the temperature profile.

### 5.3.2.1 Stress solution

After computing the temperature profile around the wellbore, the stress resolution is calculated using Kirsch equations. The equations were reproduced from Aadnoy and Chenevert for any wellbore inclination and azimuth which was originally developed by Hiramatsu and Oka [112] [113].

$$S'_x = (S_x \cos^2 \phi + S_y \sin^2 \phi) \cos^2 \gamma + S_v \sin^2 \gamma \quad (5.61)$$

$$S'_y = (S_x \sin^2 \phi + S_y \cos^2 \phi) \quad (5.62)$$

$$S'_v = (S_x \cos^2 \phi + S_y \sin^2 \phi) \sin^2 \gamma + S_v \cos^2 \gamma \quad (5.63)$$

$$\tau_{xy} = 0.5(S_y - S_x) \sin(2\phi) \cos^2 \gamma \quad (5.64)$$

$$\tau_{xz} = 0.5(S_x \cos^2 \phi + S_y \sin^2 \phi - S_v) \sin(2\gamma) \quad (5.65)$$

$$\tau_{yz} = 0.5(S_y - S_x) \sin(2\phi) \sin \gamma \quad (5.66)$$

$$\begin{aligned} \sigma_r = & 0.5(S'_x + S'_y) \left(1 - \frac{a^2}{r^2}\right) + 0.5(S'_x - S'_y) \left(1 + 3\frac{a^4}{r^4} - 4\frac{a^2}{r^2}\right) \cos(2\theta) \\ & + \tau_{xy} \left(1 + 3\frac{a^4}{r^4} - 4\frac{a^2}{r^2}\right) \sin(2\theta) + \frac{a^2}{r^2} P_w - P + S_r^{\text{TP}} \end{aligned} \quad (5.67)$$

$$\begin{aligned} \sigma_t = & 0.5(S'_x + S'_y) \left(1 + \frac{a^2}{r^2}\right) - 0.5(S'_x - S'_y) \left(1 + 3\frac{a^4}{r^4}\right) \cos(2\theta) \\ & + \tau_{xy} \left(1 + 3\frac{a^4}{r^4}\right) \sin(2\theta) - \frac{a^2}{r^2} P_w - P + S_t^{\text{TP}} \end{aligned} \quad (5.68)$$

$$\sigma_z = S'_v - 2\nu(S'_x - S'_y) \frac{a^2}{r^2} \cos 2\theta - 4\nu\tau_{xy} \frac{a^2}{r^2} \sin 2\theta - P + S_z^{\text{TP}} \quad (5.69)$$

$$S_r^{\text{TP}} = \frac{\alpha_b(1-2\nu)}{1-\nu} \frac{1}{r^2} \int_{r_w}^r P(r, t) r dr + \frac{E\alpha_m}{(1-\nu)} \frac{1}{r^2} \int_{r_w}^r T(r, t) r dr \quad (5.70)$$



$$S_t^{TP} = -\frac{\alpha_b(1-2\nu)}{1-\nu} \left[ \left( \frac{1}{r^2} \int_{r_w}^r P(r,t)rdr \right) - P(r,t) \right] - \frac{E\alpha_m}{(1-\nu)} \left[ \left( \frac{1}{r^2} \int_{r_w}^r T(r,t)rdr \right) - T(r,t) \right] \quad (5.71)$$

$$S_z^{TP} = \frac{\alpha_b(1-2\nu)}{1-\nu} P(r,t) + \frac{E\alpha_m}{(1-\nu)} T(r,t) \quad (5.72)$$

where  $S_x$ ,  $S_y$ , and  $S_v$  are geological principal stresses as shown in Figure 5.3.  $S_x'$ ,  $S_y'$ , and  $S_v'$  are transformed principal stresses.  $\tau'$  is the shear stress due to transformation.  $\sigma_r$ ,  $\sigma_t$ , and  $\sigma_z$  are the effective radial, tangential (hoop), and vertical stresses respectively. They are effective stresses because pore pressure ( $P$ ) is subtracted from them.

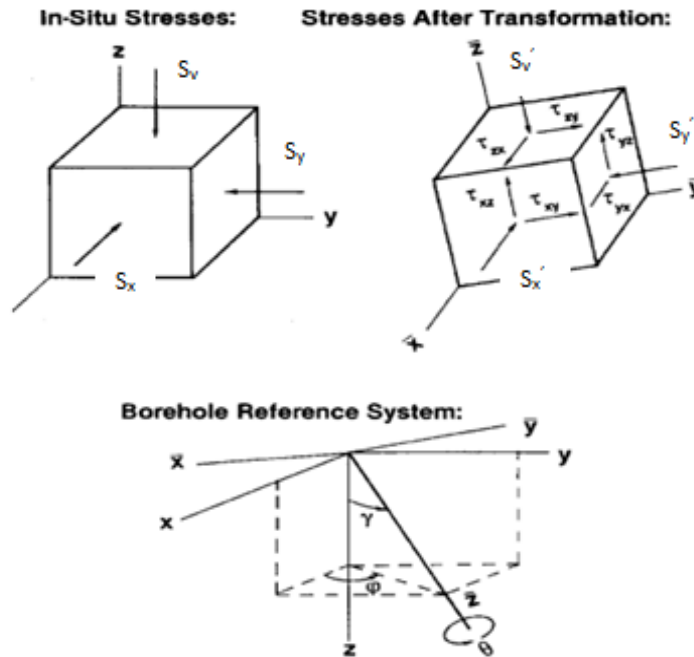


Figure 5. 3: Stress transformation around a borehole [112]

$P_w$  and  $P$  are the wellbore pressure and pore pressure respectively.  $\phi$  is the azimuth of the wellbore,  $\gamma$  is the wellbore inclination angle, and  $\theta$  is the wellbore angle measured around the wellbore wall from  $x$ -axis (maximum horizontal stress).  $r$  is the radial distance away from the wellbore wall, while  $a$  presents the wellbore radius.  $STP$ 's are the stress induced by pore pressure and temperature changes.  $\alpha_b$  is the Biot's coefficient and  $E$  is the Young's modulus of the rock. At the wellbore wall equations (5.70) and (5.71) reduce to:

$$S_r^{TP} = 0 \quad (5.73)$$

$$S_t^{TP} = \frac{\alpha_b(1-2\nu)}{1-\nu} P(r, t) + \frac{E\alpha_m}{(1-\nu)} T(r, t) \quad (5.74)$$

### 5.3.3 Remarks

Although an analytical solution has been derived for case 1, a numerical scheme similar to case 2 (finite difference) has also been applied to case 1 too. This way, the results of the analytical and the numerical method can be compared. This will be shown in the following chapter.

In low permeability formations, induced stresses cause an immediate pore pressure change due to undrained loading effect which is captured by the Mode 3. The Mode 3 effect is significant for shale formation and lasts for a longer period compared to high permeability formation [11] [12]. The undrained and drained conditions will impact the mechanical moduli of a formation since they will have different value at each condition. Therefore, the stress estimations around a wellbore will depend on the imposed condition. The undrained effect for high permeability formations (non-shale formations) can be ignored according to Chen and Ewy and Cui. et al. [12] [99] [127].

## 5.4 FAILURE CRITERIA

Failure envelopes are applied to the results to quantify breakdown and breakout events. Shear failure criteria for this study is based on Mohr-Coulomb and modified Lade criteria.

### 5.4.1 Mohr-Coulomb

Jaeger and Cook [114] defines Mohr-Coulomb criterion as follow:

$$F = \sigma_1 - (\sqrt{(1+\mu^2)} + \mu)^2 \sigma_3 - UCS \quad (5.75)$$

and tensile failure is defined by Zoback [61] as:

$$\sigma_t < -TS \quad (5.76)$$

where  $\sigma_1$  and  $\sigma_3$  are maximum and minimum principal component stresses on Mohr-Coulomb diagram as shown in Figure 5.4.

$$\sigma_1 = \frac{\sigma_t + \sigma_r}{2} + \sqrt{\tau_{rt}^2 + \left(\frac{\sigma_t + \sigma_r}{2}\right)^2} \quad (5.77)$$

$$\sigma_3 = \frac{\sigma_t + \sigma_r}{2} - \sqrt{\tau_{rt}^2 + \left(\frac{\sigma_t + \sigma_r}{2}\right)^2} \quad (5.78)$$

$$\tau_{rt} = \left[ 0.5(S'_x - S'_y) \sin(2\theta) + \tau_{xy} \cos(2\theta) \right] \left( 1 - 3\frac{a^4}{r^4} + 2\frac{a^2}{r^2} \right) \quad (5.79)$$

$$UCS = \frac{2S_o}{(\sqrt{1+\mu^2} - \mu)^2} \quad (5.80)$$

So, UCS, and TS are the cohesion, unconfined cohesive strength, and tensile strengths of the rock respectively, where  $\tau_{rt}$  is the shear stress in radial coordinates, and  $\mu$  is the friction coefficient of the rock. If  $F$  is a positive value, the rock will exhibit shear (compressive) failure. On the other hand, if equation (5.76) holds true, tensile failure occurs.

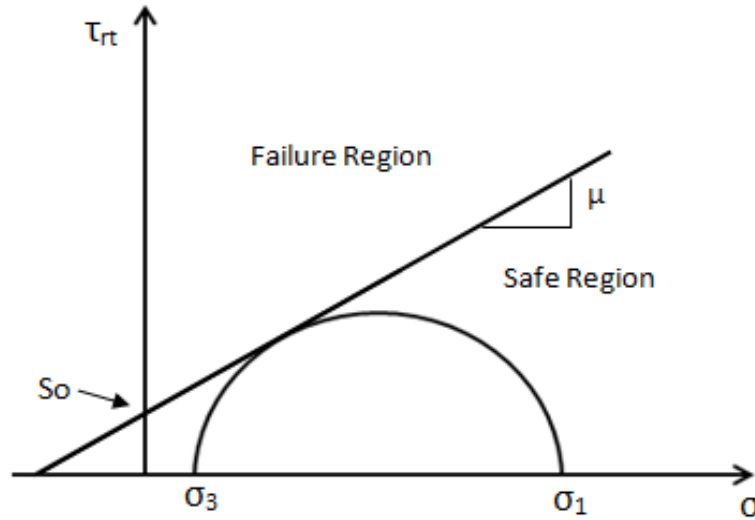


Figure 5. 4: Schematic Mohr-Coulomb diagram with friction angle and initial cohesion

### 5.4.2 Modified Lade

This failure envelope is the modification of the Lade failure criterion developed by Ewy [72]. The major difference between modified Lade and Mohr-Coulomb is the addition of intermediate stress into the failure envelope. Ewy defines the failure criterion on a wellbore wall as follow:

$$I_1'' = (\sigma_r + S_1) + (\sigma_\theta + S_1) + (\sigma_z + S_1) \quad (5.81)$$

$$I_3'' = (\sigma_r + S_1)(\sigma_\theta + S_1)(\sigma_z + S_1) - (\sigma_r + S_1)\tau_{\theta z} \quad (5.82)$$

$$\frac{(I_1'')^3}{I_3''} \geq (27 + \eta) \quad (5.83)$$

where the parameter  $S_1$  is related to the cohesion and friction angle of the rock as follow:

$$S_1 = \frac{S_o}{\tan \beta} \quad (5.84)$$

and parameter  $\eta$  is the internal friction of the rock.

$$\eta = \frac{4 \tan^2 \beta (9 - 7 \sin \beta)}{1 - \sin \beta} \quad (5.85)$$

$\beta$  is the friction angle of the rock and is related to  $\mu$ , friction coefficient, by

$$\mu = \tan \beta \quad (5.86)$$

If equation (5.83) holds true, the rock will exhibit shear failure.

### 5.4.3 Failure criteria comparisons

There are different criteria that are used in the field of geomechanics to quantify failure in a wellbore. Five commonly used failure criteria are:

1. Mohr-Coulomb: the simplest and commonly used criteria. This criterion is expressed in terms of the shear and normal stress or maximum and minimum principal stresses. This criterion does not consider the effect of intermediate principal stress as shown in Figure 5.5.

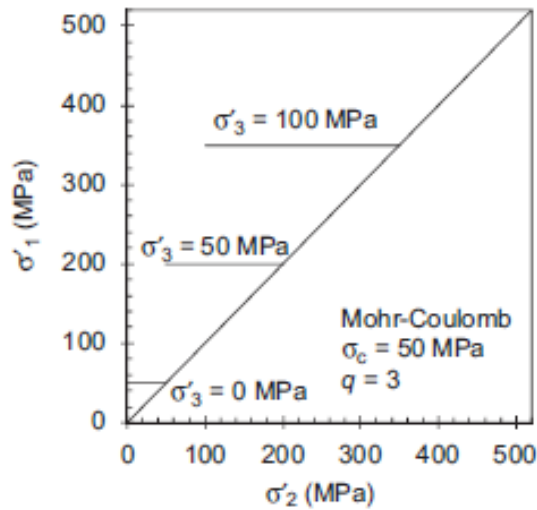


Figure 5. 5: Mohr-Coulomb criteria plot with effective stresses [13]

2. Drucker-Prager: this criterion considers all three principal stresses, and its material constants can be related to the Mohr-Coulomb parameters if the Drucker-Prager surface circumscribes the Mohr-Coulomb pyramid [115]. This criterion overestimated the effect of intermediate principal stress, as shown in Figure 5.6.

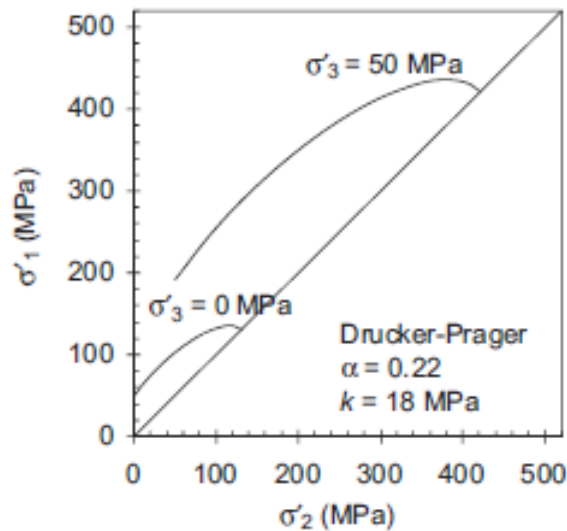


Figure 5. 6: Drucker-Prager criteria plot with effective stresses [13]

3. Modified Lade: this failure criterion is the modification of the Lade and Duncan failure criterion developed by Ewy [72]. The modified Lade criterion, unlike

the Drucker–Prager criterion, predicts a strengthening effect of the intermediate principal stress as shown in Figure 5.7.

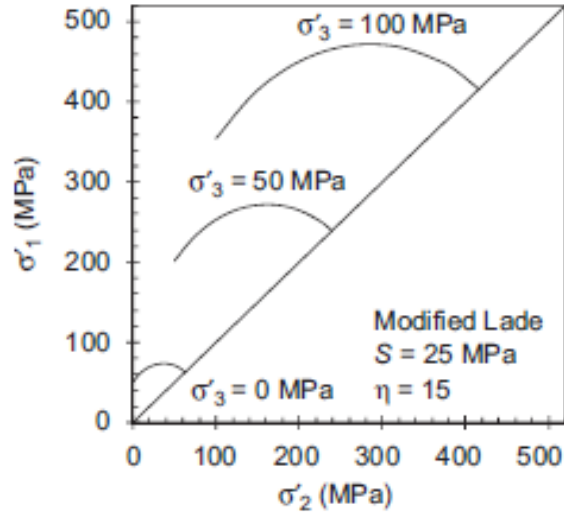


Figure 5. 7: Modified Lade criteria plot with effective stresses [13]

4. Mogi-Coulomb: Al-Ajmi and Zimmerman developed this criterion [116]. Similar to the modified Lade criterion, it accounts for the intermediate principal stress and predicts a strengthening effect of the intermediate principal stress as shown in Figure 5.8.

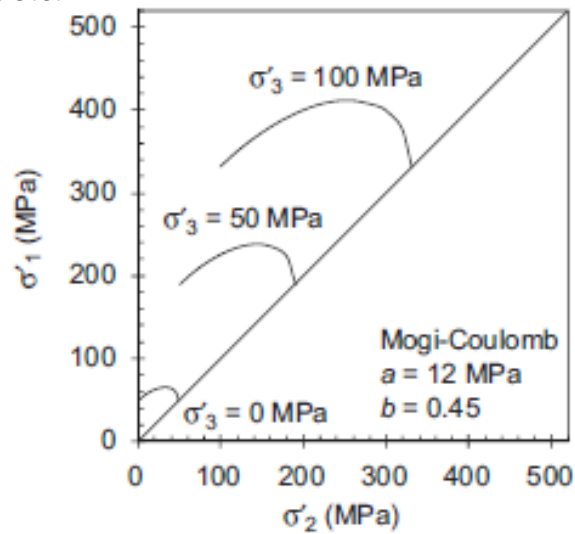


Figure 5. 8: Mogi-Coulomb criteria plot with effective stresses [13]

5. 3D Hoek-Brown: it has been used widely in rock mechanics since it was developed for rock materials and masses. Its parameters are determined from routine unconfined compression tests, and it has been applied successfully to a wide range of intact and fractured rock types [117]. Zhang and Zhu introduced the intermediate stress to the Hoek-Brown criterion to make a 3D envelope. Like modified Lade and Mogi-Coulomb criteria, it produces comparable results as shown in Figure 5.9.

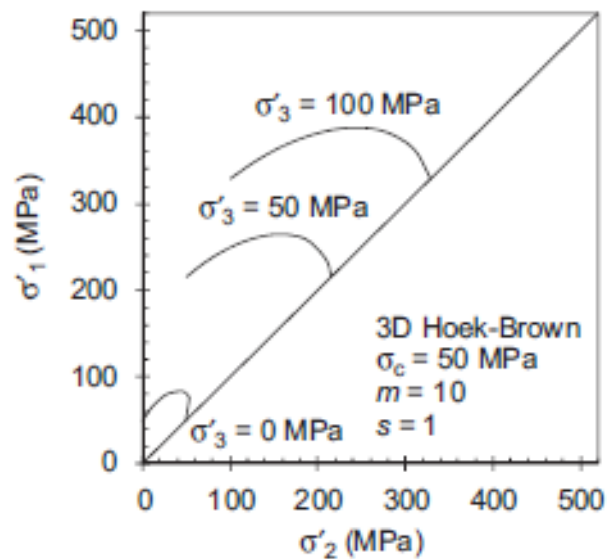


Figure 5. 9: 3D Hoek-Brown criteria plot with effective stresses [13]

Zhang et al. compared these five criteria in prediction of minimum mud weight required for ensuring wellbore stability of a vertical borehole in Dunam dolomite [118]. As shown in Figure 5.10, that the Mohr-Coulomb criterion predicts the highest minimum mud pressure while Drucker-Prager predicts the lowest mud pressure. The modified Lade, Mogi-Coulomb, and 3D Hoek-Brown criteria predict the minimum mud pressure that are close to each other, and in between the Mohr-Coulomb and Drucker-Prager criteria predictions. The Mohr-Coulomb underestimates the strength of the rock since it does not consider the effect of the intermediate principal stress, while, Drucker-Prager

overestimates the strength of the rock due to a great emphasis was put on intermediate principal stress. The minimum mud pressures predicted by the Mohr–Coulomb criterion will be too conservative while those from the Drucker–Prager criterion will be unsafe.

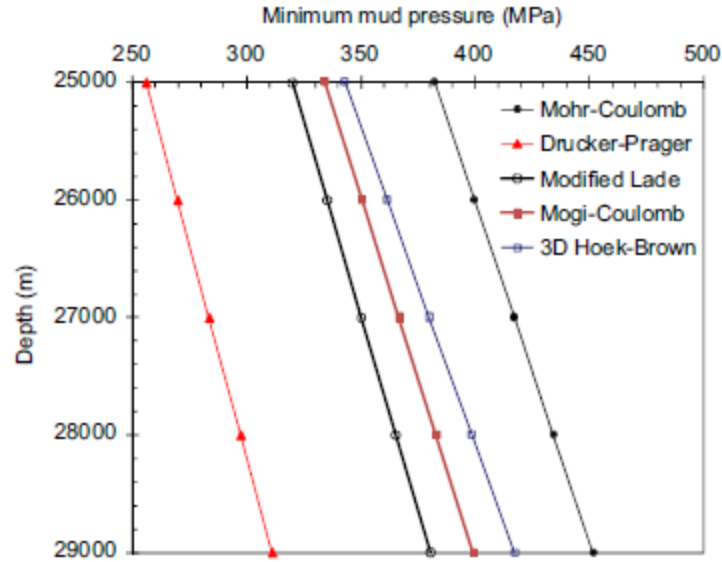


Figure 5. 10: Minimum overbalance pressure in Dunham dolomite based on different rock criteria [13]

A liner elastic model is coupled with a rock strength criterion to establish the minimum mud weight required to encounter wellbore shear failure. Both field observations and lab experiments have shown that linear elastic models tend to overestimate the stress concentration around a borehole, predicting a much higher minimum mud weight [24] [25]. This is because the linear elastic models do not consider the large plastic deformation of rock before failure, which reduces stresses or energy around a wellbore by a certain amount. The elastic models are coupled with the peak-strength failure criteria assuming that the wellbore failure is synonymous to one point at the borehole wall reaching the peak-strength [2]. However, the peak-strength point is a point in the material reaching its yield limit, therefore, a plastic deformation zone starts around that point on the wellbore. That point will exhibit a low stress and large deformation. If the deformations are within the



tolerance of the drilling activity, the wellbore can be considered stable. In fact, building a criterion based on deformation/strain instead of stresses is more suitable in wellbore failure prediction when plasticity comes into play.

There are frequent cases that predicted minimum mud weight to combat shear failure crosses fracture gradient. This will produce a negative safe mud window meaning either fracturing (lost circulation) or wellbore collapse or differential pipe sticking will occur no matter what the mud weight is chosen. Ideal mud weight design chooses the lowest mud weight to maximize the possible mud weight window. However, this cannot be done with linear elastic models. Therefore, the development of a plastic model is necessary since it predicts a lower mud weight and expanding the drilling mud weight window. In the past decades, substantial work has been focused toward investigation of the elastoplastic rock behavior and development of elastic plastic predictive model. Of course, the models presented in this dissertation are based on linear elastic rock behavior. The readers are encouraged to study recent publications on elastoplastic models. The very first work on elastoplastic stress analysis around a wellbore was pioneered by Fenner in 1938 [119]. Over the years, numerous models to predict the failure zone and plastic deformation have been developed [120] [121] [122] [123] [124]. Although, substantial work has been dedicated toward plastic modeling, a fully coupled thermoporoelastic model has not been yet developed.

## CHAPTER 6: THERMOPOROELASTIC SOLUTIONS

Wellbore instability has been a troublesome problem for decades. The instability happens in two forms: shear (compressive) or tensile (breakdown) failures. When pressure in a wellbore is lower than the effective stress of a formation, shear failure (breakout) will happen. On the other hand, when pressure is higher than the rock strength, breakdown (tensile failure) occurs. The latter scenario is the basis for lost circulation events. Thermal stresses can substantially change the magnitude of the fracture gradient of a formation (stress required to initiate a fracture). The formation temperature usually is warmer than the wellbore temperature due to geothermal gradient and continuous circulation of mud in the wellbore. This temperature difference causes a thermally induced stress around the wellbore. A small variation in temperature results in a large stress concentration since thermal expansion coefficient of a rock is very small. Pickens observed that a 1°C change induces a 1 MPa pressure in the field [3]. While there are many available models exploring thermoporoelastic effect, thermal analyses are ignored during drilling practices, discrediting the significance of thermal stress. This chapter investigates the transient thermal equations developed in **Chapter 5** with numerical examples and emphasizes the importance of induce thermal stresses. Finally, various failure criteria have been applied to the results to classify tensile (breakdown) and shear (breakout) failures around the wellbore wall.

### 6.1 INDUCED THERMAL STRESSES

When a wellbore is drilled, the rock is replaced by a drilling fluid that has a different temperature gradient compared to that rock. Usually, the wellbore temperature is cooler than the rock temperature being drilled; this is true as the wellbore gets deeper. Therefore, a cooling zone occurs around the wellbore. Pepin et al. [125] investigated mud temperature

effect on fracture gradient for several ChevronTexaco wells. They have suggested that the reduction of the fracture gradient due to cooling around the wellbore may be a major contributor to lost circulation events. Three different leak-off tests (LOT) at different bottom hole temperatures (BHT) were performed. In the first test, the BHT was cooled down to 33°C. Then BHT was heated to 56°C and 67°C in the following tests respectively. They observed a rising fracture gradient (FG) as the BHT increased. In fact, the FG increased by more than 1.5 ppg (pound per gallon) from the first test to the last test as shown in Figure 6.1. This finding motivates anyone to believe the importance of thermal effect on fracture gradient as well as wellbore stability.

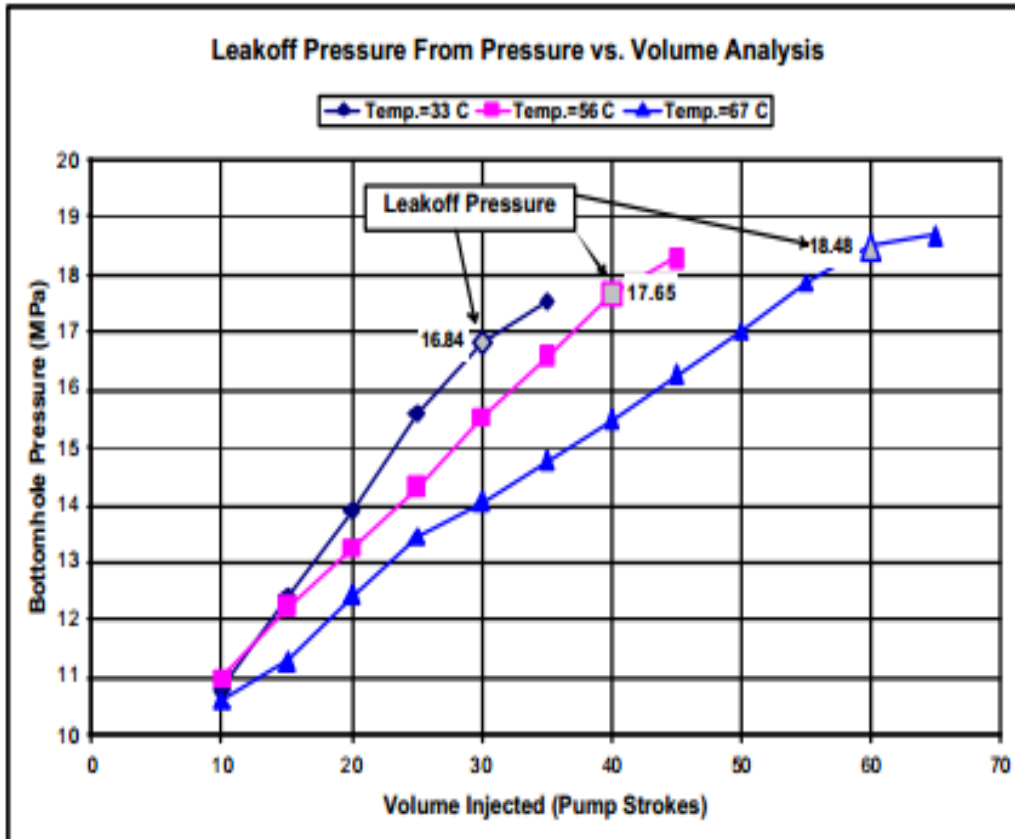


Figure 6. 1: Leak-off pressure tests at various bottom-hole temperatures [125]

Stresses in poroelastic media are defined not only by mechanical stresses and pore

pressure, but also depends on thermal stresses. Any change in pore pressure will redefine the stress resolution in the media. In turn, it could lead into deformation of the media. This effect is stimulated with thermal loadings, either expansion or contraction. It is important to realize that a small change in temperature change can lead into a large pore pressure change due to small thermal expansion coefficient of the media. In fact, a temperature-pressure ratio of 1, meaning a 1°C change induces a 1 MPa pore pressure change, has been measured in the field [3]. The pressure-temperature correlation was suggested by Zemansky et al. [126] as follow:

$$\Delta P = \frac{\alpha_m \Delta T}{c_f} \quad (6.1)$$

where  $\alpha_m$  and  $c_f$  are thermal expansion coefficient of rock and fluid compressibility respectively.

The wellbore temperature is different from that of the rock formation due to geothermal gradient and circulation of mud inside the wellbore. This temperature difference (thermal stress) in any type of formations such as sandstone or shale may induce fluid flow and change in pore pressure. For low permeability formations such as shale, temperature variation will result in direct thermally induced stress and transient pore pressure change since thermal diffusion (conduction) dominates hydraulic diffusion (convection) [127].

## 6.2 CASE 1: ANALYTICAL SOLUTION FOR LOW PERMEABILITY FORMATION

As discussed previously in **Chapter 5**, Case 1 is suitable for low permeability formations where conductive heat transfer dominates hydraulic diffusivity. As shown in Table 6.1, some of the data from Wang and Papamichos paper [128] are used to evaluate

the validity of the models developed in the previous chapter. Also, poroelastic model is applied for comparison, an indication for the thermal stress importance.

In this case, horizontal stresses are equal and the wellbore pressure is the same as the pore pressure. This minimizes the effect of tectonic stresses and pore pressure in the study, and pure effect of thermal stresses can be evaluated. Figures 6.2 and 6.3 show the results for stress solutions for tangential (hoop stress) and radial stresses along the radial direction at different times. In this example, the wellbore temperature is greater than the formation temperature, so the temperature front is from the wellbore into the formation. This means that the near wellbore region is heating up, elevating pore pressure and compressive strength of the rock. This trend can also be seen in tangential graphs in the figure. A sharp drop in the stress profile can be seen near the wellbore since the pore pressure has risen, reducing the effective stress. Since in this example, the permeability is low the fluid diffusivity is negligible. Therefore, the fluid can not travel quickly and it is trapped inside the pores. As temperature rises, the fluid inside the pores is heated up and its temperature increases, so the induced pore stress increases. When pore pressure increases, the effective stress decreases. This is why a sharp stress drop is estimated near the wellbore. Farther away from the wellbore, the temperature disturbance diminishes, and the poroelastic solution matches thermoporoelastic results. These abnormalities are not observed in radial stress profile since the induced thermal stresses are more pronounced in the tangential stress.

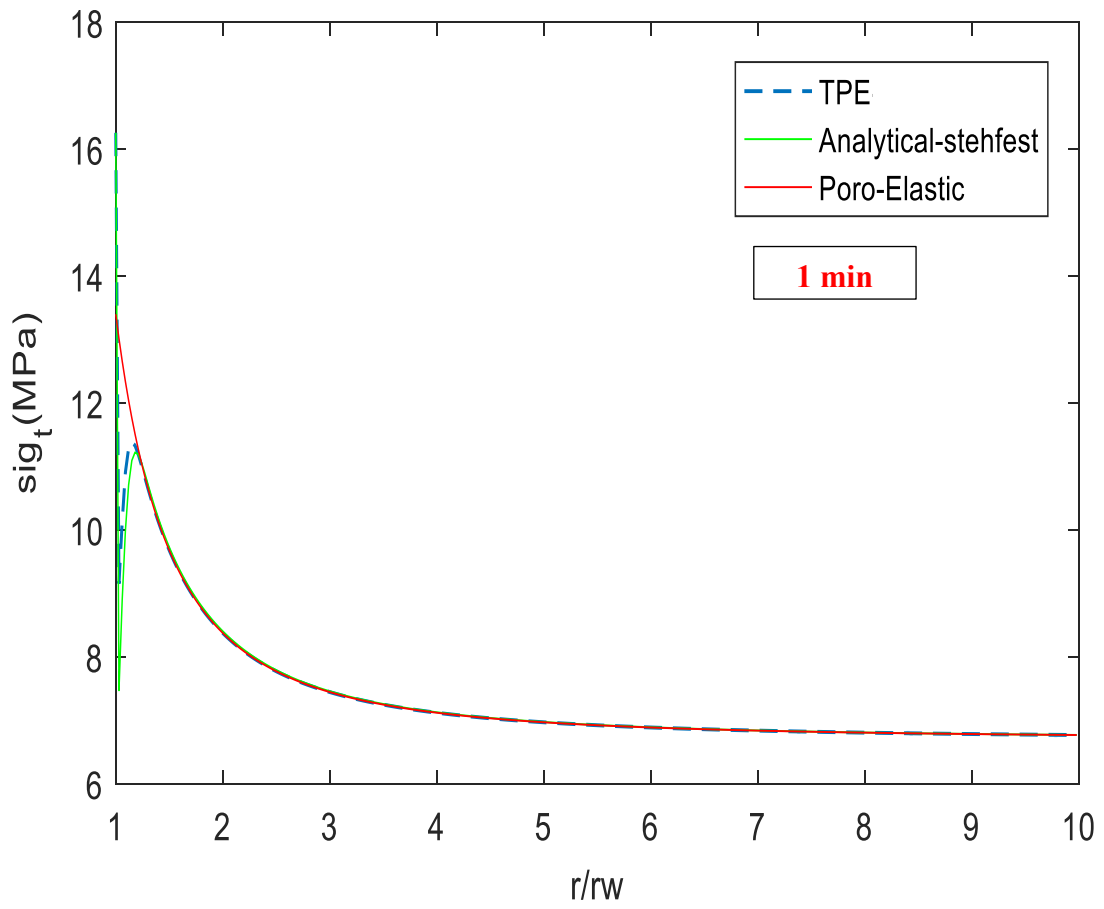
The numerical thermoporoelastic solution is in a good agreement with the analytical solution developed by Wang and Papamichos using Detournay and Cheng approach [36] [128]. However, the agreement decays with time. This is because the development of the analytical solution has a time limitation for its accuracy. It is suggested that the model is suitable for short non-dimensional time of 0.1. The non-dimensional time described as:

$$\tau = \frac{t\alpha}{r_w^2} \quad (6.2)$$

where  $t$  is time,  $r_w$  is wellbore radius, and  $\alpha$  is thermal diffusivity coefficient. On the other hand, the numerical model does not have any time constraint, therefore, it is suitable for longer times, producing more reliable results compared to the analytical model. Also, the radial stress constructed by the analytical model seems to feel the temperature disturbance at a longer distance away from the wellbore wall compared to the numerical model. The predicted onset where thermoporoelastic equals the poroelastic model is consistent for the numerical model when comparing the tangential and radial stress profiles.

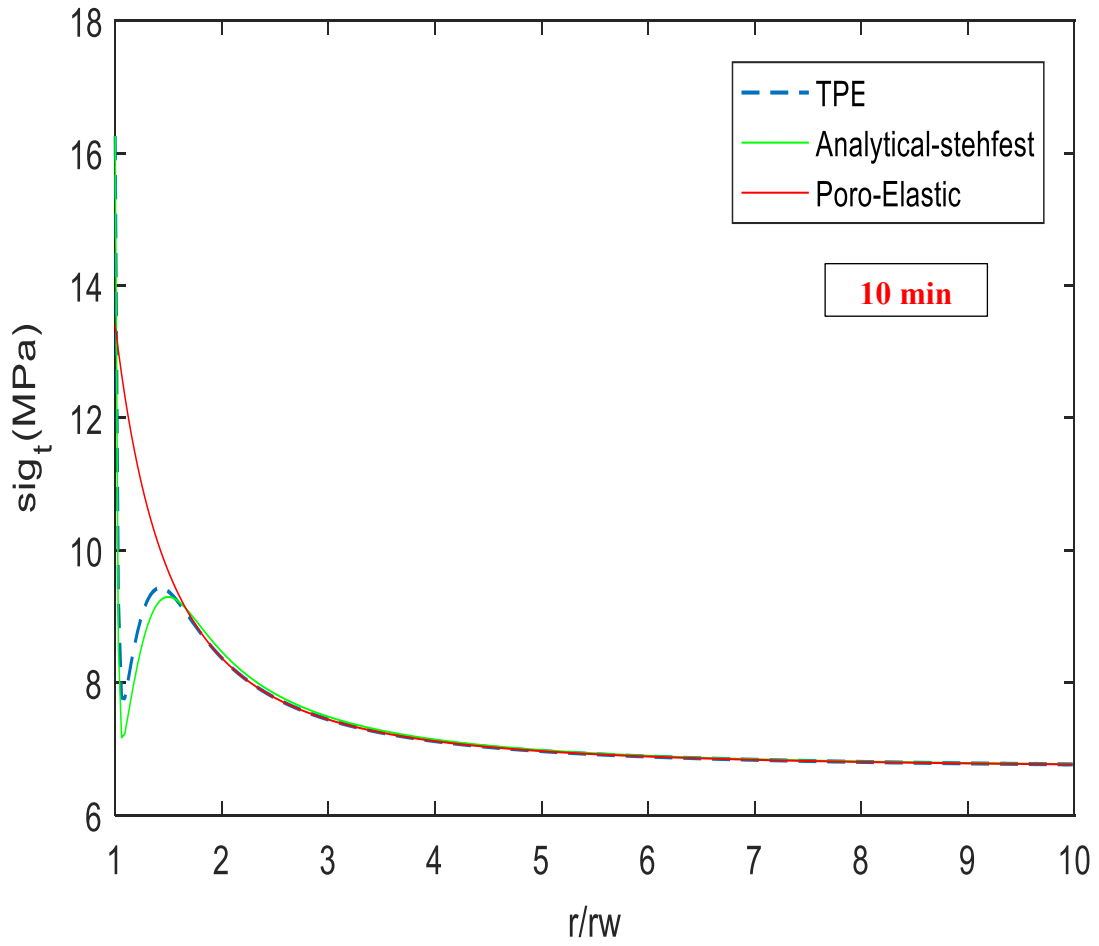
By comparing the poroelastic and thermoporoelastic models, it can be concluded how important it is to model induced thermal stresses around a wellbore since the results greatly change near the wellbore when there is a temperature disturbance. This discrepancy impacts the mud weight window for drilling operations which could aid in forecasting the formation breakouts or breakdowns, and casing programs.

In low permeable formations, the thermoporoelastic model suggests that the maximum or minimum hoop stress may not occur at the wellbore walls which is contrary to the classical models such as elastic and poroelastic models, suggesting that the maximum or minimum stresses to occur at the wellbore walls. Therefore, the failure may initiate away from the wall and travel to the walls.



(a)

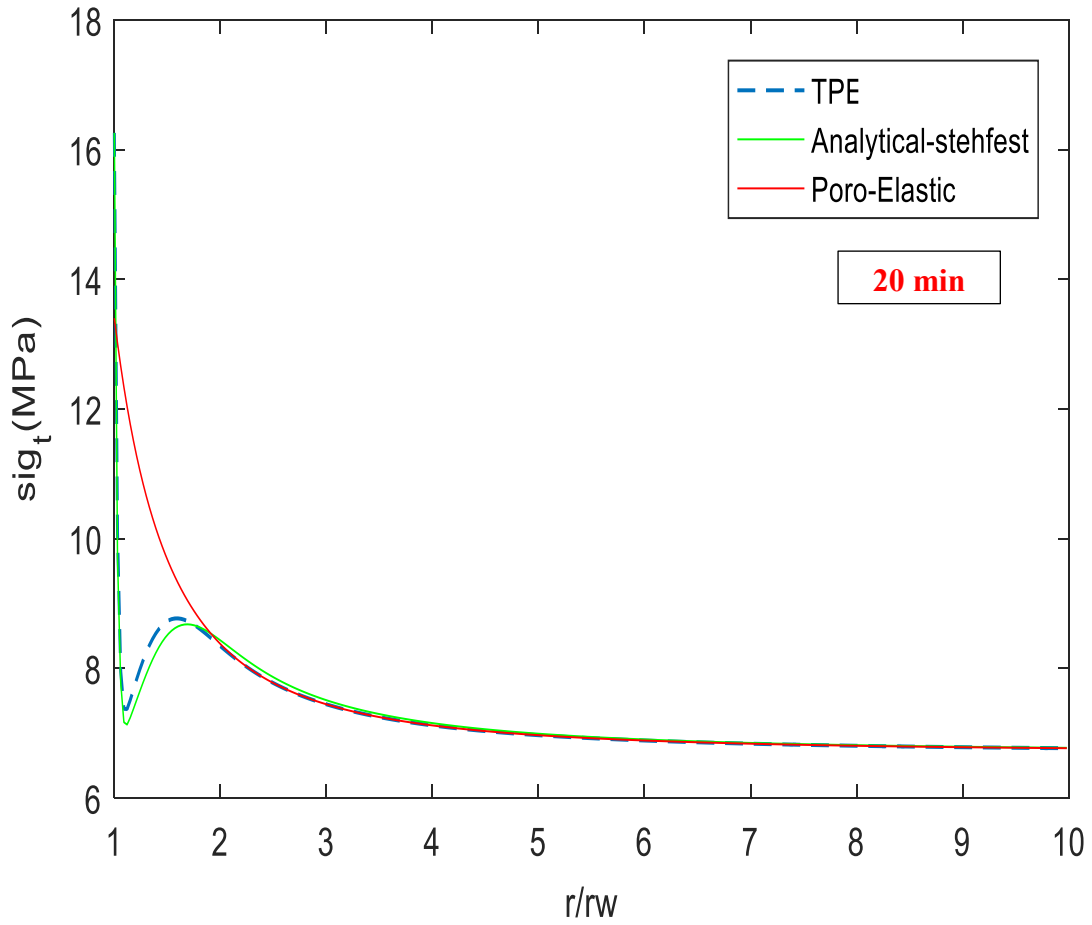
Figure 6. 2



(b)

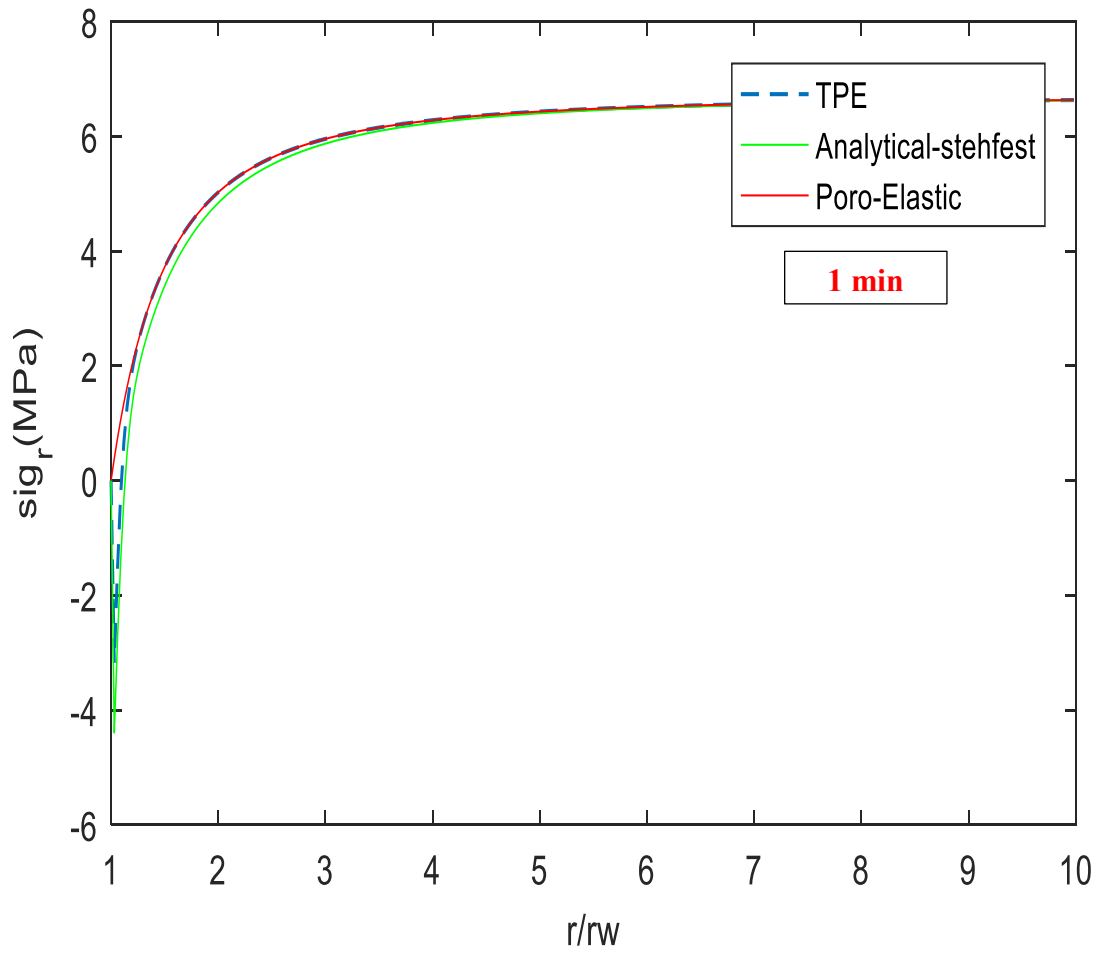
Figure 6. 2





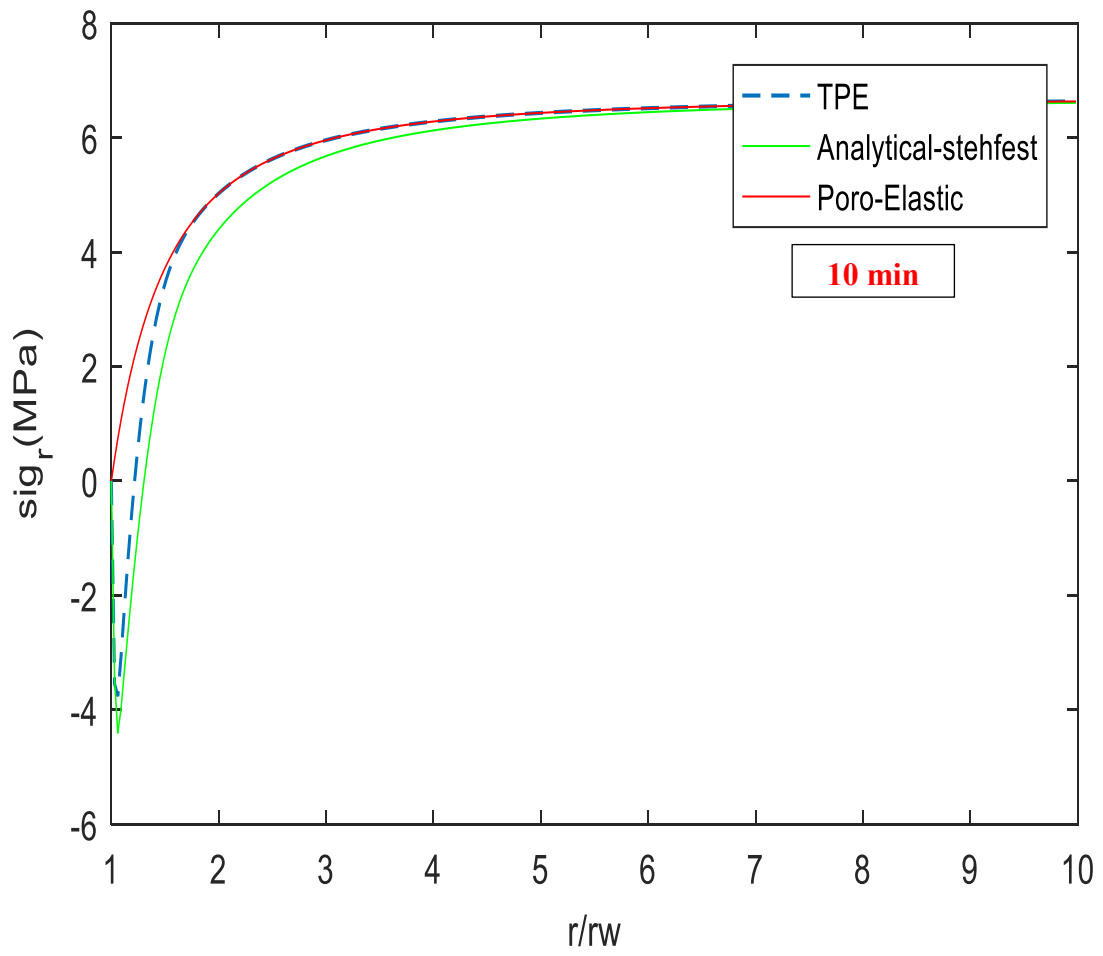
(c)

Figure 6. 2: Effective tangential stress along radial distance for various periods - low permeability formation with conductive heat transfer domination. Blue dashed line is the thermoporoelastic model developed in this dissertation, and green curve is for the analytical solution developed by Wang and Papamichos. The analytical solution is transformed from the Laplace domain into time domain using Stehfest method



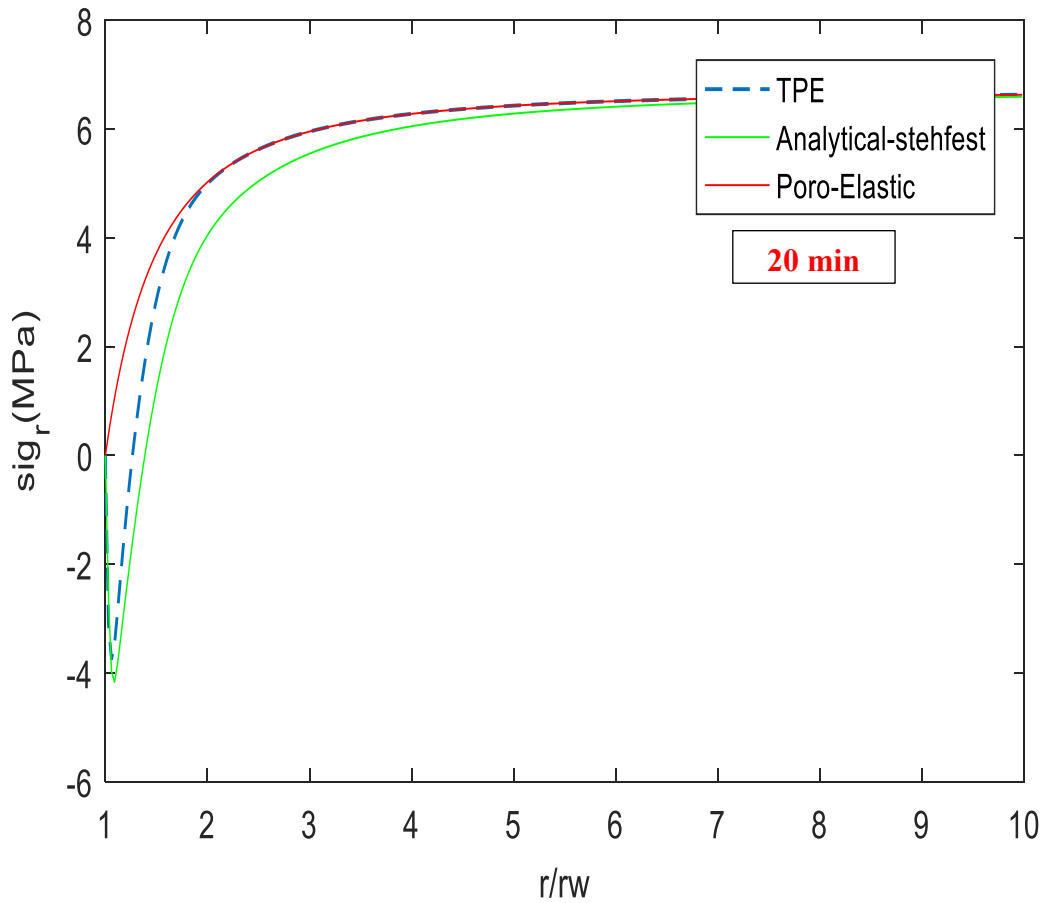
(a)

Figure 6. 3



(b)

Figure 6. 3



(c)

Figure 6. 3: Effective radial stress along radial distance (a) 1 min, (b) 10 min, and (c) 20 min - low permeability formation with conductive heat transfer domination

### 6.3 CASE 2: NUMERICAL SOLUTION FOR HIGH PERMEABLE FORMATION

Results for a high permeable formation such as sandstone are presented. Table 6.2 lists the data for the case. The tensile strength of the rock is assumed to be zero since it is assumed that a fracture initiates in a joint or existing fracture during drilling operations [112]. But in many cases, as when there are no pre-existing fractures, the rock's actual tensile strength is not zero and should be taken into account, additional complexities in

analyses notwithstanding [19]. However, for simplicity, the rock tensile strength is assumed to be zero in this analysis.

Two different scenarios were modeled. The first scenario assumes that there is no thermally induced stress, while the second scenario includes a thermally induced stress. Figures 6.4, 6.5, 6.6, and 6.7 are the results for the first case. As shown in Figure 6.4, the hoop stress around the wellbore is always positive, meaning that the stress is compressive. This is because thermal stress has not been considered. Since there is no thermal stress in this case, it is expected that there would be no tensile failure, as shown in Figure 6.5, blue area in this figure represents no failure region. The tensile failure criterion in this analysis is based in the Zoback tensile failure, equation (5.76). Figures 6.6 and 6.7 show shear failure results based on Mohr-Coulomb and modified Lade. Red color represents failure area. Shear failure increases with increasing azimuth angle.

The comparison between Mohr-Coulomb and modified Lade can be seen from Figures 6.6 and 6.7. Mohr-Coulomb is over-estimating the shear failure around the wellbore wall, while, modified Lade presents a more realistic situation since it accounts for the intermediate stress in the model. In general, Mohr-Coulomb under-estimates the strength of the rock since it does not include intermediate stress in its criterion [72]. Another reason for this discrepancy between Mohr-Coulomb and modified Lade is due to the formulation of their failure criteria. Mohr-Coulomb uses a linear relationship, however, modified Lade defines failure based on ratios as discussed in **Chapter 5**.

Figures 6.8, 6.9, 6.10, and 6.11 show the results for scenario 2, thermally induced stress analysis. In this case, the wellbore is cooled down by 30°C. The effective hoop stress can either be compressive or tensile as shown in Figure 6.8. Positive stress means compression, while negative is for tensile stress, following the geomechanics sign convention. The magnitude of compressive stress in Figure 6.8 is lower than

Figure 6.4 due to thermal cooling of the wellbore. Since the wellbore is cooled down, the compressive stress is reduced.

Figure 6.9 shows the tensile failure of the wellbore. Since the tangential stress reduced, the chance for breakdown (tensile failure) is increased. The opportunity of shear failure according to Mohr-Coulomb has reduced as shown in Figure 6.10. It can be seen in the figure that the red area (failure area) has decreased, while, the blue area (safe area) has increased. This means that the thermal cooling helped the wellbore become safer and less likely to collapse. Also, modified Lade predicts the same trend as shown in Figure 6.11. Shear failure decreases as rock experiences thermal cooling. However, Mohr-Coulomb still over-estimates the shear failure around the wellbore wall compared to modified Lade.

Reduction in shear failures and increase in tensile failures by cooling down the wellbore have also been observed by Li, Cheng, and Ewy in their works [2] [127]. In general, tensile and shear failure figures can be used for prediction of failure at different wellbore azimuth and inclination angles. Figure 6.12 shows shear and tensile failures at different times. The shear failure analysis in these figures is based on modified Lade. As time increase, the shear failure decreases and approaches a steady state (equilibrium) condition after 100 sec. Tensile failure increases with time too, but becomes stable earlier than shear failure, for example before 100 sec.

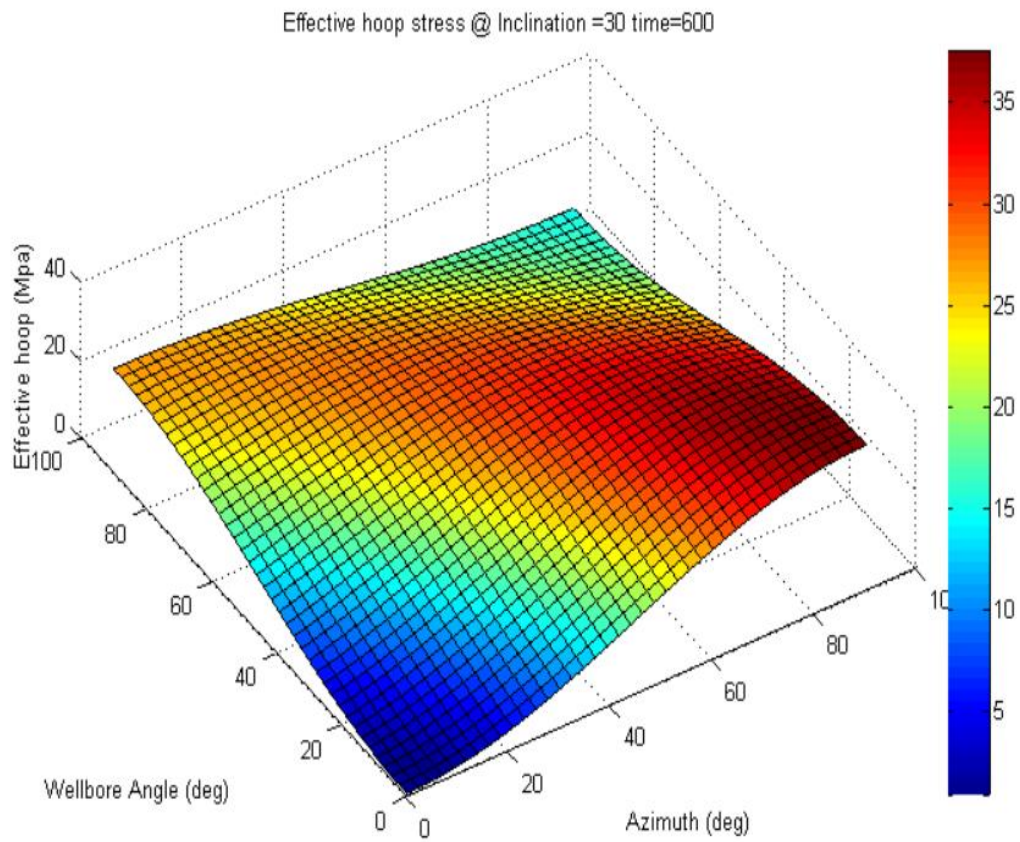


Figure 6. 4: Effective hoop stress without thermal stress (isothermal condition) - high permeability formation with convective heat transfer domination

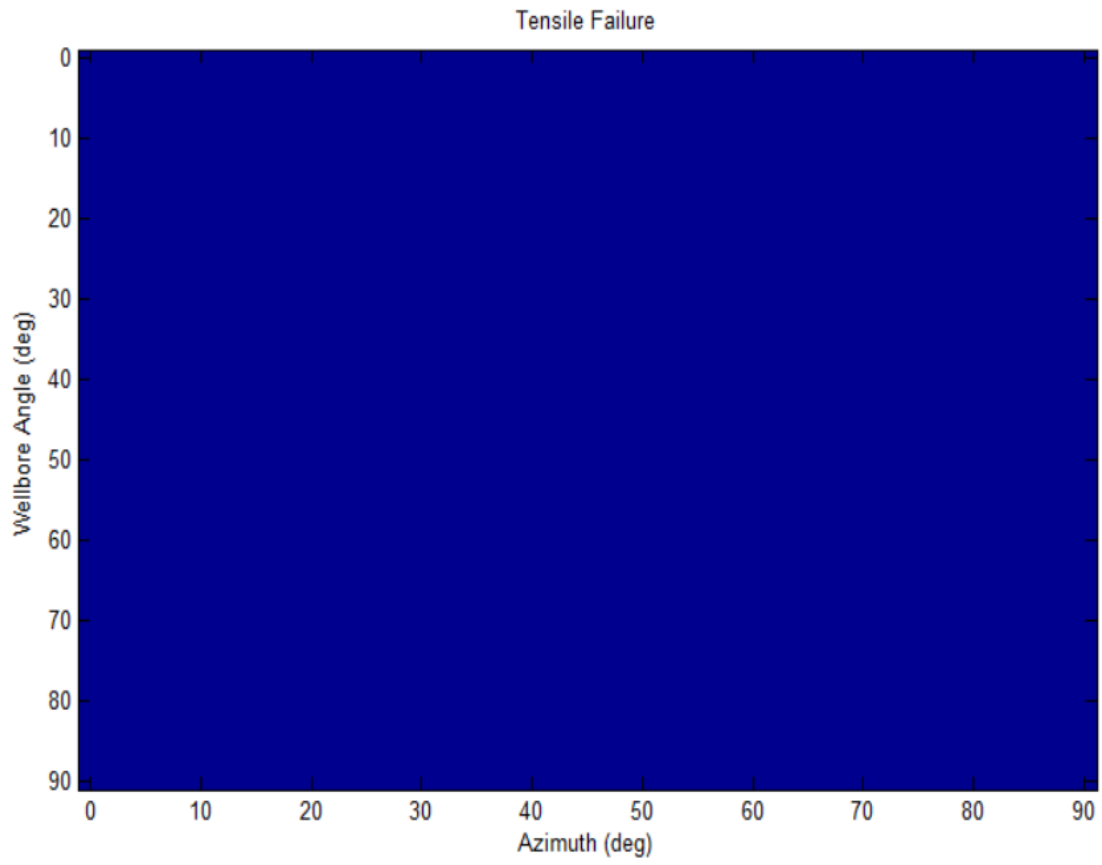


Figure 6. 5: Tensile failure for case 2, without thermal stress. Blue color represents no failure



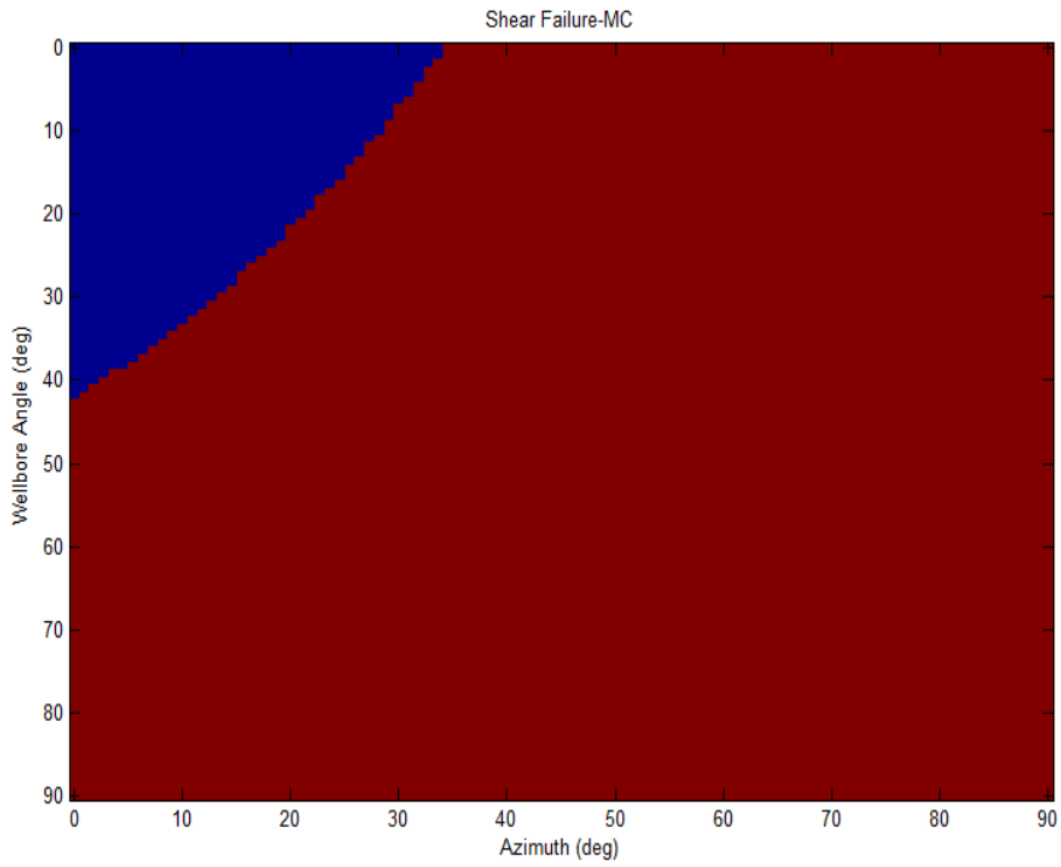


Figure 6. 6: Shear failure based on Mohr-Coulomb criteria for case 2 at 10 min. Red area represents the failure region

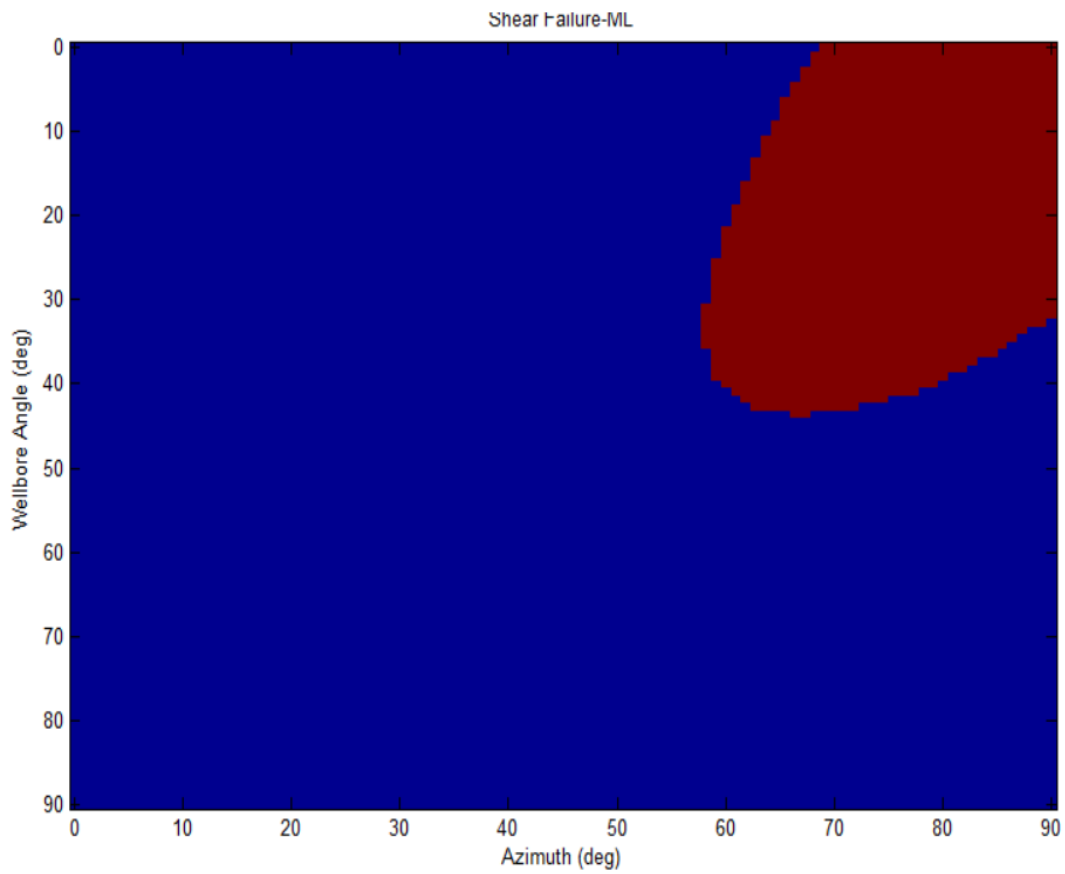


Figure 6. 7: Compressive (shear) failure based on modified Lade criteria for case 2 at 10 min

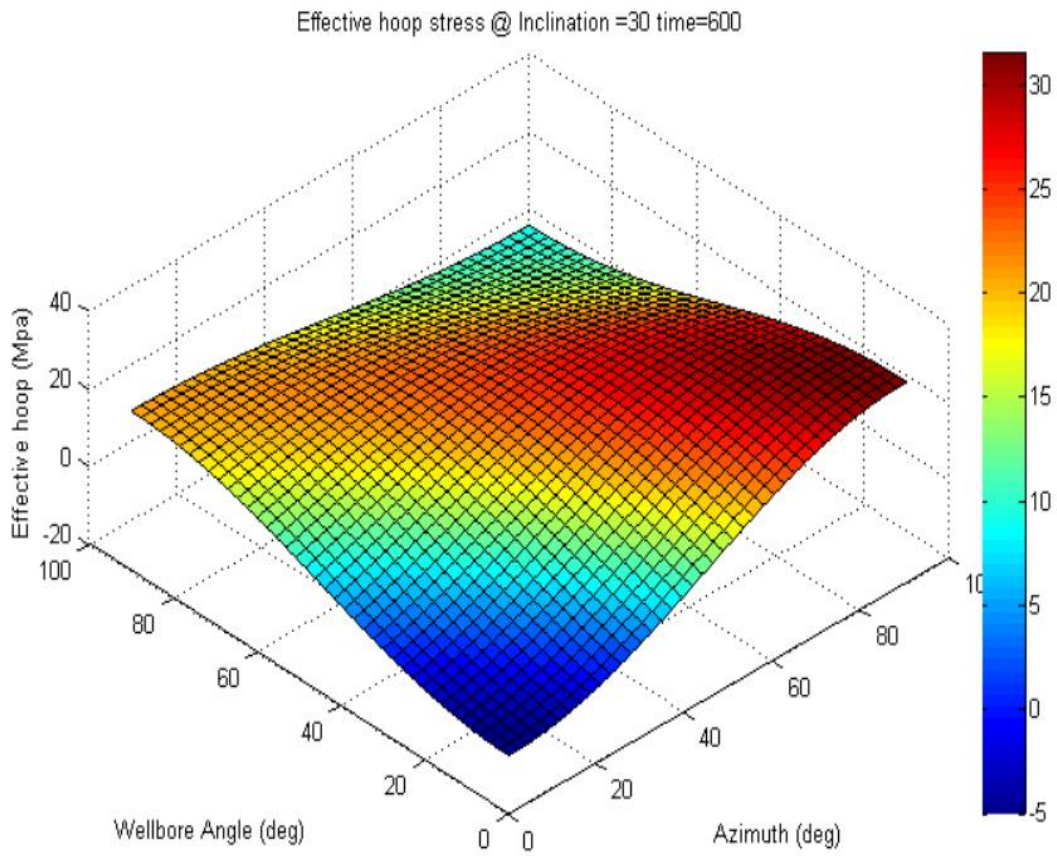


Figure 6. 8: Effective hoop stress including thermally induced stress - high permeability formation with convective heat transfer domination

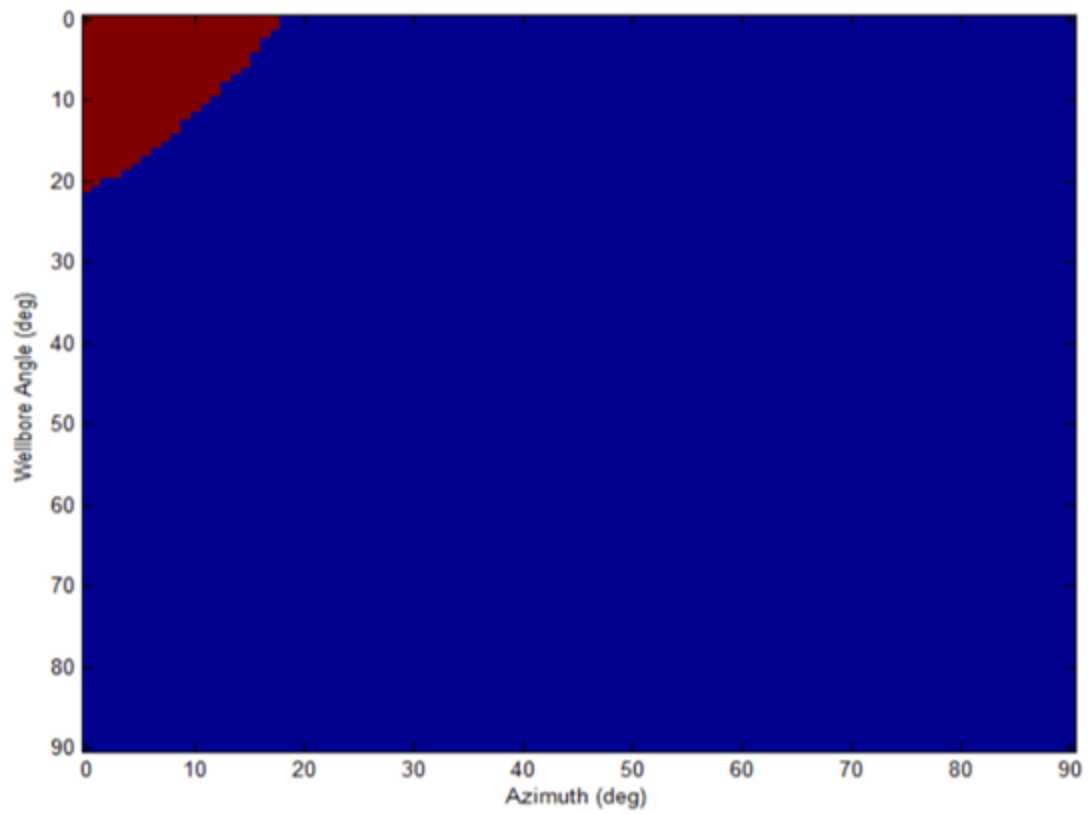


Figure 6. 9: Tensile failure prediction for high permeability formation with convective heat transfer domination (case 2) at 10 min

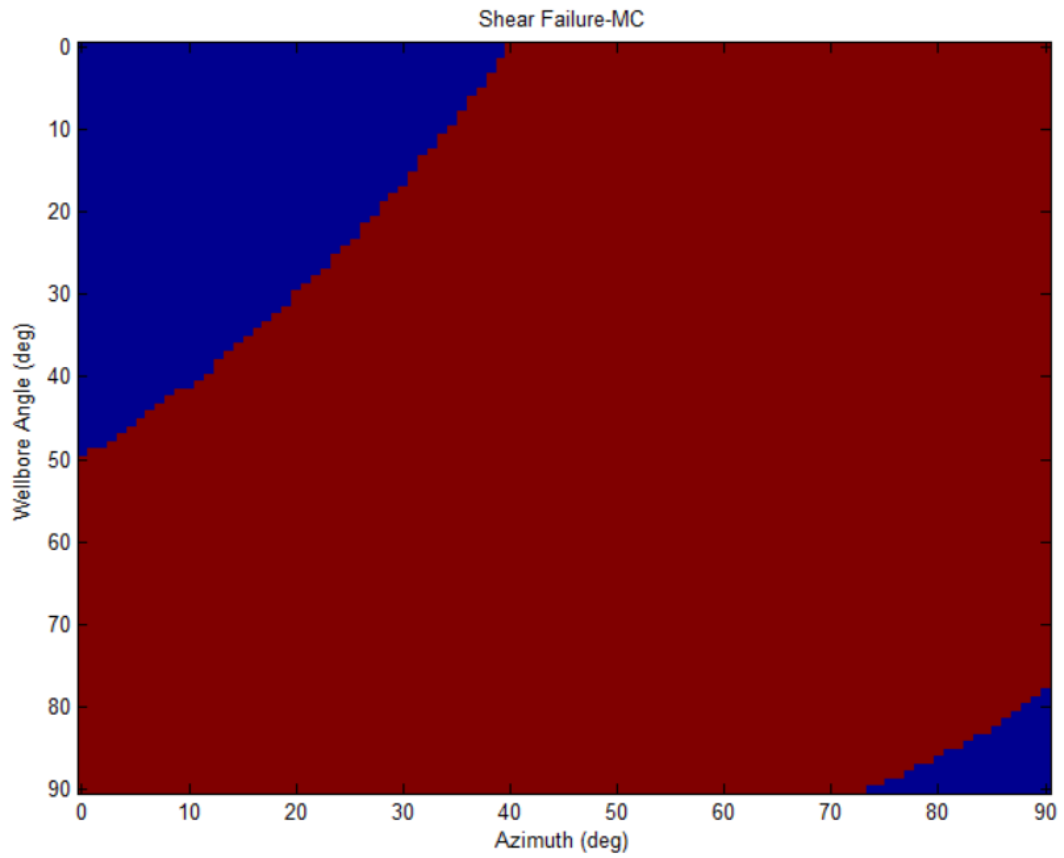


Figure 6. 10: Compressive (shear) failure based on Mohr-Coulomb for case 2, thermally induced stress at 10 min

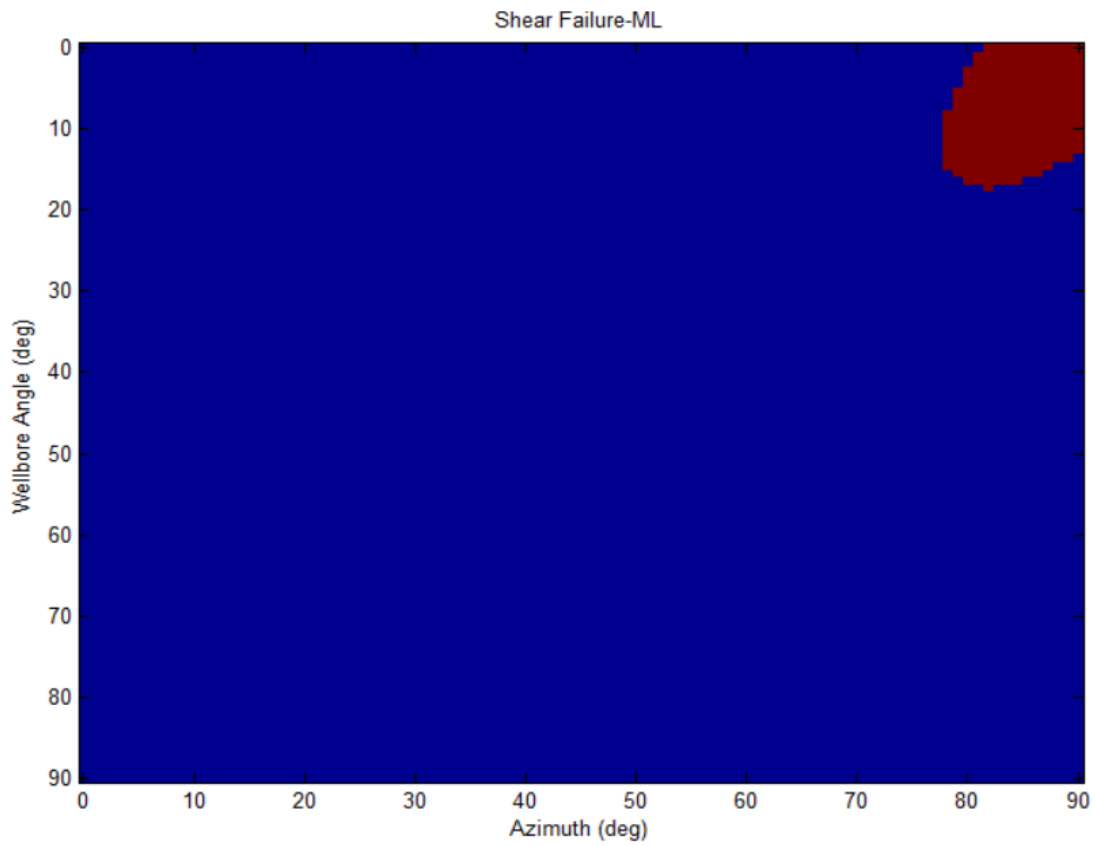
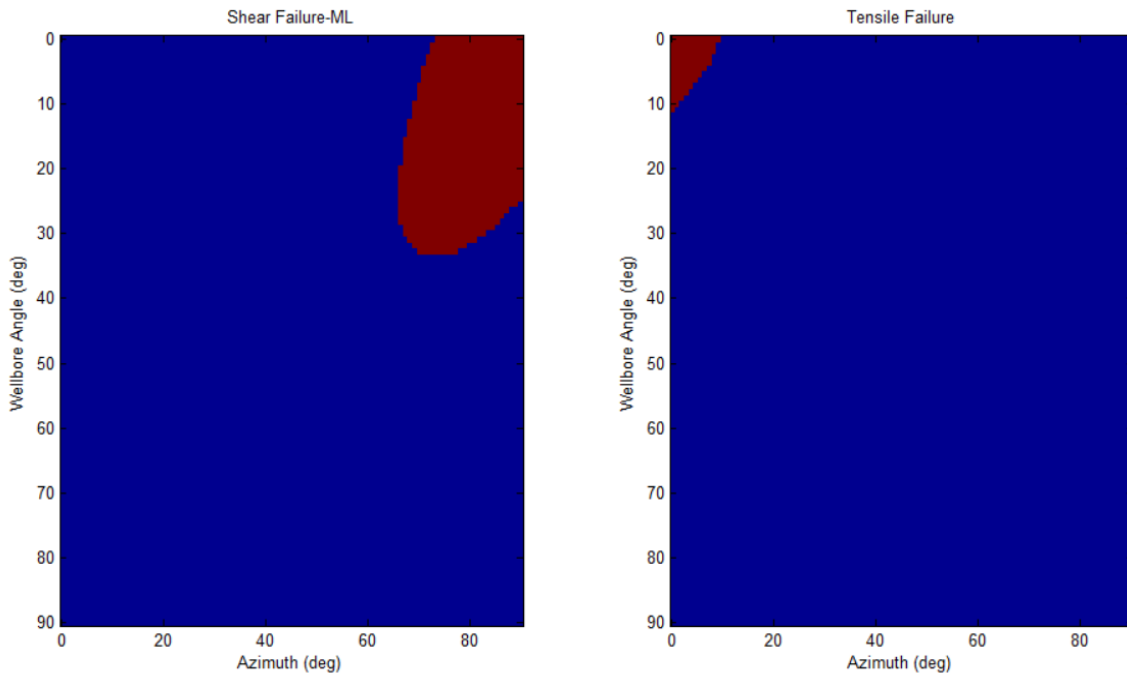
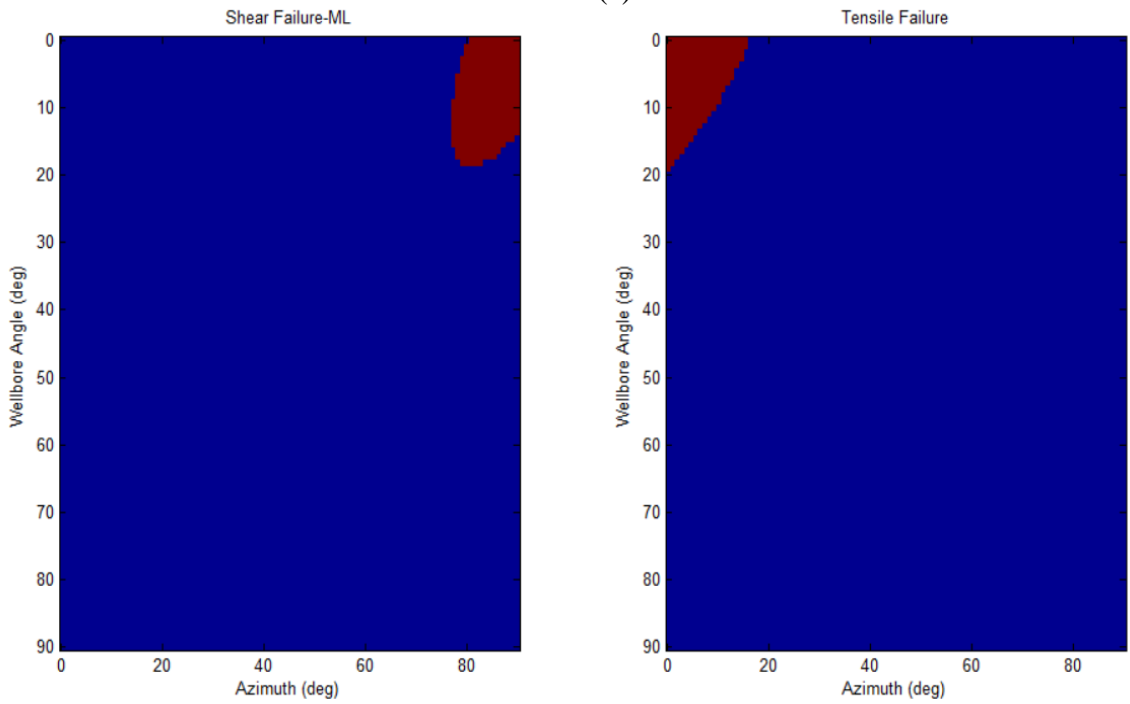


Figure 6. 11: Compressive (shear) failure based on modified Lade for case 2, thermally induced stress, at 10 min

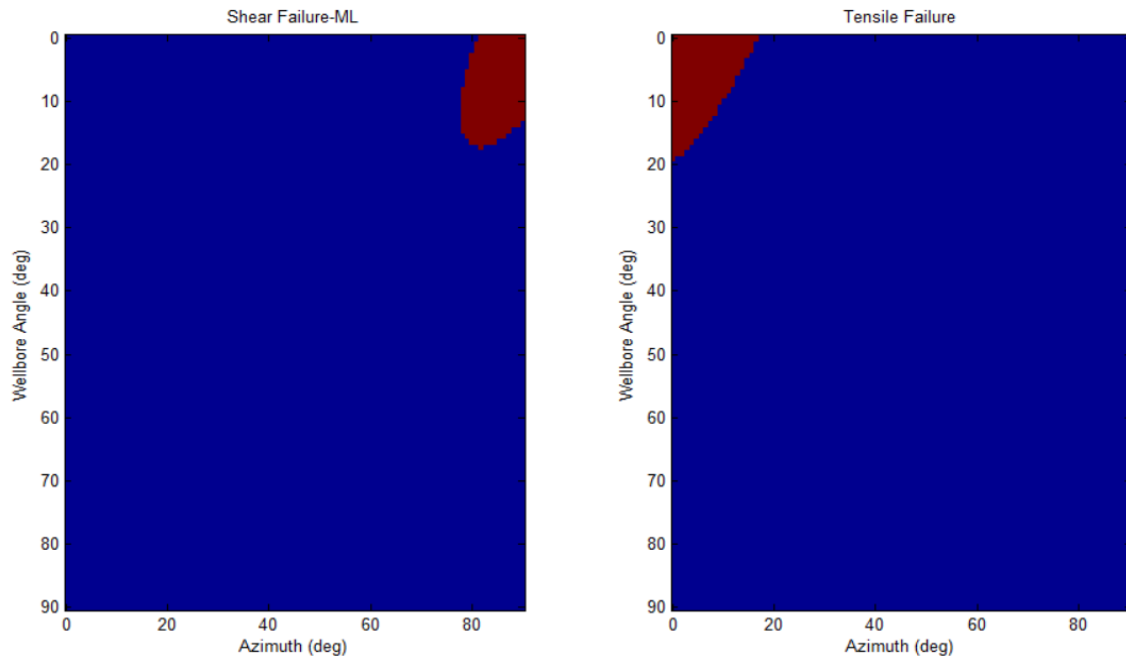


(a)



(b)

Figure 6. 12



(c)

Figure 6. 12: Shear and tensile failures evolution - at different times. (a) 10 sec, (b) 300 sec, and (c) 600 sec

#### 6.4 CONCLUSIONS

The effect of temperature coupled with fluid flow (pore pressure) into a porous formation was investigated in transient analyses. Mohr-Coulomb and modified Lade failure envelopes, and Zoback tensile failure [61] criteria are applied to the results to study the breakout and breakdown failures on the wellbore wall. For low permeable formations, where conduction dominated the heat transfer, convective coupling may be ignored. In these formations, the hoop stress minimum and maximum may occur away from the wellbore walls, and not at the walls. The developed numerical model was in a good agreement with the analytical solution as long as the time constraint for analytical solution permitted.

For large permeability, it may be assumed that the fluid diffusion becomes steady state before the temperature begins to change, and the effect of thermal diffusion becomes



small. Therefore, that heat transfer is dominated by hydraulic diffusion. In this study, it was concluded that the effect of temperature on stress around the wellbore is very important to consider. Thermally induced stress can change stress concentration around the wellbore and affect the likelihood of shear and tensile failures.

When a wellbore is cooled down, hoop stress will be lowered. Therefore, the stability with respect to shear failure increases, while, tensile failure increases. It was shown in this chapter that tensile failure approaches equilibrium earlier than shear failure does. Mohr-Coulomb under-estimates the strength of the rock, therefore, over-estimates the chance of shear failure based on the analysis. Modified Lade produces a more realistic estimation by including the intermediate stress and using a more accurate failure criteria formulation. Furthermore, these analyses can be used to predict troublesome conditions (tensile and shear failures) during drilling operations.

Table 6. 1: Parameters for case 1-low permeability formation with conductive heat transfer domination

<b>Variables</b>	<b>Value</b>	<b>Unit</b>
Minimum Horizontal Stress ( $S_h$ )	16.7	MPa
Maximum Horizontal Stress ( $S_H$ )	16.7	MPa
Overburden Stress ( $S_v$ )	21.5	MPa
Pore Pressure (P)	10	MPa
Wellbore Pressure ( $P_w$ )	10	MPa
Temperature Difference ( $\Delta T$ )	20	$^{\circ}\text{C}$
Well Inclination ( $\Upsilon$ )	0	degree
Wellbore Angle ( $\theta$ ) and Azimuth( $\phi$ )	0	degree
Wellbore Radius (r)	0.1	m
Biot's Coefficient ( $\alpha_b$ )	1	-
Young's Modulus (E)	3336	MPa
Undrained Poisson's Ratio ( $\nu_u$ )	0.46	-
Poisson's Ratio ( $\nu$ )	0.3	-
Thermal Volumetric Expansion of Rock ( $\alpha_m$ )	9E-05	$1/^{\circ}\text{C}$
Thermal Volumetric Expansion of Fluid ( $\alpha_f$ )	5E-04	$1/^{\circ}\text{C}$
Coupling Coefficient	0.31	-
Hydraulic Diffusivity	7.15E-09	$\text{m}^2/\text{s}$
Thermal Diffusivity	7.15e-7	$\text{m}^2/\text{s}$

Table 6. 2: Parameters for case 1-high permeability formation with convective heat transfer domination

<b>Variables</b>	<b>Value</b>	<b>Unit</b>
Minimum Horizontal Stress ( $S_h$ )	23	MPa
Maximum Horizontal Stress ( $S_H$ )	1.3 $S_h$	MPa
Overburden Stress ( $S_v$ )	1.3 $S_H$	MPa
Pore Pressure (P)	18	MPa
Wellbore Pressure ( $P_w$ )	19	MPa
Temperature Difference ( $\Delta T$ )	-30	$^{\circ}C$
Well Inclination ( $\Upsilon$ )	30	degree
Wellbore Angle ( $\theta$ ) and Azimuth( $\varphi$ )	0-90	degree
Wellbore Radius (r)	0.15	m
Investigation Zone (rL)	1	m
Formation Tensile Strength (TS)	0	MPa
Thermal Conductivity of Rock (k)	2.61	J/s/m/Kelvin
Density of Rock ( $\rho_b$ )	2.65	g/cc
Heat Capacity of Rock ( $C_b$ )	1000	J/kg/Kelvin
Permeability of Rock (k)	0.1	Darcy
Porosity of Rock ( $\phi$ )	0.15	-
Fluid Viscosity ( $\mu$ )	1	cp
Skempton Coefficient (B)	0.73	-
Biot's Coefficient ( $\alpha_b$ )	1	-
Young's Modulus (E)	5000	MPa
Undrained Poisson's Ratio ( $\nu_u$ )	0.4	-
Poisson's Ratio ( $\nu$ )	0.3	-
Thermal Volumetric Expansion of Rock ( $\alpha_m$ )	4.0E-5	$1/^{\circ}C$
Thermal Volumetric Expansion of Fluid ( $\alpha_f$ )	5.00E-04	$1/^{\circ}C$
Friction Coefficient ( $\mu$ )	0.6	-
Friction Coefficient Angle ( $\beta$ )	30	degree
Cohesion of Rock ( $S_o$ )	7	MPa

## CHAPTER 7: LOCAL THERMAL NON-EQUILIBRIUM

This chapter discusses the application and effect of local thermal non-equilibrium (LTNE) in porous media. Physical insights into how LTNE affect the temperature profiles and thermal stresses will be provided through analyses. Analytical and numerical solution approaches are discussed in this section. Conductive and convective heat transfers are considered. Finally, effects of LTNE on the current thermoporoelastic model will be discussed.

### 7.1 INTRODUCTION TO LOCAL THERMAL NON-EQUILIBRIUM

In classical thermodynamics in porous media such as rock formations, a single temperature is defined for the medium regardless of phases presented in the medium. This is due to the assumption that the fluid temperature and solid temperature reach a local equilibrium temperature instantly, also known as local thermal equilibrium (LTE) theory. However, this theory has not been widely investigated experimentally in rock formations. LTE ignores additional pore and thermal stresses in the porous medium caused by temperature variations of the fluid and solid phases. Therefore, a more realistic approach is necessary to model both temperatures separately, known as local thermal non-equilibrium (LTNE). This approach is based on applying energy balance on both phases, fluid and rock matrix. LTNE effects have been investigated by many researchers in different media. Alazmi and Vafai investigated the effects of LTNE and thermal dispersion on free surface flow through porous media [129]. Wang et al. examined LTNE effects in biological organs related to hyperthermia treatments [130]. He and Jin developed a transient LTNE model for pure heat conduction transfer in porous media [131]. Others such as Nield and Bejan [107], Nield [132], Kuznetsov [133], and Rees and Pop [134] reviewed both theories and applications of the LTNE effects in convection heat transfer in porous

*Some of the work of this chapter is based on:*

*\*Gandomkar, A and \*\*Gray, K.E. Local Thermal non-Equilibrium in Porous Media with Heat Conduction. Intl. J. of Heat and Mass Trans. 124, pp. 1212-1216, 2018*

*\* Corresponding author, conducted research and modeling*

*\*\*Coauthor and research supervisor*

media. He et al. studied convective cooling or heating induced thermal stresses in a fluid saturated porous medium undergoing local thermal non-equilibrium [135]. However, their model assumes a convective heat boundary and ignores the convective heat transfer mechanism. Yang et al. considered the effects of LTNE with forced convective flow in an annulus filled with a porous medium, but their model assumes a steady state condition in Cartesian coordinates [136]. Xu et al. examined non-equilibrium heat transfer in a metal-foam solar collector with no-slip boundary condition for steady state condition in Cartesian coordinates [137]. However, the objective of this chapter is to present transient models in radial coordinates considering conductive and convective heat transfers. The necessary equations for fluid saturated porous media undergoing local thermal nonequilibrium (LTNE) with conductive and convective heat transfers are presented, and the effects of LTNE on a circular hole in an infinite medium such as rock formations are investigated. First, a series of equations necessary to solve temperature profiles for the fluid and solid matrix with pure heat conduction are presented. The Laplace and Stehfest methods were employed in formulating the solutions. Next, conductive and convective heat transfers are modeled. MATLAB numerical method is employed in solving this condition. The models are then validated against He and Jin model for a circular wellbore subjected to uniform temperature at the wellbore boundary. Later, the thermoporoelastic models developed in the previous chapters are updated with the effect of LTNE. The effects of LTNE in porous media with conductive and convective heat transfers, heat transfer coefficient, and fluid flow are investigated.

## **7.2 CONDUCTIVE HEAT TRANSFER**

In this section, LTNE model with pure conductive heat transfer mechanism has been considered.

### 7.2.1 LTNE conductive model

Under LTNE conditions, the temperatures for solid phase and fluid phase in an isotropic and homogenous porous medium are given by the following heat equations [107]:

$$\nabla \cdot (\phi k_f \nabla T_f) - \nabla \cdot [(\rho c)_f v T_f] = \frac{\partial}{\partial t} [\phi (\rho c)_f T_f] - h(T_s - T_f) \quad (7.1)$$

$$\nabla \cdot ((1 - \phi) k_s \nabla T_s) = \frac{\partial}{\partial t} [(1 - \phi) (\rho c)_s T_s] + h(T_s - T_f) \quad (7.2)$$

where,  $k_f$  and  $k_s$  are the thermal conductivities of fluid and solid phases respectively.  $v$  is the fluid velocity,  $h$  is the heat transfer coefficient, and  $T_f$  and  $T_s$  are the fluid and solid temperatures.  $\rho$  is the density of each phase and  $\phi$  is the porosity of the medium. The second term in (7.1) represents the convective heat flow. This section considers conductive heat transfer in radial direction only and ignores convective heat transfer.

New parameters are introduced to make equations (6.1) and (6.2) dimensionless as follow:

$$A = \frac{\phi (\rho c)_f}{(1 - \phi) (\rho c)_s}, \quad B = \frac{\phi k_f}{(1 - \phi) k_s}, \quad C = \frac{h}{(1 - \phi) (\rho c)_s}, \quad D = \frac{k_s}{(\rho c)_s} \quad (7.3a, b, c, d)$$

and temperatures become dimensionless using:

$$\theta_f = \frac{T_f - T_{\text{formation}}}{T_{\text{ref}}}, \quad \theta_s = \frac{T_s - T_{\text{formation}}}{T_{\text{ref}}} \quad (7.4a, b)$$

$T_{\text{ref}}$  is the reference temperature, and wellbore temperature is chosen to be the reference temperature as shown in Figure 7.1.  $T_{\text{formation}}$  is the initial formation temperature. If properties such as porosity, thermal conductivities, and heat capacities are constants, equations (7.1) and (7.2) become:

$$A \frac{\partial \theta_f}{\partial t} - B D \nabla^2 \theta_f + C(\theta_s - \theta_f) = 0 \quad (7.5)$$

$$\frac{\partial \theta_s}{\partial t} - D \nabla^2 \theta_s - C(\theta_s - \theta_f) = 0 \quad (7.6)$$

Equations (7.5) and (7.6) are PDE's in radial coordinates and can be solved simultaneously for the temperature profiles of fluid and solid phases. The initial and boundary conditions are:

$$\theta_f = \theta_s = 0 \quad @ \quad (r,t) \Big|_{t=0} \quad (7.7)$$

$$\theta_f = \theta_s = \theta_w \quad @ \quad (r,t) \Big|_{r=r_w} \quad (7.8)$$

$$\theta_f = \theta_s = 0 \quad @ \quad (r,t) \Big|_{r=\infty} \quad (7.9)$$

$\theta_w$  is the change between wellbore temperature and formation temperature, and it is defined as:

$$\theta_w = \frac{T_{\text{wellbore}} - T_{\text{formation}}}{T_{\text{ref}}} \quad (7.10)$$

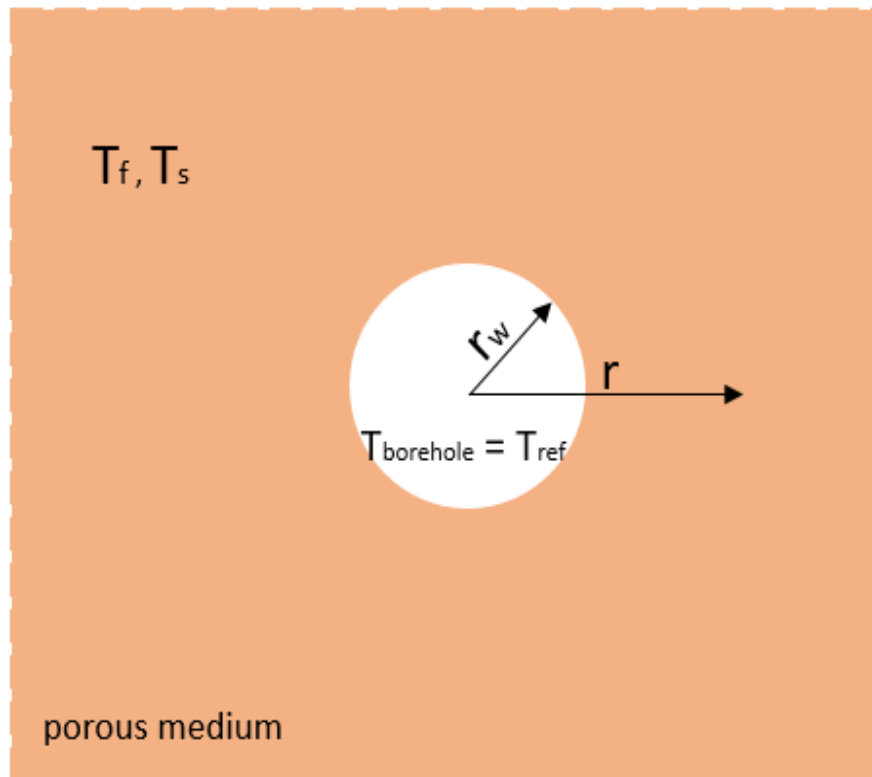


Figure 7. 1: A borehole in an infinite rock formation subjected to a constant temperature at the borehole

Equations (7.5) and (7.6) are solved using the Laplace transform subjected to initial condition in (7.7) and boundary conditions (7.8) and (7.9):

$$As\bar{\theta}_f - BD\nabla^2\bar{\theta}_f + C(\bar{\theta}_s - \bar{\theta}_f) = 0 \quad (7.11)$$

$$s\bar{\theta}_s - D\nabla^2\bar{\theta}_s - C(\bar{\theta}_s - \bar{\theta}_f) = 0 \quad (7.12)$$

Rewrite (7.12) in terms of the fluid phase and substitute into (7.11) and solve for the solid phase. The result will be:

$$\nabla^4\bar{\theta}_s - M\nabla^2\bar{\theta}_s + N\bar{\theta}_s = 0 \quad (7.13)$$

where:

$$M = \frac{C}{B} \left[ As \frac{D}{C} + Bs \frac{D}{C} + BD + D \right] \quad (7.14)$$

$$N = \frac{C}{B} \left[ \frac{As^2}{C} + As + s \right] \quad (7.15)$$

The roots to Eq. (13) are given by:

$$q_{1,2} = \frac{-M \pm \sqrt{M^2 - 4N}}{2} \quad (7.16)$$

using Carslaw and Jaeger analyses [110], the solution to equations (7.11) and (7.12) are as follow:

$$\bar{\theta}_f = \frac{\theta_w}{sD(q_1 - q_2)} \left[ \left( \frac{A}{B} s - Dq_2 \right) \frac{K_0(r\sqrt{q_1})}{K_0(a\sqrt{q_1})} - \left( \frac{A}{B} s - Dq_1 \right) \frac{K_0(r\sqrt{q_2})}{K_0(a\sqrt{q_2})} \right] \quad (7.17)$$

$$\bar{\theta}_s = \frac{\theta_w}{sD(q_1 - q_2)} \left[ (s - Dq_2) \frac{K_0(r\sqrt{q_1})}{K_0(a\sqrt{q_1})} - (s - Dq_1) \frac{K_0(r\sqrt{q_2})}{K_0(a\sqrt{q_2})} \right] \quad (7.18)$$

Further details on Carslaw and Jaeger solution are shown in the **Appendix**.

Stehfest Laplace inversion algorithm has been used to convert the solutions of (7.17) and (7.18) from Laplace domain into real time domain [111]. Stehfest method has been chosen for its stability and accuracy. Finally, the mean temperature of the medium is calculated using:



$$\theta_{\text{LTNE}} = (1 - \phi)\theta_s + \phi\theta_f \quad (7.19)$$

The classical LTE temperature profile for short time is given by Wang and Papamichos [128]:

$$\bar{\theta}_{\text{LTE}} = \frac{\theta_a}{s} \frac{K_0\left(r\sqrt{\frac{s}{D}}\right)}{K_0\left(a\sqrt{\frac{s}{D}}\right)} \quad (7.20)$$

The solution to (7.20) is also transformed from Laplace domain to time domain using Stehfest algorithm. The unit of time given into Stehfest algorithm is in seconds and calculated as follow:

$$t = \frac{\tau a^2}{D} \quad (7.21)$$

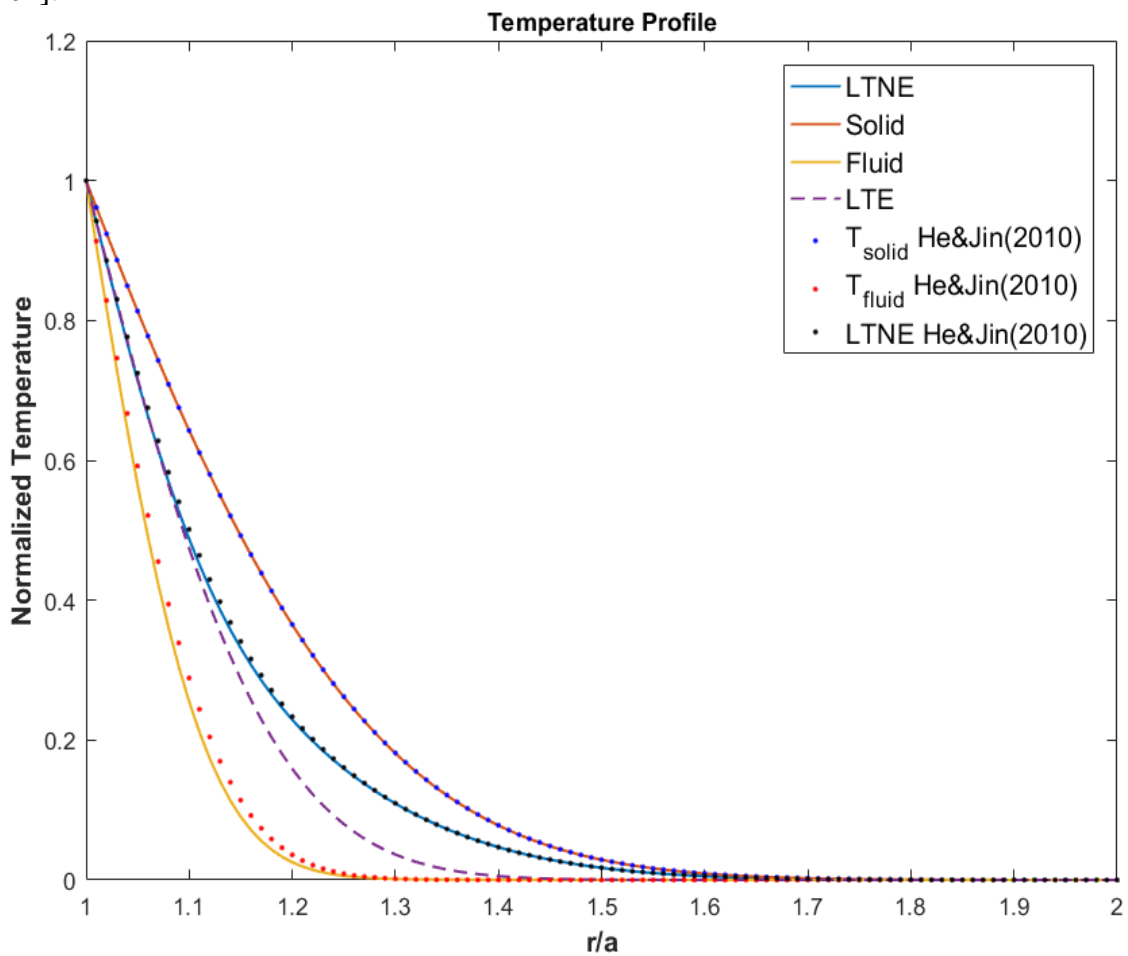
where  $\tau$  is the nondimensional time and  $a$  is the wellbore radius.

### 7.2.2 Results for conductive case

The model is validated against He and Jin model [135] as shown in Figures 7.2, 7.3, and 7.3. Table 7.1 lists the fluid and rock matrix data used for the conductive LTNE model. As shown in Figure 7.2, the model is in a good agreement with He and Jin model. However, diversion occurs between the two models as non-dimensional time increases, as shown in Figures 7.3 and 7.4. This is because He and Jin have used an approximation method to solve equations (7.11) and (7.12) for short periods, while, the present model produces exact solutions for any time. Therefore, the new model is more accurate for longer times compared to He and Jin LTNE model as shown in Figure 7.4.

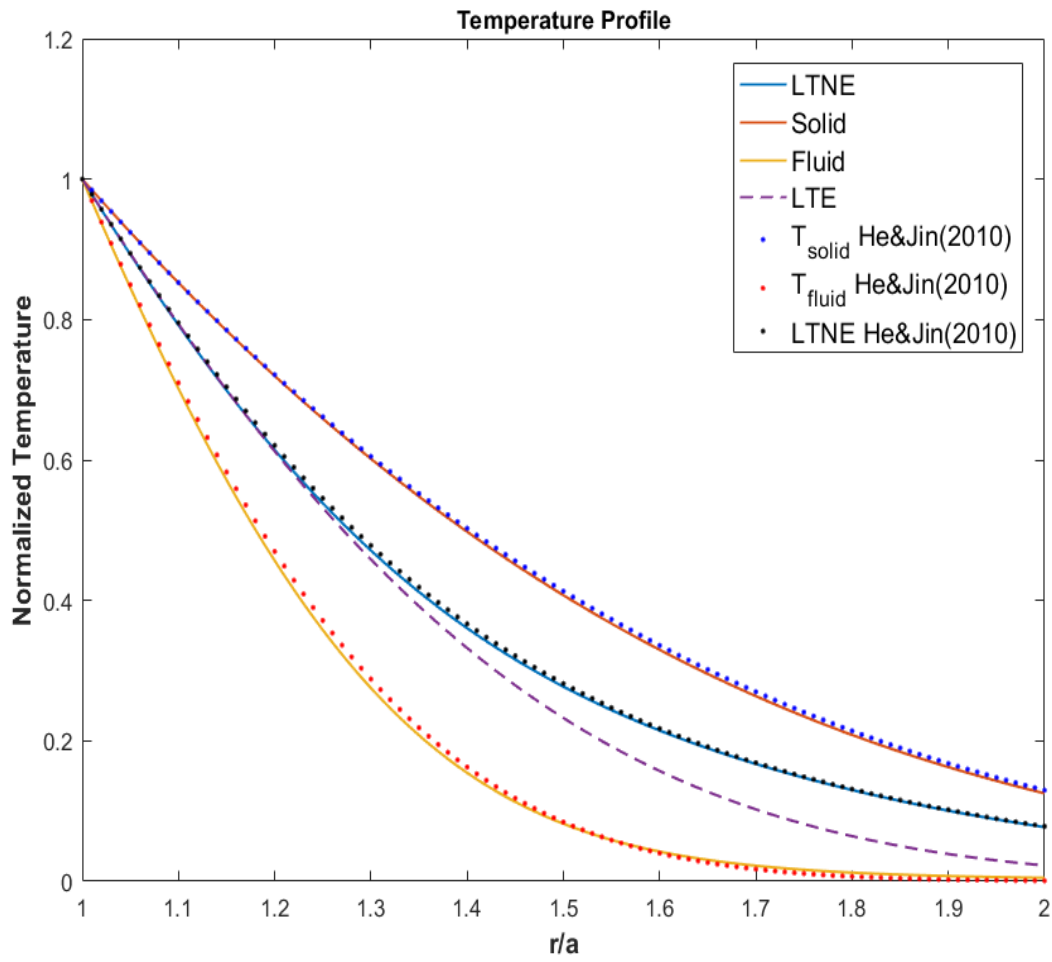
Figures 7.2 (a) and 7.2 (b) show the normalized temperatures for the rock matrix, fluid, weighted average, and classical theory (LTE) for non-dimensional times of 0.01 and 0.1 against radial distance. It can be seen from the graphs that the weighted average temperature (LTNE) is always higher than the classical theory temperature (LTE). Also,

rock matrix (solid phase) temperature is the highest temperature due to its higher thermal conductivity. Figure 7.2 (b) shows that the temperature gap between the lines increases, indicating that the LTNE effect is more pronounced as time increases. It can also be concluded from the results that the temperatures never equilibrate at any time which is contrary to the classical theory assumption that the two phases of solid and fluid reach equilibrium instantly. This trend was also observed by Lu and Xiang in their analyses [104].



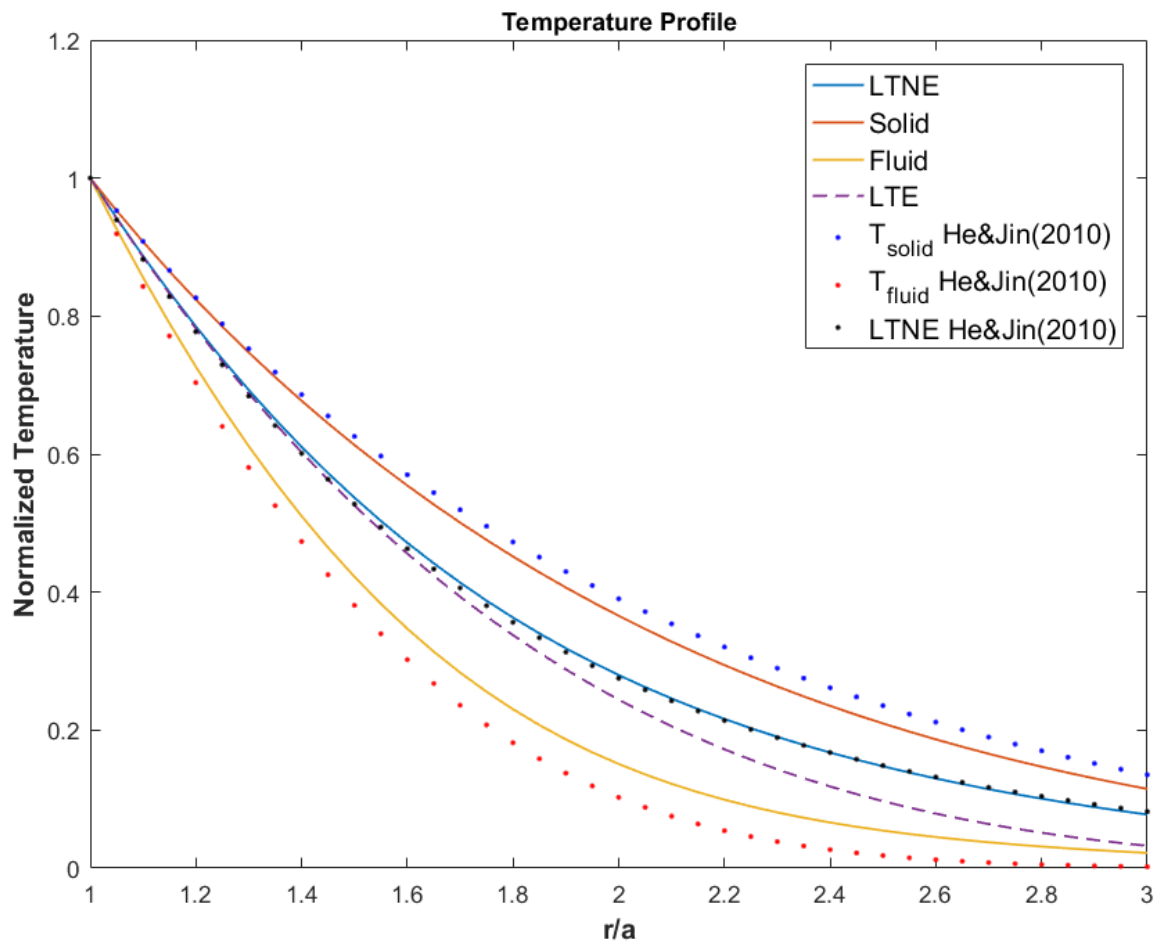
(a)

Figure 7. 2



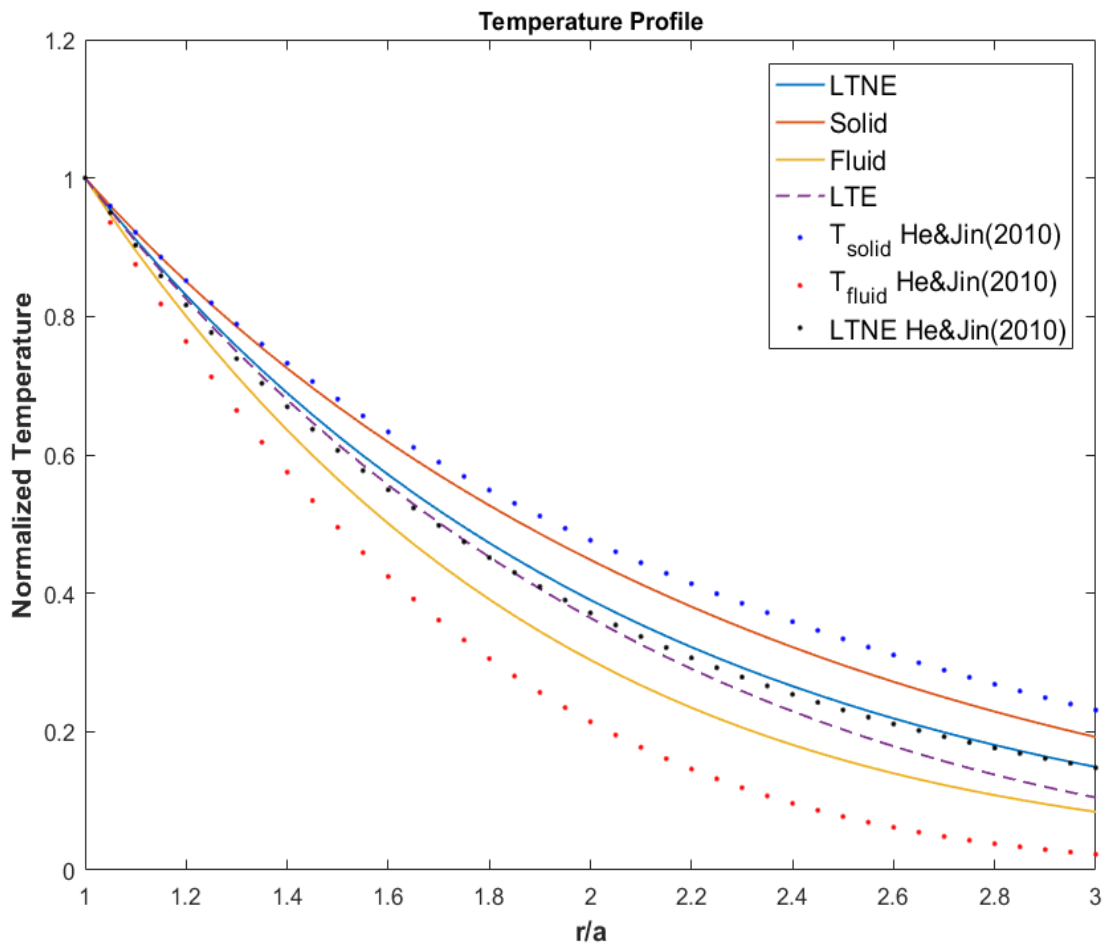
(b)

Figure 7. 2: Normalized temperature profiles along radial distance for pure conductive heat transfer at short periods (a)  $\tau = 0.01$  and (b)  $\tau = 0.1$  [143]



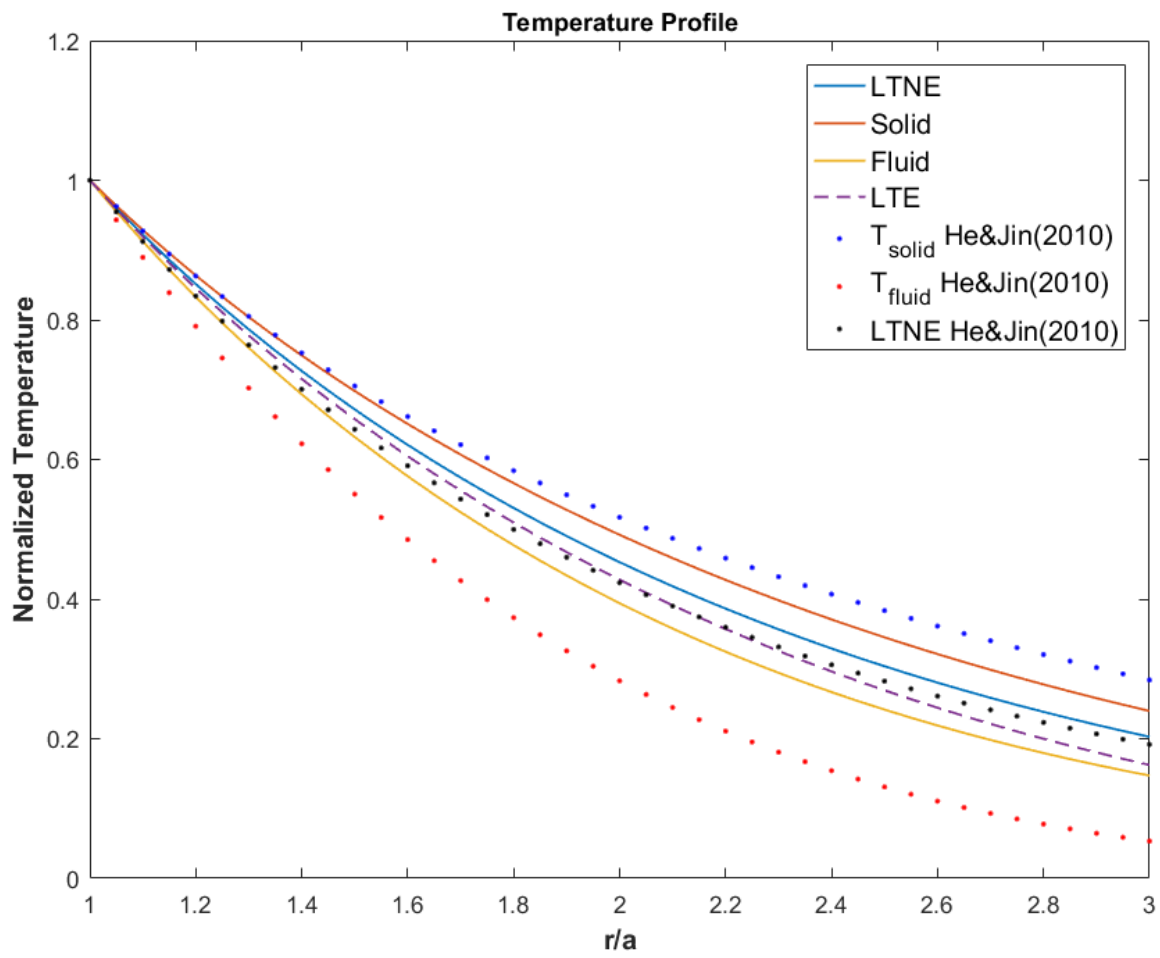
(a)

Figure 7.3



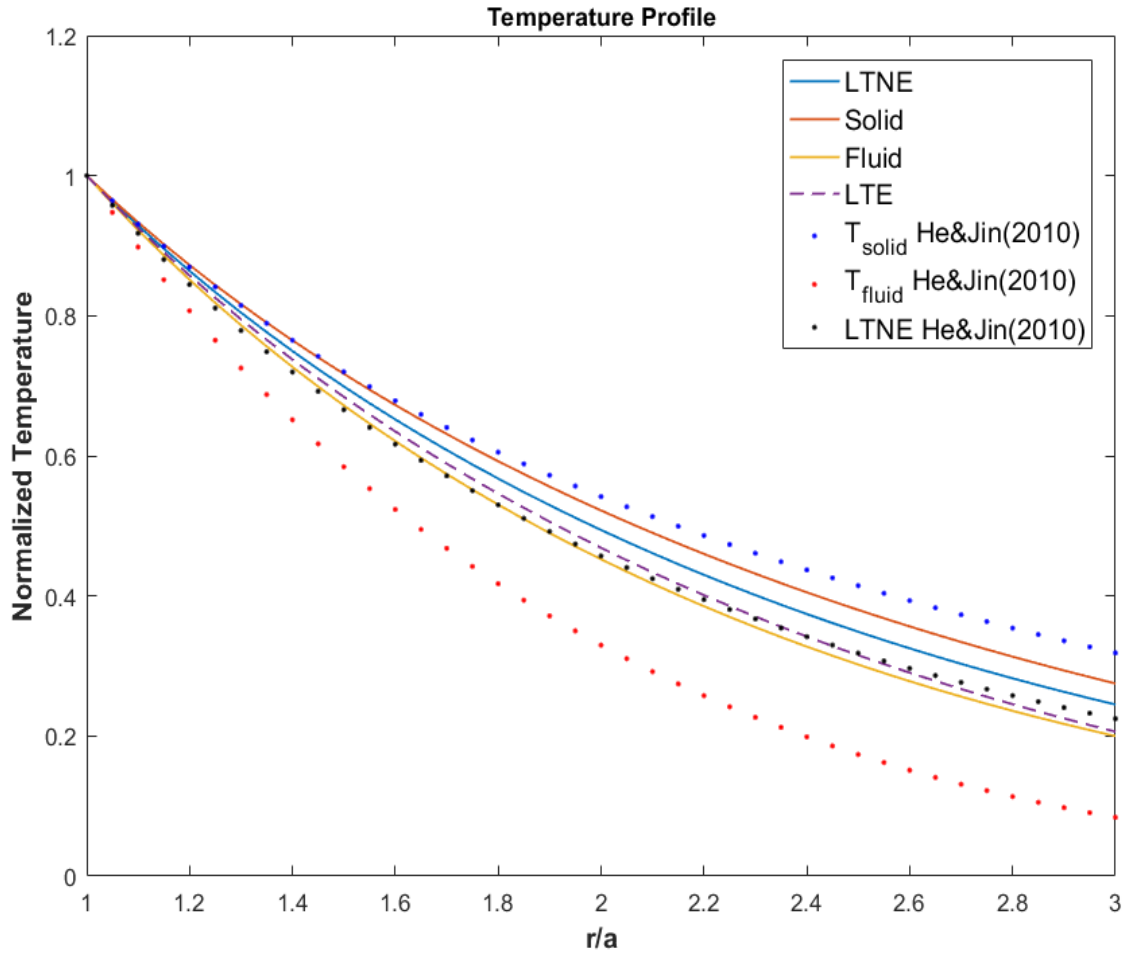
(b)

Figure 7. 3: Normalized temperature profiles along radial distance for conductive heat transfer for moderate times (a)  $\tau = 0.5$  and (b)  $\tau = 1.0$  [143]



(a)

Figure 7. 4



(b)

Figure 7. 4: Normalized temperature profiles along radial distance for conductive heat transfer for longer periods (a)  $\tau = 1.5$  and (b)  $\tau = 2.0$  [143]

In the present section, the LTNE effects in an isotropic and homogenous porous media with heat conduction transfer only in radial direction are analyzed. In the subsequent section, convective heat transfer is added to the present model to examine the LTNE effects with both heat transfer mechanisms.

### 7.3 CONDUCTIVE AND CONVECTIVE HEAT TRANSFERS

Convective heat transfer is added to the conductive heat transfer modeled in section 7.2. Hence, two heat mechanisms are considered simultaneously.

### 7.3.1 LTNE conductive and convective model

The second term in equation (7.1) represents the convective heat flow. In this section, both convective and conductive heat transfers are considered in the radial direction only. If properties such as porosity, thermal conductivities, heat capacities are constants, and fluid velocity ( $v$ ) has a linear profile and does not change with each location ( $\frac{\partial v}{\partial r} = 0$ ), equations (7.1) and (7.2) become:

$$A \frac{\partial \theta_f}{\partial t} - BD \nabla^2 \theta_f + C(\theta_s - \theta_f) - D \nabla \theta_f = 0 \quad (7.22)$$

$$\frac{\partial \theta_s}{\partial t} - D \nabla^2 \theta_s - C(\theta_s - \theta_f) = 0 \quad (7.23)$$

equations (7.22) and (7.23) are PDE's in radial coordinates and can be solved simultaneously for temperature profiles of fluid and rock matrix. The initial and boundary conditions are still unchanged, and equations (7.7), (7.8), and (7.9) are applicable.

Equations (7.22) and (7.23) are solved using MATLAB partial differential numerical solver, pdepe. MATLAB pdepe solves initial-boundary value problems for systems of parabolic and elliptic PDE's in the one space variable. The time given into the program come from equation (7.21).

### 7.3.2 Results for conductive and convective heat transfers

Initially, the conductive and convective model is compared to the conductive model. As shown in Figure 7.5, the conductive and convective model presented here is in a good agreement with the analytical model developed in section 7.2. Figure 7.5 shows the normalized temperatures for the rock matrix, fluid, weighted average, and classical theory (LTE) for a non-dimensional time of 0.01 against radial distance. Again, the weighted average temperature (LTNE) is always higher than the classical theory temperature (LTE) and, the rock matrix temperature is the highest.



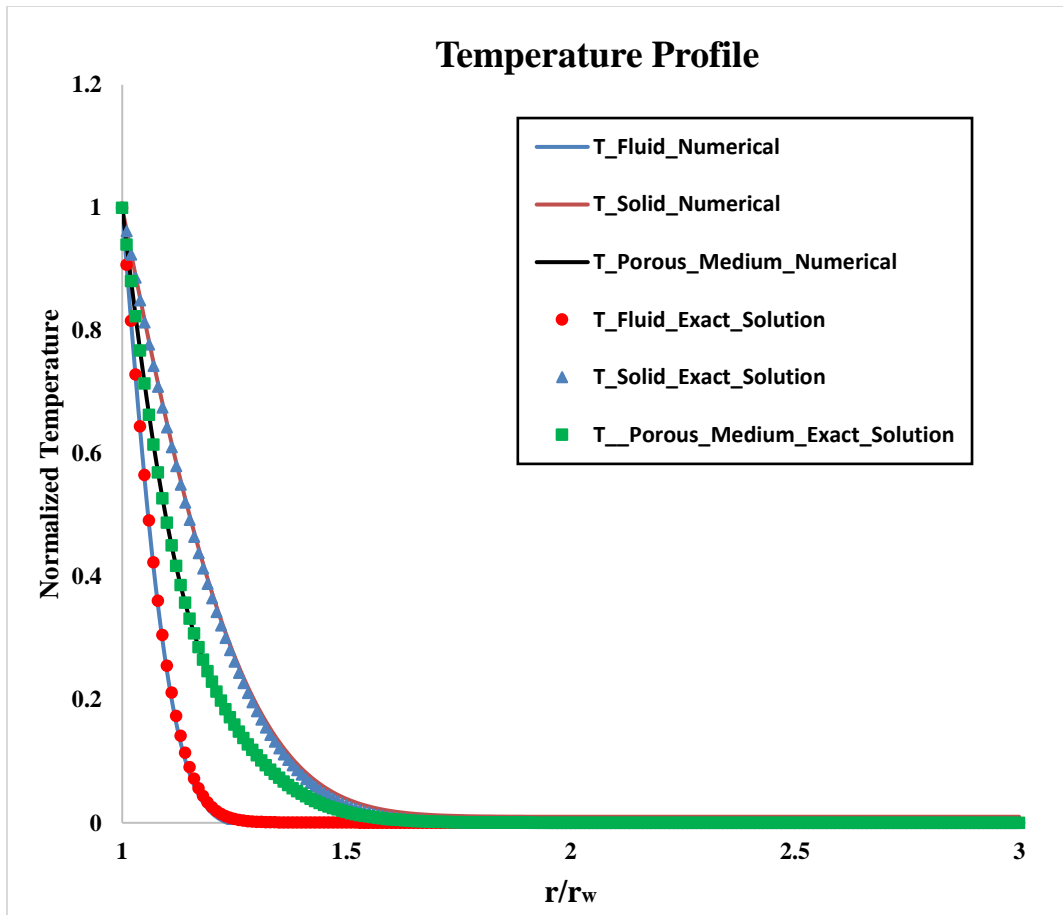


Figure 7. 5: Comparison among normalized temperature profiles produced by the exact and numerical models along radial distance for  $\tau = 0.01$

Figures 7.6, 7.7, and 7.8 show the effect of heat convection due to fluid flow inside the porous medium at different non-dimensional times. In this analysis, the fluid velocity is chosen to be 0.005 m/s at the wellbore wall ( $r = r_w$ ). It can be seen from the graphs that the heat convection has a pronounced effect on the LTNE, therefore, on the temperature profiles with increasing time. At the early time, convective heat transfer affects the temperature profiles very close to the vicinity of the wellbore wall. However, as time increases the fluid temperature profile are substantially disturbed. In fact, the temperature change for the fluid profile is far greater in each time and reaches the boundary condition temperature faster. In pure conductive heat transfer, the porous media and rock matrix

(solid phase) temperature are always greater than fluid temperature as shown in Figure 7.5. However, when the convective heat transfer is added to the system, the fluid temperature is higher than the other two temperatures due to convective flow. This could be agitated by increasing the fluid velocity.

There is an intersection point, called thermal equilibrium point, shown in Figures 7.6, 7.7, and 7.10. To the left of this point, convective heat transfer dominates conduction heat transfer. While, conduction heat transfer is dominant to the right of this point. This point is an indication that shows where a dominant heat transfer mechanism exists, and it changes location with time. If the fluid temperature is higher than the solid and medium temperatures, it indicates a convective dominated heat transfer region.

The challenge in MATLAB numerical code was stability. It requires small time steps and mesh grids to reach stability, which in turn increases computational time. High fluid velocity also caused the program some instability issues since the MATLAB pdepe is suitable for a low to moderate Péclet number (the rate of convection over the rate of conduction).

Figures 7.9 and 7.10 show effects of fluid velocity and heat transfer coefficient on the LTNE. As fluid velocity increases, the change in fluid temperature increases and overall porous medium temperature increases. The fluid velocity values shown in Figure 7.9 are the velocities at the wellbore wall. Figure 7.10 shows the results of heat transfer coefficient effect on LTNE. As the heat transfer coefficient increases, the gap between the temperature profiles decreases, meaning that the effect of local thermal non-equilibrium is minimized. At higher heat transfer coefficient values, the rock matrix (solid phase) as well as the overall medium temperatures increase. The fluid velocity,  $v$ , used in equations (7.1) and (7.22) are calculated based on Darcy's equation:

$$v = \frac{\kappa}{\mu} \nabla p \quad (7.24)$$

$$\nabla p = \frac{dp}{dr} \quad (7.25)$$

where  $\kappa$  (kappa) is the permeability of the rock,  $\mu$  is the viscosity of the fluid, and  $\nabla p$  is the pressure gradient in radial coordinates. Since the fluid is assumed to be water, the viscosity is 1 cp. The value for the permeability is assumed to be 50 mD. The remaining data are used from Table 7.1.

One of the challenges with the LTNE model is the estimation of heat transfer coefficient,  $h$ . The heat transfer coefficient has a wide range of values, 10–1000 (W/m<sup>2</sup>/K) [107], however, a value of 3000 W/m<sup>2</sup>/K has been reported in the literature [35]. With this wide range, the temperature profiles can be substantially influenced. Unfortunately, there are limited data and correlations available, therefore, more research and lab experiments are required in this field for better estimation of heat transfer coefficients in rocks. Lab experimental values of heat transfer coefficients can be calculated in an indirect manner [137] [138]. Different correlations have also been developed that relies on the size and surface area of the solid particles and estimations of Nusselt, Reynolds, and Prandtl numbers [139].

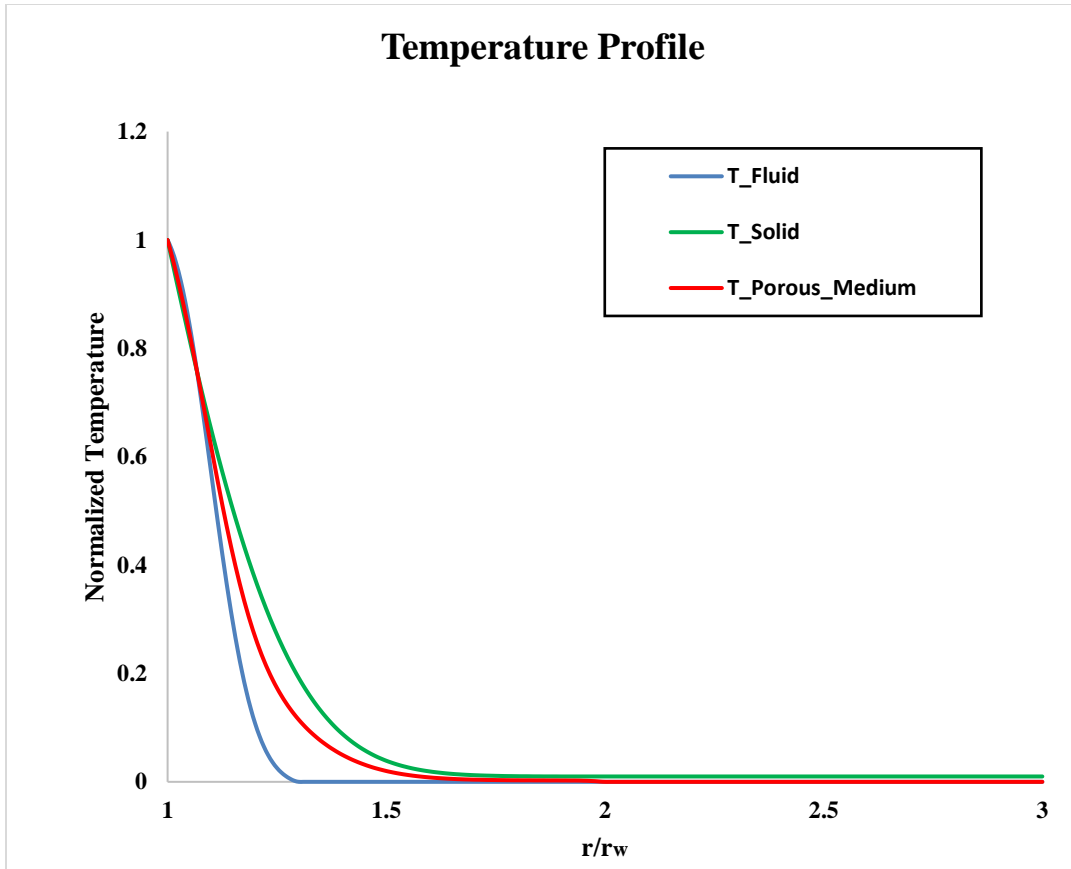


Figure 7. 6: Normalized temperature profiles with LTNE effects along radial distance for conductive and convective heat transfers at  $\tau = 0.01$

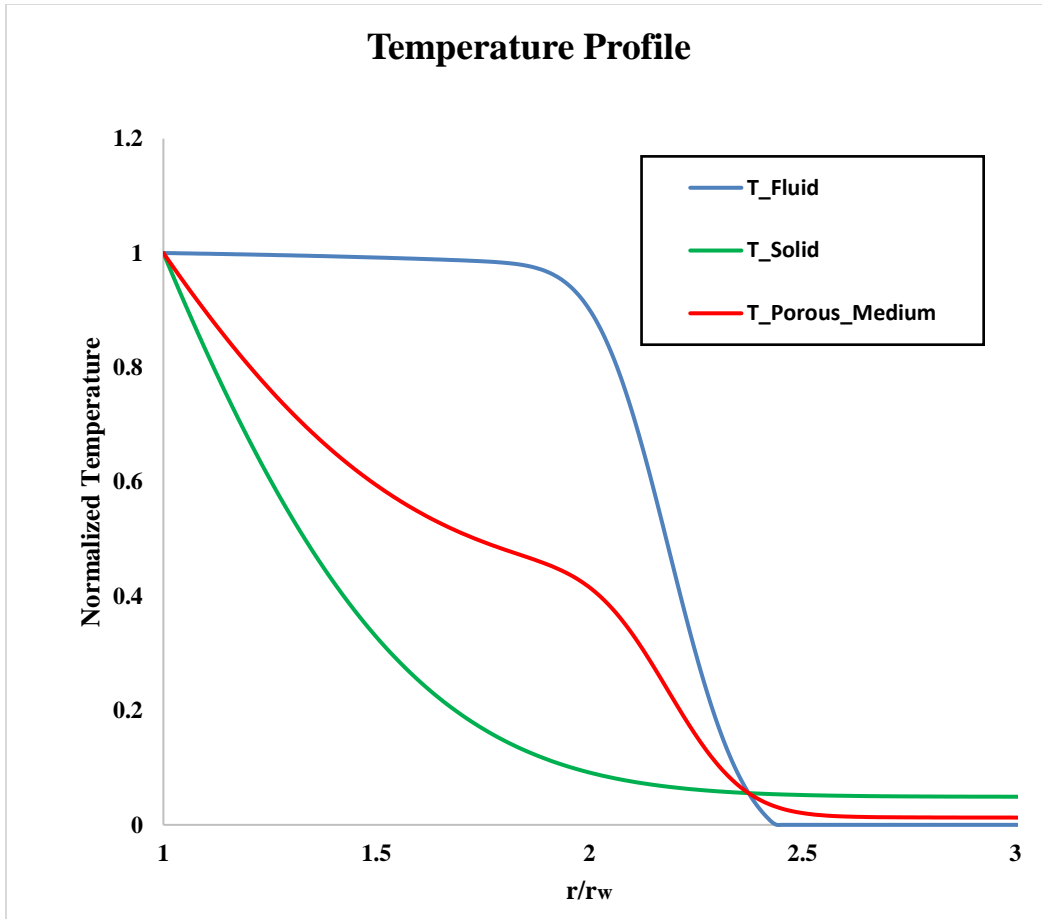


Figure 7. 7: Normalized temperature profiles with LTNE effects under conductive and convective heat transfers for  $\tau = 0.05$

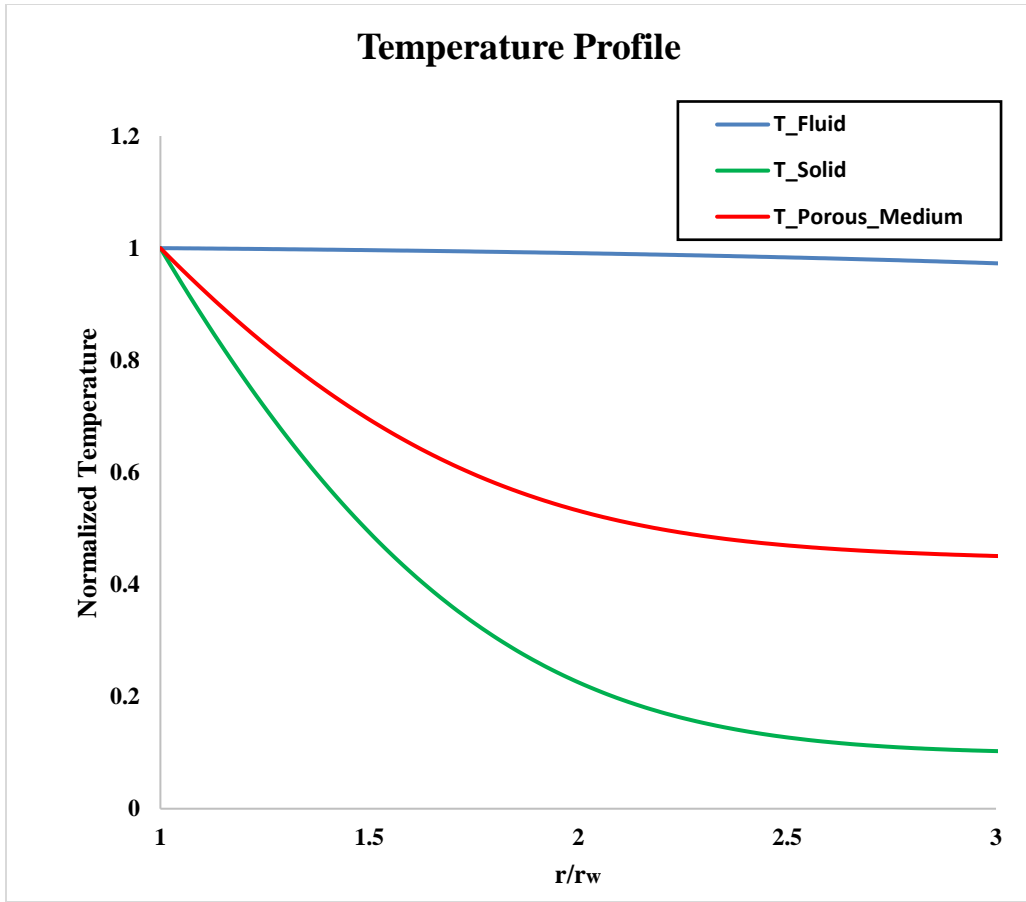


Figure 7. 8: Normalized temperature profiles with LTNE effects along radial distance for  $\tau = 0.1$  - conductive and convective heat transfers

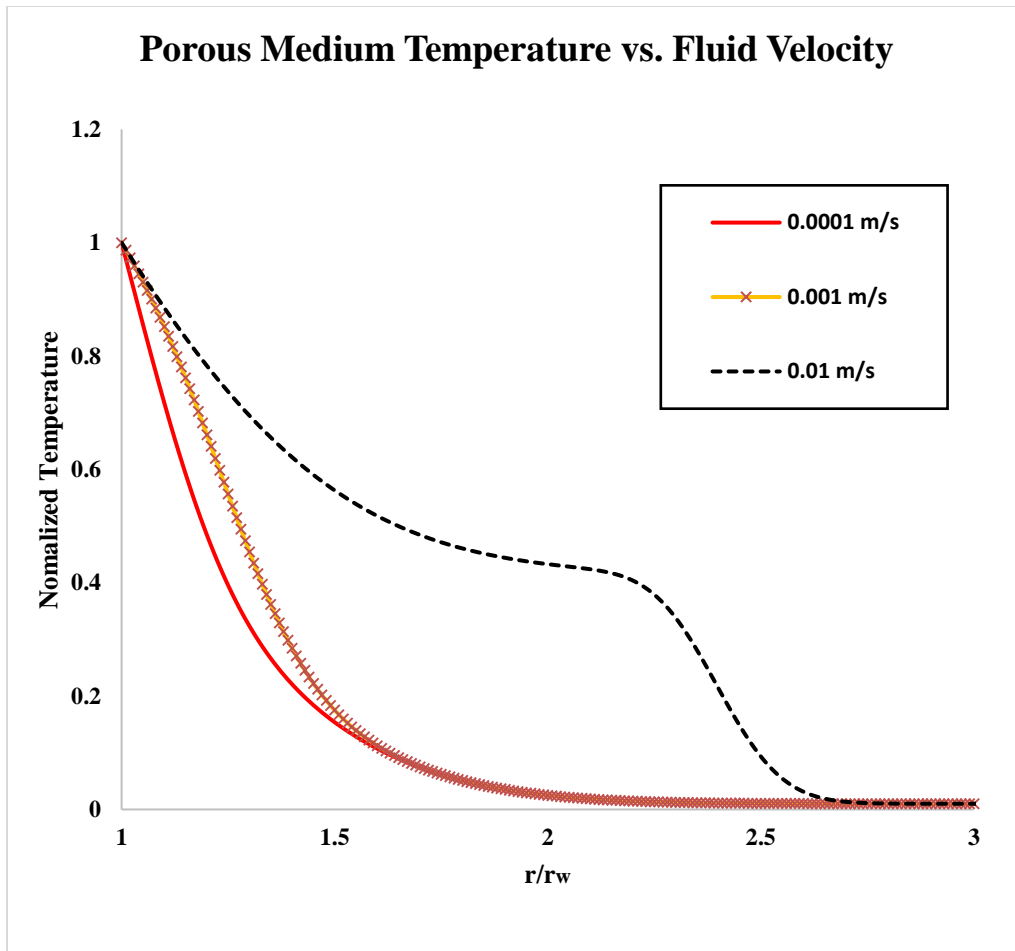
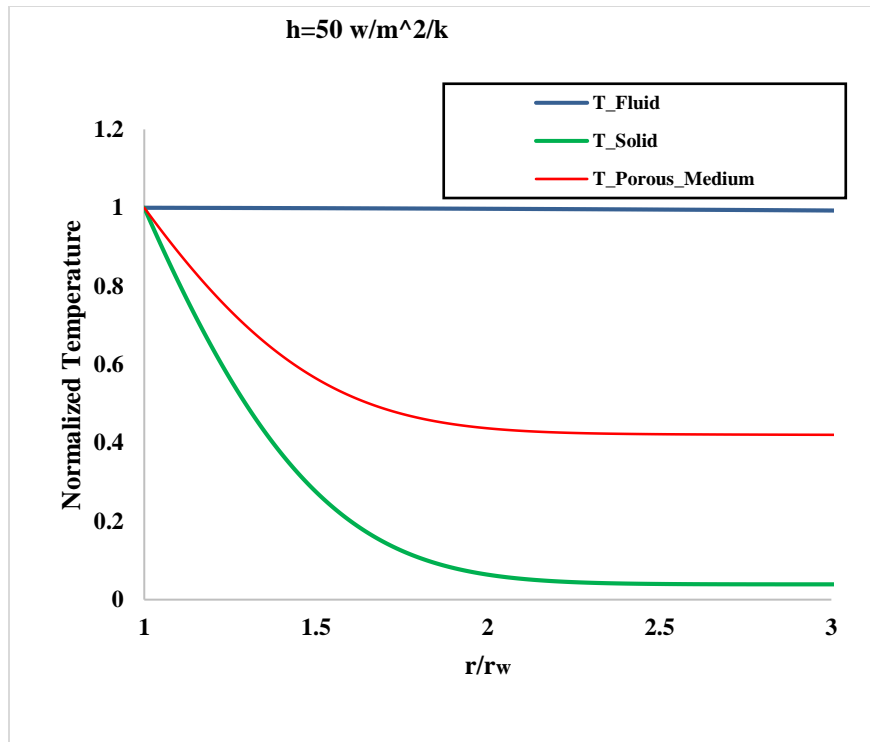
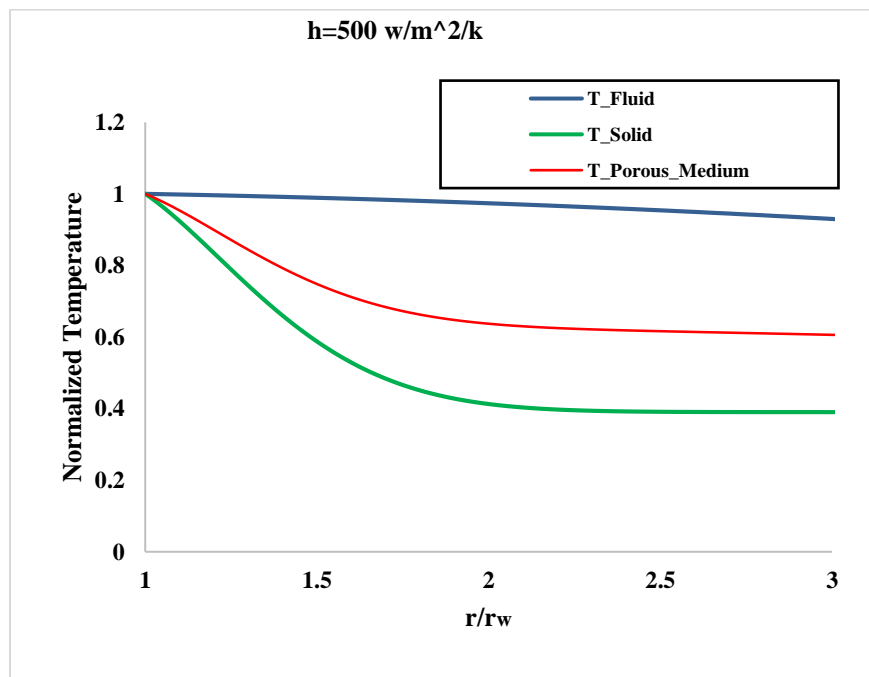


Figure 7. 9: Fluid velocity effect on porous media temperature along radial distance for  $\tau = 0.04$  under conductive and convective heat transfers



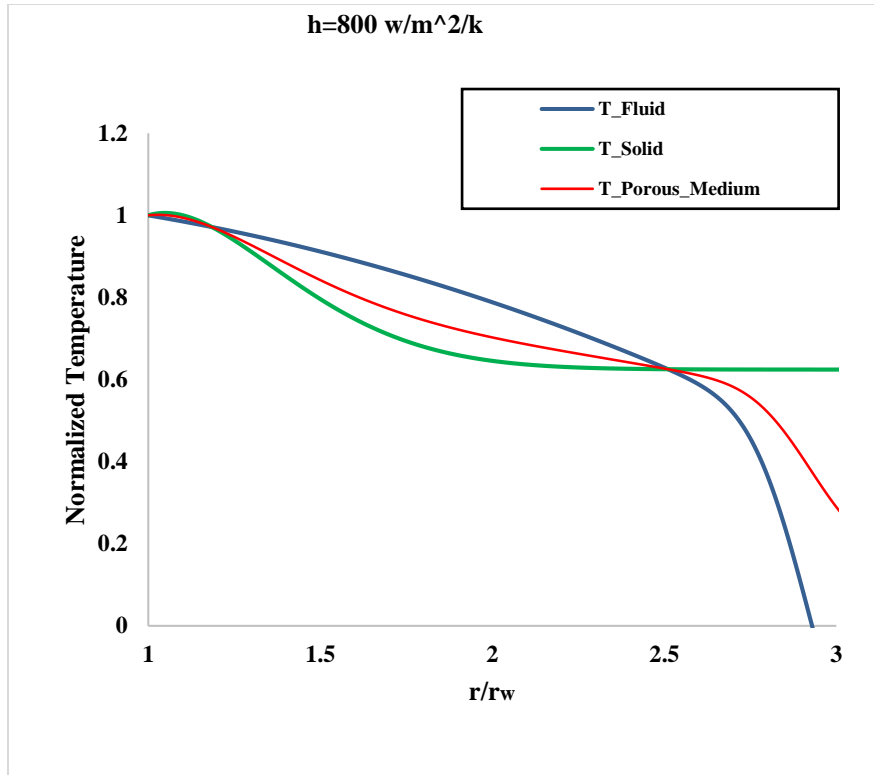
(a)



(b)

Figure 7. 10





(c)

Figure 7. 10: Normalized temperature profiles along radial distance with conductive and convective heat transfers for  $\tau = 0.04$ ,  $\kappa=50$  mD, and  $\mu=1$  cp with various heat transfer coefficients at (a) 50 W/m<sup>2</sup>/K, (b) 500 W/m<sup>2</sup>/K, and (c) 800 W/m<sup>2</sup>/K

### 7.3.3 Finite element modeling

Aside from the existing models discussed in the previous sections, a finite element modeling (FEM) has been done for comparison and validation. The only known finite element software considering heat transfer with local thermal non-equilibrium is COMSOL. COMSOL heat transfer module has been selected with LTNE which is a special multiphysics in COMCOL for this purpose. The first approach was to model a pure conductive heat transfer discussed in section 7.2. For modeling, an axisymmetric plane in 2D space has been selected as shown in Figure 7.11(a). The analysis was run in a transient

condition with extremely fine mesh. The required data used in COMSOL can be found in Table 7.1.

The finite element results produced by COMSOL does not agree well with the existing model developed in section 7.1 as shown in Figure 7.11(b). For instance, the difference between fluid temperature profiles for both models is large. Only solid and LTNE (porous media) are slightly in agreement. This brings the questions that which model is more accurate. Since the model developed in section 7.2 is in a good agreement with the analytical model, it can be concluded that the developed model is more accurate than the FEM model developed by COMSOL. In fact, COMSOL LTNE module is fairly a new feature, and requires more update in the future. Another disadvantage of COMSOL model is the lack of convective heat transfer option. There is no option in COMSOL to input data for convective heat transfer mechanism. Therefore, the comparison between the two models for convective heat transfer was not possible.

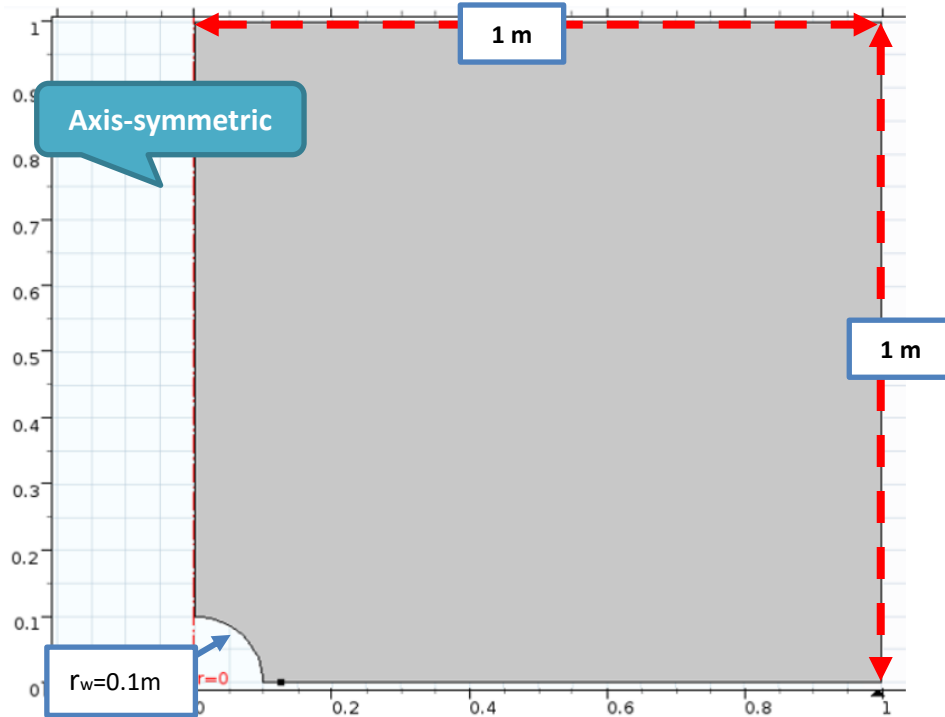
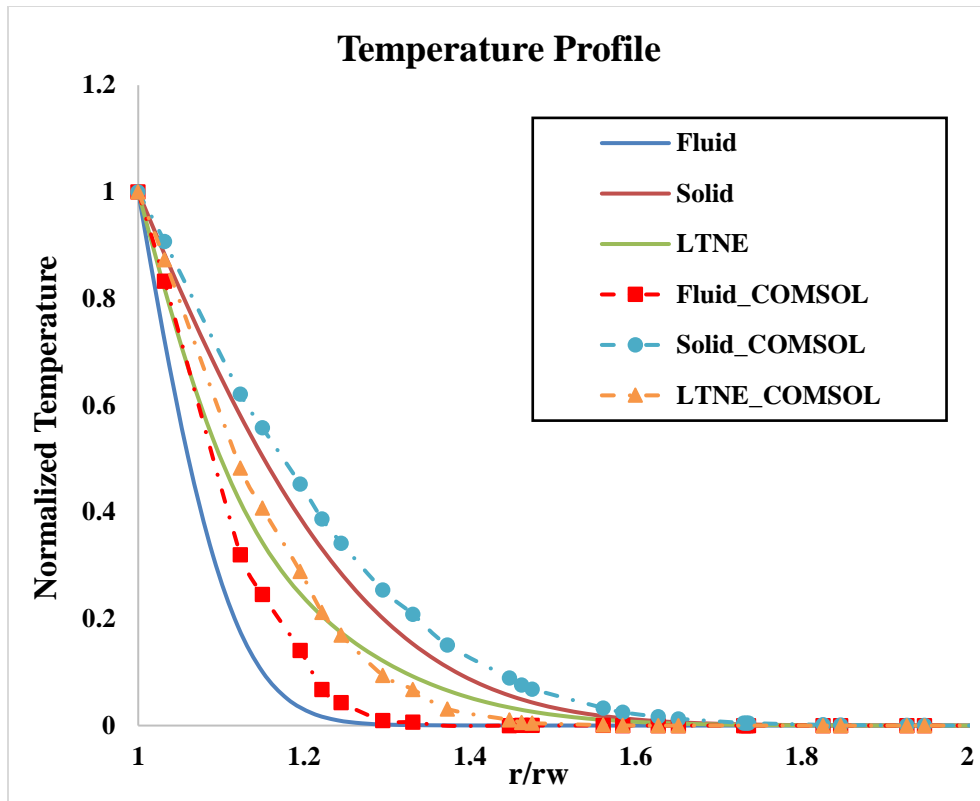


Figure 7. 11



(b)

Figure 7. 11: LTNE conductive model versus COMSOL finite element model in (a) schematic diagram of COMSOL model (b) results produced by the models

#### 7.4 THERMOPOROELASTICITY UNDER LTNE

In this section, the thermoporoelastic model examples that have been done in **Chapter 6** will be updated with the LTNE models and compared with the previous results.

##### 7.4.1 Case 1: analytical solution for low permeability formation

Case 1 suggests that the conductive heat transfer dominates the convective heat transfer since the pore fluid flow is negligible. Using the conductive LTNE model, a new temperature profile for the media is defined and used in the thermoporoelastic model. Figures 7.12 and 7.13 illustrate the tangential and radial stresses profiles of LTNE and LTE thermoporoelastic models along with poroelastic model. From the figures, the results vary

when the LTNE approach is used. Within the vicinity of the wellbore where the temperature disturbance is greater, the discrepancy is notable between the models. This discrepancy elevates with time too. However, this trend dies out away from the wellbore. An important remark from the results is that the LTE and LTNE model do not produce the same results as time passes, suggesting that the local equilibrium never reaches between fluid and solid matrix, contrary to classical theory assumption. The LTNE effects are more pronounced on tangential stress compared to radial stress as shown in Figures 7.12 and 7.13. This proves that using LTNE is suggested in modeling wellbore stability since estimation of tangential stress is a key factor in formation breakdown and breakout.

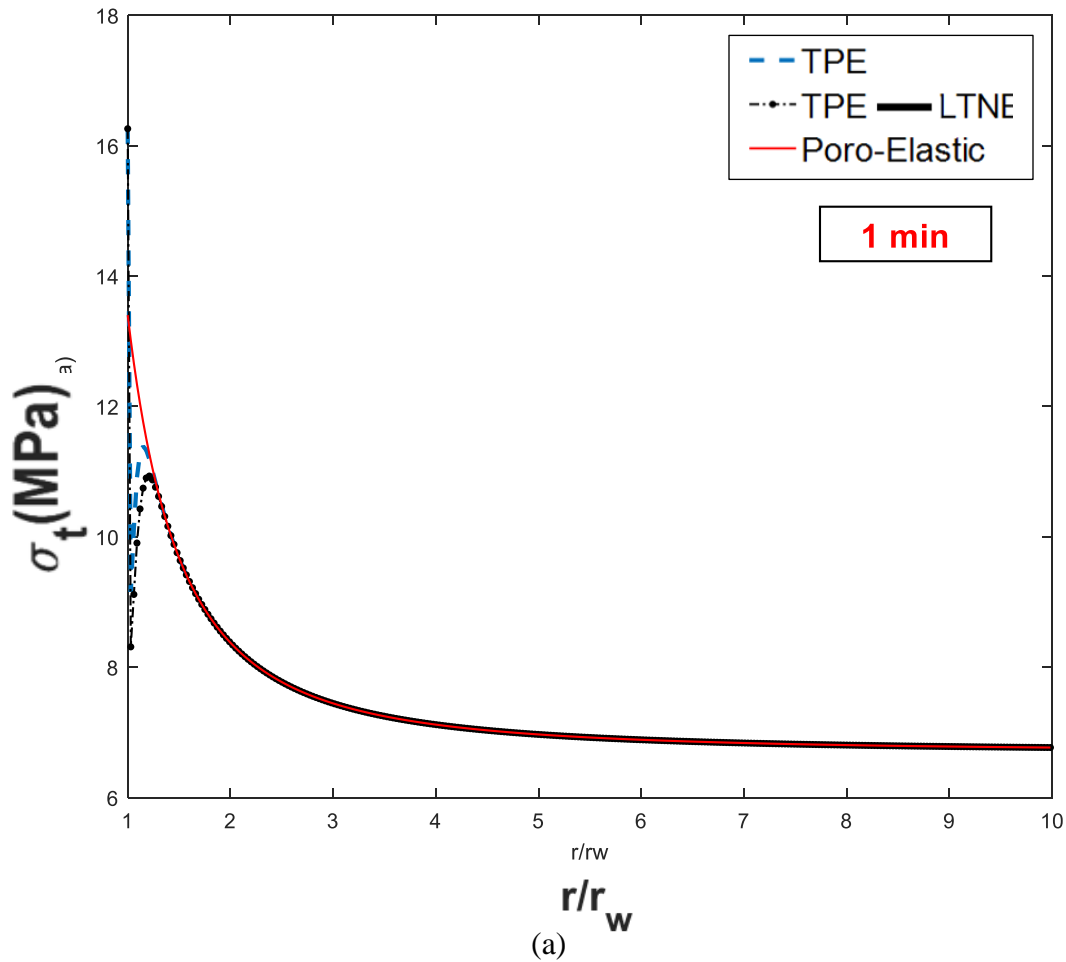


Figure 7. 12

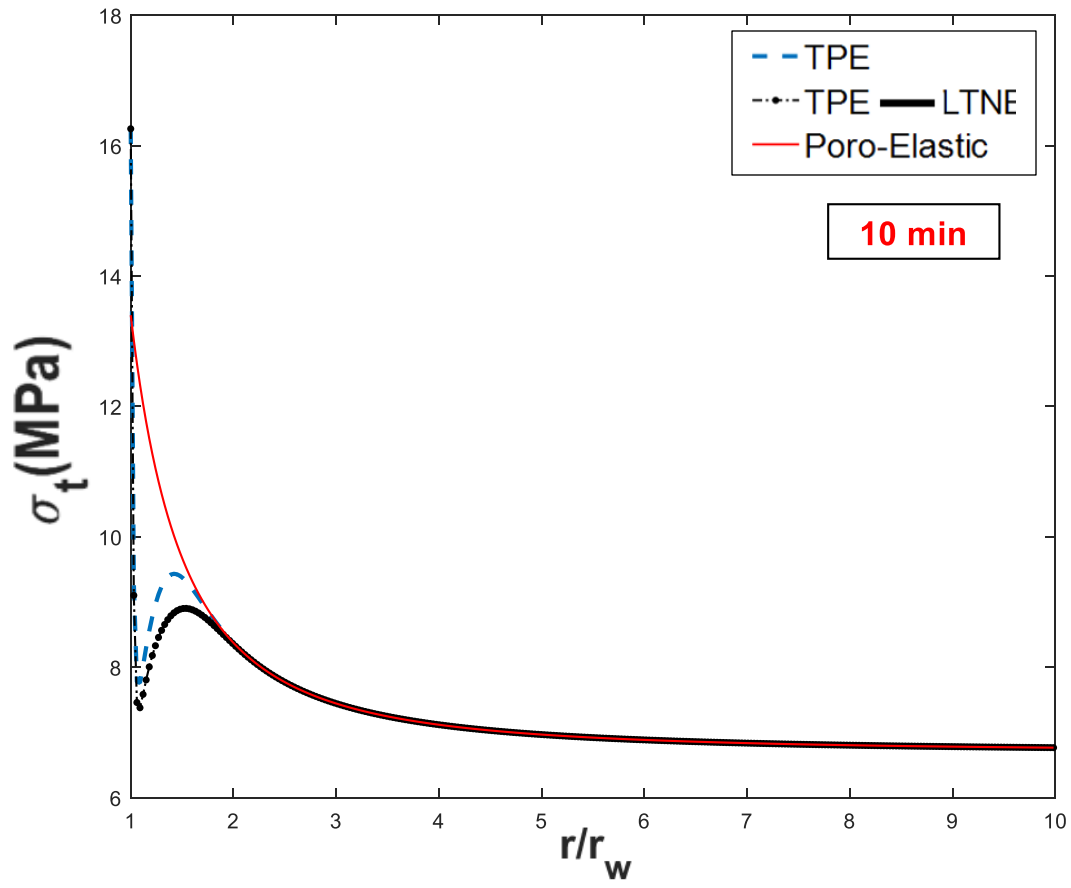
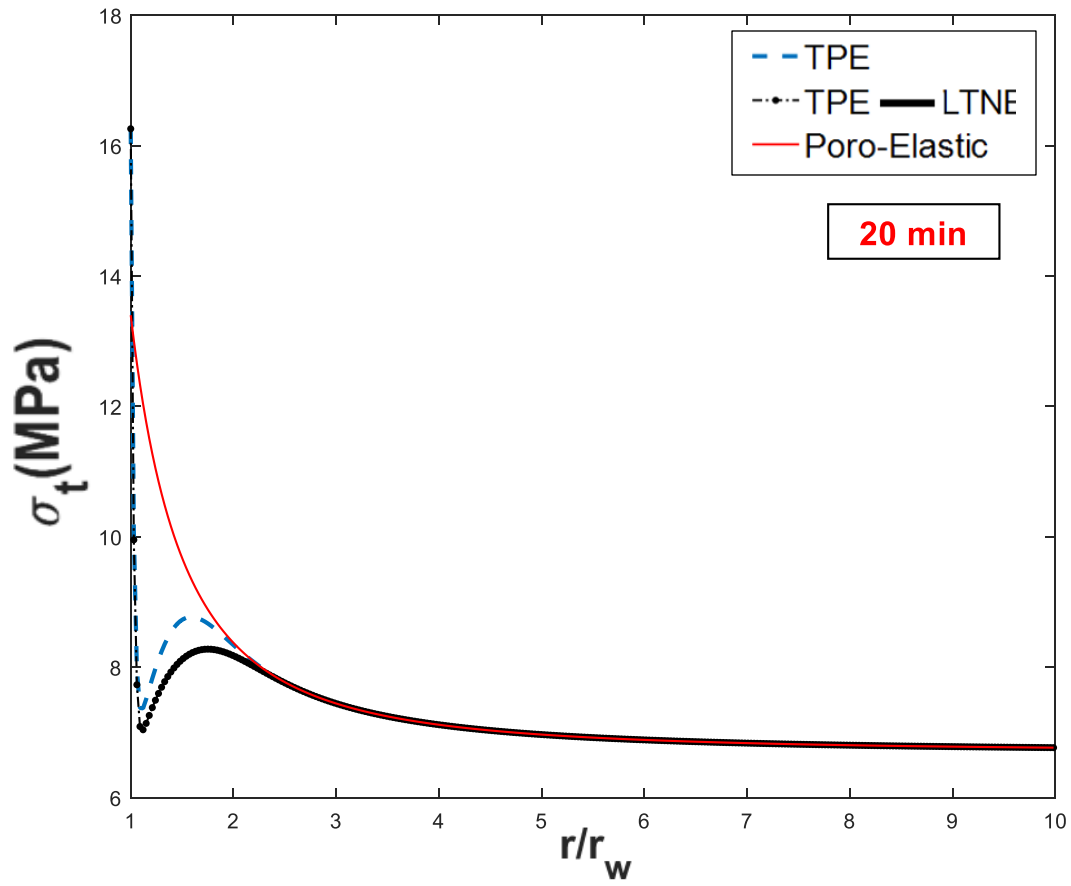
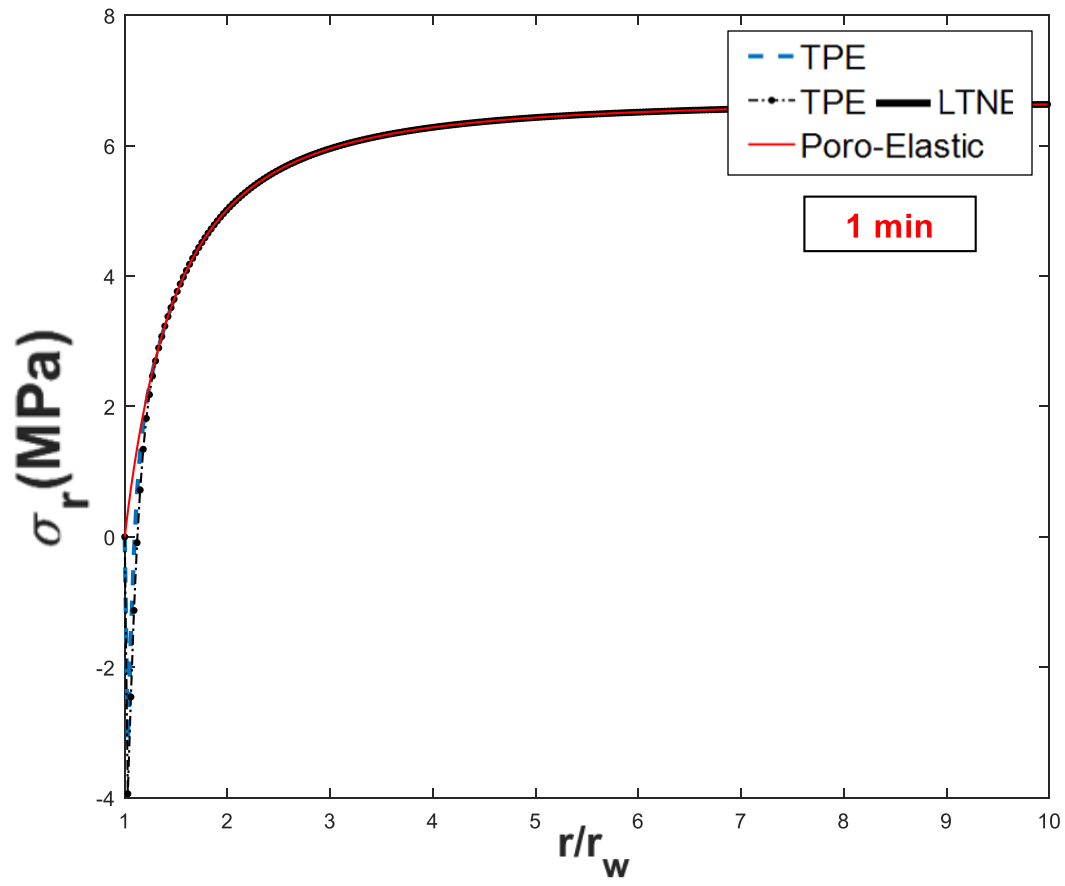


Figure 7.12



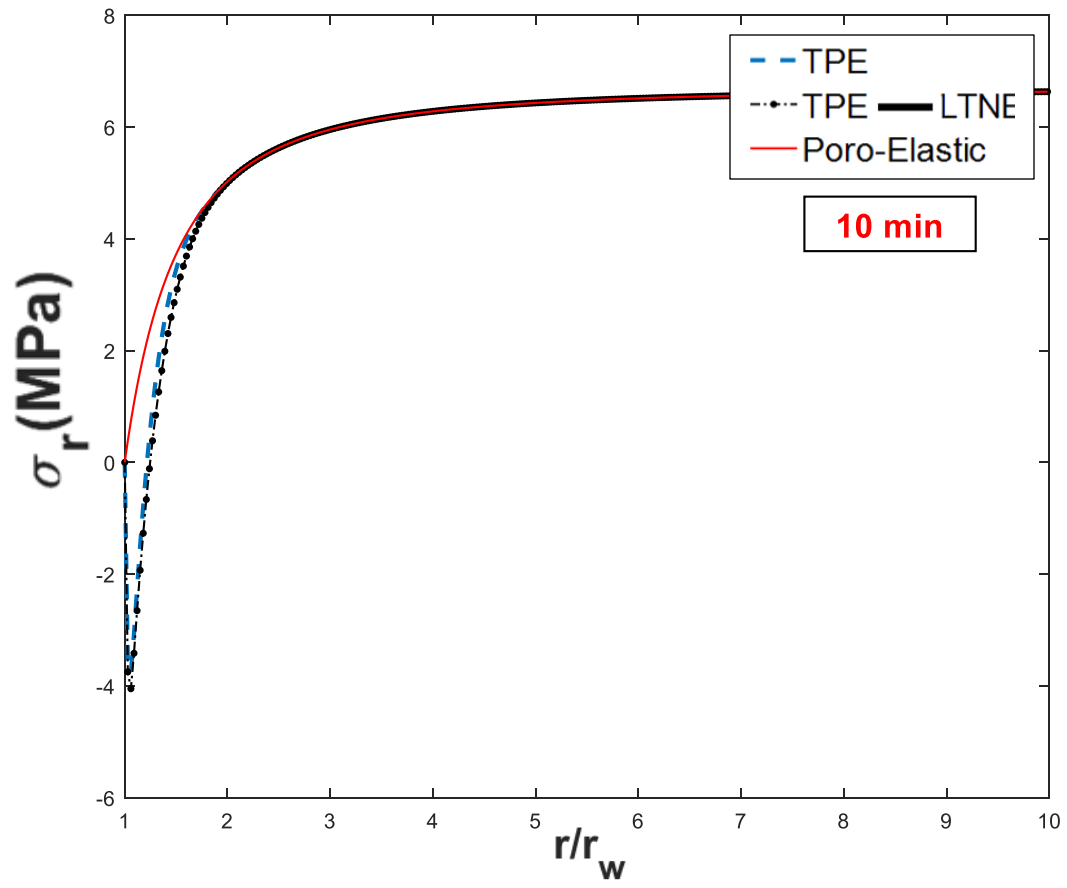
(c)

Figure 7. 12: Effective tangential stress along radial distance produced by different stress models under pure conductive heat transfer for (a) 1 min, (b) 10 min, and (c) 20 min. Red solid line: poroelastic model, blue dashed line: thermoporoelastic model, and black dotted line: thermoporoelastic model under LTNE condition



(a)

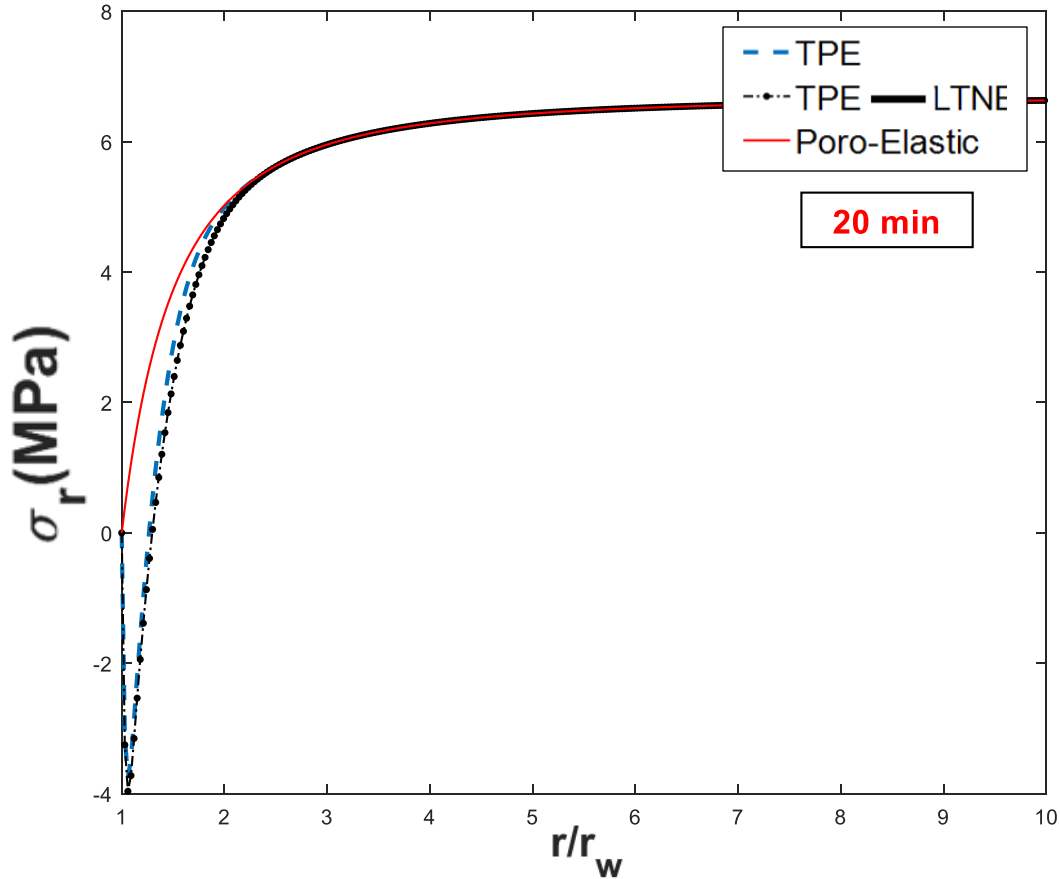
Figure 7.13



(b)

Figure 7. 13





(c)

Figure 7. 13: Effective radial stress along radial distance under pure conductive heat transfer (a) 1 min, (b) 10 min, and (c) 20 min

#### 7.4.2 Case 2: numerical solution for high permeable formation

This case is suitable for high permeability formation such as sandstone or high-pressure injection. The conductive and convective LTNE model is used in this example to update the thermoporoelastic model. As permeability becomes larger, the effect of thermal diffusion becomes smaller. The effects of LTNE are even more pronounced in high permeability formations as shown in Figures 7.14 and 7.15. Since the fluid inside the rock matrix can freely move, convective heat transfer dominates the heat transfer process, and

it changes the temperature profile greatly. This temperature change effect can be seen on the stress profiles. These disturbances change the mud weight window and wellbore stability analyses substantially. The LTNE model presents a more realistic physical implication of the system. The LTNE effect on radial stress is noticeable in a high permeable formation where convection is dominant compared to a low permeable formation where conduction heat transfer dominates.

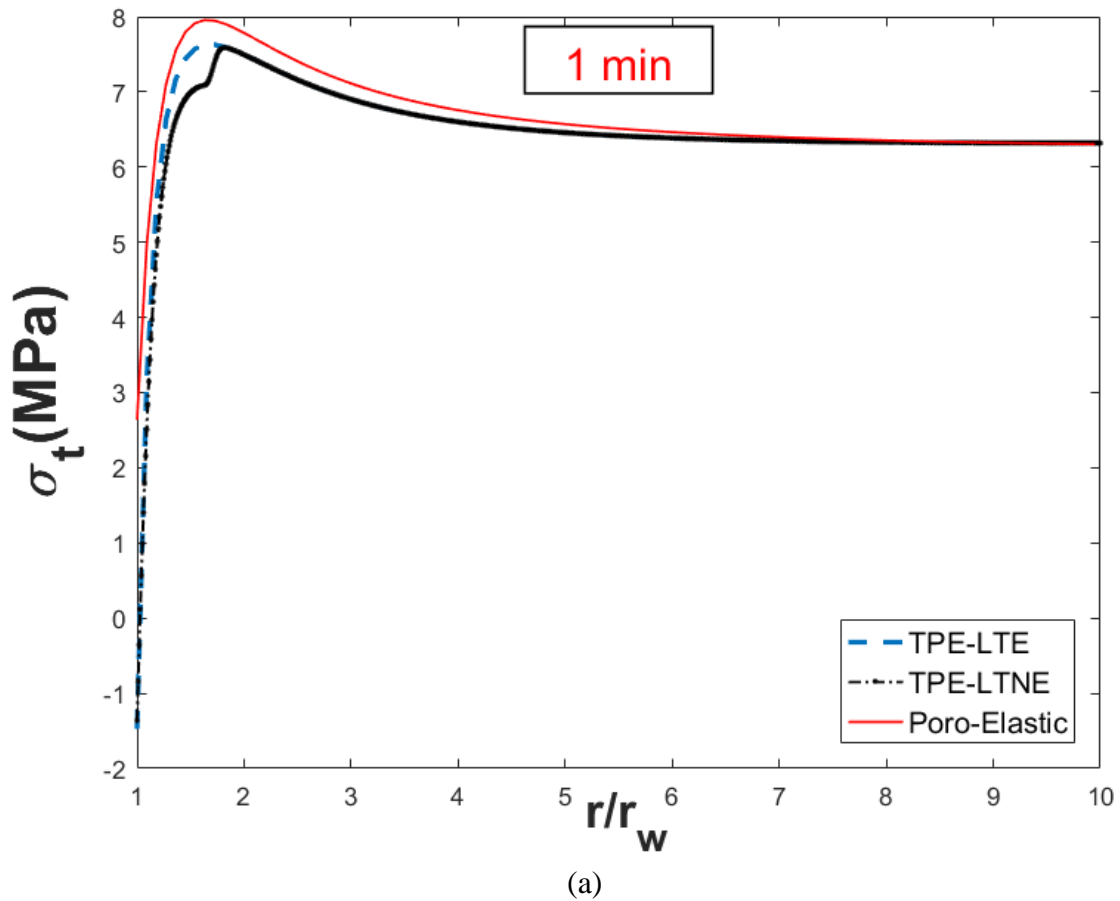


Figure 7. 14

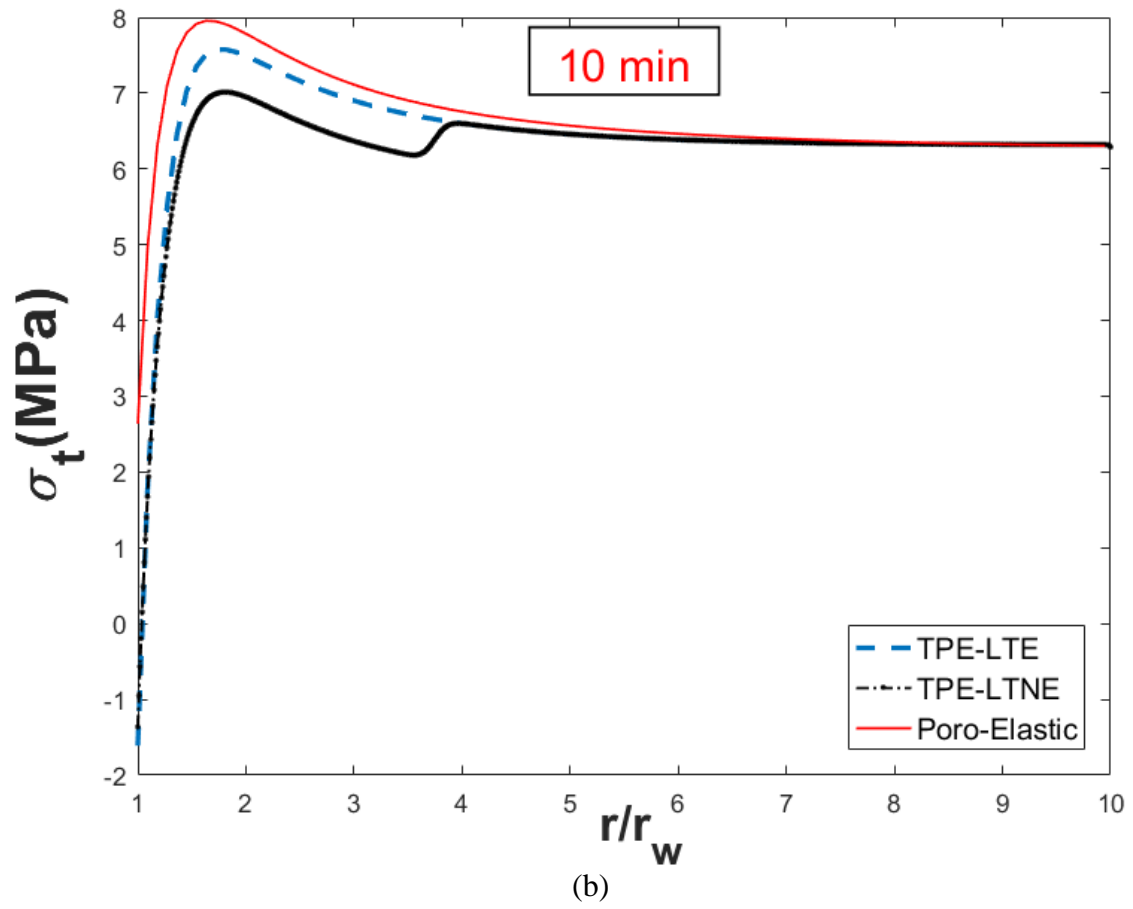
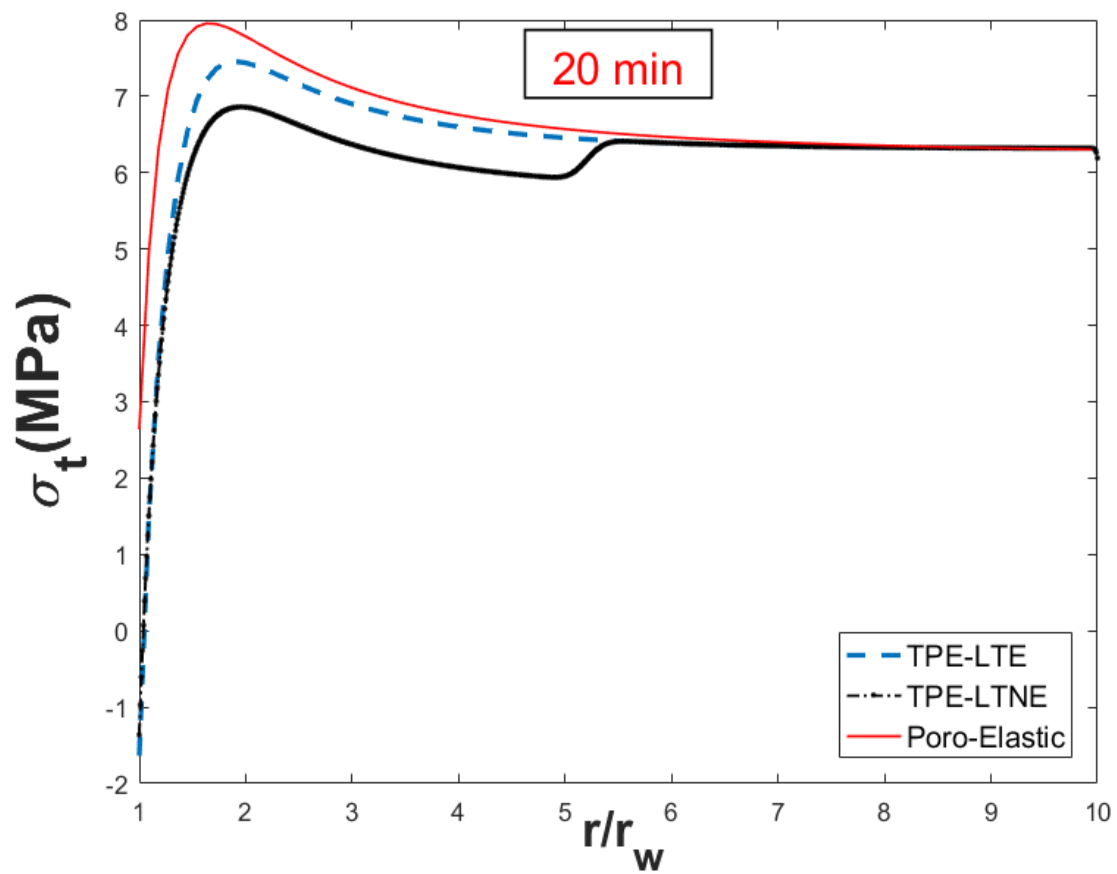
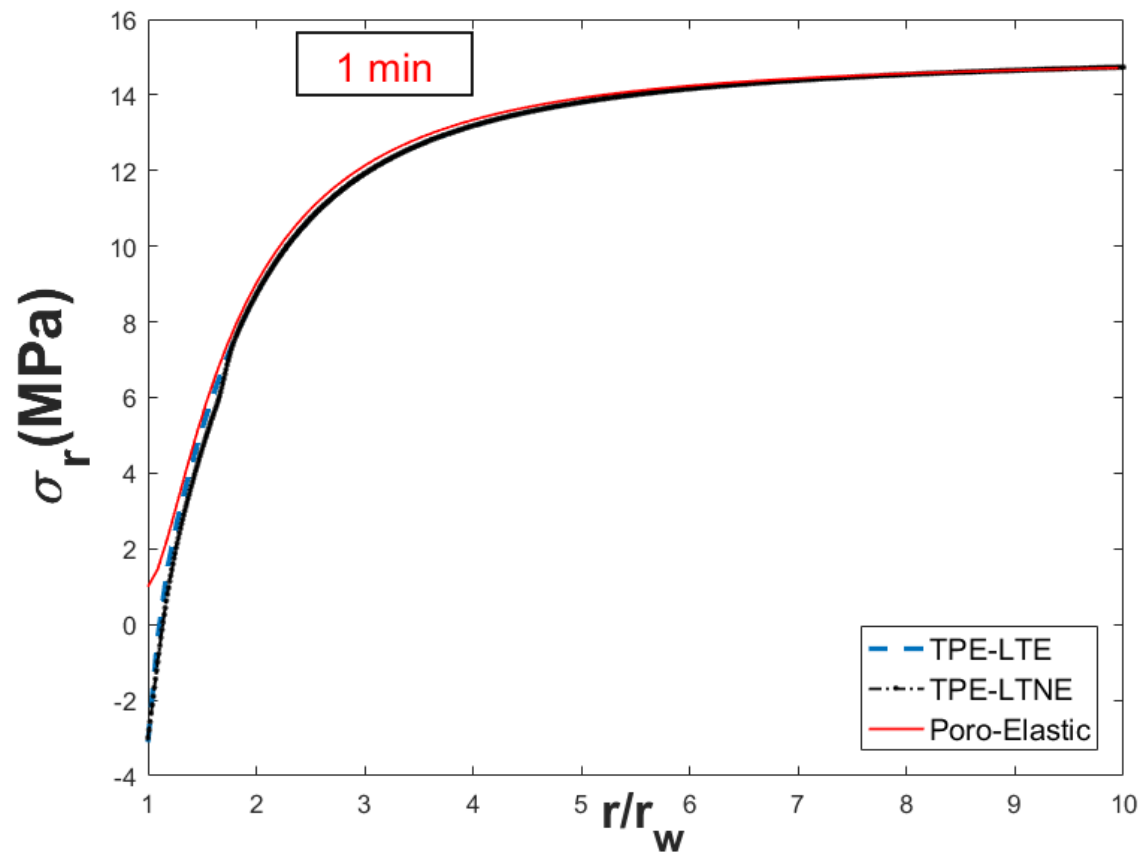


Figure 7.14



(c)

Figure 7. 14: Effective tangential stress along radial distance under both conductive and convective heat transfer mechanisms (a) 1 min, (b) 10 min, and (c) 20 min



(a)

Figure 7. 15

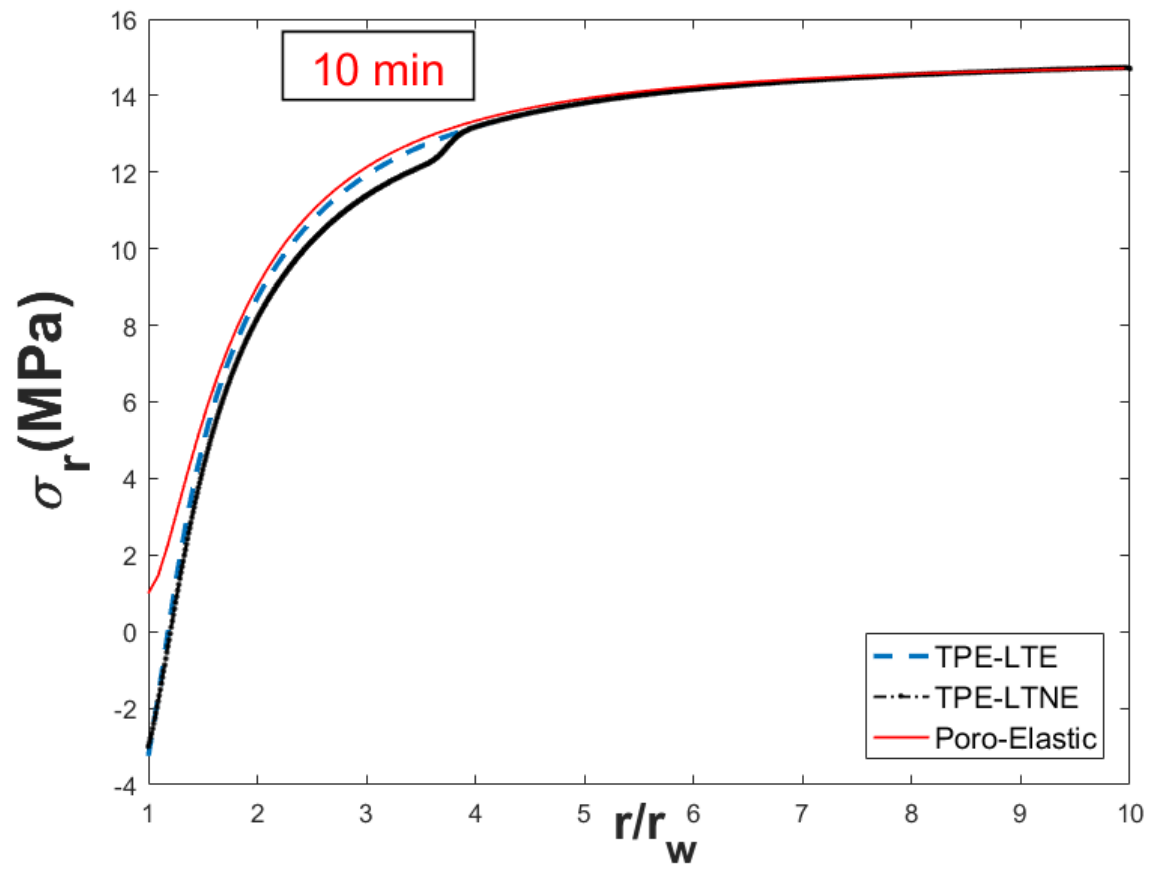
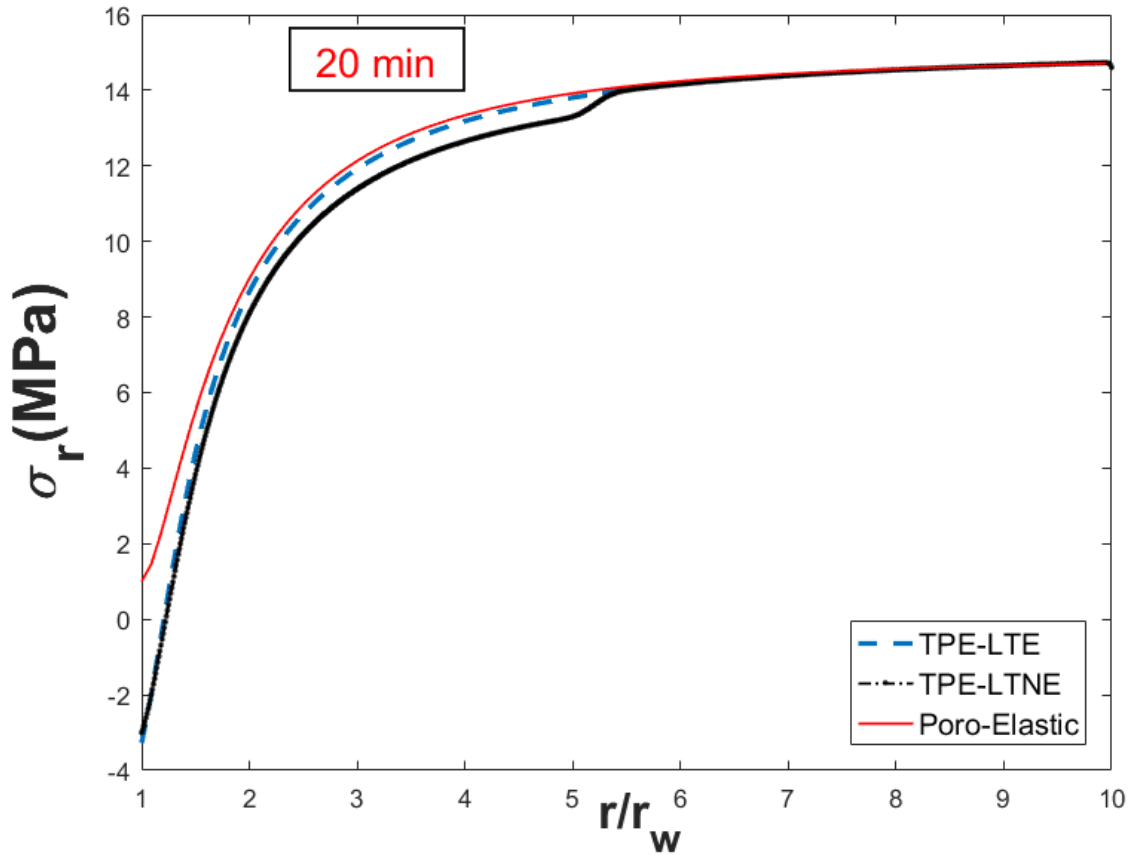


Figure 7. 15



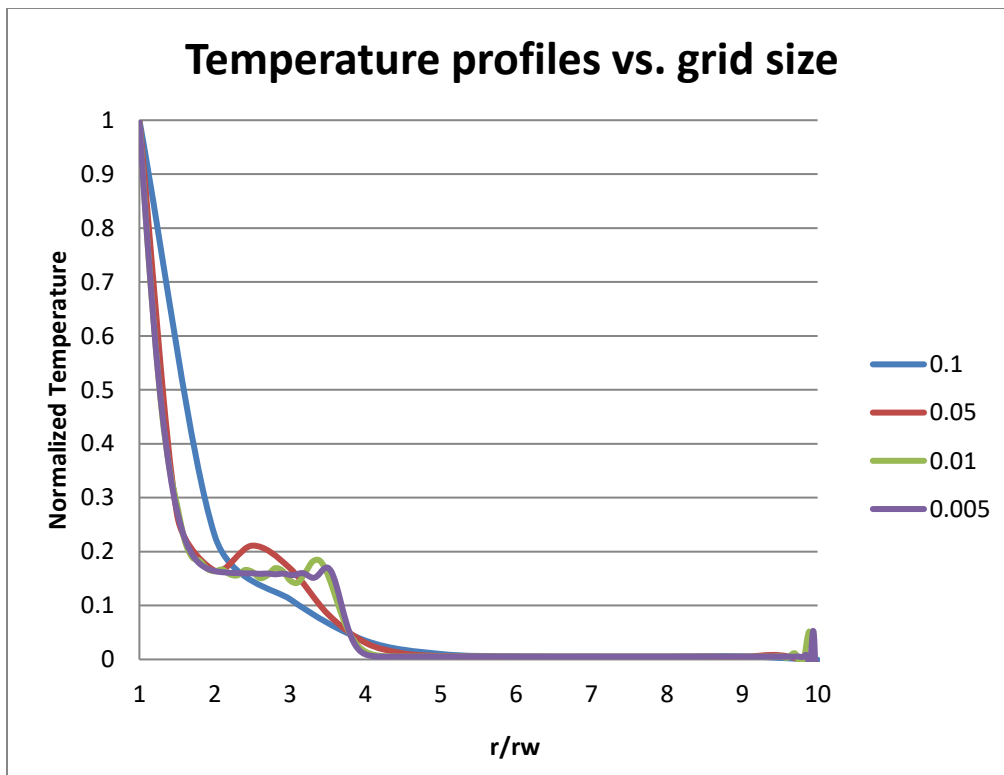
(c)

Figure 7. 15: Effective radial stress along radial distance under both conductive and convective heat transfer mechanisms (a) 1 min, (b) 10 min, and (c) 20 min

### 7.4.3 Remarks on numerical solution approach

Since some of the solutions are produced under a numerical approach, it is important to check if the solution converges. Since the numerical model for the convective heat transfer is an explicit simulation, divergence is expected using a large time step. An optimal grid size and time step must be found for the numerical scheme. The time for convective heat transfer simulation is calculated using the number of grids. For instance, if the grid length is 100, then the time will be equally spaced from the initial time to the last time in 100 segments. This way, the grid size needs to be optimized for simulation stability and convergence. Different grid sizes have been run to find the optimal value of the grid

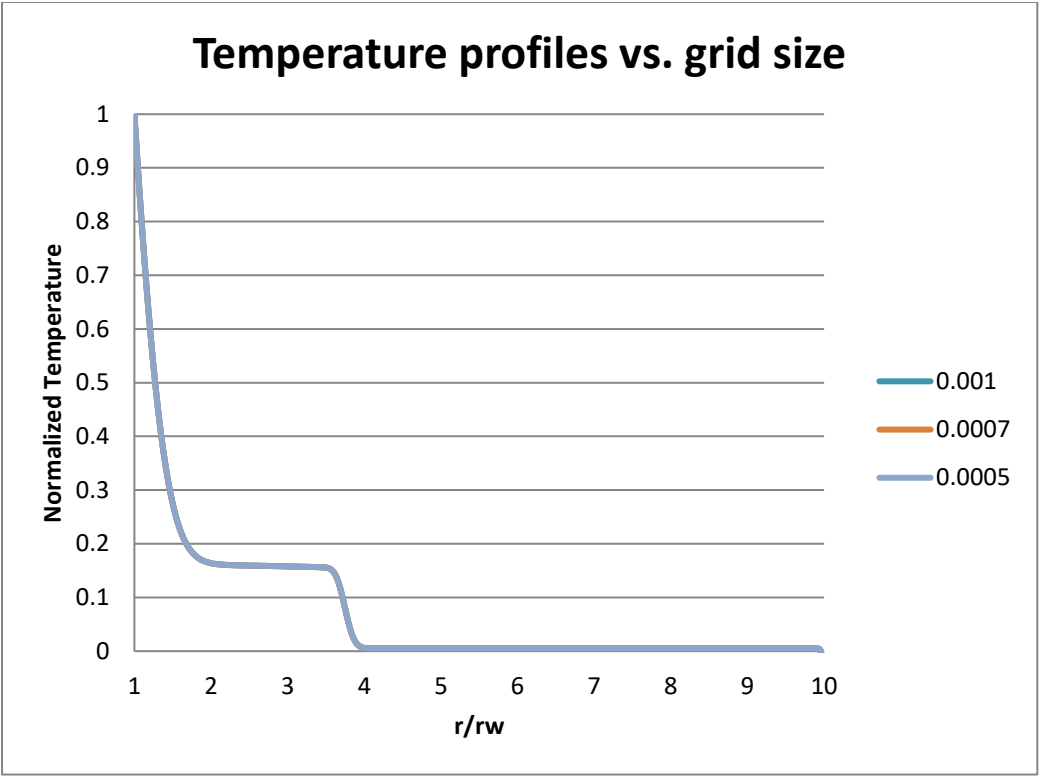
size for the simulation stability using result comparisons and norm analyses as shown in Figures 7.16 and 7.17. At large grid sizes, the solution is not stable as shown in Figure 7.16(a), but, as the grid size decreases solution is stable and reliable. The optimal grid size value is 0.001 for this simulation since any smaller grid size produces the same results as show in Figure 7.16(b). In these figures, the normalized temperature is the weighted average temperature given by equation (7.19). From the norm plot, it can be concluded that small grid sizes guarantee numerical convergence and stability. Grid size is the increment or step size that the simulation takes at each iteration from the wellbore wall (initial location) to reach the final boundary (last destination). Of course, smaller grid size may guarantee stability, but computational time increases substantially. Therefore, optimal value could be found through comparison or norm error analyses.



(a)

Figure 7. 16





(b)

Figure 7. 16: Effect of grid sizes on simulation results and convergence. (a) large grid sizes (b) small grid size

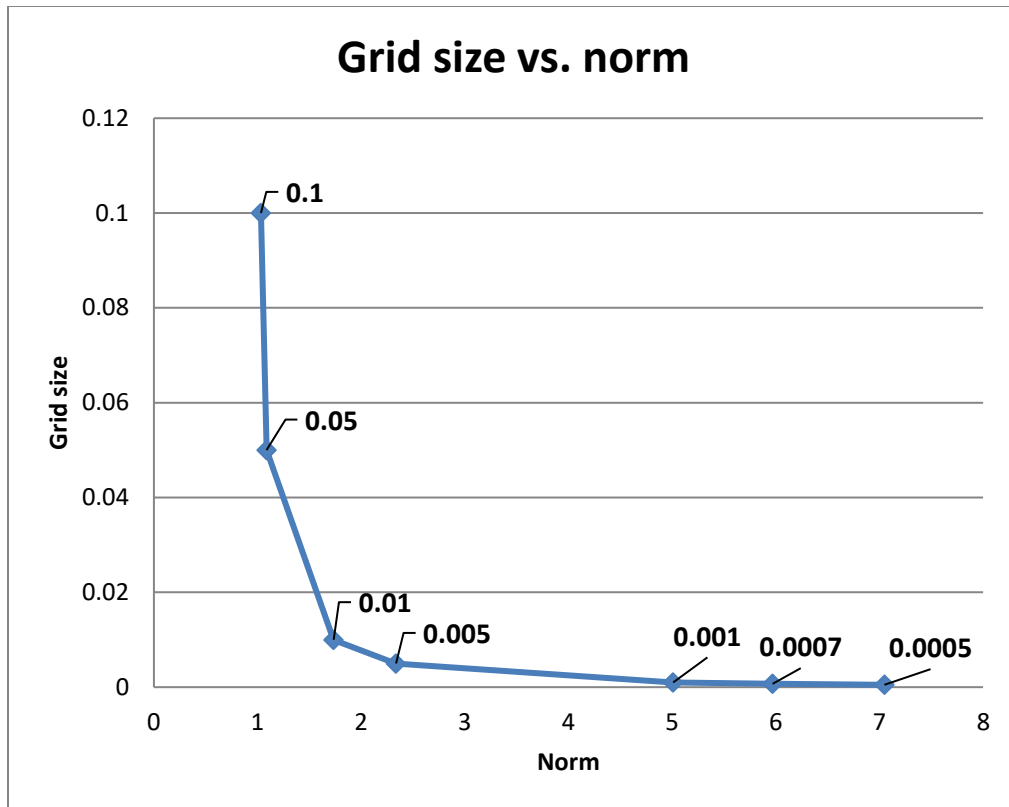


Figure 7. 17: Grid size effect on norm and simulation stability

## 7.5 CONCLUSIONS

It is believed that the LTNE effects are only important in formations where fluid flow is high enough that convective heat transfer dominates inside the medium, such as fractured formations or high permeability formations [104] [140] [141]. However, from the analyses shown in this chapter, it can be concluded that the effects of LTNE are important in any rock formations.

The LTE and LTNE effects for fully saturated porous media (rock formation) are considered in this chapter. Using LTNE approach, transient temperature profiles for solid (rock matrix) and fluid phases are defined. Using the weighted average method, a temperature for the porous medium is defined. The LTNE effects are examined around a circular hole in an infinite rock medium undergoing convective and conductive heat

transfers. The borehole boundary conditions such as temperature and fluid velocity were uniform throughout the investigations.

The Laplace transform method was employed, along with Stehfest algorithm for the LTNE solution to develop an exact solution. MATLAB numerical partial differential equation solver, pdepe, was utilized for the LTNE solution in permeable formation where convective heat transfer dominates. Under conductive and convective heat transfers two dominant heat transfer regions are developed inside porous media. These regions are separated by an intersection point, called thermal equilibrium point. Convective heat transfer dominates when temperature of fluid phase is greater than solid phase temperature.

It is concluded that LTNE effects can influence temperature profiles. This means that the pore pressure and stress profile around a wellbore can also be influenced due to induced temperature and fluid flow caused by LTNE effects. It was noted that properties of a porous medium significantly influence the effects of LTNE. For instance, heat transfer coefficient of a media can maximize or minimize the effects of LTNE.

Table 7. 1: Properties for the LTNE model

<b>Parameter</b>	<b>Rock Matrix</b>	<b>Fluid</b>
Thermal Conductivity, $k$ (w/m/ Kelvin)	2.4	0.6
Density, $\rho$ ( $\text{kg/m}^3$ )	2600	1000
Specific Heat Capacity, $c$ (J/kg/ Kelvin)	920	4200
Heat Transfer Coefficient, $h$ ( $\text{w/m}^2/\text{ Kelvin}$ )	50	
Porosity, $\phi$	0.4	
wellbore radius, $a$ (m)	0.1	
$\Theta_w$	1	

## **CHAPTER 8: CONCLUSIONS AND RECOMMENDATIONS**

### **8.1 CONCLUSIONS**

Prediction of thermoporoelastic behavior is important for wellbore stability during drilling, completion, and production of oil and gas wells. Coupled thermoporoelastic behavior is one of the complex phenomena in rock mechanics. This dissertation aimed at development of fully coupled thermoporoelastic models with local thermal non-equilibrium suitable for shale and sandstone formations. The developed models along with failure criteria qualitatively investigated the impact of induced thermal stresses on wellbore stability.

The coupled thermoporoelastic models in this dissertation were developed for wellbores with any orientations experiencing non-isothermal drilling conditions. The role of thermal stress on wellbore failures such as breakout and breakdown were investigated through several examples. The model also considers the effect of local thermal non-equilibrium condition (LTNE). The LTNE effects on the thermoporoelastic models were also investigated with examples.

It is concluded that for low permeable formations, where conduction dominated the heat transfer, the hoop stress minimum and maximum may occur away from the wellbore walls. For permeable formation, it may be assumed that the fluid diffusion reaches steady state before the temperature begins to change, and the effect of thermal diffusion becomes small. Therefore, that heat transfer is dominated by hydraulic diffusion. In this dissertation, it is concluded that the effect of temperature on stress around the wellbore is very important to consider. Thermally induced stress can change stress concentration around the wellbore and affect the likelihood of shear and tensile failures. When a wellbore is cooled down, hoop stress will be lowered, therefore, the stability with respect to shear failure increases, while tensile failure increases.

LTE and LTNE effects for fully saturated porous media (rock formation) are considered in this dissertation. Using LTNE, transient temperature profiles for solid (rock matrix) and fluid phases are defined. Using the weighted average method, a temperature for the porous medium is defined. LTNE effects are examined around a borehole in an infinite rock medium undergoing convective and conductive heat transfers. It is believed that the LTNE effects are only important in formations where fluid flow is high enough that convective heat transfer dominates inside the medium, such as fractured formations or high permeability formations. However, from the analyses shown in this dissertation, it can be concluded that the effects of LTNE may be important in any rock formations.

The LTNE effects can influence temperature profiles. This means that the pore pressure and stress profiles around a wellbore can also be influenced due to induced temperature by the LTNE effects. It is noted that properties of a porous medium significantly affect the LTNE effects. For instance, heat transfer coefficient of a media can maximize or minimize the effects of LTNE.

## **8.2 RECOMMENDATIONS**

The following recommendations are made for future development based on the current models:

- Pore volume expansion behavior in non-isothermal condition is not fully understood in sandstone and shale formations. This parameter is very critical in accuracy of thermoporoelastic model. further lab experiments are required in investigation of pore volume expansion behavior.
- The significance of local thermal non-equilibrium effect depends on the value of heat transfer coefficient. This parameter has a wide range of values in rock samples. There are several empirical correlations predicting the

value of heat transfer coefficient. However, further lab investigations are needed to establish the values of this parameter in different rock formations. This parameter also has a dependency on fluid flow. The current LTNE model developed in this dissertation assumes a constant value. A dynamic LTNE model where heat transfer coefficient is coupled with fluid flow may be necessary.

- The models in this dissertation are based on linearly elastic, homogenous, and isotropic materials behaviors, but rarely a rock will behave perfectly in such manners. For improvements, rock non-linearity, plasticity, and anisotropy should be coupled with the current models.
- The assumption of one dominant heat transfer was invoked in the modeling to relax the coupling, so finding the solution became straightforward. The next model should utilize finite element modeling without relaxing the coupling conditions.
- The fully coupled diffusivity equations in this dissertation are modeled in radial direction only. Investigation of dependency and results of these equations in axial and tangential directions would be important in development of future thermoporoelastic model.
- A uniform temperature distribution was assumed along the borehole. In reality, due to circulation of mud, the temperature inside the borehole changes with time. The development of a transient borehole temperature distribution and incorporation of such a model into the thermoporoelastic models would be an important improvement to the current work.
- Results are based on theoretical modeling in this dissertation. Validation of the results and model via laboratory experiments are vital and necessary.

- Mechanical in-situ stress, pore pressure, and induced thermal stress are considered in the development of the thermoporoelastic models presented in this dissertation. However, chemical effect has a major role in stress alteration around a wellbore and wellbore stability, especially in water sensitive shale formations. Coupling the current thermoporoelastic models with the chemical effect would be a great deal of enhancement.
- Mud cake buildup on the wellbore wall will reduce the permeability near the wellbore region and fluid flow into the formation. In turn, it dictates heat transfer mechanism. It is important to incorporate mud cake evolution in the future modeling.

## APPENDIX

This section contains a brief overview of Carslaw and Jaeger [110], the Laplace transformation: on problems of a cylinder.

The temperature profile for a circular hole in an infinite medium with zero initial temperature and constant temperature,  $V$ , on the surface of the hole is given by:

$$\frac{d^2\bar{V}}{dr^2} + \frac{1}{r} \frac{d\bar{V}}{dr} - \frac{s}{K} \bar{V} = 0, \quad r > a \quad (\text{A.1})$$

where  $\bar{V}$  is the temperature in Laplace domain and  $a$  is the radius of the hole. Equation (A.1) is a modified Bessel function of zeroth order, and its solution is:

$$\bar{V} = C_1 I_0\left(\sqrt{\frac{s}{K}}r\right) + C_2 K_0\left(\sqrt{\frac{s}{K}}r\right) \quad (\text{A.2})$$

where  $I_0$  and  $K_0$  are the modified Bessel functions of first kind and second kind of zeroth order, respectively.  $C_1$  and  $C_2$  are constants and can be found using the boundary conditions. As  $r$  increases in equation (A.2), the solution approaches infinity which is not possible physically since the temperature is finite as  $r \rightarrow \infty$ . Therefore, the constant ( $C_1$ ) in the first term of equation (A.2) must be zero, and (A.2) will become:

$$\bar{V} = C_2 K_0\left(\sqrt{\frac{s}{K}}r\right) \quad (\text{A.3})$$

Only one boundary condition is required to solve the second constant. This would be the boundary temperature at the hole.  $V$  is the temperature at the hole boundary. After applying this boundary condition, the solution is:

$$\bar{V} = \frac{VK_0\left(\sqrt{\frac{s}{K}}r\right)}{sK_0\left(\sqrt{\frac{s}{K}}a\right)} \quad (\text{A.4})$$

The solution is for an isotropic and homogeneous medium made of one material. If the medium has more than one material or phases, superposition can be employed. For



example, in this study, there is a medium of two phases, rock matrix and fluid. Therefore, equations (7.17) and (7.18) are the results of this technique.

## REFERENCES

1. Kang, Y., Yu, M., Miska, S. Z., & Takach, N. Wellbore Stability: A Critical Review and Introduction to DEM, 2009
2. Li, X. Thermoporoelastic Modeling of Inclined Boreholes. Ph.D. dissertation, University of Oklahoma, Oklahoma, USA, 1998
3. Pickens, J.F., Grisak, G.E., Avis, J.D., Belanger, D.W., and Thury, M. Analysis and Interpretation of Borehole Hydraulic Tests in Deep Boreholes: Principle, Model Development, and Application. *Water Resources Research*, 23 (7), 1341-1375, 1987
4. Shadravan, A. and Amani, M. HPHT 101-What Petroleum Engineers and Geoscientists Should Know About High Pressure High Temperature Wells Environment. *Energy Sci & Tech (CS Canada)*, 4 (2), pp. 36-60, 2012
5. Hubbert, M. K. and Willis, D. G. Mechanics of Hydraulic Fracturing. *JPT, Trans. AIME*, 210, pp. 153-166, 1957
6. Kirsch, E.G. Die Theorie der Elastizität und die Bedürfnisse der Festigkeitslehre, *Zeitschrift des Vereines deutscher Ingenieure*. 42, pp. 797- 807, 1898
7. Fairhurst C. Methods of Determining In-Situ Rock Stresses at Great Depth. Technical Report TRI-68 Missouri River Div. Corps of Eng., 1968
8. Bradley, W. B. Failure of Inclined Boreholes. *J. Energy Res. Tech. Transactions of ASME*, 101, pp. 232-239, 1979
9. Haimson, B.C. and Fairhurst, C. Initiation and Extension of Hydraulic Fractures in Rocks. *SPE Journal*, 7, pp. 310-318, 1967
10. Biot, M. A. General Theory of Three-Dimensional Consolidation. *J. Appl. Phys.*, 12, 155-164, 1941

11. Detournay E. and Cheng, A. H. D. Poroelastic Response of a Borehole in a Non hydrostatic Stress Field. *Intl. J. Rock Mech. Min. & Geomech. Abstract*, 25 (3), pp. 171-182, 1988
12. Cui, L., Cheng, A. H. D., and Abousleiman, Y. Poroelastic Solution for an Inclined Borehole. *J. Appl. Mech, Transactions of ASME*, 64, pp. 32-38, 1997
13. Bradford, L. D. R. and Cook, J. M. A Semi-Analytical Elastoplastic Model for Wellbore with Applications to Sanding. *Rock Mechanics, Petroleum Eng., Proc. Of Eurock'94, Rotterdam*, 1994
14. McLellan, P. J. and Wang, Y. Predicting the Effects of Pore Pressure Penetration on the Extent of Wellbore Instability: Application of a Versatile Poro-elastoplastic Model *Rock Mechanics, Petroleum Eng., Proc. Of Eurock'94, Rotterdam*, 1994
15. Goodman, R. E. and St John, C. M. Finite Element Analysis for Discontinuous Rocks. *Numerical Methods in Geotechnical Eng.*, pp 148-175, 1977
16. Goodman, R. E. and Shi, G. *Block Theory and Its Application to Engineering*. Prentice-Hall, Englewood, NJ, 1985
17. Cundall, P. A. A Computer Model for Simulating Progressive Large Scale Movements in Blocky Rock Systems. *Proc. Symp. Of the Intl. Soc. Of Rock Mech.* 11-8, 1971
18. Fjær, E., Holt, R.M., Horsrud, P., Raaen, A.M., and Risnes, R. *Petroleum Related Rock Mechanics*. 2<sup>nd</sup> edition, *Development in Petroleum Science* 53, Elsevier, 2008
19. Morita, N., and Gray, K.E. A Constitutive Equation for Nonlinear Stress-Strain Curves In Rocks And Its Application To Stress Analysis Around A Borehole During Drilling. *SPE 55th Annual Technical Conference and Exhibition, Dallas, Texas, USA* 1980
20. Santarelli, F.J., Brown, E.T., and Maury, V. Technical Note Analysis of Borehole Stresses Using Pressure-dependent, Linear Elasticity. *Intl. J. Rock Mech. Min. and Geomech*, 23 (6) pp. 445-449, 1986

21. Zoback M. D., Moos D., Mastin L. and Anderson R. N. Wellbore breakouts and in situ stress. *J. Geophys. Res*, 90, pp 5523-5530, 1985
22. Kaiser, P.K., Guenot, A., and Morgensntern, N.R. Deformation of Small Tunnels-IV. Behavior During Failure. *Int. J. Rock Mech. Min. and Geomech*, 22 (3) pp. 141-152, 1985
23. Geertsma J. Some Rock Mechanical Aspects of Oil and Gas Well Completions. *SPE Journal*, 25 (6), 1985
24. Rawlings, C. G., Barton, N. R., Bandis, S. C., Addis, M. A., and Gultierrez, M. S. Laboratory and Numerical Discontinuity Modeling of Wellbore Stability. *JPT*, 45 (11) pp. 1086-1092, 1993
25. Veeken, C. A. M., Walters, J. V., Kenter, C. J., and Davis, D. R. Use of Plasticity Models for Predicting Borehole Stability. In *Rock at great depth*, Rotterdam, 1989
26. Kim, J. and Moridis, G.J. Numerical Analysis of Fracture Propagation during Hydraulic Fracturing Operations in Shale Gas Systems. *Rock Mechanics and Mining Science Journal*, 76, pp. 127-137, 2015
27. Stanchits, S., Burghardt, J., and Surdi, A. Hydraulic Fracturing of Heterogeneous Rock Monitored by Acoustic Emission. *Rock Mechanics and Rock Engineering Journal*, 48 (6): 2513-2527, 2015
28. Yang, T.H., Tham, L.G., Tang, C.A., Liang, Z.Z., and Tsui, Y. Influence of Heterogeneity of Mechanical Properties on Hydraulic Fracturing in Permeable Rocks. *Rock Mechanics and Rock Engineering Journal*, 37 (4), pp. 251-275, 2004
29. Schiffman, R. L. A Thermoelastic Theory of Consolidation. *Environmental Geophysics and Heat Transfer*. 4, 78, 1971
30. Booker, J. R. and Savvidou, C. Consolidation Around a Spherical Heat Source. *Intl. J. Solid Structures*, 20, pp. 1079-1090, 1984

31. Booker, J. R. and Savvidou, C. Consolidation Around a Point Heat Source. *Intl. J. Num. Anal. Method in Geomech.*, 9, pp. 173-184, 1985
32. Seneviratne, H. N., Carter, J. P., and, Booker, J. R. Analysis of Fully Coupled Thermomechanical Behavior Around a Rigid Cylindrical Heat Source Buried in Clay. *Intl. J. Num. Anal. Mech. Geomech.*, 17, pp. 715-733, 1993
33. Bear, J. and Corapcioglu, M. Y. A Mathematical Model for Consolidation in a Thermoelasticity Aquifer due to Hot Water Injection or Pumping. *Water Resources Research*, 17 (3), pp. 723-736, 1981
34. Herbert, G. W. Cold Waterflooding a Warm Reservoir. *SPE 5083*, 1974
35. Hojka, K. Dusseault, M. B., and Bogobowicz A. D. Analytical Solution for Transient Thermoelastic Stress Fields Around a Borehole during Fluid Injection into Permeable Media. *J. Canadian Petroleum Tech.*, 32 (4), pp. 49-57, 1993
36. Wang, Y., Papamichos, E., and Dusseault, M. B. Thermal Stresses and Borehole Stability. *Rock Mechanics, Tools and Techniques*, 2, pp. 1121-1127, 1994
37. Lewis, R. W. A Coupled Finite Element Model for the Consolidation of Non Isothermal Elastoplastic Porous Media. *Transport in Porous Media*, 1, pp. 155-178, 1986
38. Smith, D. W. and Booker, J. R. Green's Functions for a Fully Coupled Thermoporoelastic Material. *Intl. J. Num. Anal. Meth. Geomech.*, 17, pp. 139-163, 1993
39. McTigue, D. F. Flow to a Heated Borehole in Porous, Thermoelastic Rock: Analysis. *Water Resources Research*, 26 (8), pp. 1763-1774, 1990
40. Nowinski. J. L. *Theory of Thermoelasticity with Applications*. Sijthoff and Noordhoff Intl. publishers, Alphen ann den Rijn, 1978
41. Somerton W.H. *Thermal Properties and Temperature-Rated Behaviors of Rock/Fluid System*. Elsevier Science Publishers, 1992

42. Mercer, J. W. and Faust, C. R. A Review of Numerical Simulation of Hydrothermal Systems. *Hydrological Science Bulletin*, 24 (3), 1979
43. Chin L., Boade, R. R., Prevost, J. H., and Landa, G. H. Numerical Simulation of Shear-Induced Compaction in the Ekofisk Reservoir. *Intl. J. Rock Min. Sci. & Goemch. Abstract*, 30 (7) pp. 1193-1200, 1993
44. Hanse, K. S., Prats, M., and Chan, C. K. Finite-Element Modeling of Depletion Induced Reservoir Compaction and Surface Subsidence in the South Belridge Oil Field, California. SPE 2607, Western Regional Meeting, Anchorage, 1993
45. Lewis, R. W., Roberts, G. K., and Zienkiewicz, O. C. A Non-Linear Flow and Deformation Analysis of Consolidation Problems. *Proc. 2<sup>nd</sup> Intl. Conf. Num Meth. Geom.* pp. 1106-1118, Blacksburg, 1976
46. Ghalambor, A., Salehi, S., and Shahri, M. Integrated Workflow for Lost Circulation Prediction. SPE, International Petroleum Conference and Exhibition in Lafayette, LA, USA, 2014
47. Salehi, S. and Nygaard, R. Numerical Modeling of Induced Fracture Propagation: A Novel Approach for Lost Circulation Materials (LCM) Design in Borehole Strengthening Applications of Deep Offshore Drilling. SPE, Annual Technical Conference and Exhibition, San Antonio, TX, USA, 2012
48. Pasic, B., Gaurina-Medimurec, N., and Matanovic, D. Wellbore Instability: Causes and Consequences. *Rudarsko-geološko-naftni zbornik*, 19, pp. 87-98, 2007
49. Dixon, M. Smectite/Illite Distribution and Diagenesis in the South Timbalier Area, Northern Gulf of Mexico. Master thesis, University of New Orleans, 2005
50. Osisanya, S.O. Practical Approach to Solving Wellbore Instability Problems. the 50th anniversary of the SPE Distinguished Lecturer program, 2012

51. Zoback, M.D., Barton, C.A., Brudy, M., Catillo, D.A., Finkbeiner, T., Grollmund, B.R., Moos, D.B., Peska, P., Ward, C.D., and Wiprut, D.J. Determination of Stress Orientation and Magnitude in Deep Wells. *Intl J. of Rock Mech & Min Sci*, 40, pp. 1049-1076, 2003
52. Barton, C.A., Discrimination of Natural Fractures from Drilling-Induced Wellbore Failures in Wellbore Image Data-Implications for Reservoir Permeability. SPE, International Petroleum Conference and Exhibition in Mexico held in Villahermosa, Mexico, 2000
53. Soorush, H., Khlaifat, A., Qutob, H., Rasouli, V., and Tokhmchi, B. A New Approach to Identify Breakout Zones in Tight Gas Shale. SPE, Middle East Uncon. Gas Conf., Muscat, Oman, 2011
54. Feng, Y., and Gray, K.E. A Fracture-Mechanics-Based Model for Wellbore Strengthening Applications. *J. Natural Gas Sci. and Eng.*, 29 (2016) 392-400, 2016
55. Feng, Y., Arlanoglu, C., Podnos, E., Becker, E., Gray, K.E. Finite-Element Studies of Hoop-Stress Enhancement for Wellbore Strengthening. *SPE Drill. Complet.* 30, 38-51, 2015
56. Murchison, W.J. Lost Circulation for the Man on the Rig. Murchison Drilling Schools, Inc., 2006
57. Jin, X., Shah, S.N., Roegiers, J., and Hou, B. Breakdown Pressure Determination-A Fracture Mechanics Approach. SPE, ATCE, New Orleans, September, 2013
58. Siren, T. Suikkanen, J. Heikkinen, E., Valli, J., and Hakala, M. Determining the In-situ Stress with Thermally Induced Borehole Breakout. 13th ISRM, International Congress of Rock Mechanics. International Society for Rock Mechanics, 2015
59. Yan, C., Deng, J., Lai, X., Li, X., and Feng, Y. Borehole Stability Analysis in Deepwater Shallow Sediments. *ASME, J. Energy Res. Tech.*, 2014

60. Aadnoy, B. S., and Belayneh, M. Elasto-Plastic Fracturing Model for Wellbore Stability Using Non-Penetrating Fluids. *J. Pet. Sci. Eng.*, 45(3–4), 179–192, 2004
61. Zoback, M.D. *Reservoir Geomechanics*, Cambridge University Press, Cambridge, UK, 464p, 2007
62. Stephens, G. and Voight, B. Hydraulic Fracture Theory for Conditions of Thermal Stress. *Int. J. Rock Mech. Min. Sci. & Geomech.*, 19, pp. 279–284, 1982
63. Nowacki, W. *Thermoelasticity*. Addison-Wesley, Reading, MA, 1962
64. Kurashige, M. A Thermoelastic Theory of Fluid-Filled Porous Media Materials, *Int. J. Solids Structures*, 25 (9), pp. 1039-1052, 1989
65. Coussy, O. *Poromechanics*. John Wiley and Sons Ltd, West Sussex, England, 2004
66. Ritchie, R. H. and Sakakura A. Y. Asymptotic expansions of the heat conduction equation in internally bounded cylindrical geometry. *J. appl. Phys.*, 27, 1453–1459, 1956
67. Jaeger, J.C. The Solution of One-Dimensional Boundary Value Problems by the Laplace Trans-Formation. *The Mathematical Gazette*, 23, 253, 62–67, 1939
68. Schmitt, D.R., and Zoback, M.D. Diminished pore pressure in low porosity crystalline rock under tensional failure: apparent strengthening by dilatancy. *J. Geophysc. Res.* 97, pp. 273–288, 1992
69. Zhai, Z. and Abou-Sayed, A. Fully Coupled Chemical-Thermo-Poro Mechanical Effect on Borehole Stability, *SPE ATCE*, 14-17 June, 2011
70. Abousleiman, Y. and Ekbote, S. Solution for the Inclined Borehole in a Porothermoelastic Transversely Isotropic Medium. *ASME J. App. Mech.*, 72, 102-114, 2004
71. Tao, Q and Ghassemi, A. Poro-thermoelastic borehole stress analysis for determination of the in-situ stress and rock strength. *Geothermics*, 39, 250-259, 2010



72. Ewy, R.T. Wellbore-Stability Predictions by Use of a Modified Lade Criterion. SPE Drilling and Completion Journal, 14 (2), 85-91, June 1999
73. Walton, G., Kalenchuk, K.S., and Hume, C.D. Borehole Breakout Analysis to Determine the In-Situ Stress state in Hard Rock. ARMA, US RMGS, San Francisco, 2015
74. Chang, C., and Moore, C.J. Borehole Breakout Formation and Stress Estimation in Unconsolidated Deepwater Sediments. ARMA, US RMGS, Chicago, 2012
75. Gercek, H. Poisson's Ratio Values for Rocks. Int. J. Rock Mech. Min. Sci. & Geomech., 44, pp. 1–13, 2007
76. Vishal, V., Pradhan, S.P., Singh, T.N. Tensile Strength of Rock Under Elevated Temperature. Geotec. and Geol. Eng., 29 (6), 1127-1133, 2011
77. Medlin, W.L, and Masse, L. Laboratory Investigation of Fracture Initiation Pressure and Orientation. Soc. Petrol. Eng. J. 19, 129–144, 1979
78. Yew, C.H. and Weng, X. Mechanics of Hydraulic Fracturing, 2<sup>nd</sup> edition, Elsevier, Waltham, MA, USA, 2015
79. Gao, M. Jin, W., Zhang, R. Jing, X., Bin, Y., and Duan, H. Fracture Size Estimation Using Data from Multiple Boreholes. Intl. J. Rock Mech. & Min. Sci., 86, 29-41, 2016
80. Saad, M. H. Elasticity – Theory, Applications, and Numerics. 3<sup>rd</sup> edition, Academic Press of Elsevier, MA, USA, 2014
81. Hilderbrand, F. B. Advanced Calculus for Applications. 2<sup>nd</sup> edition, Prentice Hall, NJ, USA, 1976
82. Kreyszig, K. E. Advanced Engineering Mathematics, 8<sup>th</sup> edition, Wiley, NY, USA, 1999
83. Biot, M. A. Theory of Elasticity and Consolidation for a Porous Anisotropic Solid. J. Appl. Phys., 26, 182-185, 1955

84. Biot, M. A. Thermoelasticity and irreversible thermodynamics. *J. Appl. Phys.*, 27 (240), 1956
85. Gambolati, G. Mathematical Simulation of the Subsidence of Venice: 1. Theory. *Water Resources Research*, 9 (3), 1973
86. Rice, J. R. and Cleary, M. P. Some Basic Stress-Diffusion Solutions for Fluid Saturated Elastic Porous Medium with Compressible Constituents. *Rev. Geo phys. Space Phys.* 14, pp. 227-241, 1976
87. Cleary, M. P. Fundamental Solutions for Fluid-Saturated Porous Media and Application to Localized Rupture Phenomena. Ph.D. Dissertation, University Microfilms International, Ann Arbor, MI, 1976
88. Skempton, A. W. The Pore-Pressure Coefficients A and B. *Geotechnique*, 4 (4), pp. 143-147, 1954
89. Edmondson, T. Thermal Diffusivity of Sedimentary Rocks Subjected to Simulated Overburden Pressure. Master's Thesis, University of California, Berkeley, 1961
90. Woodside, W. and Messmer, J. Thermal Conductivity of Porous Media II: Consolidated Rocks. *J. Appl. Phys.* 32, pp. 1699-1706, 1992
91. Tikhomirov, T. Conductivity of Rocks and Their Relationship with Density, Saturation, and Temperature. *Neftianoe Khoziaistra*, 46 (4:36), 1968
92. Abdulagatov, I.M., Emirov, S.N., Abdulgatov, Z.Z, and Askerov, S.Y. Effects of Pressure and Temperature on the Thermal Conductivity of Rocks. *J chem Eng*, 51, pp. 22-33, 2006
93. Sweet, J. Pressure Effects on Thermal Conductivity and Expansion of Geologic Materials. Technical Report DOE Report # SAN 78-1991, 1978
94. Wong, T. and Brace, W. Thermal Expansion of Rocks: Some Measurements at High Pressure. *Tectonophics*, 57, pp. 95-117, 1979

95. Sorey, M. L. Numerical Modeling of Liquid Geothermal Systems. Geol. Surv. Prof. Pap. U.S., 1044D, 1978
96. Perry, R. H. Green, D. W., and Maloney, J. O. Perry's Chemical Engineer's Handbook, McGraw-Hill, Inc., NY, USA, 1984
97. Geertsma, J. The Effects of Fluid Pressure Decline on Volumetric Changes of Porous Rocks. Pet. Trans., AAIME, 210, pp. 331-340, 1957
98. Carrol, M. M. Mechanics Response of Fluid-Saturated Porous Material. In F.P.J. Rintott and B. Tabarrok, editors, Theoretical and Applied Mechanics, Proc. 15th IUTAM, NY, 1980
99. Cui, L. Poroelasticity with Application of Rock Mechanics, Ph.D. Dissertation, The University of Delaware, Newark, DE, 1995
100. Mackenzie, J. K. The Elastic Constants of a Solid Containing Spherical Holes, Proc. Phys. Soc, Section B, 63, pp. 2-11, 1950
101. Bourbie, T, Coussy, O., and Zinszner, B. Acoustics of Porous Media. 1987
102. Hassanzadegan, A., Guerizec, R., Reinsch, T., Blocher, G., Zimmermann, G., and Milsch, H. Static and Dynamic Moduli of Malm Carbonate: A Poroelastic Correlation. Pure and Applied Geophysics, 173 (8), pp. 2841-2855, 2016
103. Nur, A. and Byerlee J.D. An Exact Effective Stress Law for Elastic Deformation of Rock with Fluids. J. Geophys. Res, 76 (26), pp. 6414-6419, 1971
104. Lu, W. and Xiang, Y. Analysis of the Instantaneous Local Thermal Equilibrium Assumption for Heat Exchange between Rock Matrix and Fracture Water. Adv. Material Research, (594–597), pp. 2430–2437, 2012
105. Combarous, M. A. and Bories, S. A. Hydrothermal Convection in Saturated Porous Media, Adv. Hydroscience, 10, pp. 231-307, 1975

106. Vafai, K. and Sozen, M. Analysis of Energy and Momentum Transport for Fluid Flow through a Porous Bed, *J. Heat Transfer*, 112 (3), pp. 690-699, 1990
107. Nield, D., A. and Bejan, A. *Convection in Porous Media*, 3<sup>rd</sup> edition, Springer, Berlin, 2006
108. Eckert, E. R. G. and Drake, R. M. *Heat and Mass Transfer*, 2<sup>nd</sup> edition, R.E. Krieger Publishing Company, 1959
109. Robertson, E. C. *Thermal Properties of Rocks*. US DOI Geol. Surv., Report # 88-441, 1988
110. Carslaw, H.S. and Jaeger, J. C. *Conduction of Heat in Solids*, 2<sup>nd</sup> edition, Oxford, London, 1959
111. Stehfest, H. Algorithm 368: Numerical Inversion of Laplace Transforms, *Commun. ACM*, (13), pp. 47–49, 1970
112. Aadnoy, B.S. and Chenevert, M.E. Stability of highly Inclined Boreholes. *SPE Journal*, *SPE Drilling Engineering*, 1987
113. Hiramatsu, Y. and Oka, Y. Analysis of Stresses around a Circular Shaft or Drift Excavated in Ground in a Three-Dimensional Stress State. *J. Min. metall. Inst. Japan*, 78, (884) 93-98 1962
114. Jaeger, J.C., and Cook, N.G.W. *Fundamentals of Rock Mechanics*, Methuen Co. Ltd, London, UK, 1969
115. Drucker D. and Prager W. Soil Mechanics and Plastic Analysis or Limit Design. *Q Appl Math*, 10, pp.157-165, 1952
116. Al-Ajmi A.M., Zimmerman R.W. Relation between the Mogi and the Coulomb Failure Criteria. *Int J Rock Mech Min Sci*, 42 (3), pp. 431-439, 2005
117. Zhang L., Zhu H. Three-Dimensional Hoek–Brown Strength Criterion for Rocks. *J Geotech Geoenviron Eng ASCE*, 133 (9), pp. 1128-1135, 2007

118. Zhang, L., Cao, P., and Radha, K.C. Evaluation of Rock Strength Criteria for Wellbore Stability Analysis. *Intl J of Rock Mech & Min Sci.*, 47, pp. 1304-1316, 2009
119. Fenner, R. Untersuchungen zur Erkenntnis des Gebiegsdruckes. *Gluckauf*, pp. 681--715, 1938
120. Mortita, N. Whitfill, D. L., Massie, I., and Knudsen, T.W. Realistic Sand production Prediction: Numerical Approach. *SPE*, 1987
121. Muhlhaus, H.B. Stability of Deep Underground Excavations in Strongly Cohesive Rock. In *Proc. 6th ISRM cnogr*, pp. 1157-1161, 1987
122. Guenot A. and Santarelli, F.J. Borehole Stability: a New Challenge for an Old Problem. In C. et al. (eds), editor. *Key questions in rock mechanics*, pp. 453-460, 1988
123. Aadnoy, B.S., and Belayneh, M. Elasto-Plastic Fracturing Model for Wellbore Stability using Non-Penetrating Fluids. *J Pet Sci & Eng*, 45 (3-4), pp. 179-192, 2004
124. Roshan, H. and Oeser, M. A Comprehensive 3D Thermo-Chemo-Poroelastic Model for Evaluation of Borehole Stability in Chemically Active Rocks. *Asia Pacific Oil and Gas Conference and Exhibition*, 2011
125. Pepin, G., Gozalez, M. Bloys, B.J., Lofton, J., Schmidt, J., Naquin, C., and Scot, E. Effect of Drilling Fluid Temperature on Fracture Gradient: Field Measurement and Model Predictions. *NARMS*, Houston, TX, June 5-9, 2004
126. Zemansky, M.W., Abbot, M.M., and Ness, H.C. *Basic Engineering Thermodynamics*, 2<sup>nd</sup> edition., McGraw-Hill, New York, 1975
127. Chen, G. and Ewy, R. Thermoporoelastic Effect on Wellbore Stability. *SPE Journal*, 121-29 June, 2005
128. Wang, Y. and Papamichos, E. Conductive Heat Flow and Thermally Induced Fluid Flow around a Wellbore in a Poroelastic Medium. *Water Resource Research*, 30 (12), pp. 3375-3384, 1994

129. Alazmi, B. and Vafai, K. Analysis of Variable Porosity, Thermal Dispersion and Local Thermal Nonequilibrium on Free Surface Flows Through Porous Media, *ASME J. Heat Mass Trans.*, (126), pp. 389–399, 2004
130. Wang, K., Tavakkoli, F., Wang, S., and Vafai, K. Analysis and Analytical Characterization of Bioheat Transfer during Radiofrequency Ablation. *J. of Biomechanics*, (48), pp. 930–940, 2015
131. He, L., W., Jin. Z., H., and Zhang, Y. Convective Cooling/Heating Induced Thermal Stresses in a Fluid Saturated Porous Medium Undergoing Local Thermal Non-Equilibrium. *Intl. J. of Solids and Structures*, 49, pp. 748–758, 2012
132. Nield, D.A. Effects of Local Thermal Nonequilibrium in Steady Convection Processes in Saturated Porous Media: Forced Convection in a Channel. *Journal of Porous Media* 1, pp. 181–186, 1998
133. Kuznetsov, A. Non-Thermal Equilibrium Forced Convection in Porous Media, in Ingham and Pop (eds.), *Transport Phenomena in Porous Media*, pp. 103–130, Elsevier, Oxford, 1998
134. Rees, D., A., S. and Pop, I. Local Thermal Non-Equilibrium in Porous Media Convection, in Ingham and Pop (eds.), *Transport Phenomena in Porous Media III*, pp. 147–173, Elsevier, Oxford, 2005
135. He, L., W. and Jin. Z., H. A Local Thermal Nonequilibrium Poroelastic Theory for Fluid Saturated Porous Media. *J. of Thermal Stress*, (33), pp. 799–813, 2010
136. Yang, C., Kuwahara, F., Liu, W., and Nakayama, A. Thermal Non-Equilibrium Forced Convective Flow in an Annulus Filled with a Porous Medium. *The Open Transport Phenomena Journal*, 3, pp. 31–39, 2011

137. Zhang, G., Zhu, J., Li, J., and Wang, Q. The Analytical Solution of the Water-Rock Heat Transfer Coefficient and Sensitivity Analyses of Parameters. World Geothermal Congress, 2015
138. Dixon A. G. and Cresswell, D. L. Theoretical Predictions of Effective Heat Transfer Mechanisms in Regular Shaped Packed Beds. *AIChE Journal*, 25, pp. 663–676, 1979
139. Grangeot, G., Quintard, M. and Whitaker, S. Heat Transfer in Packed Beds: Interpretation of Experiments in Terms of One- and Two-Equation Models. *Heat Transfer, Inst. Chem. Engrs, Rugby*, 5, pp. 291–296, 1994
140. Shaik, A., R., Rahman, S., S., Tran N., H., and Tran, T. Numerical Simulation of Fluid-Rock Coupling Heat Transfer in Naturally Fractured Geothermal System. *Applied Thermal Engineering*, 31 (10). pp. 1600–1606, 2011
141. Ogino, F., Yamamura, M., and Yoshida, T. Heat transfer from Hot Dry Rock to Water Flowing through a Fracture Surrounded by Secondary Crack Network. *Geothermal Science and Technology*, 6, pp. 139–162, 1999
142. Zhu, T. GEOL 615 Course, Some Useful Numbers on the Engineering Properties of Materials (Geologic and Otherwise)
143. Gandomkar, A and Gray, K.E. Local Thermal non-Equilibrium in Porous Media with Heat Conduction. *Intl. J. of Heat and Mass Trans.* 124, pp. 1212-1216, 2018